ssion of Interest to the
perconducting Super Collider Laboratory

SSCL-SR-1165
SSC-EOI0010

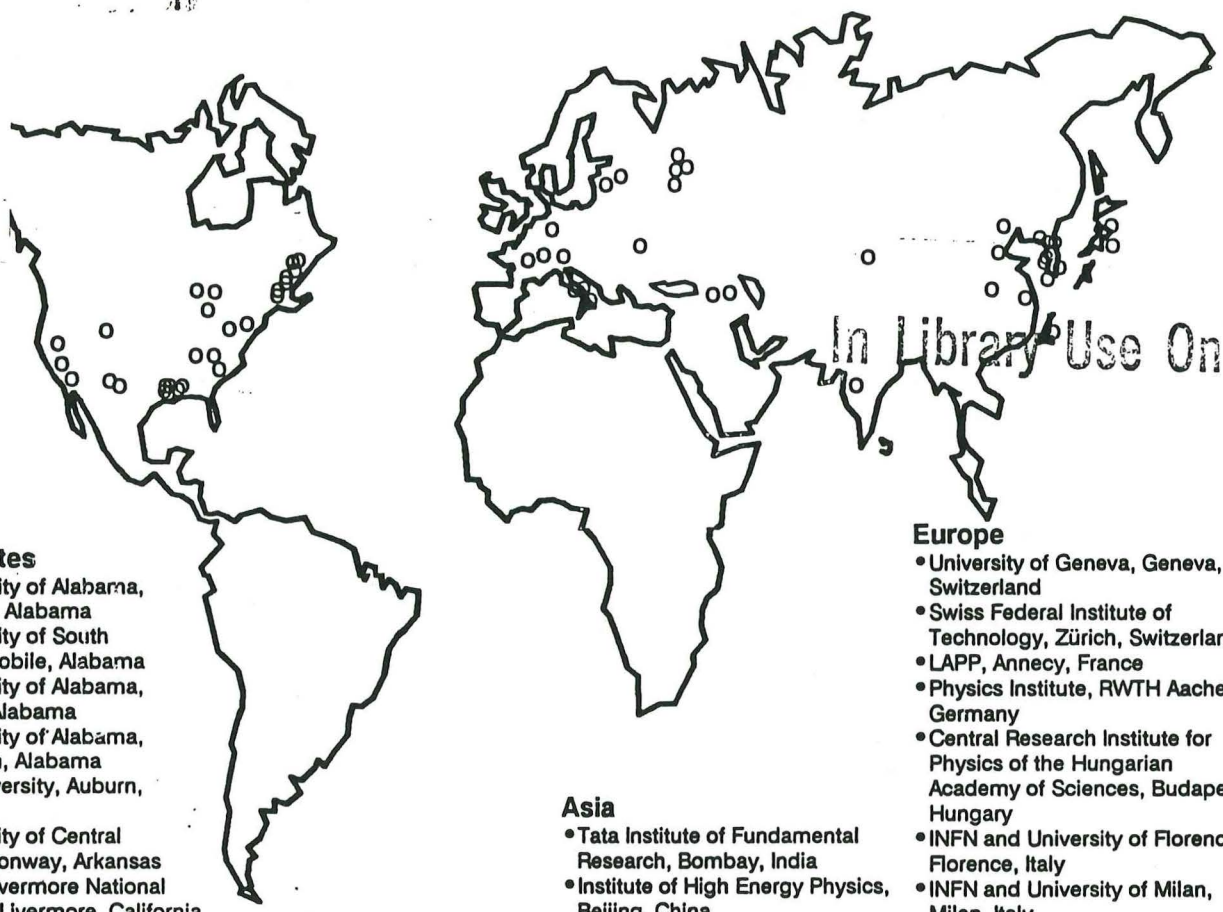

United States

- The University of Alabama, Tuscaloosa, Alabama
- The University of South Alabama, Mobile, Alabama
- The University of Alabama, Huntsville, Alabama
- The University of Alabama, Birmingham, Alabama
- Auburn University, Auburn, Alabama
- The University of Central Arkansas, Conway, Arkansas
- Lawrence Livermore National Laboratory, Livermore, California
- California Institute of Technology, Pasadena, California
- University of California, San Diego, California
- Purdue University, Lafayette, Indiana
- Indiana University, Indiana
- Johns Hopkins University, Baltimore, Maryland
- Boston University, Boston, Massachusetts
- Harvard University, Cambridge, Massachusetts
- Massachusetts Institute of Technology, Cambridge, Massachusetts
- The Charles Stark Draper Laboratory, Cambridge, Massachusetts
- University of Mississippi, University, Mississippi
- Mississippi State University, Starkville, Mississippi
- Jackson State University, Jackson, Mississippi
- Princeton University, Princeton, New Jersey
- Los Alamos National Laboratory, New Mexico
- University of New Mexico, New Mexico
- Columbia University, New York
- LeCroy Corporation, Chestnut Ridge, New York
- Carnegie Mellon University, Pittsburgh, Pennsylvania
- Brown University, Providence, Rhode Island
- University of Tennessee, Knoxville, Tennessee
- Memphis State University, Memphis, Tennessee
- Vanderbilt University, Nashville, Tennessee
- Oak Ridge National Laboratory, Oak Ridge, Tennessee
- University of Utah, Salt Lake City, Utah
- Howard University, Washington, DC

Asia

- Tata Institute of Fundamental Research, Bombay, India
- Institute of High Energy Physics, Beijing, China
- Chinese University of Science and Technology, Hefei, China
- Shanghai Institute of Ceramics, Shanghai, China
- High Energy Physics Group, Taiwan, China
- Waseda University, Science and Engineering Research Laboratory, Tokyo, Japan
- Saitama College of Health, Saitama, Japan
- Kyungpook National University, Taegu, Korea
- Gyeongsang National University, Jinju, Korea
- Chungnam National University, Daejeon, Korea
- Cheonnam National University, Kwangju, Korea
- Kangreung National College, Kangreung, Korea
- Korea University, Seoul, Korea
- Seoul National University, Seoul, Korea
- Sangli College, Wonju, Korea
- Taegu University, Taegu, Korea

Europe

- University of Geneva, Geneva, Switzerland
- Swiss Federal Institute of Technology, Zürich, Switzerland
- LAPP, Annecy, France
- Physics Institute, RWTH Aachen, Germany
- Central Research Institute for Physics of the Hungarian Academy of Sciences, Budapest, Hungary
- INFN and University of Florence, Florence, Italy
- INFN and University of Milan, Milan, Italy
- INFN and University of Naples, Naples, Italy
- University of Rome, Rome, Italy

U.S.S.R.

- Joint Institute for Nuclear Research (JINR), Dubna
- Leningrad Nuclear Physics Institute, Leningrad
- Institute of Theoretical and Experimental Physics, ITEP, Moscow
- Kurchatov Atomic Institute, Moscow
- Institute for High Energy Physics, Serpukhov
- Institute of Nuclear Physics, Novosibirsk
- Yerevan Physics Institute, Yerevan, Armenia
- Institute of Physics, Academy of Sciences of the Georgian SSR, Tbilisi
- Institute of Physics, Academy of Sciences of the Estonian SSR, Tartu

By the

L * COLLABORATION

Expression of Interest

to the Superconducting Super Collider Laboratory by the L* Collaboration

May 1990

The University of Alabama, Tuscaloosa, Alabama, USA
L.Baksay, J.Busenitz, D.DiBitonto, L.Junkins, X.Liu, T.Pennington,M.Timko, D.Whitcomb, L.Wurtz, Y.Yu

The University of South Alabama, Mobile, Alabama, USA
K.Clark, M.Jenkins

The University of Alabama, Huntsville, Alabama, USA
J.Gregory, Y.Takahashi

The University of Alabama, Birmingham, Alabama, USA
J.Harrisson, E.Robinson

Auburn University, Auburn, Alabama, USA
J.Williams

The University of Central Arkansas, Conway, Arkansas, USA
H.Woolverton

Lawrence Livermore National Laboratory, Livermore, California, USA
E.Ables, R.Bionta, H.Britt, A.Chargin, G.Deis, O.Edwards, O.Fackler, J.Heim, C.Henning, D .Makowicki, J.Miller, M.Mugge, W.Neff, H.S.Park, S.Shen, S.Sierskowski, K.Skulina, D.Slack, W.Stoffel, R.Vital

California Institute of Technology, Pasadena, California, USA
M.Chen, G.Gratta, D.Kirkby, R.Mount, H.Newman, R.Y.Zhu

University of California, San Diego, California, USA
J.B.Branson, M.Hebirt, E.Sheer, X.Sopczek

Purdue University, Lafayette, Indiana, USA
A.Bujak, L.Gutay, T.McMahon

Indiana University, Indiana, USA
M.Gebhard, R.Heinz, A.Komives, L.Miller, S.Mufson, J.Musser, G.Spiczak, G.Turner

Johns Hopkins University, Baltimore, Maryland, USA
H.Akbari, J.Bao, C-Y.Chien, G.Feldman, T.Fulton, C.W.Kim, J.F.Krizmanic, J.D.Orndorff, A.Pevsner, W.J.Spangler, C.Spartiotis, A.Szalay

Boston University, Boston, Massachusetts, USA
S.Ahlen, G.Bauer, J.Beatty, J.Brooks, T.Coan, M.Felcini, J.Hu, D.Levin, W.Lu, A.Marin, S.Otwinowski, D.Osborne, J.Rohlf, D.Warner, B.Zhou

Harvard University, Cambridge, Massachusetts, USA
K.Kamar, P.McBride, J.Schuette, K.Strauch

Massachusetts Institute of Technology, Cambridge, Massachusetts, USA
A.L. Anderson, U.Becker, P.Berges J.D.Burger, Y.H.Chang, M.Chen, I.Clare, R.Clare, T.S.Dai, F.J.Eppling, M.Fukushima, M.P.J.Gaudreau, K.Giboni, C.Grinnell, E.S.Hafen, P.Haridas, G.Herten, A.Kerman, T.Kramer, T.Lainus, D.Luckey, P.Marsten, D.B.Montgomery, I.A.Pless, J.M.Qian, M.Sarakinos, S.M.Shotkin, M.Steuer, J.D.Sullivan, K.Sumorok, J.Tang, Samuel C.C. Ting, S.M.Ting, T.J.Wenaus, M.White, S.X.Wu, B.Wyslouch, C.H.Ye

The Charles Stark Draper Laboratory, Cambridge, Massachusetts, USA
R.Araujo, J.Barry, E.Berk, M.Fury, M.Hansberry, T.Hines, G.Holden, F.Nimblett, J.Paradiso, W.Toth, L.Wilk

University of Mississippi, University, Mississippi, USA
L.Cremaldi, J.Furgeson, S.Harper, J.Reidy, J.Zhang

Mississippi State University, Starkville, Mississippi, USA
L.Croft, B.Piercey

Jackson State University, Jackson, Mississippi, USA
F.Lott

Princeton University, Princeton, New Jersey, USA
J.Bakken, M.Convery, P.Denes, D.Lea, P. Piroué, K.Read, H.Sicotte, D.Stickland, R.Sumner, D.Wright

Los Alamos National Laboratory, New Mexico, USA
D.Alde, R.Barber, J.Boissevain, D.Campbell, T.Carey, G.Dransfield, R.Farber, P.Ferguson, V.Gavron, D.Giovanelli, R.Gupta, J.Hanlon, S.Hecker, C.Hosford, J.Kapustinsky, W.W.Kinnison, E.Knapp, B.Kortegaard, R.Kruger, K.Lackner, A.Lapedes, D.M.Lee, M.Leitch, R.Lemons, R.Little, T.Lopez, M.Mattis, M.Merrigan, D.Metzger, W.O.Miller, G.Mills, F.A.Morse, J.M.Moss, E.Mottola, M.Merrigan, S.Newfield, R.Perkins, R.Prael, W.Rodriguez, S.P.Rosen, C.Sadler, V.D.Sandberg, G.H.Sanders, D.Sharp, R.Slansky, B.Smith, W.Sommer, G.Stephenson, D.Strottman, J.Sunier, T.Thompson, G.T.West, D.H.White, J.Williams, W.Wilson, K.Woloshun, H.J.Ziock

University of New Mexico, New Mexico, USA
J.Ellison, D.Finley, S.Humphries, B.H.Wildenthal

Columbia University, New York, USA
E.Aprile, Reshmi Mukherjee

LeCroy Corporation, Chestnut Ridge, New York, USA
M.Gorrics, B.Manor, R.Sumner,

Carnegie Mellon University, Pittsburgh, Pennsylvania, USA
I.Brock, A.Engler, T.Fergusson, R.W.Kraemer, F.Linde, C.Rippich, J.Smith, R.Sutton, H.Vogel

Brown University, Providence Rhode Island, USA
M.Aryal, A.De Silva, D.Rossi, M.Widgoff

University of Tennessee, Knoxville, Tennessee, USA
S.C.Berridge, W.M.Bugg, G.T.Condo, Y.C.Du, T.Handler, H.J.Hargis, E.L.Hart, R.Kroeger, A.Weidemann

Memphis State University, Memphis, Tennessee, USA
D.Franceschetti, S.Jahan, W.Jones

Vanderbilt University, Nashville, Tennessee, USA
S.Csorna

Oak Ridge National Laboratory, Oak Ridge, Tennessee, USA
D.J.Alexander, B.R.Appleton, P.E.Arakawa, J.B.Ball, F.E.Barnes, J.M.Barnes, M.L.Bauer, R.L.Beatty, J.A.Blank, L.A.Boatner, C.Bottcher, H.R.Brashear, C.R.Brinkman, T.J.Burns, J.G.Carter, B.C.Chakoumakos, M.M.Chiles, J.E.Choate, L.G.Christophoruou, F.E.Close, H.O.Cohn, R.I.Crutcher, F.C.Davis, R.E.DePew, J.H.DeVan, T.H.Dunigan, M.S.Emery, H.Faides, T.A.Gabriel, T.A.Herrick, M.J.Hollis, D.T.Ingersoll, J.O.Johnson, J.W.Johnson, H.E.Knee, D.P.Kuban, R.J.Lauf, D.L.McCorkle, S.A.McElhaney, D.L.McElroy, J.W.Moore, F.Plasil, R.T.Primm III, M.J.Rennich, R.T.Santoro, T.E.Shannon, B.H.Singletary, V.K.Sikka, T.P.Sjoreen, M.S.Smith, J.W.Stapleton, M.R.Strayer, R.W.Swindeman, A.W.Trivelpiece, J.R.Tubb, J.F.Wendelken, D.M.Williams, A.C.Williamson, A.Wintenberg, C.Y.Wong, K.G.Young

University of Utah, Salt Lake City, Utah, USA
H.Bergeson, M.Salamon

Howard University, Washington DC, USA
R.M.Catchings, J.Lindesay

University of Geneva, Geneva, Switzerland
M.Bourquin

Swiss Federal Institute of Technology, Zürich, Switzerland
H.Anderhub, J.Behrens, A.Biland, M.Dhina, G.Faber, M.Fabre, R.Fabbretti, K.Freudenreich, M.Haensli, H.Hofer, I.Horvath, E.Isiksal, M.Jongmanns, H.Jung, J.Lettry, P.Lecomte, P.LeCoultre, L.Li, X.Lue, M.MacDermott, M.Maolinbay, D.McNally, M.Pohl, G.Rahal-Callot, P.Razis, H.Rykaczewski, D.Ren, B.Spiess, H.Suter, J.Ulbricht, G.Viertel, H.VonGunten, S.Waldmeier, J.Weber, L.Zehnder

LAPP, Annecy, France
J.J.Blaising, R.Morand, M.Schneegans, M.Vivargent

Physics Institute, RWTH Aachen, Germany
P.Blömeke, M.Buchholz, E.Coulig, H.Haan, K.Hilgers, W.Karpinski, H- H.Kleinmanns, O.Kornadt, W.Krenz, T.Lehmann, K.L.Lübelsmeyer, T.Meinholz, D.Pandoulas, J.Y.Pei, M.Rhöhner, R.Siedling, D.Schmitz, K.Schmiemann, M.Schöntag, A.Schultz von Dratzig, J.Schwenke, G.Schwering, M.Toporowsky, W.Wallraff, W.Xiao, Y.Zeng, J.Zhou

Central Research Institute for Physics of the Hungarian Academy of Sciences, Budapest, Hungary
Gy.Bencze, E.Dénes, E.Nagy, J.Tóth, L.Urbán

INFN and University of Florence, Florence, Italy
A.Baldini, M.Bocciolini, M.Bruzzi, A.Cartacci, G.Ciancaglini, C.Civinini, R.D'Alessandro, E.Gallo, M.Meschini, M.Pieri, P.Spillantini, J.F.Wang

INFN and University of Milan, Milan, Italy
E. Borchi, A. Penzo, P. G. Rancoita, L. Riccati, A. Villari, L. Vismara

INFN, Naples and University of Naples, Naples, Italy
A. Aloisio, M. G. Alviggi, E. Brambilla, G. Chiefari, R. De Asmundis, E. Drago, V.Innocente, S. Lanzano, L. Merola, M. Napolitano, S. Patricelli, C. Sciacca

University of Rome, Rome, Italy
L. Barone, B. Borgia, F. Cesaroni, F. De Notaristefani, E. Longo, G. Mirabelli, S. Morganti

Tata Institute of Fundamental Research, Bombay, India
T.Aziz, S.Banerjee, S.R.Chendvankar, S.N.Ganguli, S.K.Gupta, A.Gurtu, A.K.Jain, P.K.Malhotra, K.Mazumdar, R.Raghavan, K.Shankar, K.Sudhakar, S.C.Tonwar

Joint Institute for Nuclear Research (JINR), Dubna, USSR
E.Belyakova, A.Cheplakov, A.Cheremukhin, S.Dolya, V.Dunin, Yu.Ershov, N.Fadeev, A.Feshchenko, V.Genchev, I.Geshkov, I.Golutvin, N.Gorbunov, I.Gramenitsky, I.Ivanchenko, M.Kadykov, V.Kalagin, A.Karev, V.Karzhavin, M.Kazarinov, S.Khabarov, V.Khabarov, Yu.Kiryushin, D.Kiss, V.Krivokhizhin, V.Kukhtin, R.Lednicky, I.Lukyanov, V.Lysyakov, A.Makhankov, V.Minashkin, N.Nogaytsev, V.Odintsov, V.Perelygin, D.Peshekhonov, V.Peshekhonov, D.Pose, V.Prikhodko, A.Prokesh, A.Rashevsky, I.Savin, S.Sergeev, M.Shafranov, I.Shpak, A.Skrypnik, G.Smirnov, D.Smolin, V.Sviridov, G.Sultanov, A.Vishnevsky, Yu.Yatsunenko, O.Zaimidoroga, M.Zamyatin, A.Zarubin, V.Zhiltsov, E.Zubarev

Leningrad Nuclear Physics Institute, Leningrad, USSR
V.Andreev, A.Denisov, Y.Dokshitser, V.Ivochkin, V.Janovsky, A.Kaschuk, V.Khoze, A.Krivshich, P.Levtchenko, V.Mayorov, A.Nadtochy, V.Razmyslovich, Y.Ryabov, V.Samsonov, A.Sarantsev, V.Schegelsky, A.Schetkovsky, Y.Sokornov, A.Shevel, N.Smirnov, E.Spiridenkov, V.Suvorov, A.Tsaregorodtsev, G.Velichko, S.Volkov, A.Vorobyov, An.Vorobyov, Y.Zalite

Institute of Theoretical and Experimental Physics, ITEP, Moscow, USSR
A.Arefiev, A.Artamonov, A.Babaev, V.Bocharov, S.Burov, N.Bystrov, M.Chumakov, A.Dolgolenko, V.Dolgoshein, V.Efremenko, V.Ephstein, A.Epifanzev, A.Fedotov, Yu.Galaktionov, V.Gemanov, P.Gorbunov, A.Gordeev, B.Gordeev, P.Gorichev, Yu.Gorodkov, E.Grigoriev, R.Gurin, Yu.Kamyshkov, V.Khovansky, Yu.Kirilko, A.Klimentov, Yu.Kornelyuk, V.Koutsenko, A.Kovalenko, S.Kruchinin, M.Kubantsev, A.Kuchenkov, A.Kunin, V.Lebedenko, I.Makhlueva, A.Malinin, S.Mamontov, A.Maslennikov, V.Morgunov, A.Nikitin, N.Pankin, V.Plotnikov, V.Plyaskin, V.Pojidaev, A.Rozjkov, M.Ryabinin, I.Satsky, A.Savin, M.Savitsky, A.Selivanov, V.Semetchkin, V.Shamanov, P.Shatalov, S.Shevchenko, V.Shevchenko, K.Shmakov, V.Shoutko, E.Shumilov, A.Smirnov, M.Sokolov, S.Solomentzev, E.Tarkovsky, V.Tchudakov, I.Vetlitsky, V.A.Vinogradov, V.B.Vinogradov, I.Vorobiev, V.Zaitsev, O.Zeldovich, S.Zeldovich, N.Zvetkov

Kurchatov Atomic Institute, Moscow, USSR
S.Barabanov, A.Barkov, S.Belyaev, L.Bragin, N.Chernoplekov, T.Chunyaeva, T.Davlatyan, G.Dorofejev, V.Drozdou, V.Evdokimov, S.Frolov, E.Golubev, E.Grishin, A.Imenitov, V.Karpov, I.Karpushov, E.Klimenko, A.Kochergin, V.Kruglov, V.Kulyasov, Yu.Kurojedov, A.Kuznetsov, S.Lelekhov, O.Lusitenko, Yu.Lusitenko, A.Malofejev, V.Manko, V.Martemyanov, N.Martovetsky, V.Martynenko, A.Matvejev, V.Mokhnotuk, E.Mukhina, A.Myagkov, S. Novikov, A.Ogloblin, I.Ovchinnikov, S.Osetrov, V.Patrikejev, V.Podshibyakin, K.Polulyakh, V.Portugalsky, G.Razorenov, N.Rodina, V.Ryabov, A.Safronov, M.Sedov, V.Selivanov, B.Seregin, E.Shatnyi, M.Solodnev, S.Svertnev, S.Terentjev, E.Velikhov, P.Volkov, A.Voropaev, P.Vorotnikov, T.Vostrikova, M.Vyirodov, E.Vyisotsky, I.Zotov

Institute for High Energy Physics, Serpukhov, USSR
N.Fedyakin, A.Kozelov, R.Krasnokutsky, A.Lebedev, S.Medved, Yu.Mikhailov, E.Razuvaev, R.Shuvalov, E.Slobodyuk, A.Vasiliev

Institute of Nuclear Physics, Novosibirsk, USSR
L.Barkov, A.Skrinsky, E.Solodov

Yerevan Physics Institute, Yerevan, Armenia, USSR
N.Akopov, A.Amatuni, Ts.Amatuni, R.Astabatyan, R.Avakyan, A.Avatesyan, G.Bayatyan, P.Galumyan, A.Hagomeryan, R.Kavolov, S.Kazaryan, S.Matinyan, G.Mkrtchyan, A.Oganesyan, J.Petrosyan, V.Pogosov, K.Shikhlyarov, A.Sirunyan, S.Taroyan, N.Ter-Isaakyan, G.Vartapetyan

Institute of Physics, Academy of Sciences of the Georgian SSR, Tbilisi
D.Chkareuli, G.Dvali, N.Manjalidze, G.Leptukh, P.Petman, T.Lomtadze, A.Djavrishvili, E.Zadadze, I.Iashvili, K.Ahabadze, M.Svanidze, E.Ioramashvili, N.Roinishvili, L.Gabuniya, L.Hizanishvili

Institute of Physics, Academy of Sciences of the Estonian SSR, Tartu
I.Ots, H.Uibo

Institute of High Energy Physics, Beijing, China
C.Chen, G.M.Chen, H.S.Chen, S.X.Fang, S.G.Gao, W.X.Gu, Y.F.Gu, Y.N.Guo, Y.Han, J.He, J.T.He, B.N.Jin, H.T.Li, J.Li, P.Q.Li, W.G.Li, X.G.Li, S.Z.Lin, Q.Liu, Y.S.Lu, Z.P.Mao, L.J.Pan, Z.M.Qian, G.Rong, Y.Y.Shuo, X.W.Tang, K.L.Tung, J.H.Wang, L.Z.Wang, R.J.Wu, Y.G.Wu, Z.D.Wu, R.S.Xu, Y.D.Xu, S.T.Xue, C.G.Yang, C.Y.Yang, K.S.Yang, Q.Y.Yang, Z.Q.Yu, B.Y.Zhang, C.C.Zhang, D.H.Zhang, L.S.Zhang, S.Q.Zhang, D.X.Zhao, M.Zhao, Z.P.Zheng, G.Y.Zhu, Q.M.Zhu, Y.C.Zhu, Y.S.Zhu, H.L.Zhuang,

Chinese University of Science and Technology, Hefei, China
H.F.Chen, Z.F.Gong, C.H.Gu, C.Li, Z.Y.Lin, W.G.Ma, C.R.Wang, X.L.Wang, Z.M.Wang, Z.Z.Xu, B.Z.Yang, J.B.Ye, X.Q.Yu, Z.P.Zhang

Shanghai Institute of Ceramics, Shanghai, China
X.L.Fang, P.X.Gu, J.K.Guo, C.F.He, G.Q.Hu, S.K.Hua, H.J.Li, J.L.Li, P.J.Li, Q.Z.Li, Z.L.Pan, D.Z.Shen, G.S.Shen, E.W.Shi, W.T.Su, X.X.Wang, Z.Y.Wei, Y.Y.Xie, L.Xu, Z.L.Xue, D.S.Yan, Z.W.Yin, X.L.Yuan, Y.F.Zhang, G.M.Zhao, Y.L.Zhao, W.Z.Zhong, R.M.Zhou

High Energy Physics Group, Taiwan, China
C.Chang, A.Chen, W.Y.Chen, H.Y.Cheng, Y.C.Gau, S.S.Gau, Y.Y.Lee, W.T.Lin, W.T.Ni, Y.D.Tsai, S.C.Yeh

Waseda University, Science and Engineering Research Laboratory, Tokyo, Japan
T.Doke, J.Kikuchi

Saitama College of Health, Saitama, Japan
K.Matsuda

Kyungpook National University, Taegu, Korea
D.Son, S.K.Cho, J.K.Ko

Gyeongsang National University, Jinju, Korea
J.S.Song,I-G.Park, S-K.Choi, K.S.Chung

Chungnam National University, Daejeon, Korea
H.Y.Lee

Cheonnam National University, Kwangju, Korea
J..Kim

Kangreung National College, Kangreung, Korea
D.W.Kim, G.S.Kang

Korea University, Seoul, Korea
J.S.Kang

Seoul National University, Seoul, Korea
J.Kim

Sangji College, Wonju, Korea
Y.Y.Keum

Taegu University, Taegu, Korea
D.S.Kim

Spokesperson:
Samuel.C.C.Ting
MIT-LNS, Bldg.44
51 Vassar Street
Cambridge, MA02139, USA

A. PHYSICS CONSIDERATIONS

Advancements in physics are based on the close interplay between experiment and theory. Advancements in theory are based on the ability of theorists to explain existing experimental results and to predict new phenomena to be confirmed by experiments. Revolutions in physics occur when an experimental result contradicts the theoretical prediction which leads to the creation of new theory. There is no theory that can disprove an experimental result, whereas a theory, however logical and elegant, cannot be valid if it does not conform to experimental observations. Over the last quarter of the century, careful experimentation in physics, such as the observation of CP violation in K decay, the discovery of the J particle, and the discovery of high temperature superconductors have opened up new fields of research in physics. These observations were carried out by experiments even though there was no apriori theoretical interest.

Over a period of a quarter of a century, there have been many fundamentally important discoveries in elementary particle physics. These discoveries, which gave us more confidence in the Standard Model, were all made by precision experiments on leptonic and photonic final states. Indeed, one can recall the following examples:

1)The discovery of two neutrinos [1.1] came from measuring μ and e final states.

2)The discovery of the J particle [1.2] shown in Fig.1.1 was done by an experiment on e^+e^- final states with a mass resolution of 0.1% and a hadron background rejection of $1/10^{10}$.

3) The τ lepton [1.3] was discovered with a 4π detector measuring coincidence of μe final state.

4)The discovery of P_c state by the DASP collaboration [1.4] at DORIS in July 1975 from a very clear and elegant observation of 2 γ transition of Ψ' is one of the most important confirmation of the existence of charm quarks.

5)The Υ particle [1.5] (Fig.1.2) was discovered by an experiment with a μ pair mass resolution of 2%.

6)The proof that the J particle is indeed a bound state of $c\bar{c}$ quarks comes from precision inclusive photon measurements with NaI crystals by the crystal ball group [1.6] (Fig.1.3). The identification that the Υ particle is from a bound state of $b\bar{b}$ quarks comes from inclusive photon measurements by the CUSB [1.7], and CLEO groups [1.8] as well as by the ARGUS and Crystal Ball groups [1.9].

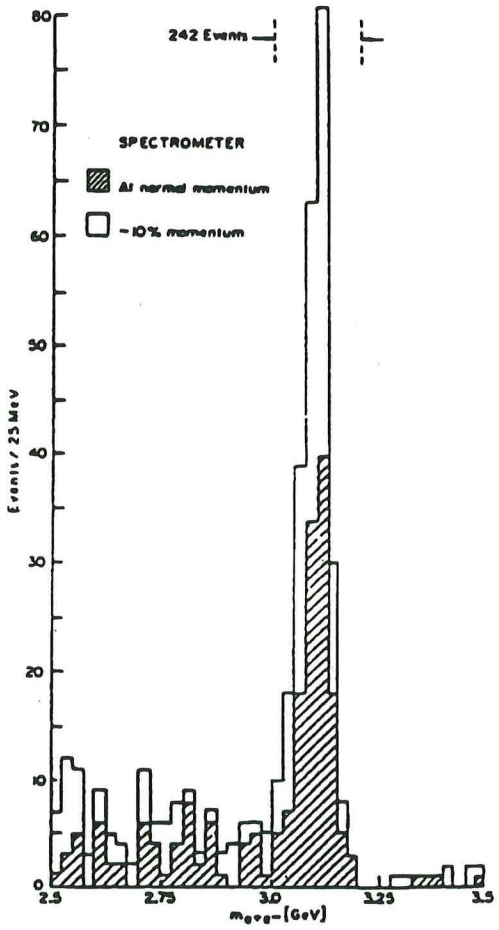

Fig. 1.1 The discovery of the J particle

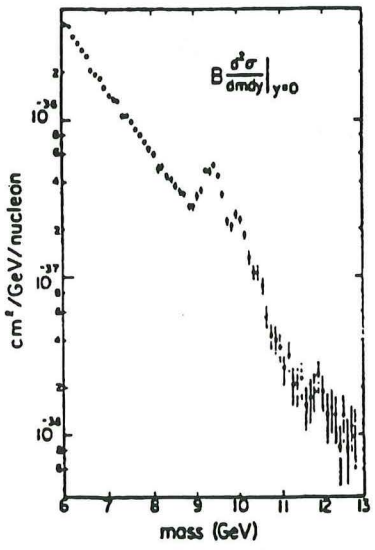

Fig. 1.2 The discovery of the Υ particle: Muon pair spectrum observed at Fermi National Laboratory with a detector having a mass resolution of 2%.

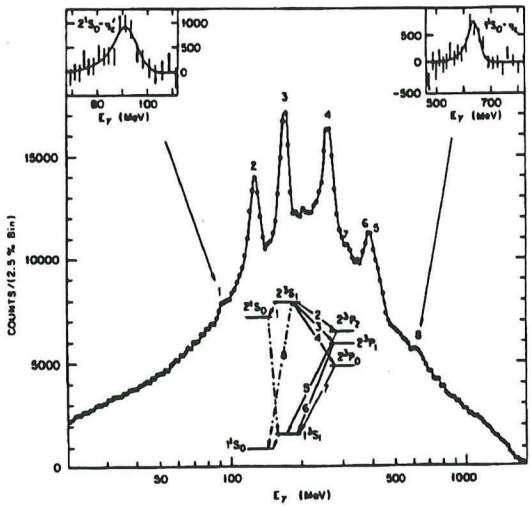

Fig. 1.3 Inclusive photon spectrum at the Ψ' from the Crystal Ball experiment at SLAC, showing essentially all of the charmonium spectrum.

7)The discovery of the Z^0 particle [1.10] (shown in Fig.1.4) was done with a large solid angle detector measuring e^+e^- and $\mu^+\mu^-$ final states.

8)The $W^{\pm}$ [1.11] were found by measuring their large momentum single electron and muon decays.

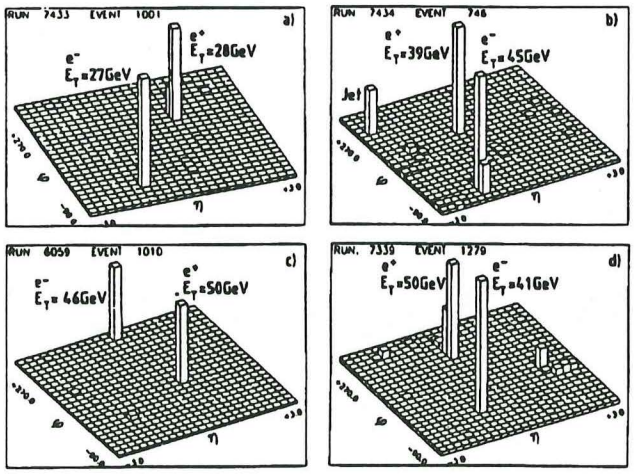

Fig. 1.4 The discovery of the Z^0 particle: The spectrum shows a e^+e^- correlation from Z^0 decay at UA1, CERN.

These facts lead us to make the following observations:

i)These discoveries were not predicted when the original accelerators were constructed (the Z and W excepted).

ii)None of these discoveries were made by detecting hadronic final states.

iii)In general, the decay rate of heavy particles into single lepton, single photon and lepton pairs is much smaller than the decay rate into hadrons. However, since the background of single lepton, single photon and lepton pair is generally very small, if an experiment can be done cleanly, precisely, with good resolution and good hadron rejection, **one can easily distinguish the signals from the background**, as shown in Figs.1.1 to 1.4.

iv)The need for resolution can be easily established by recalling not only the history of the J particle but also by the recent precision muon pair experiment done at Fermi National Laboratory where the original resonance seen in Fig. 1.2 was shown to be a composite of many states [1.12] (Fig.1.5).

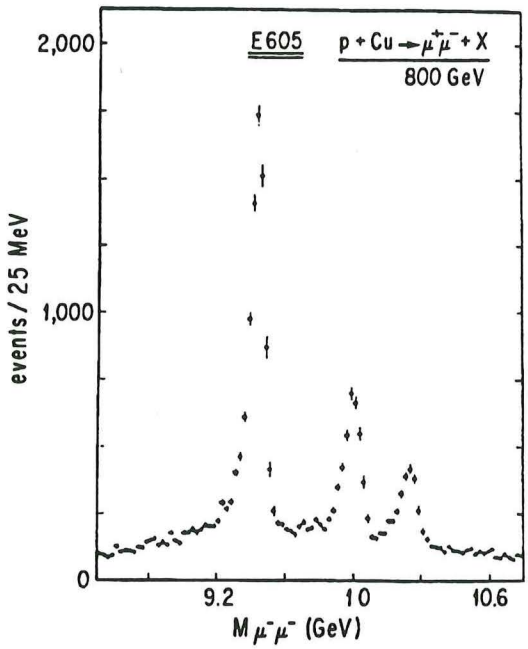

Fig. 1.5 The Υ spectrum as observed at Fermi National Laboratory with a precision muon pair spectrometer. The graph comes from a preprint by M.R.Adams, University of Illinois, Chicago

B. PHYSICS OBJECTIVES

We are interested in proposing a 4π detector to be used at the SSC Laboratory to measure precisely inclusive leptons and photons with a hadron rejection $\frac{\text{lepton}}{\text{hadron}} \sim 10^{-4}$ for $P_t > 0.1$ TeV and measure lepton pairs with a mass resolution $\frac{\Delta m}{m} \sim 1\%$ at a mass of 1 TeV. Hadron jets would also be measured. Our intent is to search not only for particles predicted by existing theories, such as Higgs, but more importantly **to look for new and unpredicted phenomena,** which is the main purpose for the construction of the Superconducting Super Collider.

C. EXPERIENCE

It has taken many physicists in the L* collaboration nearly 25 years to develop the techniques to perform an experiment measuring γ, leptons and lepton pairs with

high precision and large solid angle. The graph below is a summary of this learning process by the MIT group.

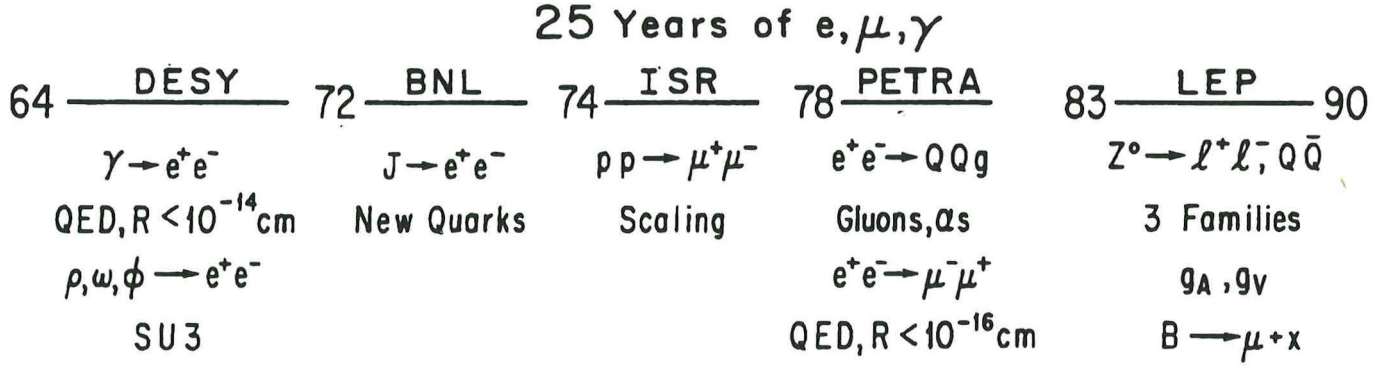

Twenty-five years ago, at DESY, in the process of checking the validity of quantum electrodynamics and studying leptonic decay of vector mesons, the DESY-MIT group developed techniques to measure leptons in a high intensity γ beam of 10^{11} per second. They obtained a rejection $\frac{ee}{hh} = \frac{1}{10^6}$ and a mass resolution of $\frac{\Delta m}{m} \sim 1\%$.

In the early seventies, at Brookhaven, based on the experience acquired at DESY, the MIT-BNL group designed a spectrometer able to measure lepton pairs in a high intensity proton beam of 10^{12} per second (equivalent to a luminosity of 10^{36} $cm^{-2}s^{-1}$) with a $\frac{ee}{hh} = \frac{1}{10^{10}}$ rejection and a mass resolution of $\frac{\Delta m}{m} \sim 0.1\%$. This led to the discovery of the J particle.

Subsequently, the CERN-Harvard-MIT-Naples-Pisa group designed an experiment at the ISR, CERN, with a 2π solid angle measuring μ pair production with a luminosity of 10^{31} to 10^{32}. This experiment was carried out with the classical method of surrounding intersection regions with a vertex chamber followed by magnetized iron sandwiched with large drift chambers [1.13]; It measured $pp \rightarrow \mu\mu$ scaling precisely.

In the late seventies, at PETRA, the Aachen -DESY -JENNIKHEF- MIT group built a 4π calorimeter detector [1.14] (MARK J) measuring electrons, muons and hadron jets. This experiment measured precisely muon pair assymetry with a systematic error of 1%. The result confirmed the prediction of the Standard Model. At the same time, the Aachen- Desy- ... group (TASSO) built the first modern large solid angle detector surrounding the interaction region with an excellent central tracking detector followed by an electromagnetic detector with good angular coverage. The work of the PETRA groups form much of the fundation of experimental support for our understanding of QCD. Also in this period, the CERN-Dubna group (BCDHS collaboration) built a high luminosity spectrometer at the SPS to study precisely deep inelastic scattering of muons. Their results form strong independent support of QCD.

At LEP, many physicists in this EoI participated in building a 4π detector L3 (see Chapter II) which measures a 100 GeV particle decaying into a pair of muons with a mass resolution of 1.7%. L3 also measures electrons and photons with a coordinate resolution of $\approx$ 1mm, an energy resolution of 5% at 100 MeV and an energy resolution of 1% at 2 GeV. The hadron calorimeter in L3 measures hadron energy with a resolution of $(\frac{55}{\sqrt{E}} + 5)\%$ and $\Delta\theta = 3.0°$, $\Delta\varphi = 2.5°$ for jets. The L3 detector has a good hadron rejection. The momentum of μ(e) is measured twice, first in the vertex chamber with a value of P_v, and second, by the precision muon chambers with a value P_μ , or in BGO with value P_e . The muon energy loss ΔE is measured by the sampling calorimeter which also monitors hard photon radiation. The energy balance,

$$P_v = \Delta E + P_\mu \quad \text{or} \quad P_v = P_e$$

eliminates hadrons. The properties of L3 make it the only LEP detector adaptable for use at the LEP Hadron Collider (LHC).

Over the last 15 years, the MIT group (U.Becker and his colleagues) has conducted a continuous systematic R&D effort to investigate precision instrumentation for muon physics. This research effort has covered the following areas:

1) **Gas study**: selection of the best gas for large area drift chambers in a magnetic field.

2) **Chamber construction**: development of methods to build simple high resolution muon chambers covering an area of $\approx 1000m^2$.

3) **Supporting structure**: development of supporting structures for precise alignment of the chambers, in collaboration with Draper Laboratory.

4) **Alignment systems**: development of high precision alignment systems with UV laser verification.

This program involved the coordinated efforts of many universities in the United States, in particular Harvard (K.Strauch) and Northeastern (M.Gettner) as well as of research centers in Spain, CIEMAT-Madrid (J.A.Rubio), The Netherlands (P.Duinker), Switzerland, ETHZ (P.Seiler) and Italy, Naples (C.Sciacca). The success of this program enabled us to build the ISR and PETRA experiments on time and within specifications. The success of this program is one of the main reasons why we have been able to build the ultra precise L3 detector at LEP. The fact that the L3 muon chamber system operates exactly according to the design is the main reason why we are proposing to build an extremely precise muon detector at the SSC.

The precision measurement of inclusive photons and electrons in L3 also results from many years of experience in measuring electrons in high background environment. To make a clean measurement of electrons and photons, it is important to eliminate two main backgrounds:

1) The $\pi^0 \Rightarrow 2\gamma \Rightarrow e^+e^-$ background from photon conversion. This implies :

a)a minimum amount of material in front of the electron (photon) detector.

b)a precision tracking detector in a magnetic field to separate the $\gamma \Rightarrow e^+e^-$ pairs.

c)a fine grain detector which can measure the e^+ and e^- separately and thus reject the $\gamma \Rightarrow e^+e^-$ pair.

2) The (π,e) confusion background: this is the case when a hadron enters the electron detector and behaves like an electron: this can occur either in the case of gas Cherenkov detectors due to the knock-on process or in the case of crystal detectors through shower fluctuations. This background can be most effectively rejected by measuring the electron momentum twice. First, by placing in front of the electron detector a precision spectrometer measuring the momentum P_1 of the electron, and secondly, by measuring the momentum P_2 in a second spectrometer or crystal detector. The constraint $P_1 = P_2$ effectively eliminates the (π,e) confusion background.

It was the careful application of these observations that enabled the BNL - MIT group to construct the BNL-J particle spectrometer which had an $\frac{ee}{hh}$ rejection of $\frac{1}{10^{10}}$ and a mass resolution $\frac{\Delta m}{m} \approx \frac{1}{1000}$

The application of such observations enabled the L3 group to construct the precision electromagnetic detector where the momentum and coordinate of the electron is measured first in the thin vertex chamber and then again with the fine grain BGO crystals detector.

In the last decade, the Shanghai Institute of Ceramics, under the leaderships of D.S.Yan and Z.W.Yin and in collaboration with Caltech (H.Newman), Carnegie-Mellon (A.Engler), Princeton (P.Piroué), LAPP Annecy (M.Vivargent), Lausanne (R.Weill), Rome (B.Borgia), Aachen (D.Schmitz), Lyon (J.P.Martin), Geneva (M.Bourquin) have systematically performed large scale R&D on:

1)Mass production at low cost of large, radiation resistant, high optical quality crystals.

2)Cutting crystal surfaces to 200μm accuracy.

3)Methods of coating crystal surface to obtain uniform pulse height response.

4)Electronics and data acquisition system to collect data with a linearity of 0.1% and a dynamic range of 20 bits.

5)Cooling system to ensure the temperature is constant to 0.1°C over large volumes.

6)Production of a thin structure to support the crystals to minimize the amount of inactive material in the detector.

7)A calibration system to ensure that the response of all crystals is known at all times.

8)Most importantly, continued R&D efforts to produce doped fast crystals for high intensity pp colliders.

The success of these R&D efforts enabled the L3 group to build the precise electromagnetic calorimeter consisting of 12000 crystals, to measure electrons and photons with a resolution of $(1.3/\sqrt{E}+0.5)\%$.

References

[1.1] Phys. Rev. Let. 9, (1962) 36.
[1.2] Phys. Rev. Let. 33 (1974) 1404
[1.3] Phys. Rev. Let. 35, (1975) 1489.
[1.4] Phys. Lett. 57B, (1975)
[1.5] Phys. Rev. Let. 39, (1977) 252.
[1.6] Proceedings of the 1981 International Symposium on Lepton and Photon Interactions at High Energies (1981) 165
[1.7] Phys. Rev. Let. 49 (1982) 1612 ; Phys. Rev. Let. 51 (1983) 160
[1.8] Phys. Rev. Let. 52 (1984) 799
[1.9] First report by ARGUS and Crystal Ball groups presented by P.M.Tuts in "Proceedings of the symposium on Leptons and Photons Interactions at High Energies, Cornell,1983
[1.10] Phys. Lett. 126B, (1983) 398.
[1.11] Phys. Lett. 122B, (1983) 103.
[1.12] Mark R. Adams, University of Illinois Preprint.
[1.13] U. Becker et al., NIM 128 (1975), 593.
[1.14] D.P. Barber et al, Phys. Report 63 (7) 333.

A. THE L* EXPERIMENT

Figures II.1 and II.2 show the side and middle section views of the L* design. It has the following detector elements:

1. A magnet system that consists of a central magnet providing a field of 0.75 T and forward-backward magnets with a field of 0.3 T. The central magnet can be either of conventional design with aluminum coil or a superconducting coil with iron return or a superconducting coil with a superconducting return coil to replace iron.

2. A precision muon detector provides a resolution:

$$\frac{\Delta P}{P} \approx 2.4\% \quad at \quad P = 0.5\ TeV \text{ or}$$

$$\frac{\Delta m}{m} \approx 1.7\% \quad \text{for} \quad m = 1\ TeV$$

over the polar angular region down to $|\theta| > 2°$

3. A very fast hadron calorimeter (central part and forward-backward part) covering down to $\theta = 2°$, made of nonmagnetic stainless steel-lead sandwich with silicon or liquid scintillator detectors. The calorimeter response has a rise time of 2–5 ns and is constructed with a tower geometry pointing to the intersection region, with $\Delta\eta\Delta\varphi = 0.04 \times 0.04$, where η is the pseudorapidity and ϕ is the azimuthal angle. There is also a very forward part down to $\theta = 0.3°$

4. A transport system designed to easily remove and exchange the central tracking chamber and electromagnetic detector for either high luminosity ($>10^{34}$ cm^{-2}s^{-1}) run or runs with additional hadron calorimetry to replace the electromagnetic calorimeter for jet studies.

5. A precision electromagnetic detector covering the angular region $2° < \theta < 178°$ made of either high-resolution crystal, such as $BaF_2(La)$ currently under development by L* in collaboration with the Shanghai Institute of Ceramics and Leningrad, or liquid xenon. The electromagnetic calorimeter provides an energy resolution $\Delta E/E \approx (1.3/\sqrt{E} + 0.5)\%$ and a coordinate resolution $\Delta\theta = 0.2°$, $\Delta\varphi = 0.2°$, with an e/π rejection $\approx 10^{-4}$.

The combined electromagnetic and hadron calorimeter has a total of 12 λ, and the fine sampling

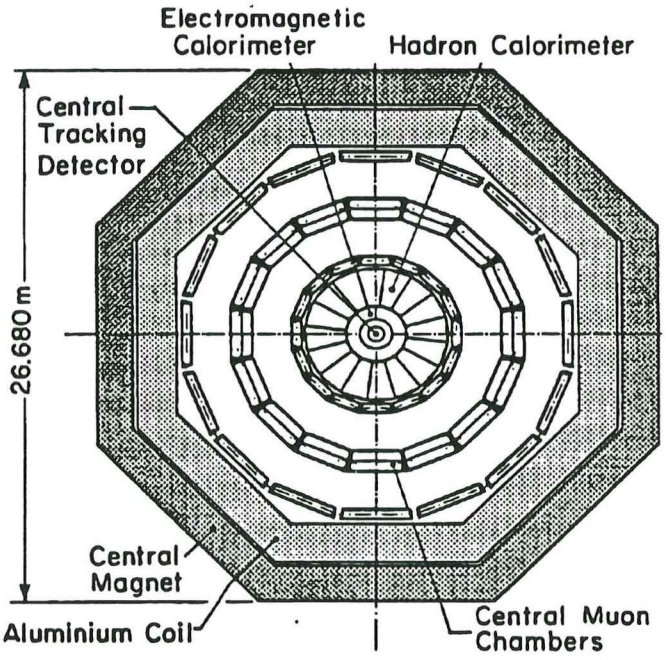

Fig. II.2. Middle section view of L*.

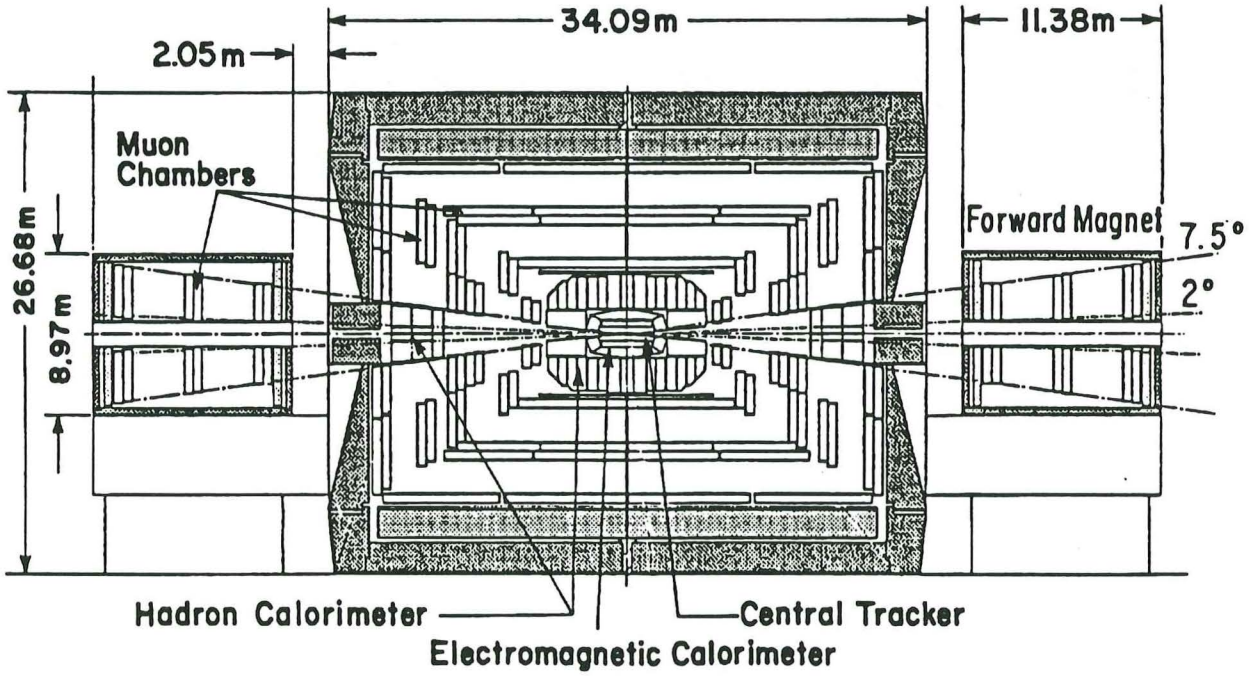

Fig. II.1. Side view of L*.

allows us to measure and track muons as well as measure radiated photons from muons.

6. A central tracking detector measuring a 0.5-TeV particle with a resolution of ≈50% so as (a) to distinguish the sign of e^+ and e^- from a 1-TeV particle $T \rightarrow e^+ e^-$, (b) to measure the multiplicity of charged particles surrounding e and μ, and (c) to measure the momentum of e and μ to match with precision e and μ measurements in specialized e and μ detectors.

B. THE L3 EXPERIMENT

The L3 experiment is the largest experiment in high energy physics, and it can be used at LHC. Therefore, it is instructive to review some of the key elements of the L3 experiment. In 1982 based on the experience we gained at DESY, Brookhaven, ISR-CERN, and PETRA, we began to build the L3 detector [II.1]. It is designed to study e^+e^- collisions in the 200-GeV range with emphasis on high-resolution measurement of electrons, photons, and muons. It is an effort involving a worldwide collaboration of 500 physicists belonging to 33 institutions from 13 countries. Preparation of the experiment from its conception to the beginning of data taking in summer 1989 took 8 years and 1100 technical man-years of effort. The components of the L3 detector are shown in Fig. II.3.

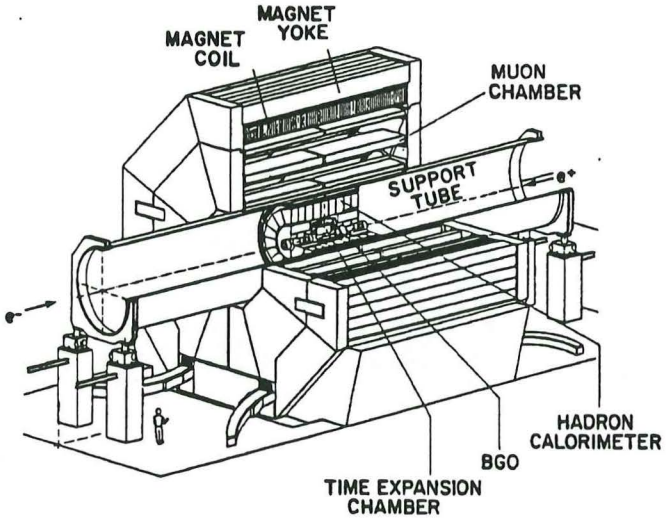

Fig. II.3. The L3 detector.

B. 1. Magnet

Since the momentum resolution $\Delta P/P$ of charged particles in a magnetic field increases as $\Delta P/P \propto 1/BL^2$, we have chosen a relatively low field in a large volume to optimize muon momentum resolution. The magnet has an inner radius of 6 m, and it provides a $BL^2 =$ 180 kG/m^2, 2 to 10 times larger than other detectors in high energy physics today. Figure II.4 shows the finished magnet with the near-side doors open. Figure II.5 is the result of the survey of the centers of the coil packages and shows how accurately the 1000-ton coil is aligned.

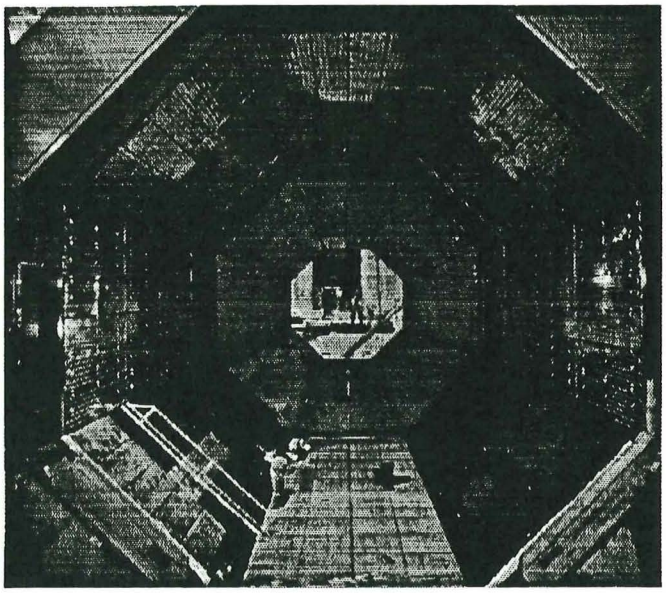

Fig. II.4. The completed L3 magnet.

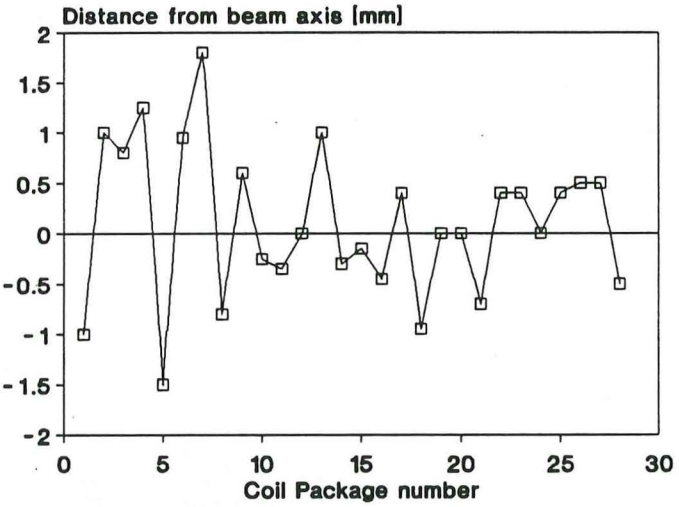

Fig. II.5. L3 coil alignment.

B. 2. Muon Detector

The momentum of muons p_μ is measured very precisely in free space with three layers of drift chambers. To obtain a momentum resolution $\Delta P/P$ of 2.4% at 50 GeV, nearly 10 years of effort from 1976 to 1986 were devoted to research, tests, construction, support system, and alignment system. The muon detector system covers a volume of 1000 m^3 and operates in a 5-kG field.

There is a total of 80 large drift chambers, each with an approximate area of 12 m^2. The muon chambers are supported by a specially designed structure which monitors the chamber positions to ±30 μm. Each chamber measures the muon coordinate to 50 μm and measures the angle to 1–2 mrad. This system enables us to measure a 100-GeV particle decaying into a pair of muons with a mass resolution: $\Delta m/m \approx 1.7\%$. Figure II.6 shows the muon chamber system inside the magnet.

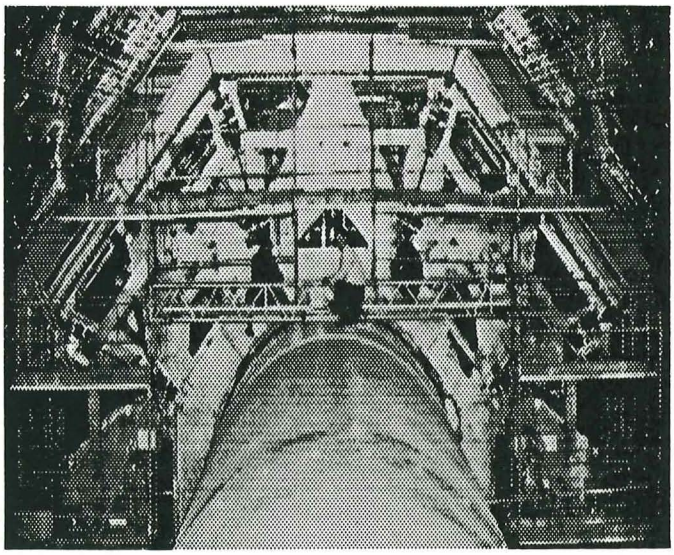

Fig. II.6. The muon chambers system inside the L3 magnet.

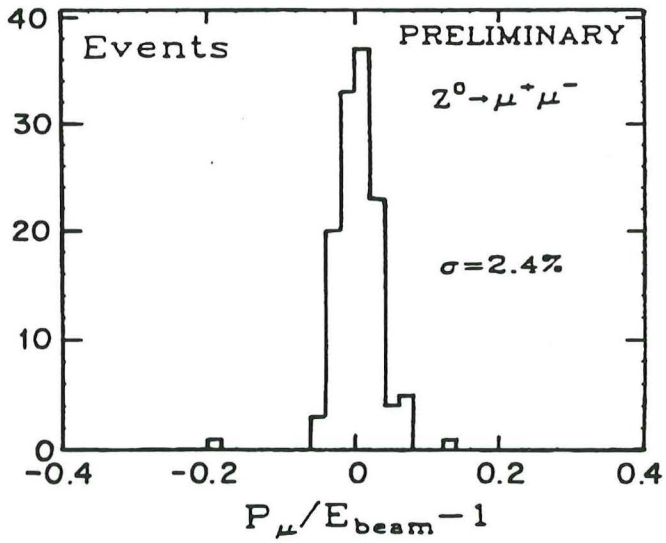

Fig. II.8. Momentum Resolution of the L3 Muon Detector

Figure II.7 shows a $Z^0 \to \mu\mu\gamma$ event. Figure II.8 shows that the measured resolution attains the predicted value of $\Delta P/P \approx 2.4\%$ at Z^0 mass.Figure II.9 shows the only available measured forward-backward charge asymmetry at LEP, by L3. This asymmetry enables us already to obtain the vector and axial vectoor coupling constants rather precisely: $|g_a| = 0.495 \pm .007$, $|g_v| = 0.066^{+.046}_{-.027}$ Figure II.10 shows the inclusive muon event from $Z^0 \to b\bar{b} \to \mu + X$.

The clean measurement of inclusive muons from muon chambers enabled L3 to study $Z \to b\bar{b}$ decays uniquely in the first month of LEP, as shown in Fig. II.11 with $P_T > 1.6$ GeV: the $Z \to \mu + X$ sample is dominated (91%) by $Z \to b\bar{b}$ events. For this, L3 obtained $\Gamma_{b\bar{b}} = 353 \pm 25 \pm 25$ MeV.

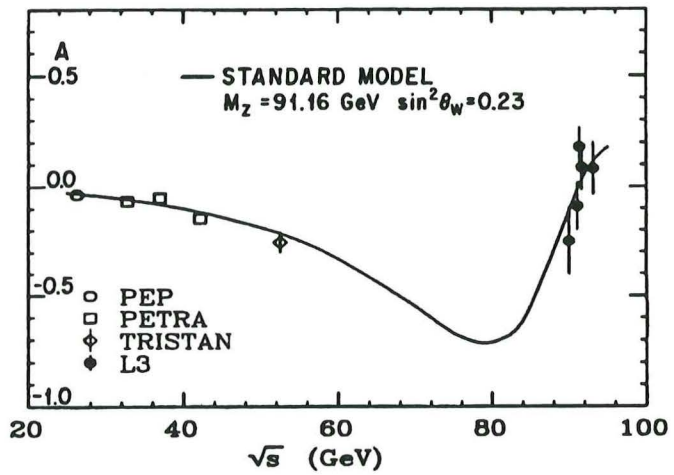

Fig.II.9 The measured forward-backward charge asymmetry A from L3 as well as from other groups at lower energies.

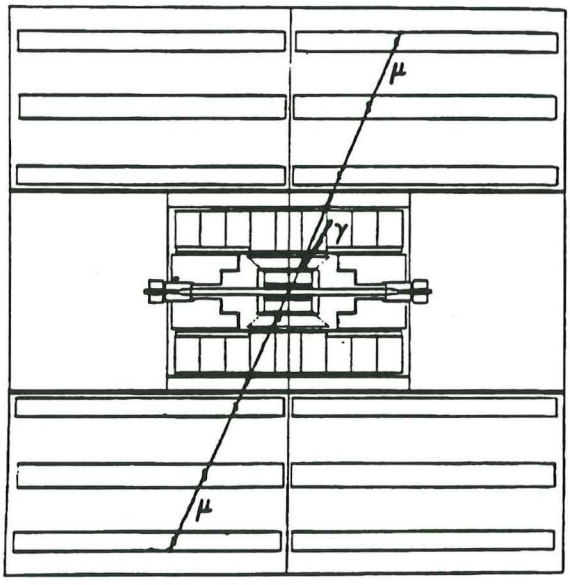

Fig. II.7. A $Z^0 \Rightarrow \mu\mu\gamma$ event

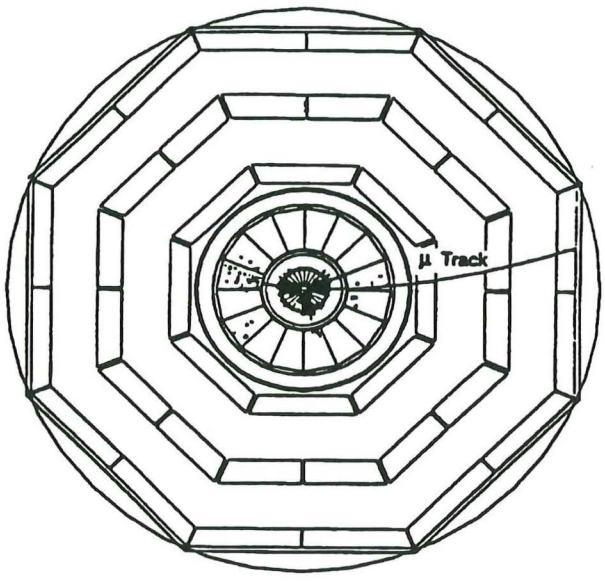

Fig. II.10. An Inclusive Muon Event.

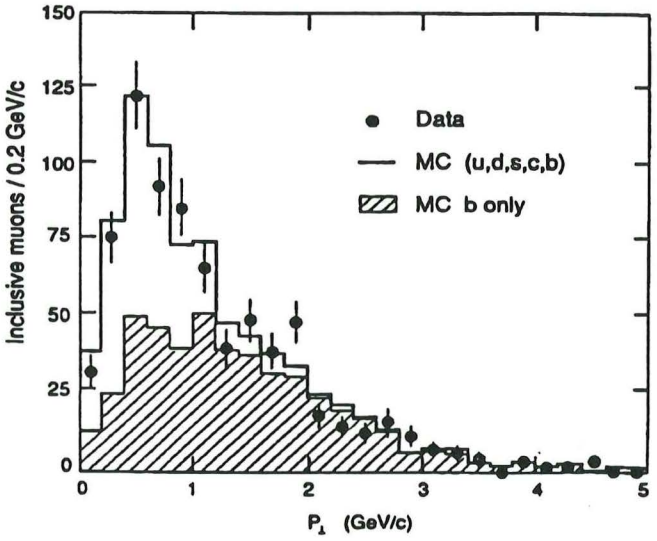

Fig. II.11. Transverse Momentum Distribution of Inclusive Muons

B. 3. Hadron Calorimeter

The hadron calorimeter measures hadron energies with a resolution of $55\%/\sqrt{E} + 5\%$ and $\Delta\theta = 3°$, $\Delta\varphi = 2.5°$ for jets. This provides a clean muon sample by absorbing hadrons close to the interaction point to minimize in-flight pion decays and by tracking muons through the uranium absorber. The calorimeter also measures muon energy loss. The central calorimeter is constructed in towers as shown in Fig. II.12.

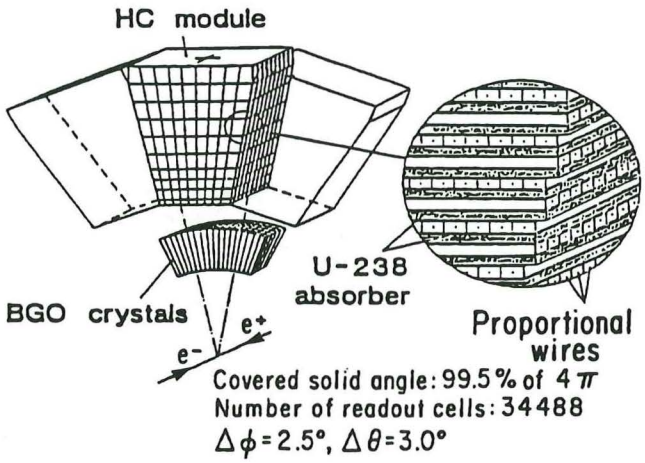

Fig. II.12. The Tower Structure of the Barrel Hadron Calorimeter

The calorimeter is made of approximately 10 000 proportional chamber planes sandwiched with 300 tons of ^{238}U absorber. It has been designed and built by an international collaboration from USSR, China, United States, India, Germany, and Switzerland. Figure II.13 shows the measured energy resolution of the hadron calorimeter.

B. 4. Electromagnetic Calorimeter

The electromagnetic calorimeter uses 12 000 crystals of a new type (BGO). It measures photon and electron energies with an accuracy of better than 1% above 2 GeV

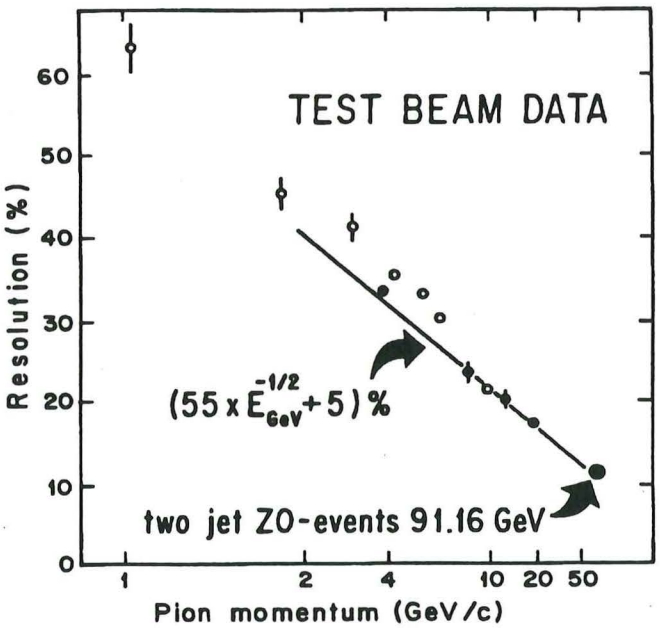

Fig. II.13. The Measured Energy Resolution of the L3 Hadron Calorimeter.

and 5% at 100 MeV. The measured resolution $\sigma = 0.52\%$ at 50 GeV is shown in Fig. II.14.

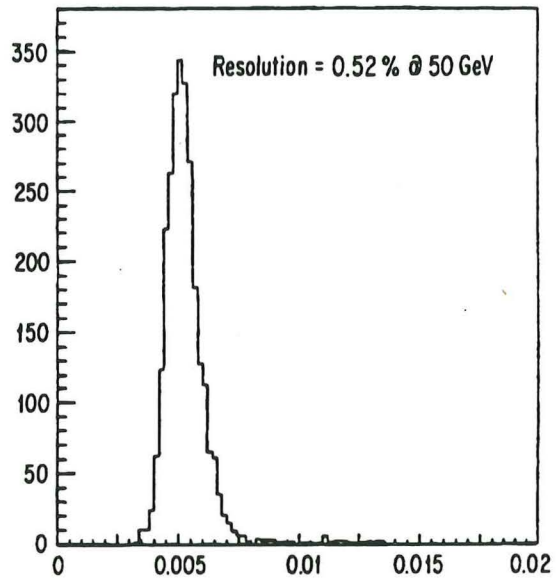

Fig. II.14. The Measured Energy Resolution of the L3 Electromagnetic Calorimeter

The measured position resolution for photons is ±1 mm. The 2-photon spectrum is shown in Fig. II.15, where the π^0 and η signals are clearly seen.

B. 5. Vertex Detector

A central detector tracks charged particles with a ≈40μm average single-wire accuracy in the bending plane and 450-μm double-track resolution. In the non-bending plane, the z-coordinates are measured by four additional wire chambers providing 300-μm single-track

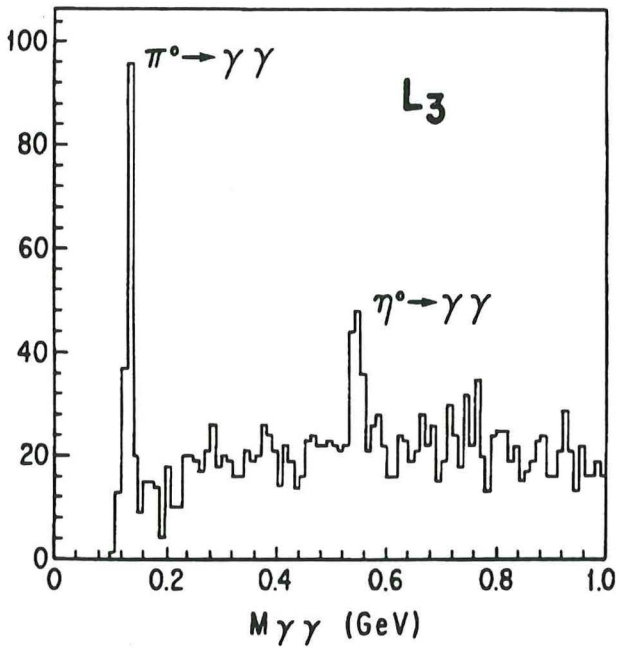

Fig. II.15. $\gamma\gamma$ spectrum measured with the L3 BGO Electromagnetic Calorimeter.

resolution and 7-mm double-track resolution. Figure II.16 shows the correlation between the measured P_T by the vertex chamber compared with the measured E_T via BGO.

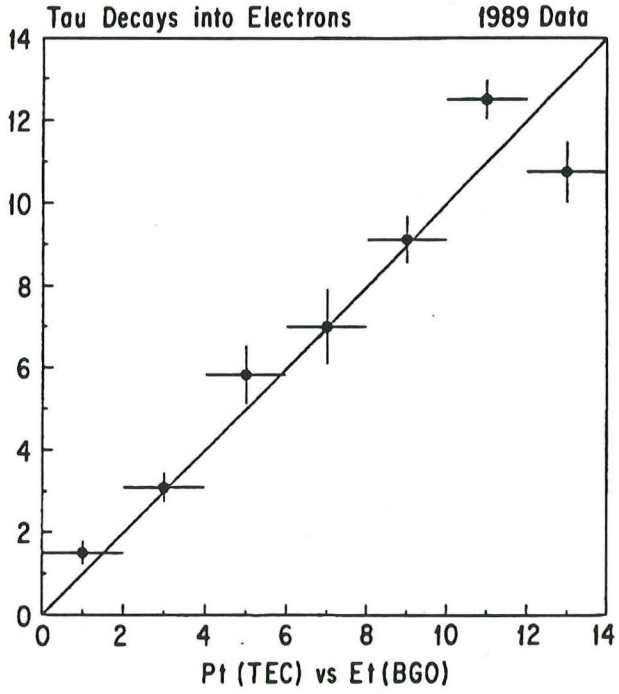

Fig. II.16. Measured correlation between BGO Energy and transverse momentum from the Vertex Chamber.

The L3 detector provides good hadron rejection. The muon energy loss ΔE is measured by the sampling calorimeter, which also monitors hard photon radiation. The properties of L3 make it well adaptable for use at the LEP Hadron Collider (LHC).

Reference

[2.1] "The Construction of the L3 Experiment," Nucl. Instr. Meth. A289 (1990), 35.

A. GENERAL MAGNET DESIGN CONSIDERATIONS

The design of the L* magnet is based on the experience gained with the L3 magnet at LEP. The muon momentum resolution is closely related to the properties of the magnet. For L* the magnet and muon spectrometer design have to measure 500 GeV/c muons with 2% resolution and with a large acceptance. Because the momentum resolution

$$\frac{\Delta p}{p} \propto \frac{p}{B \times L^2}$$

improves quadratically with the measured track length L and only linearly with the field strength B, we choose for the central spectrometer a large volume solenoid (inner diameter = 19.2 m, inner length = 29.5 m) of moderate field strength (0.75 T) along the beam direction. This field value and a required uniformity of better than 10% are dictated by the requirements of the drift chamber detector.

To have good resolution and acceptance for the Higgs $\Rightarrow Z^0 Z^0 \Rightarrow 4\mu$ decays, two external spectrometers having their field direction perpendicular to the beam are situated upstream and downstream of the central solenoid (Fig. III.1). They cover polar angles $|\theta| > 2°$. Their field strength is 0.3 T and their inner dimensions are 9.2 m parallel and 8.2 m perpendicular to the beam. Therefore, they provide a value of BL^2 that is $\geq$ 20.5 Tm^2, which is comparable to the central spectrometer.

The magnetic field must be shielded. For a large magnet with an iron return yoke, the construction and assembly of the yoke is the most time consuming part. Our proposed solution (see Sect. B) is a straightforward extrapolation of a proven design. In this respect, the L3 magnet may be considered as a half-scale model. The experience gained during the assembly of the L3 iron shield led us to consider a new design for the poles. This will simplify the assembly and suppress heavy welding in the underground area. In line with our past experience in heavy lifting, we have chosen to install a temporary gantry crane able to handle individual 1000-ton pieces. For the coil of the central magnet we discuss two options: (1) resistive Al coils (Sect. B) such as L3 and (2) superconducting coils (Sect. C). In addition, in Sect. D we present a design where the return yoke iron is replaced by a second superconducting coil system. The cryogenic system needed for the superconducting coils is described in Sect. E. The forward-backward magnets are discussed in Sect. F. Finally, in Sect. G we give a list of the members of the magnet system group.

Table III.1 displays the main differences between the three coil options for the central solenoid.

The main advantage of the Al coil version is that a similar device has already been constructed and R&D is minor. The main advantage of the two versions with superconducting coils is their reduced power consumption. Additional advantages of the double coil option are:

Table III.1. Coil Options

Parameter	Aluminum Coil	SC Coil	Double SC Coil	Unit
Power Consumption	22	2	2	MW
Outer Diameter	26.7	25.0	30.0	m
Mass of Iron	48 200	41 350	-	ton
Mass of Coil(s)	7700	1103*	4000*	ton
Operating Current	66	23	25	kA

*Including structure and vacuum vessel.

(1) a substantial decrease in total weight, and (2) it can be completely fabricated and tested in a surface facility.

B. CENTRAL SOLENOID WITH RESISTIVE COIL

The general design (Fig. III.1) is directly derived from the L3 concept, i.e., like a building but with more iron than concrete. For L*, the magnet structure is divided into two symmetric halves separated by a 50-cm gap. The central support, to carry the weight of the hadron calorimeter, is located in this gap. Without changing the general concept, the aluminum solenoid can be replaced by a superconducting one, as described in Sect. C.

B.1. Resistive Coil and Ancillary Equipment

Introduction

Experience gained with the L3 magnet shows that the following points are important:

Use of general manufacturing techniques with semi-finished products supplied by industry, taking into account local capabilities concerning power, water consumption, as well as railway, road, and sea transport.

Match the required flatness of plates and bars to the production capabilities of the suppliers.

Balance the investment in handling tools with manpower and planning requirements.

Because the magnetic volume and the central induction are given by the physics requirements, the three remaining free parameters are the type and alloy quality of the conductor, the rated current, and the total electrical power. We have only considered a coil of high conductivity aluminum because the material cost of a copper coil of the same electrical power is three times higher.

The rated current is a compromise between the manufacturing capabilities of large plants for delivering thick plates with good flatness tolerance and homogeneity, mechanical workshops capable of machining the plate edges with high precision, the development of techniques for electron beam welding of thick plates and the balance between the investment in manpower, handling tools, and storage area. The inductance of the

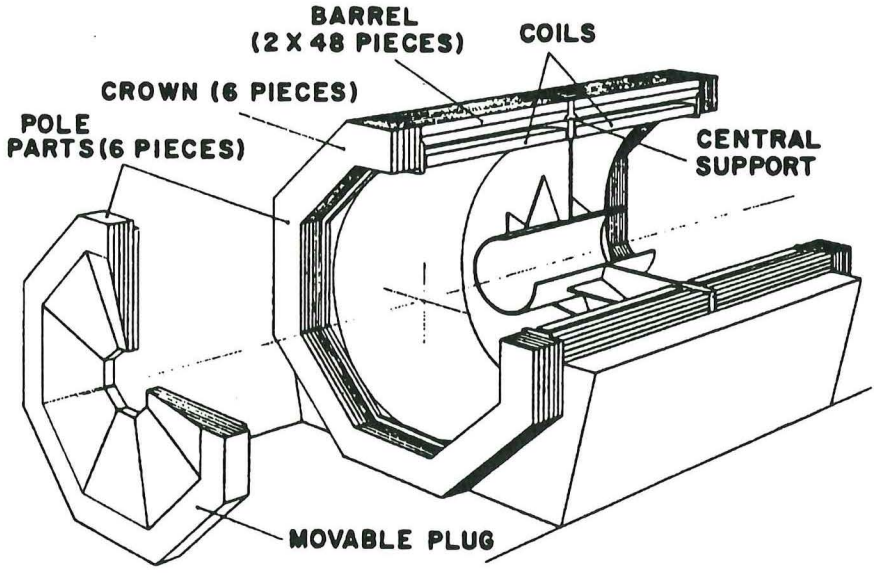

Fig. III.1. General view of the L* magnet.

coil and the problems related to the transport of high currents have also been considered.

An octagonal coil gives the best compromise between the requirements of the industrial production, the number of welds, and the circular section of a perfect coil.

Description of the Coil

The L3 coil construction technique is directly applicable. Because of the dimensions, only an electron-beam welding technique is adequate. The inter-turn insulation covers about 10% of the pancake surface. This represents 40 tons of solid insulation for the entire coil. The number of turns connected to each hydraulic circuit is determined by the rated pressure of the demineralized water system. A demineralized water flow of 720 m^3/h is needed for the removal of the coil power alone. Table III.2 shows the main parameters of the coil.

Figure III.2 shows a six-turn package for the L3 magnet. It can be considered as a half-scale model of an L* pancake. The aluminum sectors used to build the coil have dimensions of 925 × 155 × 9 cm^3. Experience with L3 indicates that at an electron gun voltage of 60 kV, the welding of a 9-cm-thick plate demands a current of 700 mA, requiring an electronic welding gun of about 50 kW in normal operation. There are in total 2400 joints to be made. From our experience with L3, we expect a production rate of 25-30 joints per shift per week once the procedure is well established.

The cooling requires 720 m^3/h of demineralized water with a temperature gradient of 25°C. An important parameter is the number of hydraulic circuits in the magnet coils. Three types of circuits must be considered, as follows:

Table III.2. Main Parameters of the Coil

Parameter	Data	Unit
Current	66	kA
Coil resistance at 60° C	4.6	mΩ
Coil total voltage	300	V
Central induction	0.75	T
Inner coil diameter	19.6	m
Current density	46.3	A/cm^2
Ampere-turns	19.1×10^6	A
Inductance	1.4	H
Stored Energy	2660	MJ
Number of turns	288	
Conductor section	155×9	cm^2
Conductor weight	7800	ton
Cooling pipes weight	860	ton
Water flow (coil)	720	m^3/h
Water pump power	0.8	MW
Coil DC power	20	MW

1. The cooling of the aluminum sectors on the inner and outer edges of the turns. For reliability reasons, either circuit is able to provide all of the required cooling power.

2. Cooling of the connections between pancakes. The pancake is defined as the series hydraulic connections of six turns, corresponding to a unit weighing 180 tons. For reliability reasons the connections between two pancakes must also be cooled on both sides.

3. The cooling of the current leads of the magnet.

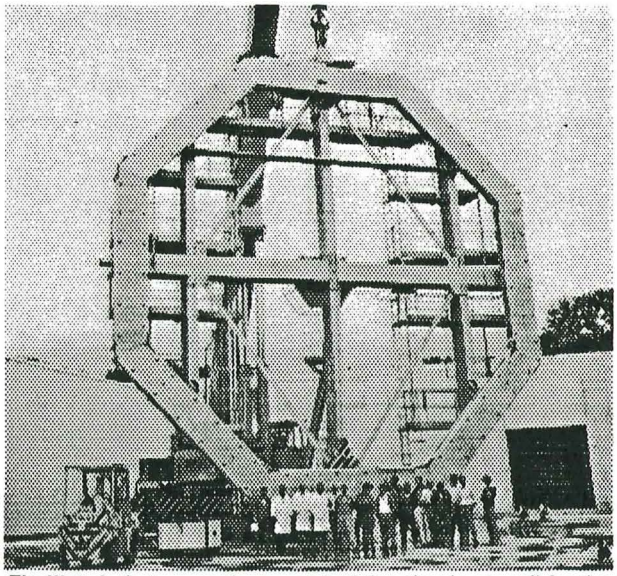

Fig.III.2. A six-turn package, part of the aluminum coil for the L3 magnet.

The pancake's cooling piping determines the maximum pressure drop. With six turns in series, the maximum pressure drop will be about 12 bar. Taking into account the return pressure, the pressure at the outlet of the circulating water pump must be 20 bar.

The Power Supply and Bus-Bars

Although a 30-kA system has been used successfully for L3, handling 70 kA in the L* bus-bar system requires some development for the power supply. The DC part of the power supply must be divided into six modules to be compatible with normal thyristor production. The inductance of the bus-bars allows a parallel connection of the six modules, and the current addition is realized at the level of the current leads of the magnet. To decrease the wave ratio and increase the power factor on the mains, the high-voltage transformer is divided into two independent units with six-phase secondaries. The current stabilization at a level of 0.01% presents no difficulties because of the long time constant of the magnet, which is approximately 300 s. A power of 1 MW is dissipated in the water cooled bus-bars, requiring 40 m^3/h of demineralized water, and the low voltage involved allows a construction with noninsulated bus-bars weighing about 30 tons in total. To eliminate stray fields, individual bus-bars of opposite polarities will be interleaved. This system allows for a compact construction. The power supply and the interface of the DC modules with the bus-bar system requires a surface of about 50 m^2 indoors. Transformers fed from the high-voltage mains will be installed in an adjacent yard of 50 m^2.

Thermal Shield

The internal volume of the magnet is protected from the heat losses of the coil by a thermal barrier consisting of 10 cm of inert thermal insulation and an active thermal shield stabilized at a constant temperature of 20°C± 1°C by an adequate water system equipped with heat exchangers. This thermal shield load requires 20 m^3/hour of demineralized water.

Water Cooling System

L* requires a dedicated Low Conductivity Water (LCW, conductivity < 1 μSiemens) system designed to remove the 27 MW dissipated by the main solenoid and the two spectrometer magnets together with their bus-bars and thermal shield. This power represents a total demineralized water flow of approximately 1000 m^3/h. This closed loop circuit will be cooled via a water/water heat exchanger by the SSC cooling system. As the main part of the magnet circuit is in aluminum, this circuit must not be mixed with other LCW systems. A secondary loop will be derived from the main circuit to maintain at a constant temperature the cooling shields of the three magnets. The power supply electronics will be cooled by an independent LCW system.

Monitoring

Running a magnet of such a low energy density is reliable. However, the magnet must be equipped with enough monitoring detectors to allow the localization of potential troubles during assembly and operation periods. Therefore, each pancake will be monitored for (1) water flow in each hydraulic circuit, (2) maximum temperature, and (3) voltage distribution. Taking into account the fragility of these monitoring detectors and the dimensions of the magnet, the number of detectors installed will be doubled for redundancy.

Field Mapping

A system similar to the one used to map the L3 field will be used for the L* magnets. In L3, about 1000 calibrated magneto-resistors are permanently mounted on top of the muon chambers and on the frames close to the poles. Because 2/3 of the sensors are mounted on the boundary of the volume and 1/3 are distributed over the inner volume, we will need approximately 1000 sensors for the forward-backward spectrometer magnets and 5000 sensors for the central solenoid.

B.2. Magnetic Flux Return Frame

Description of the Magnet Flux Return Frame

The design of the iron structure is very similar for both the aluminum and the superconducting versions. The flux return frame is octagonal with poles at both ends. The 8-sided barrel geometry provides good mechanical stability for the barrel, which is fabricated from stacked bars, and reduces the number of welded joints in the coil. Each pole consists of a self-supporting steel crown on the outside and a movable plug at the center to give access

to the inner detectors. The return frame design is also directly extrapolated from the design of L3. Table III.3 lists the main parameters.

Table III.3. Main Parameters of the Return Frame

Parameter	Data	Unit
Barrel thickness	178	cm
Barrel weight	32200	ton
Max. pole thickness	230	cm
Pole crown weight (one)	3600	ton
Pole plug weight (one)	3300	ton
Total Iron weight	48200	ton
Ext. barrel diameter	26.7	m
Ext. magnet length	34	m

We have minimized the cost of the structure by using simple manufacturing techniques, and kept the work in the underground area to a minimum. In particular, with the past experience of L3 in mind, structural welding in the underground area has been avoided where possible. This leads to the necessity of handling, from the surface manufacturing facilities to the underground assembly area, bulky and heavy pieces up to the full magnet diameter, and with a maximum unit weight of 900 tons (compatible with the 1000-ton gantry crane) during the magnet assembly period. Even under these conditions, the assembly of the magnet is on the critical path.

Detailed Description of the Iron Structure

This central support, which separates the magnet in two halves, has two independent roles: (1) to support with minimum loss of solid angle the central detectors (mainly the 2000-ton hadron calorimeter), and (2) to be used as an intermediate support for the roof of the magnetic barrel because we cannot manufacture and transport 28-m-long bars. The central support consists of a stainless-steel membrane fixed with gussets at its inner rim to the hadron calorimeter support casing, and fixed at its outer rim to a carbon steel ring supporting the top three barrel-bar octants.

At both ends of the magnet, a self-supporting octagonal crown takes the weight of the roof of the magnetic barrel. These crowns consist of several independent rings, 0.3 m thick, stacked side by side.

The barrel is constructed from individual steel bars arranged in an octagonal geometry. The three bottom octants, laying on an octagonally shaped concrete cradle, provide a foundation for the whole assembly. The three top octants rest on the central support ring in the middle, and on the crown at the extremities. On each side, 128 prestressed tie bars connect directly the central support to one of the crowns to give a permanent 10 000-ton axial force needed for structural integrity.

The central hole of the crown is filled with a movable pole plug that rests on a step built into the corresponding crown. The plug is optimized as a variable thickness disk to obtain a constant induction (1.7 T) in the iron. This 3300-ton pole plug can be displaced in the beam direction, on grease pads, to give access to the inner part of the magnet to load the muon chamber assemblies and the inner detectors. The construction of the movable plug is similar to the construction of the crown.

The grease pad system foreseen is similar to that used to support the 340-ton L3 magnet doors and the 1000-ton loaded L3 support tube. This is a stepping system that allows movement in 1-mm steps. To move the pole plug, the load is transmitted to the grease where the pressure reaches 500 bar and the friction factor is less than 0.001.

Structural Integrity of the Return Frame

The field strength is relatively low, causing an equivalent magnetic pressure of only 2.25 bar on the poles; however, the enormous surface on which these forces act creates stresses in the poles. Values for stresses and deformation of the pole plugs, which are the most stressed elements, have been scaled from measurements made on the L3 magnet. For the same stress level, the thickness for out-of-plane bending must be 900 mm and the deformation of the inner rim of the inside hole will be approximately 8 mm toward the interaction point. Thus, for both the crown and the plug the first three rings must be mechanically coupled.

Structural Integrity of the Central Support

A simplified finite element model was created using four noded quadrilateral and three noded triangular plate elements. Two load cases were considered: (1) the nominal load of the hadron calorimeter together with the top three octants of the return frame barrel, and (2) a similar case in which the calorimeter load is off-centered by 275 cm. The study shows a sound behavior of the central support even for out-of-plane loads.

B.3. Coil Manufacturing

In Industry

For a construction of this type, it is essential to base the design on an industrial production to obtain a high production rate at a low unit price. Therefore, the machining of the basic sector and welding of the cooling pipes are all performed in the factory. Then, pieces are sent to the site for the next manufacturing operations.

Onsite Facilities for Coil Manufacture

Two $62 \times 26 \times 14$ m^3 magnet coil halls each equipped with a 200-ton traveling crane, placed near the construction shafts will be used to assemble by welding and test the pancakes. The finished coil units will be stored outside

in pits covered by a tent. The two magnet halls and the storage pits will be serviced by a cart/rail system to allow the transport of the 600-ton units. The storage pits will be accessible by the 1000-ton gantry crane used for the magnet assembly.

Coil Manufacturing Process

Just as for L3, individual turns will be assembled in pancakes and then in units of three pancakes representing indivisible loads of 600 tons. The finished coil units, ready for assembly, will be completely equipped with all cooling circuits, the panels for the thermal shield, and the monitoring detectors. Each finished coil unit will be submitted before storage to a full hydraulic, electrical, and thermal test to insure its integrity.

B.4. Iron Manufacturing

In Industry

All elements will be manufactured in finished units of 60 to 100 tons to suit transport requirements. All elements destined to be assembled by welding to form unit pieces will be submitted to trial assembly before shipping. Machining necessary for precision surface matching will be done, and the weld preparations will be adjusted to minimize mechanical or machining work on site.

Onsite

A 140×40 m^2 concrete slab, placed near the construction shafts and serviced by the gantry crane, will be used to assemble and store the central support. Then various iron rings for the pole and pole plug structures will be assembled as 800-ton pieces. A mobile crane will service the area, and a mobile tent will be installed to protect welding in progress. The bars will be stored on parking lots or on future building footprints inside the laboratory, and they will be moved near the underground hall as required, to be assembled by mechanical fastening in 335-ton units ready to be lowered.

B.5. Assembly Sequence

To limit assembly time in the underground area, the various pieces will be prepared, as far as possible, as individual loads of 600 to 800 tons, ready to be handled by the gantry crane. For normal and superconducting versions, the assembly sequence proceeds along the same lines. The movable plugs will be lowered first with the support bases of the forward-backward spectrometer. Each spectrometer magnet will then be lowered on its support in two halves weighing 800 tons each. Each assembly, composed of the movable plug and its associated spectrometer magnet, will then be moved to the end of the hall using the grease pad system, and the assembly of the central magnet will proceed (Fig. III.3). First, a magnetic base, well aligned with respect to the beam, will be constructed along the full length of the magnet with three barrel bar octants resting on the concrete cradle. These sets of bars, weighing 380 tons each, will be placed in position using the two 200-ton traveling cranes of the experimental area coupled together. Then the central support will be inserted between these bars, resting on them (Fig. III.4). Shimming will be used to align this central support on the beam axis. At this stage, the assembly of the coil will start. For the aluminum version, the coil will be lowered as 16 independent, fully tested 600-ton units (Fig. III.5). For the superconducting version, the two coils in their cryostat will be lowered as two completed and fully tested units weighing 600 tons each (Fig. III.6). In each case, the coil elements will be connected in series in the underground area. Then the crowns will be built (Fig. III.7), and both halves of the magnet will be covered with barrel bars. During this time, the coils will be connected to their ancillary equipment (Fig. III.8). Then, the tie bars will be prestressed to the required value to stabilize the flux return frame. The movable plugs, which were erected first, together with the forward spectrometers will then be moved in position to complete the magnetic flux return frame (Fig. III.9). The magnet will be tested at full current before continuing the assembly of the L* detectors.

Planning

The schedule for the iron return frame magnet manufacturing and assembly is presented in Fig. III.10.

C. CENTRAL SOLENOID WITH SUPERCONDUCTING COIL

Superconducting magnets are frequently used both in high-energy physics and fusion research. For example, ALEPH and DELPHI magnets are operating successfully at LEP/CERN, while the T-15 magnet at the Kurchatov Institute, the Large Coil Test (LCT) coils at Oak Ridge National Laboratory (ORNL), and TORE SUPRA at Saclay are examples from fusion research.

In this section, we describe a central solenoid (see Table III.4), where the two aluminum coils are replaced by two superconducting coils. In the following discussion, only components that differ from those of the resistive coil will be described. The main geometrical dimensions remain the same.

C.1. Superconductor

The conductor for the L* central solenoid is made of Nb-50%Ti Rutherford type cable with a copper to superconductor ratio of 1:1. The flattened cable, made of 10 strands, is embedded together with two copper cooling tubes into four copper clad aluminum profiles that are soft soldered together. This is a reliable and inexpensive procedure. All components are readily available from the Soviet Union.

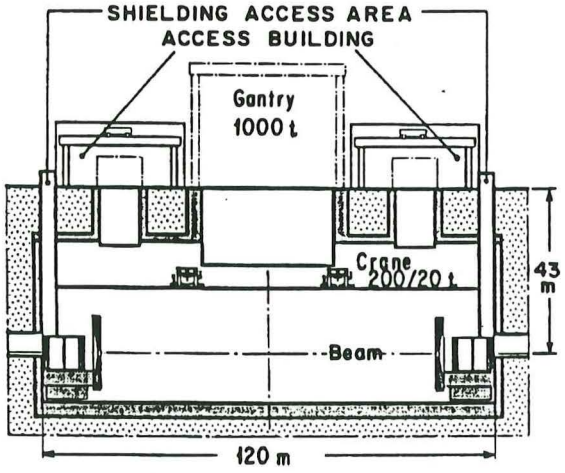

Fig.III.3. Installation sequence of the forward magnets and magnet pole plugs.

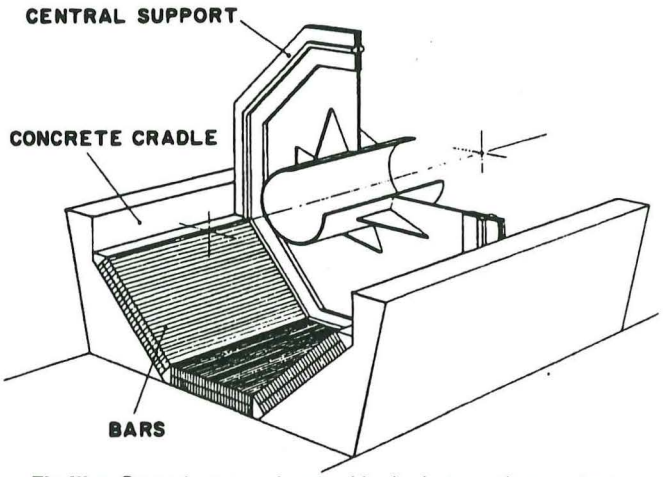

Fig.III.4. Central support inserted in the bottom three octants.

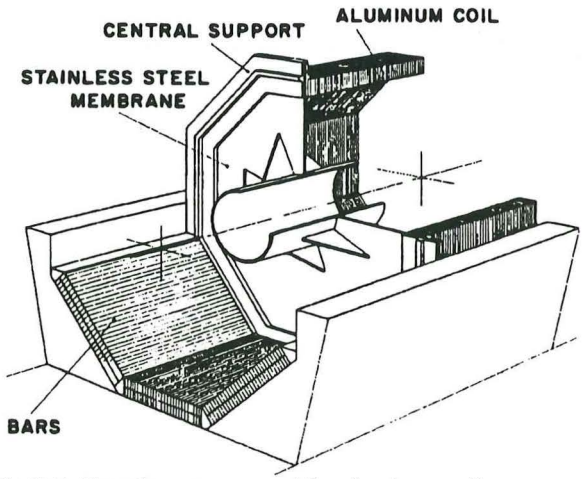

Fig.III.5. Mounting sequence of the aluminum coil.

The aluminum residual resistance ratio (RRR) is at least 500. The overall current density is 32 A/mm^2. The nominal current is 23 kA for a magnetic field of 0.75 T. The conductor is insulated by a 0.5-mm-thick half-overlapped fiberglass fabric. Additionally, the support cylinder is insulated by a 1.0-mm-thick fiberglass jacket. The superconducting coil is impregnated by an epoxy resin under vacuum. The conductor is shown in Fig. III.11, and the main parameters are listed in Table III.5.

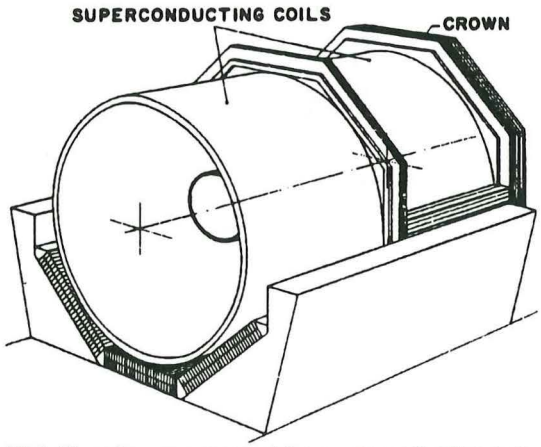

Fig.III.6. Mounting sequence of the superconducting coil.

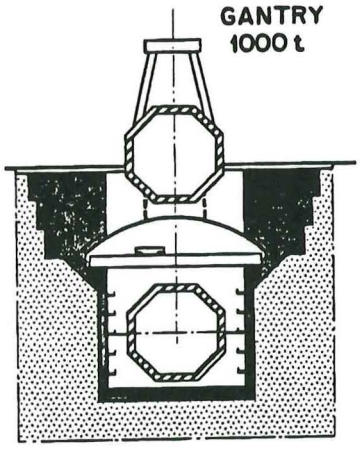

Fig.III.7. Mounting the crown ring with the 1000-ton gantry crane.

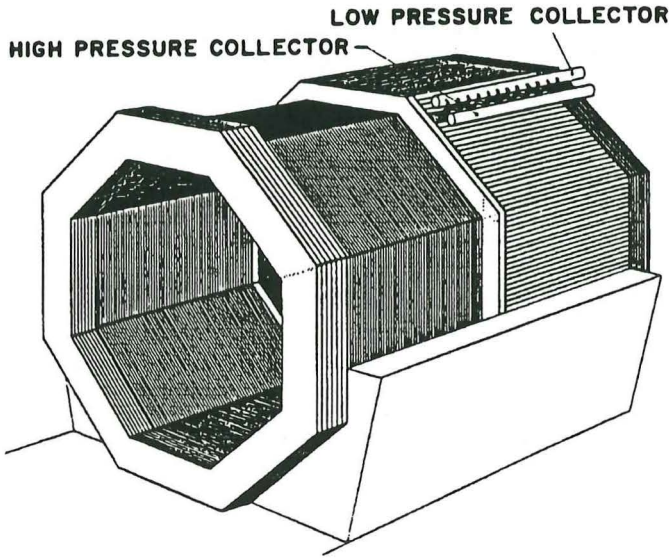

Fig.III.8. Connection of the aluminum coil to the cooling circuits.

C.2. Solenoid Winding

The superconducting coil is divided into two half-coils, each 13.485 m long. The gap in the center between the two half-coils is 103 cm, and the distance between the end of the coil and the crown is 75 cm. The coil conductor is wound onto the inside of a subunit aluminum support cylinder to form a single layer coil.

One half of the superconducting coil is subdivided into three sections, each 4 m long (Figure III.12). The sections are separated by structural rings of 0.7 m length. Each section consists of seven subunits that contain the coil windings. Figure III.13 shows the details of one of the central subunits. The winding is monolayer except for the subunits close to the structural rings. There, a second layer of nine turns restores the uniformity that is disturbed by the gap in the coil due to the structural rings.

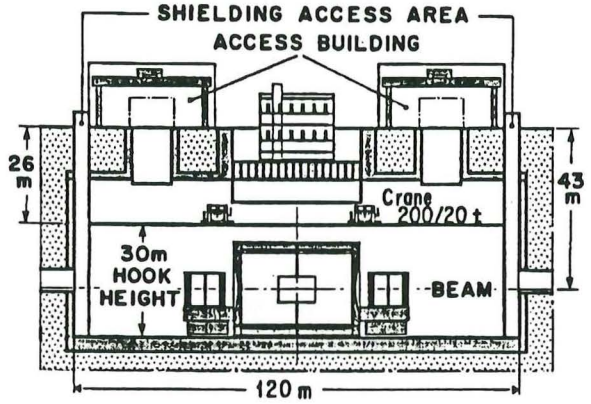

Fig.III.9. Completion of the three magnets.

Table III.4. Main Parameters of the SC Coil

Parameter	Value	Unit
Total weight of the SC coil	1103	ton
Conductor weight	152	ton
Weight of the support	200	ton
Weight of the vacuum vessels	647	ton
Weight of the thermal shields and insulation	104	ton
Magnetic induction in the useful volume	0.750 ± 0.037	T
Stored energy	2.5	GJ
Inductance	9.4	H
Operating current	23	kA
Dumping voltage	600	V

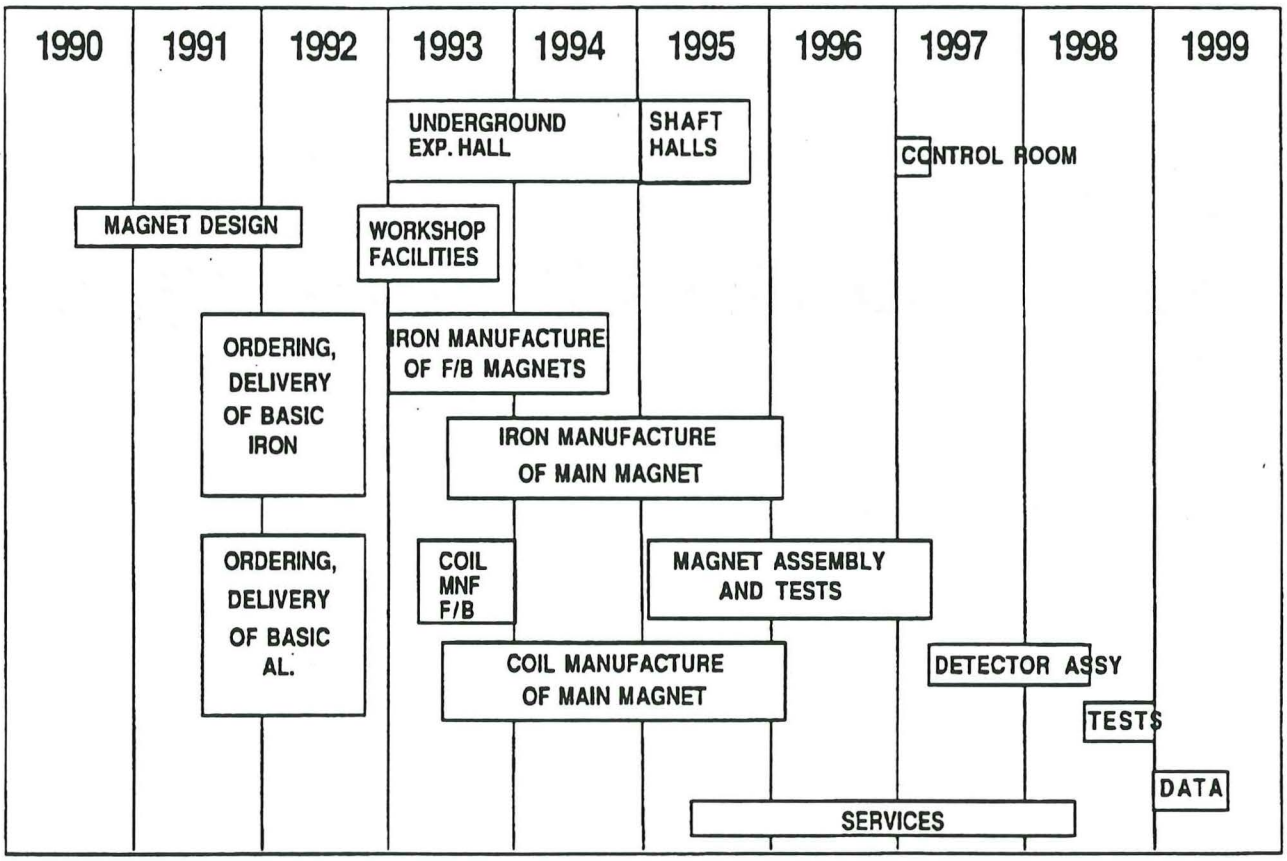

Fig.III.10. Planning for manufacturing and assembly of the L* magnet with aluminum coil.

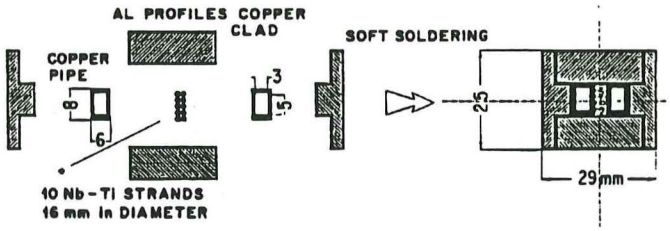

Fig.III.11. The conductor and its components.

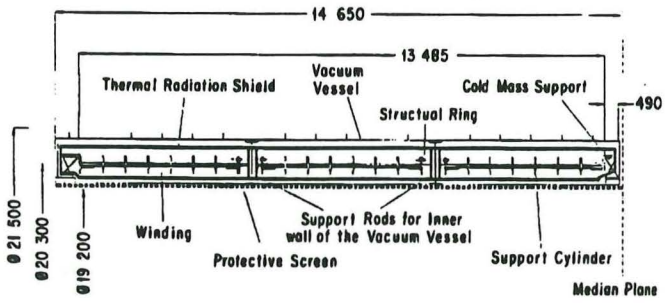

Fig.III.12. Schematic view of one-half of the superconductive coil.

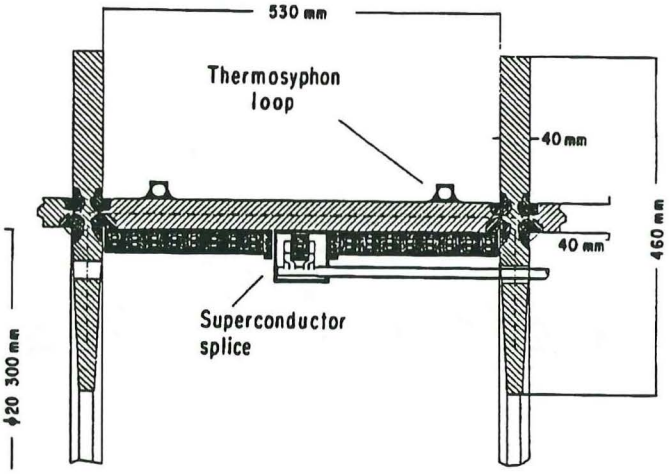

Fig.III.13. Subunit of the superconductive coil.

The structural rings allow a bolted connection between the sections to form a rigid cylinder. Twelve holes are left free in each structural ring to insert the supporting rods that connect the inner and outer walls of the vacuum vessel. These rods increase the stiffness of the vacuum vessel and carry the weight of its inner wall. Each half-coil is suspended by cold mass supports, made up of fiberglass tie rods, arranged like the spokes of a bicycle wheel. These cold mass supports carry both the weight of each coil and the axial, magnetic forces of about 4000 tons that pull the two half-coils together. The cold mass supports in the center are fixed to the vacuum vessel although they are free to slide at the extreme ends because of the thermal contraction of 60 mm. The vacuum vessel flanges that receive the forces from the cold mass supports have an adequate rigidity.

Table III.5. Main Parameters of the Conductor

Parameter	Value	Unit
SC material	Nb-50% Ti	-
S.C. strands		
SC diameter	1.6	mm
Cu to SC ratio	1:1	-
Number of filaments	210	-
Critical current at B = 2 T	4	kA
Rutherford type cable		
Number of strands	10	-
Cross section	3 × 7.5	mm^2
Critical current at B = 2 T	40	kA
Operation current	23	kA
Stabilizer		
Material	Al 99.99%	-
RRR at 4.2 K and B = 0 T	>500	-
Cross section	25 × 295	mm^2
Insulation		
Material	Fiberglass	-
Thickness	1.0	mm
Cross sections		
SC cable	22.5	mm^2
Helium channels	30	mm^2
Copper pipes	80	mm^2
Soft solder	5	mm^2
Stabilizer	617	mm^2
(a) copper	92	mm^2
(b) aluminum	525	mm^2
Conductor	725	mm^2
Insulation	96	mm^2

C.3. Power Supply and Energy Dumping System

Figure III.14 displays schematically the power supply and the energy dumping circuits. The magnet is energized with series connection of the coil sections by a commercially available current source IST 25000. The emergency discharge of the magnet, however, is in three parallel circuits. Each circuit connects symmetrically one section of each half-coil. The sections are connected to avoid asymmetric forces. The use of three parallel dumping circuits allowed an increase in the overall current density in the conductor by a factor $\sqrt{3}$ compared to the case of series connections of all coil sections (for the same quench capacity).

This can be seen from the following expression for the operating current density j_{op} as a function of the quench capacity $g(T_{max})$, the maximum voltage U_{max}, the initial discharge current I_{dis} and the stored field energy E:

$$j_{op} \leq \left(g(T_{max}) \cdot U_{max} \cdot \frac{I_{dis}}{E} \right)^{0.5}$$

For 3 parallel dumping circuits

$$I_{dis} = 3 \cdot I_{op}$$

where I_{op} is the operating current.

Each discharge circuit has an independent discharge resistor. Both sections attached to a common dump resistor are connected to each other, on one side by a superconducting bus and on the other side attached to their dump resistor and DC breaker by helium cooled current leads.

The DC current switches used in the dumping circuits are commercially available. The dumping circuit is presented in Fig. III.14. Because the breaking current of the switches is 250 kA, one can use them in parallel. These breakers limit the voltage to 600 V, allowing less stringent requirements on the simultaneous operation of all switches without overvoltages.

The low quench probability is ensured by the high stability margin of the conductor and the high redundancy of the cooling. However, a protective discharge circuit is needed for unforeseen external perturbations. It is important to have adequate diagnostic facilities to distinguish transient events such as small local disturbances from strong instabilities that force discharge of the magnet. A multibridge quench detector will be used to detect a normal zone appearing in any subunit of the coil. Two discharging speeds are envisaged: A slow, normal one, which does not heat up the supporting cylinder, and a fast one triggered by a coil signal of 20 mV during at least one second. In case of an emergency discharge, the resulting eddy currents in the support structure will heat it and the windings almost uniformly to 70°K.

C.4. Instrumentation Systems

To ensure reliable operation, the following diagnostic systems are installed:

(1) Multibridge system for normal zone detection in each of the subsections and across the whole magnet;

(2) Strain gauges to check stresses;

(3) Set of thermometers, pressure transducers, flow meters, vapor content meters, etc;

(4) Acoustic emission detectors;

(5) The field will be mapped as described in Sect. B.1.

C.5. Manufacturing of the superconducting coil

The large dimensions involved require manufacturing on the SSC site. The following operations are necessary:

- Welding of the support cylinder
- Machining of the support cylinder

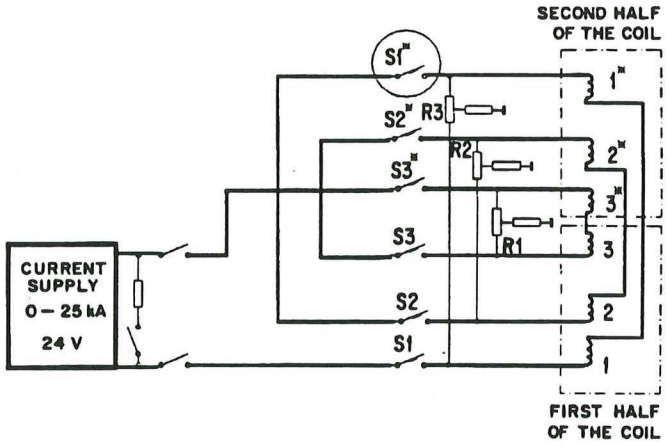

Fig.III.14. Energy dumping circuit.

- Insulation of the support cylinder
- Winding of the superconductor into the support cylinder
- Preassembly of the sections
- Coil assembly
- Testing of the coil.

A workshop of proper size has to be installed for these operations as schematically shown in Fig. III.15. The parts making up the support cylinders, made out of an aluminum-magnesium alloy, will be prepared in the Soviet Union and shipped to the site. Once welded, the support cylinder sections will be heat treated. Then they will be machined by a rotating milling cutter and insulated with fiberglass-reinforced epoxy before the conductor is wound inside the support cylinder. At the end of the winding procedure, the sections will be moved to the preassembly area for electric and hydraulic connections. After that, three sections (see also Fig. III.12) making up one coil will be bolted together, equipped with the thermal radiation shield, and placed inside the vacuum vessels.

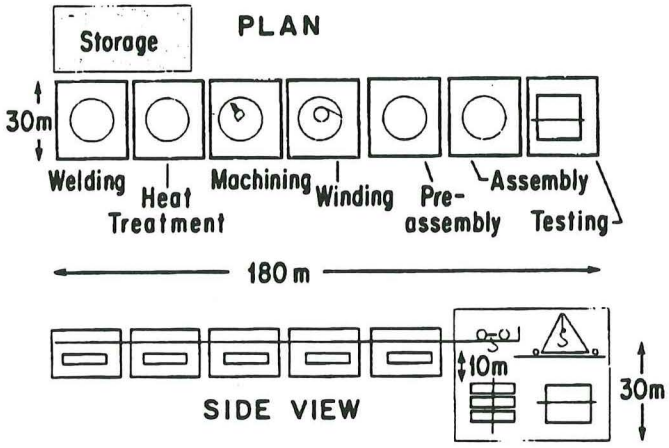

Fig.III.15. Workshop arrangement.

Finally, the coils will be tested and readied for lowering into the pit.

The manufacturing schedule is presented in Fig. III.16. The first coil will be mounted in the experimental area, while the second one will be completed.

C.6. R&D Plans

All necessary R&D, including conductor design, superconductor optimization, manufacturing technology, design, and development of the tooling is to be accomplished at the Kurchatov Atomic Institute (IAE) and tested on a model coil. The cryogenic system, with an instrumentation and control system developed by Lawrence Livermore National Laboratory (LLNL), will also be tested with the model coil. The main parameters of the coil are listed in Table III.6.

The model coil project is aimed at studying the following issues:

Develop all manufacturing processes;
Train technicians for the onsite manufacturing;

Check the basic concepts for superconductor, winding structure, cold supports, refrigeration;

Finalize the specifications of the magnet systems;

Test the instrumentation and control systems, keep current supply system, current leads.

The time requirements do not permit all work to be completed before the start of the construction of the L* magnet. However, we plan to complete each particular production step of the model coil at IAE before the corresponding step starts onsite for the manufacturing of the L* magnet.

D. SUPERCONDUCTIVE COIL WITH SUPERCONDUCTIVE SHIELD

Superconductivity makes it possible and practical to replace the iron shield with a second coaxial superconducting solenoid and to return the magnetic flux totally through the annulus between the two solenoids. The main advantage of this design is a substantial decrease in the weight of the magnet, as shown in Table III.1.

Table III.6. Main Parameters for the Model Coil

Parameter	Value	Unit
Diameter	10	m
Length	4	m
Number of conductor pieces in the model coil	8	
Number of turns	140	
One piece conductor length	550	m
Maximum magnetic field in the winding	2	T

In the double coil version, the two solenoids generate fields in opposite directions such that the field inside the inner solenoid is equal to the difference between the field generated by both solenoids, and the field in the annulus is the sum of the fields generated by both solenoids. There is no field outside the magnet. The map of the magnetic field lines is shown in Fig. III.17. The conceptual design of the magnet is shown in Fig. III.18.

To improve the field uniformity near the ends of the magnet, it is necessary to put compensating coils in the end regions (previously occupied by the iron poles).

In the proposed design, the currents in the two solenoids are adjusted so that the stray fields in the counting room will be approximately zero. The stray fields at other locations will be very small. The need for local shielding and more complex compensation will be determined in a later detailed study.

The double coil system requires approximately four times the ampere-turns of the single coil version. This assumes that the field in the annulus between the two coils is the same as the field in the bore. The number of ampere-turns is shown in Table III.7.

Increased use of superconductor for the double coil is partially balanced by the saving in the weight of the magnet (by eliminating the iron) and the reduction in cost for the delivery of the parts and the onsite construction. The following is a short description of the double coil magnet design emphasizing the differences from the single superconducting coil design.

To make handling, assembly, and lowering to the experimental hall easier, the double coil winding is divided into three parts. Each is in a separate cryostat and has approximately the same mass of 1300 tons. Electromagnetic forces are transferred through cold load bearing supports in locally evacuated space to decrease heat leakages (Fig. III.18).

Table III.7. Ampere-turns in the Double Coil Winding

Parameter	Value	Unit
Ampere-turns total	77	MA
-inner coil	46	MA
-outer coil	23	MA
-compensation coil	8	MA
-inductance	17	Henry

The absence of iron allows the use of longer fiberglass supports (10 m long). This decreases the heat leak and ensures a very rigid structure. For the two-coil geometry, it is possible to use two windings, each having a support cylinder similar to that of the single coil used with the iron shield. Structural links between supporting cylinders provide additional stiffness and support against the axial instability of the two windings.

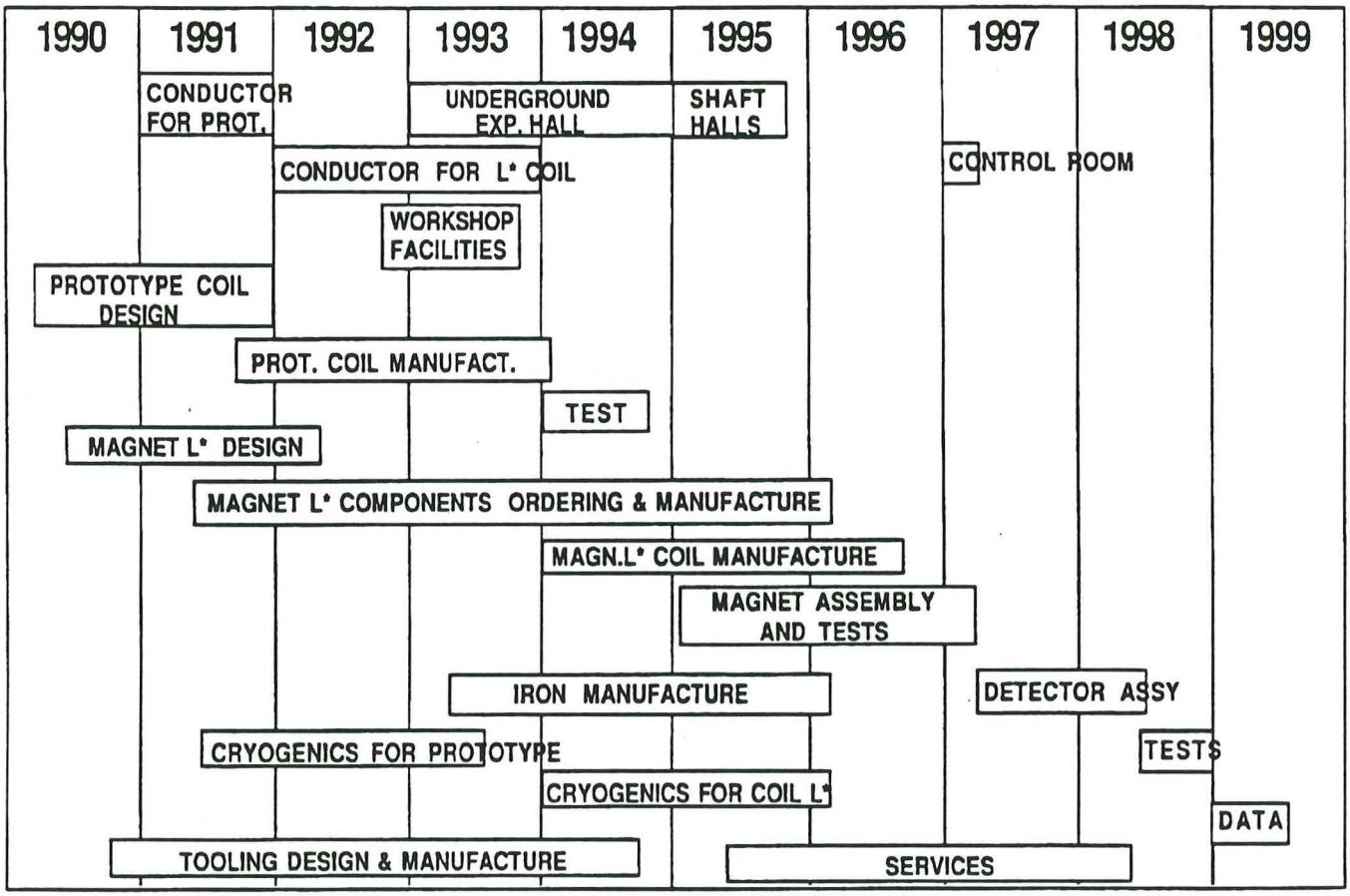

Fig.III.16. Manufacturing schedule.

Another possibility is to assemble the coil as pancakes having four turns on the inner diameter and two turns on the outer diameter wound in opposite directions (Fig. III.19). The inner diameter turns make the inner solenoid, and the outer diameter turns make the outer solenoid. Stainless-steel tape that is co-wound with the insulated conductor carries the axial and the hoop loads. Turns are bonded to thin stainless-steel plates that span the annulus between the inner solenoid and the outer solenoid. This creates a composite winding structure that is very rigid against in-plane bending. An additional structural frame between pancake modules provides stiffness against out-of-plane bending (Fig. III.20).

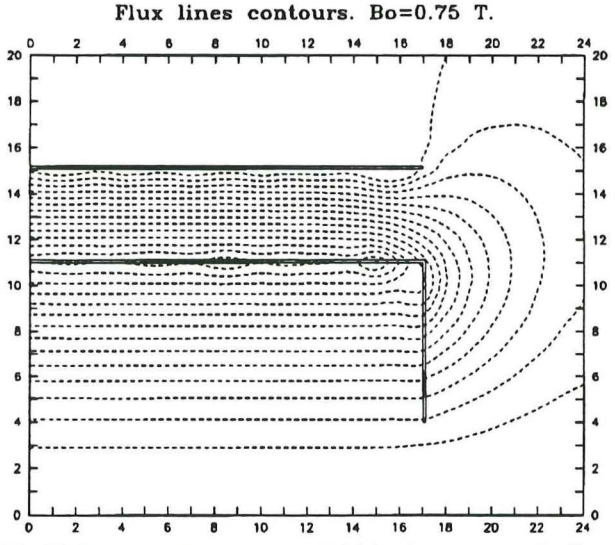

Fig.III.17. Map of the magnetic field for the superconductive coil with superconductive shield.

This structure is attractive due to the possibility of reducing manufacturing labor and eliminating welding, heat treatment, machining and winding from the inside of the magnet. Tolerance requirements resulting from the need for an intimate interface between the winding and a support cylinder are also eliminated. The stainless-steel plates carry the bending moments with negligible shear stress in the epoxy bond and with a high safety factor.

The protection problems of the double coil version are similar to those of the single coil, except more parallel energy dump circuits will be required. In the pancake-wound design there is no support cylinder to create a shorted turn closely coupled to the winding. The layout of the workshop for the manufacturing of the double coils with the pancake structure is shown in Fig. III.21.

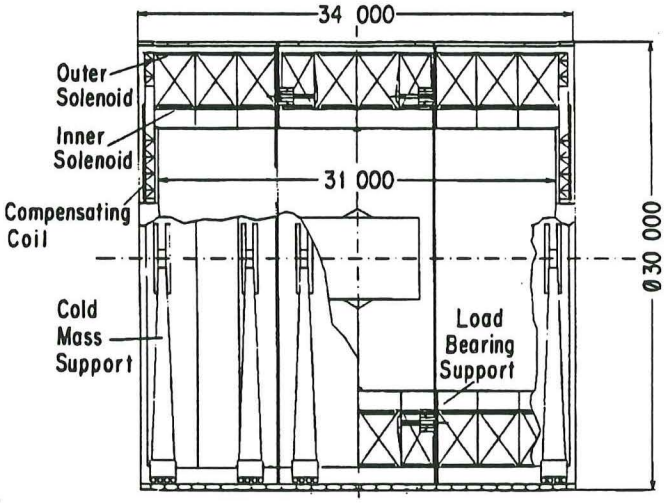

Fig.III.18. Layout of the double-coil magnet.

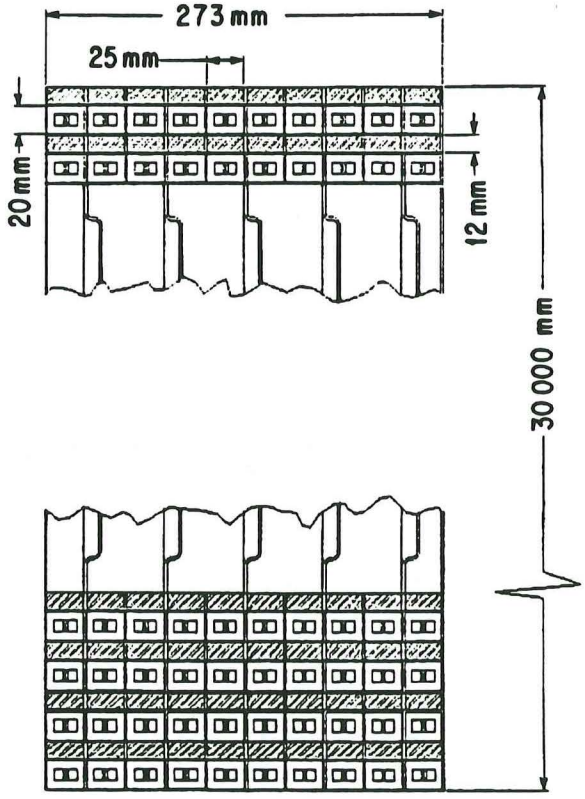

Fig.III.19. Alternate solution to produce the nested solenoids.

E. CRYOGENIC SYSTEM

Heat leaks for each of the two superconducting systems are estimated in Table III.8 The superconducting shield has about 40% higher refrigeration demand because of the larger number of current leads. Otherwise the arrangements are very similar.

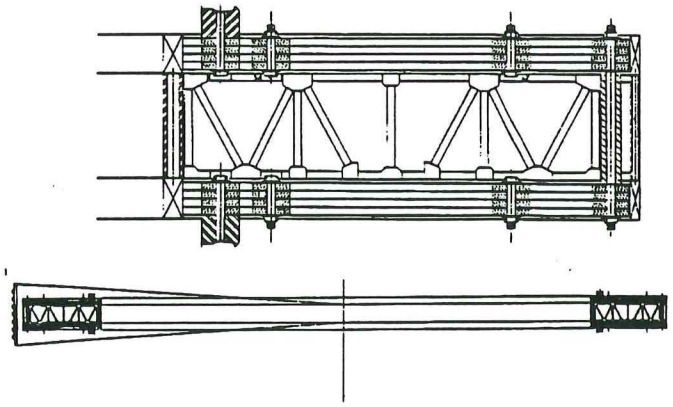

Fig.III.20. A structural frame between pancakes provides the required stiffness.

Table III.8. Magnet Heat Losses

Parameter	Value	Unit
Magnets:		
Radiation to 90°K shield ($3600m^2$ x $0.1W/m^2$)	360	W
Conduction via supports	80	W
Currents leads	530	W
(0.11 g/s per kA pair × 23kA × 70 W/g/s) VCL stack	10	W
Splices	10	W
Piping:		
75 mm diam return - 100 m long	90	W
25 mm diam supply and services - 200 m long	90	W
Dewar Losses		
60 000 l × 0.5% per day boil off × 90 W per g/s	40	W
Bayonets losses:		
30 × 3 W each	90	W
Valve losses:		
50 × 2 W each	100	W
Total 4.5°K load	1400	W

The ALEPH magnet as referenced to in Sect. C uses the thermosiphon cooling method. The fusion magnets use forced flow cooling of the conductor. In the present design, both methods are used to combine their respective advantages to offer redundancy for higher reliability. The first cooling system uses the thermosiphon technique to cool the aluminum support cylinder to which the conductor is bonded. Natural convection flow develops in vertical coolant tubes attached to the support cylinder. This cooling system is passive; it does not depend upon a refrigerator to maintain operation. The thermosiphon cooling system will function until the liquid helium volume

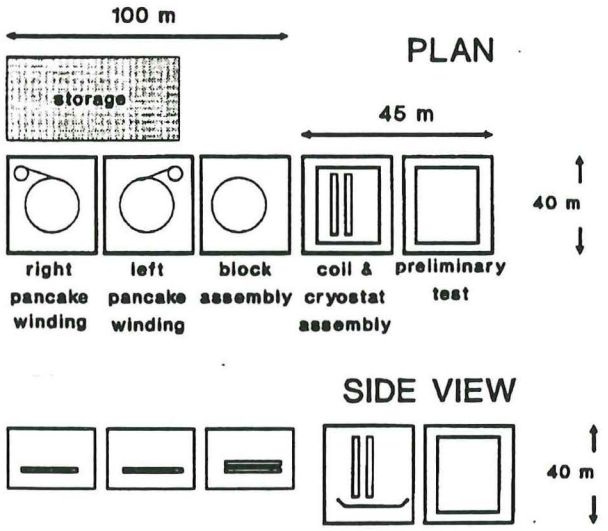

Fig.III.21. Workshop layout for the manufacturing of the nested coils version.

of the storage Dewar feeding the system is depleted. The thermosiphon natural convection loop is shown in Fig. III.22. The coil support cylinder has tubing attached to the outside which is connected to headers so that density differences in the helium columns promote free convection. About 600 g/s moves through this free convection loop. This loop handles all heat loads to the magnet, including thermal radiation, cold mass support conduction, and joint heating.

The second system uses a straightforward forced flow cooling system that circulates single phase helium adjacent to the current carrying superconductor.

This forced circulation loop (Fig. III.22) is required in addition to the natural convection loop for two reasons: (1) It provides thermal capacity adjacent to the superconductor. Metals have extremely low thermal capacity at 4.5°K. Without the higher thermal capacity of the helium, the conductor would be extremely sensitive to thermal perturbations associated with conductor motion, and the risk of a quench would be high. The helium in the conductor increases the critical energy margin up to 3.9 J per point perturbation. (2) The slight flow in the forced flow channel is in direct contact with conductor joints and distributes joint heating over large areas so it can be more readily carried away by the natural convection loop. The forced flow loop eliminates any possibility of hot spots in the conductor, and the natural loop removes all the heat.

Both of these cooling systems are sized to cool the superconducting coil independently, and the cooling system reliability is improved by having both cooling systems working together.

A large storage Dewar is also used to provide up to 40 h of operation without power.

Liquid nitrogen for the magnet thermal radiation shield will be commercially supplied by truck every eight days although the 160 m^3 storage capacity can maintain the system for 60 days. Liquid nitrogen is also used to cool the magnet from room temperature to 77°K. A liquid nitrogen/helium heat exchanger is used. The total cool-down time from room temperature to 4.5°K is about 320 h.

A 12 ×24 m^2 building contains all the cryogenic support equipment and houses the controls for cryogenic and other detector magnet support systems.

For the refrigerator plant, screw compressors will be installed. They are of proven reliability in helium operation and capable of continuous service over periods up to 8000 h without maintenance. The electric power consumption of the compressor group, including the helium cleaning system is minimized. To prevent air infiltration into the helium gas stream, the succion pressure is kept above atmospheric pressure. The coolers are of a very reliable design to avoid leaks between the helium and water circuits. For this reason, the coolers are constructed using evacuated austenitic stainless steel. The compressor waste heat is lead off by a closed-circuit cooling tower into the atmosphere.

For the cold process, the plant has a cold box placed in the main hall over ground level. The distance between the compressor group and the cold box is about 120 m. The cold box, together with the necessary equipment for control, vacuum and purge, is mounted on a platform that is movable with the hall's overhead crane as a unit. The refrigerator is equipped with gas bearing turbines. The turbines are appropriate for long-term reliable service, with minimum downtime for maintenance; They are readily accessible for maintenance and repair.

The whole measuring system is equipped with a complete set of sensors and measurement devices connected to a microprocessor in such a way that the refrigerator is able to operate with high reliability and safety in its various operation modes: helium system

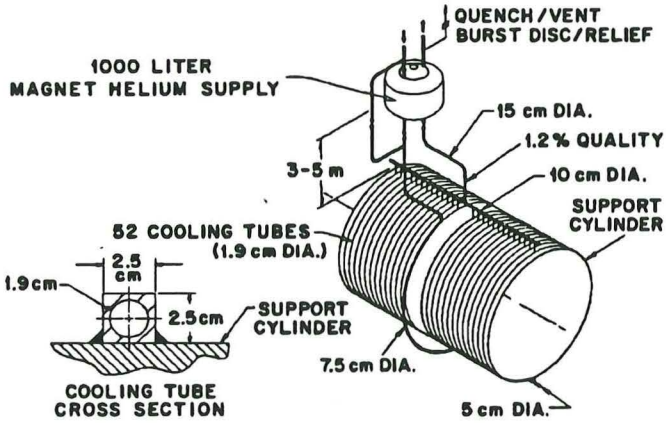

Fig.III.22. Natural convection cooling loop.

purge, cool-down, normal operation with or without users, system warm-up, and emergency.

The refrigerator is able to cool down or warm up one half of the detector magnet independently of the other half. A forced warm-up process is foreseen, with room temperature helium from the compressor system being blown into the last heat exchanger of the refrigerator.

F. FORWARD-BACKWARD SPECTROMETER MAGNETS

To complement the main solenoid for muon measurements at small angles where the bending power of the main solenoid decreases rapidly toward zero, a forward-backward spectrometer system is installed at ± 19 m from the interaction point. To suit the installation of L3 type muon chambers, a rectangular solenoid with vertical field axis is the best solution.

F.1. Determination of the Magnet Characteristics

These magnets are arranged to have the magnetic field perpendicular to the beam direction and are thus well suited for the analysis of low angle particles. A compromise has been found for an angular coverage of down to 2.0° with a 0.3-T field and a 2.5-MW power (per side). With this arrangement, the 4π coverage of precision measurement ($\Delta p/p \approx 2\%$) for $H \Rightarrow 4\mu$ is complete.

F.2. Description of the Spectrometer Magnets

The forward-backward spectrometer has been designed as two simple magnets using the L3 coil construction technique (Fig. III.23). The magnetic axis is vertical to ease the muon chamber manufacturing. The coil is split in two halves with a gap of one meter to allow for the last accelerator beam elements, which are situated 20 m from the interaction point (protruding inside the spectrometer magnet). To suppress perturbations of the field uniformity due to this gap in the coil, the turns nearest to the gap will receive a higher current. The internal volume of the magnet is protected from the heat losses

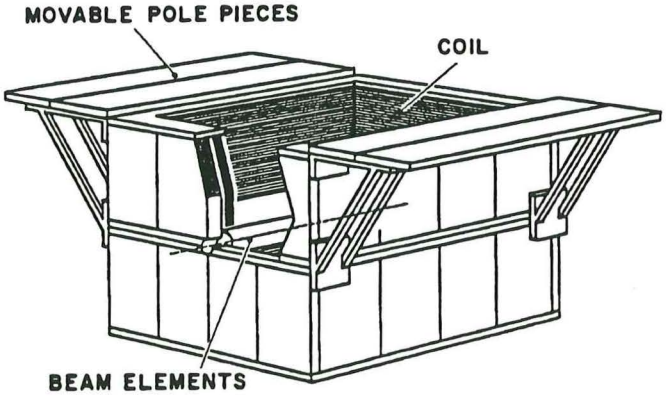

Fig.III.23. General view of a forward-backward magnet.

Table III.9. Main Parameters of the Spectrometer Coil

Parameter	Value	Unit
Current	16.3	kA
Coil resistance at 60°C	9.4	mΩ
Coil total voltage	153	V
Central induction	0.3	T
Free length along beam	9.22	m
Ampere-turns	19.6×10^6	A
Inductance	1.4	H
Stored Energy	26	MJ
Number of turns	120	-
Conductor section	30 × 5	cm^2
Conductor weight	200	ton
Water flow (coil)	90	m^3/h
Bus-bar losses	100	kW
Coil DC power	2.5	MW

of the coil through the same thermal shield described in Sect. B.

The cooling requires 90 m^3/h of demineralized water with a temperature gradient of 25°C. This water comes from the same system as the main coil. See Table III.9.

F.3. Magnetic Flux Return Frame

Because the coil is split in two, the magnet itself is also split in two halves to allow for the mounting in the experimental area in two completely finished and tested indivisible loads of 800 tons. To give access to the inner muon chambers, the upper pole is split in two halves that can slide sideways on cantilevered supports. The magnet flux return frame consists of a square barrel, coaxial with the coil, and two pole crowns per half magnet. Each pole crown is a self-supporting structure holding the barrel, that is made up of thick iron plates. See Table III.10.

Onsite Facilities for Manufacture

The halls foreseen for the manufacture of the main solenoid coil will be used to weld, equip, and test the pancakes. The external concrete slab will be used to manufacture the pole structures.

F.4. Assembly Sequence

To limit assembly time in the underground area, each spectrometer magnet will be lowered from the surface as two 800-ton loads by the gantry crane. They will be the first elements to be lowered in the experimental hall, as described in Sect. B.5.

G. QUALIFICATIONS AND MEMBERS OF THE MAGNET SYSTEM GROUP

The Kurchatov Institute and the affiliated institutes and organizations listed below represent a combination of skill, experience, and manufacturing capability well

Table III.10. Main Parameters of the Return Frame

Parameter	Value	Unit
Barrel thickness	37	cm
Pole thickness	43	cm
Pole weight (one)	320	ton
Total Iron weight	1700	ton
Ext. magnet width	900	cm
Ext. magnet length	1140	cm

qualified for the design, fabrication, testing, and installation of the L* magnet system. An overview of the recent activities of the Kurchatov Institute is given in Table III.11.

Technical leadership and program management will be provided by the Kurchatov Institute representing demonstrated and internationally recognized success with the development and operation of superconducting materials and magnet systems of many types and applications. The Kurchatov Institute has been a pioneer and continues with the Efremov Institute to be a major developer of both fusion power and associated engineering technologies.

The TOKAMAK containment configuration was first developed at Kurchatov, which currently operates the world's largest superconducting TOKAMAK system. This represents a level of technology that is adequate for the L* magnet system.

Experience with the design and manufacturing logistics systems of comparable size and complexity is represented by the heavy industry, ship building, aerospace, and other affiliates of the Kurchatov Institute.

Table III.11. Characteristics of Some Magnet Systems

Magnet	Year	Current (kA)	Maximum field (T)	Energy stored (MJ)
Solenoid Jubilee	1967	0.6	5	0.34
Solenoid Kc-250	1972	1	8(25)	2
CMS-0.25	1974	3.7	2	1.5
LIN-5B	1976	2	8.7	8
Solenoid Maxihin	1976	5	11.7	3
T-7 toroid	1978	5	5	20
T-15 toroid	1990	3.9	6.3	370

The cryogenic and control system will be designed by LLNL and provided by the United States.

The following Institutes and industrial enterprises expressed their interest to participate in the magnet manufacturing and assembly onsite at the SSC:

Soviet Union:

- Kurchatov Institute of Atomic Energy, Moscow
- Institute of Theoretical and Experimental Physics, Moscow
- Efremov Research Institute of Electrophysical Apparata, Leningrad
- All Union Research Institute for Cable Industry, Moscow
- Bochvar All Union Research Institute of Inorganic Materials, Moscow
- Uhlba Metallurgical Plant, Ust-Kamenogorsk
- Central Research Institute for Aerohydrodynamics, Moscow
- Prometei Research Institute for Structural Materials, Leningrad
- Institute for Mounting and Assembling Technology, Moscow

United States:

- MIT Plasma Fusion Center, Cambridge
- LLNL, Livermore
- ORNL, Oak Ridge

H. R&D REQUESTS

We request SSC support of five Soviet Engineers and five Soviet scientists for the next two years to work at the SSC to integrate their ideas with SSC requirements, experience, and standards.

Costs per person: 30k$ per year.

Travel costs per person: 2k$ per year.

Total cost: 320k$ per year.

We also request 180k$ for support of magnet studies in U.S. laboratories for FY 1991. Total R&D request for FY 1991 is 500k$.

A. DESIGN CONSIDERATIONS

Most of the recent discoveries of new particles (J, Υ, τ, W, Z^0) were made by measurement of leptons and lepton pairs with good ($\leq$2%) mass resolution. The L* experiment will continue this physics by detecting muons of the highest energies in a high resolution 4π spectrometer after absorbing the copious hadrons produced in a calorimeter close to the interaction point. The penetrating muons have tolerable rates and backgrounds.

The resolution of the L* detector should be of the order of the Z^0 line width for $Z^0 \rightarrow \mu\mu$ produced at several hundred GeV, specifically

$\Delta P/P$ = 2.4% at P = 500 GeV.

A momentum resolution of 2.4% and mass resolution of 1.7% have been achieved by L3 for 45-GeV muon pairs (see Fig. II.8). The L3 experiment has three layers of equally spaced precision drift chambers. Each layer samples the track with either N = 16 or 24 wires. Each wire provides a resolution better than 250 μm. The large L3 magnet has an analyzing power $BL^2 \cong 4.2$ Tm^2 to determine the momenta of muons. The same principles can be used to obtain 2.4% momentum resolution at 500 GeV as shown in Table IV.1.

Table IV.1. Comparison of L3 and L* Parameters

Parameter	L3	L*	Unit
P_T	50	500	GeV
BL^2	4.2	20.7	Tm^2
N	24	64	wires
σ_0	250	150–200	μm

In contrast to L3 where $P_T \cong$ 50 GeV/c, in L* $P_T \cong$ 500 GeV/c. This implies that in order to keep the same resolution, it is necessary to increase the analyzing power by a factor 5, increase the number of measurements from 24 wires to 64 wires, and reduce the single wire resolution from 250 μm to 150–200 μm.

At large energies photons from real radiative energy losses are well measured in the calorimeter. The resolution is expected to be $\Delta E/E \cong 0.3/\sqrt{E}$.

While tails of showers leaving the calorimeter may confuse a substantial fraction of the muon measurements in the chambers of a nonmagnetic detector, the B field in L* sweeps low energy particles away (Fig. IV.1), so that the track measurement will be accurate (Ref. IV.1).

A preliminary estimate of charged particle rates in the muon chambers has been made using ISAJET version 6.24 (Ref. IV.2) to generate proton-proton interactions at 40 TeV in the L* geometry. A parameterization of punchthrough probabilities was adjusted to match

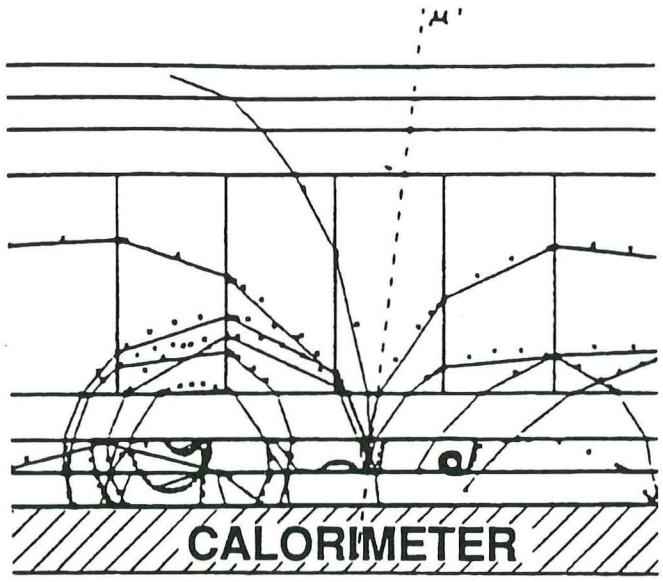

Fig. IV.1. Muon track with shower fragments. Calculation for 500-GeV muons using L3 GEANT 3.11 program of Ref. IV.1.

GHEISHA/GEANT (Ref. IV.3) simulations at 15, 100, and 300 GeV. We assumed a luminosity of 10^{33}. Figure IV.2 shows the rate of charged particles penetrating into the muon detector volume vs θ, the angle with the beam. The uncertainty in these estimates is indicated by the hatched area.

We obtain a total rate of 23 $\times$ 10^6 per second or an average of 23 particles in the detector ($2° < \theta < 178°$) at

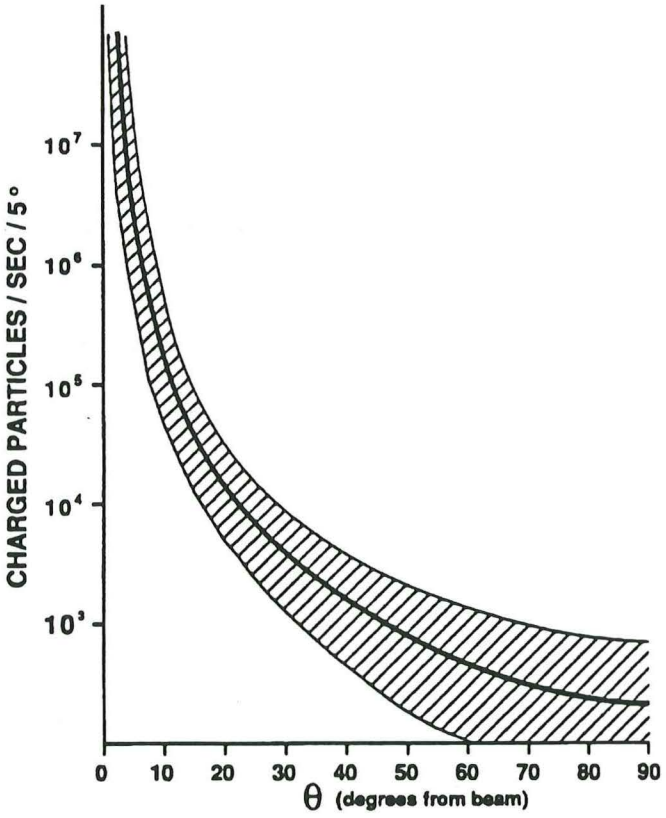

Fig. IV.2. Rates of charged particles in the L* muon detector vs θ.

some time during the 1-μs drift time of the muon chambers. On average, only one of these particles is at an angle greater than 7.5° with the beam. The remaining particles are in the forward external magnets. With beam crossings occurring every 16 ns, these rates are summarized in Table IV.2, subdivided according to the different angular regions of the detector. This table demonstrates that, except for angles below 7.5° with the beam, the occupancy in the muon detector is low.

Table IV.2. Angular Distribution of Rates in One Muon Detector Hemisphere

Range (degrees)	2.0–7.5	7.5–17.5	17.5–30	30–90
Particles/μs	11	0.3	0.03	0.013
Particles/xing	0.2	5×10^{-3}	4×10^{-4}	2×10^{-4}

At normal drift chamber operation these rates translate into an accumulation of 0.02 Coulomb/cm on the highest rate wire at 2° and 20 m from the intersection (see Fig. II.1) after 1 year of uninterrupted running at full luminosity. At 7.5° and 5.2 m from the intersection the rate is 0.004 Coulomb/cm. Hence the gas used in the chambers must be carefully chosen to avoid aging at these high rates.

B. L3 EXPERIENCE

The design of the L3 muon detector (Ref. IV.4) required more than 7 years of research and development (R&D). This effort resulted in a detector that contains 80 multisampling drift chambers, each of approximately 12 m^2 area, in 16 independent modules. The total weight of the detector is about 160 tons. The L3 muon detector, now in operation for 1 year, has reached and surpassed design specifications.

The L3 design concepts, construction techniques, and alignment procedures can be extended to detectors at higher energy machines and have guided us in our design of the L* detector. Hence, the L3 detector, as described below, serves as an introduction to the design we propose for the SSC.

The L3 detector (Fig. IV.3) measures muon momenta to an accuracy of $\Delta P/P$ = 2.4% at 45 GeV providing a mass resolution of $\Delta m/m$ = 1.7% for a 100-GeV particle decaying into a pair of muons. The muon momentum is measured in free space by three layers of drift chambers positioned between the support tube and the magnet coil.

The muon detector system operates in a 5-kGauss magnetic field parallel to the beam. The magnetic field results in a 3.7-mm sagitta for a 45-GeV muon. The sagitta is measured to within 2.4% in order to obtain the desired momentum resolution.

To achieve high resolution the error contributions to the sagitta (momentum) measurement were carefully minimized. The major contributions are

- Intrinsic chamber resolution 50 μm
- Multiple scattering 0.9% radiation length
- Alignment accuracy <30 μm

The final accuracy was verified by UV lasers and cosmic ray calibrations. These techniques result in a combined systematic error in the drift chambers, octant structures, and in the octant internal alignment better than 30 μm. In addition to measuring the muon coordinate to 50 μm, each chamber measures the local track angle better than 2 milliradians.

The muon detector is modular, consisting of two "ferris wheels" of eight "octants" each. Each octant consists of a precision mechanical structure which supports and maintains the alignment of five momentum measuring "P" chambers. There are two chambers in the outer layer, two middle chambers, and one inner chamber. The top and bottom covers of inner and outer chambers are drift chambers which measure the z-coordinate along the beam, and thus measure the polar angle θ. There are six z-chambers per octant. The middle chambers are covered by thin honeycomb panels to minimize multiple scattering. Two of these honeycomb panels contain only 0.9% of a radiation length of material. A complete octant assembly, with five "P" chambers, six z-chambers, amplifiers, UV laser system, and gas tubing is shown in Fig. IV.4. It displays the complexity of engineering and system integration experience.

The momentum measuring chambers are constructed of cast and machined aluminum endframes and extruded aluminum side panels. Each chamber contains 40 wire planes, or a total of 3000 wires for field shaping and signal measurement. Automatic fabrication procedures were developed; for example, the wire planes were wound on drums and then immediately soldered onto the final printed circuit boards. The resonant frequency of a wire is directly related to its tension and sag. Each wire plane was checked prior to loading to ensure that all wires were within the adjustment range.

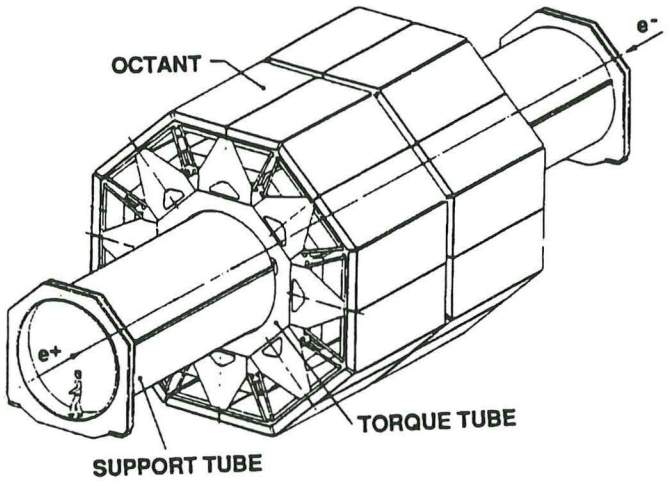

Fig. IV.3. The L3 muon detector contains 80 multisampling drift chambers in 16 independent modules. The total weight is 160 tons.

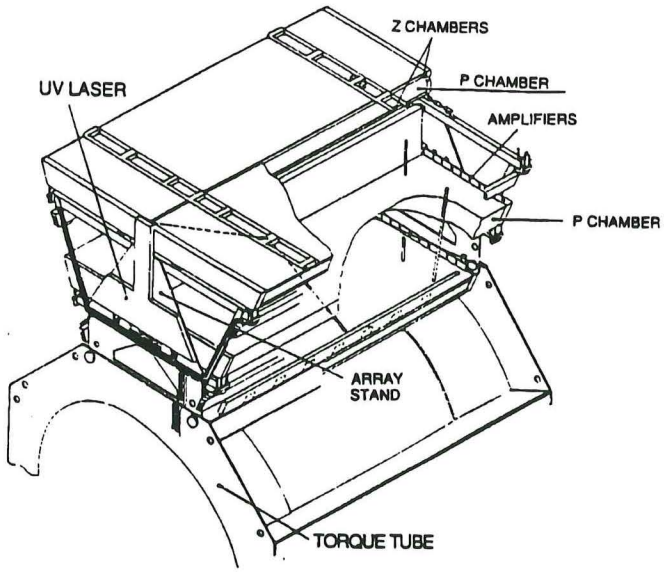

Fig. IV.4. L3 octant assembly: The 16 modules are independently aligned and functional for momentum measurement including UV calibration and optomechanical monitors.

Quality control and check procedures were incorporated to ensure high accuracy of the chambers. The key element is the precise wire positioning. A method was developed to position wires with an accuracy of better than 10 μm. A precise Invar template was used to position and glue optically flat Pyrex glass plates to carbon fiber bars to make "bridges." Wire planes are attached to the bridge glass surfaces, and held in precisely determined positions. All glass plate positions were verified using a laser interferometer system, and the deviation of the glass surface positions from ideal is shown in Fig. IV.5. It shows that 240 structures were built to 5-μm accuracy. Wire plane lengths were adjusted in the chamber to get a vibration frequency at the first harmonic of 27.85 Hz.

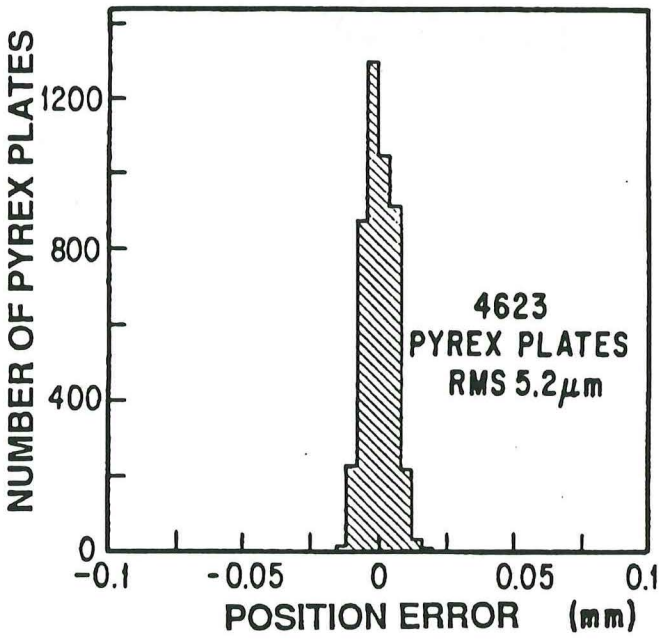

Fig. IV.5. The accuracy of all 300 wire positioning bridges produced for L3 as verified by a laser interferometer (σ = 5.2 μm).

Since the vibration frequency determines to the wire sag, this method ensures that all wires sag the same amount. There is one bridge at each chamber end, and a bridge in the middle which reduces the wire sag by a factor of 4, to 95 μm. This is within the tolerances for which a software correction is possible. A threefold internal alignment system consisting of LEDs, lenses, and quadrant photodiodes was integrated into the bridges (Fig. IV.6). Light from the LED is focused by the lens onto the quadrant photodiode. The systems were calibrated on an optical bench, and optimal alignment is achieved when all four quadrants receive equal amounts of light. The "end" bridges were positioned with respect to external references, and the "middle" bridges can be moved by means of actuators in response to the alignment systems to bring the bridges (and thus the wires) into correct alignment.

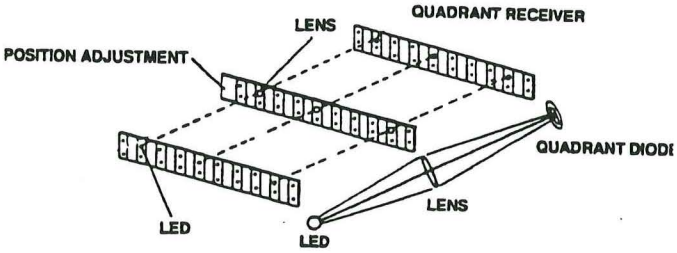

Fig. IV.6. Three-bridge wire support and alignment system. The alignment system is integrated into the wire support and reaches 5-μm accuracies.

All chambers were tested with cosmic rays. Chamber resolution with cosmic rays is shown in Fig. IV.7. This plot shows that the chamber resolution using these production techniques was better than the design goal.

The octant stands are precision structures (Ref. IV.5) which support the chambers and maintain the alignment to better than 25 μm over long time periods. These structures were designed for linear force transmission and elastic behavior, and thus behavior of the octants is fully

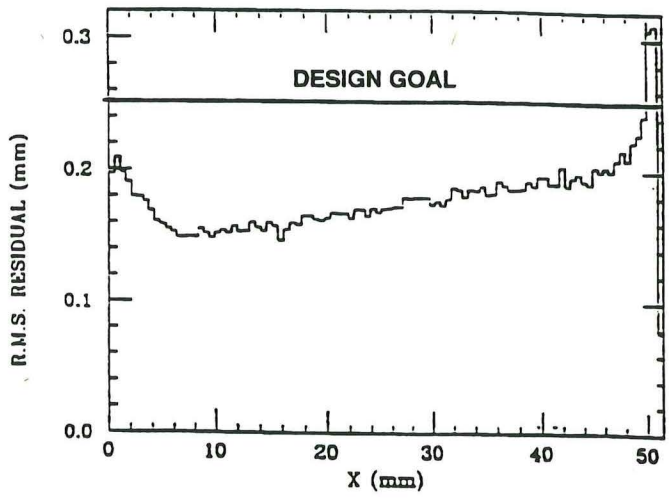

Fig. IV.7. Chamber resolution with cosmic muons vs x, distance from the wire.

predictable under all conditions of stress, load, and temperature. This was checked for each module by 360° rotation after full installation of all components (see Sect. C.1 in this chapter).

Chambers were installed into the octant supporting stands, and the octant was aligned. A dual optomechanical straightness monitor system similar to that in the bridges was used to establish octant centerlines at both ends of all octants. The redundancy guarantees accuracy. Figure IV.8 shows the direct reference of the system to the wires. A precision piece containing two LEDs and an insulated brass pin is attached to each endframe of an inner chamber. Similar pieces are mounted between the two middle and outer chambers and have two opposite insulated pins whose ends have a precise separation of 101.500 mm. The assembly between the middle chambers contains a lens, and that between the outer chambers contains two quadrant diodes. All pins are referenced to the corresponding optical component and touch one wire of a signal plane. The end bridges can be moved to just make or break electrical contact between the wire and the pin. In this way, the end bridge relative positions are known to within better than 5 μm. The middle chamber layer can be moved on its titanium flexure feet in response to readout from the straightness monitor system, to bring chamber centers into a straight line. The centerline through the three chamber layers is defined to better than 10 μm. Fig. IV.9 shows the stability of this system in the L3 detector. The two diode systems of the double set track each other to better than a few microns and the overall structure was stable to $< 4\,\mu$m over the period recorded.

A rotating laser beacon (Ref. IV.6) is mounted on each octant (Fig. IV.10) and is used to ensure that the two octant centerlines established by the two straightness monitors are parallel to each other. Position-sensitive photodiode arrays are attached to each of the three straightness monitor elements on each end of the octant and record the position of the passing laser beam. This

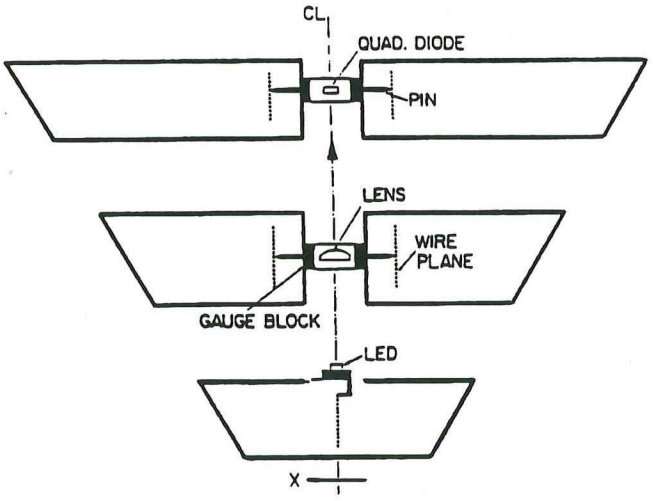

Fig. IV.8. The vertical straightness monitor establishes an octant centerline (CL) accurate to 10 μm, which is referenced to the wires of all chamber layers.

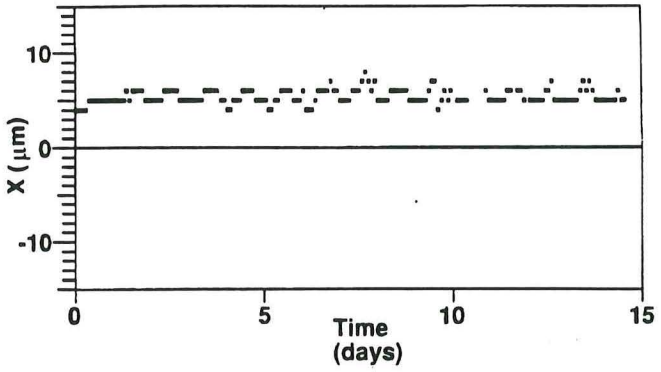

Fig. IV.9. In a functional L3 octant, the displacement (x) of the middle chamber from the octant centerline is stable to 4 μm over a 15-day period.

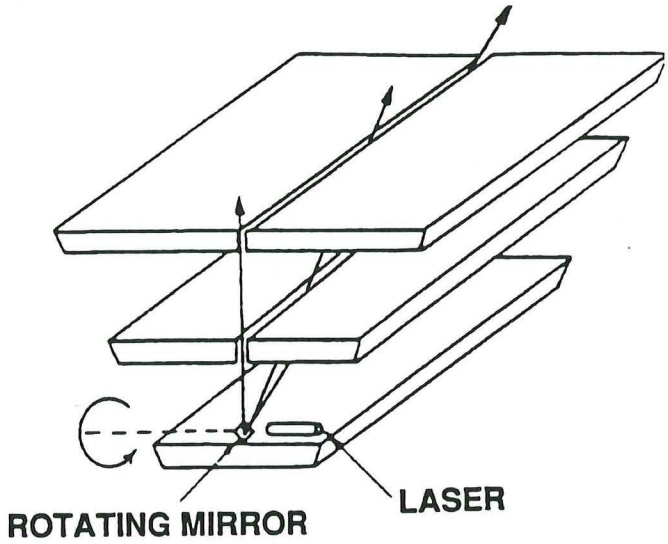

Fig. IV.10. The rotating laser beacon measures parallelism of the two octant centerlines to within 25 microradians.

system measures the angle between the two centerlines to 25 microradians. Outer and middle chambers were adjusted to reduce this angle to zero, and the remaining sagitta error is less than 10 μm.

Each octant also contains a two-stage computer controlled nitrogen UV laser (Ref. IV.7). The laser beam is directed across the outer chamber layer by means of an addressable beam steering element (Fig. IV.4) and down through all three chamber layers in eight different paths which point roughly toward the interaction region to simulate infinite momentum muons. The sagitta of laser events should be zero and thus is used to verify the alignment.

Each octant was constructed to within alignment specifications (Fig. IV.11) using the straightness monitors and laser beacon and was then tested with UV laser shots and cosmic rays. Figure IV.12 shows the results of sagitta verification with the UV laser for one octant.

Figure IV.13 shows the final alignment verification for all of the 16 octants. An optomechanical zero was determined by the straightness monitor settings. The squares show verification of the geometry by UV laser measurements, and cosmic ray data are shown in circles as

another confirmation of the alignment. All octants are shown to be aligned to within the ±30 μm specification.

The final check of the L3 muon detector accuracy comes from the direct measurement of events

$$e^+ e^- \rightarrow Z^0 \rightarrow \mu^+ \mu^-$$

with well known $\sqrt{s}$ from LEP as seen in Fig. II.7. Measuring the sagitta yields the momentum resolution shown in Fig. II.8. Including all systematic alignment errors, multiple scattering effects, and unresolved radiation losses, the resolution is

$$\frac{\Delta P}{P} = 2.4\% ,$$

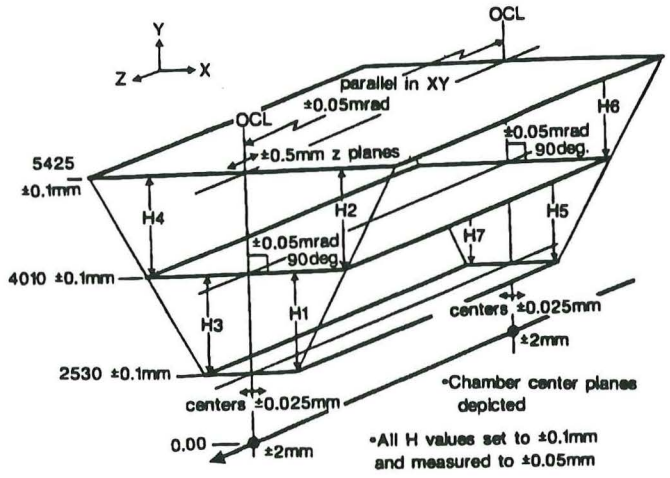

Fig. IV.11. Specifications for L3 octant alignment tolerances, to reach 30 μm combined systematics. Note the ±0.025-mm tolerances on the two octant centerlines (OCLs).

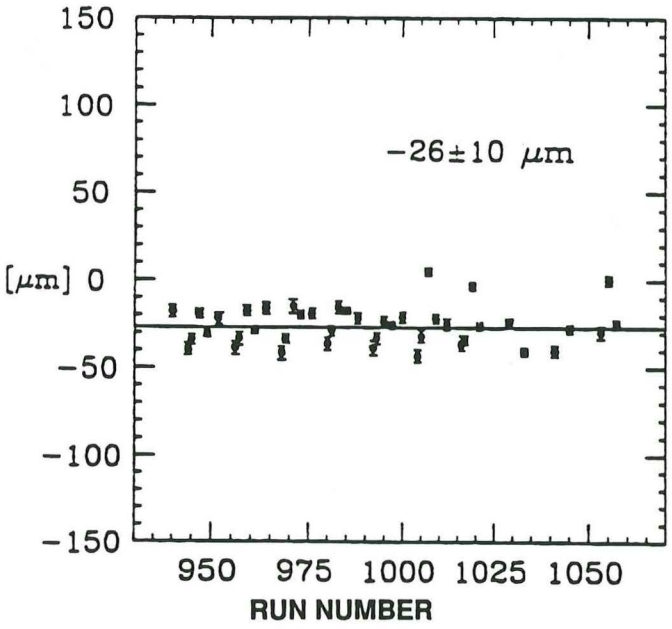

Fig. IV.12. Accuracy of the UV laser calibration, checked over an extended period. This is an independent check which verifies the alignment and the octant function.

which is the design value (Ref. IV.4). We note that the corresponding dimuon mass resolution is better by a factor of $\sqrt{2}$, that is, $\Delta m/m = 1.7\%$.

The techniques described in this section have been successfully utilized in the L3 detector at CERN. Extension of these principles allows accurate muon momentum measurement at the SSC.

C. DESIGN CHARACTERISTICS

The L3 Muon Detector provides a proven basis for the design of the L* muon detector. The main features of the muon detector design are described below, along with the approach to addressing the problems due to the different environment at the SSC.

C.1. Engineering Considerations

Increased Size

Increased distances in the radial direction, needed to increase the track bending length, require chamber support over roughly twice the distance of L3. Increased distances along the beam axis, needed to increase the measuring volume in the forward direction, require longer muon chambers and supporting structures. Although our approach, as in L3, is to modularize the detector wherever possible, the size of the smallest possible module is

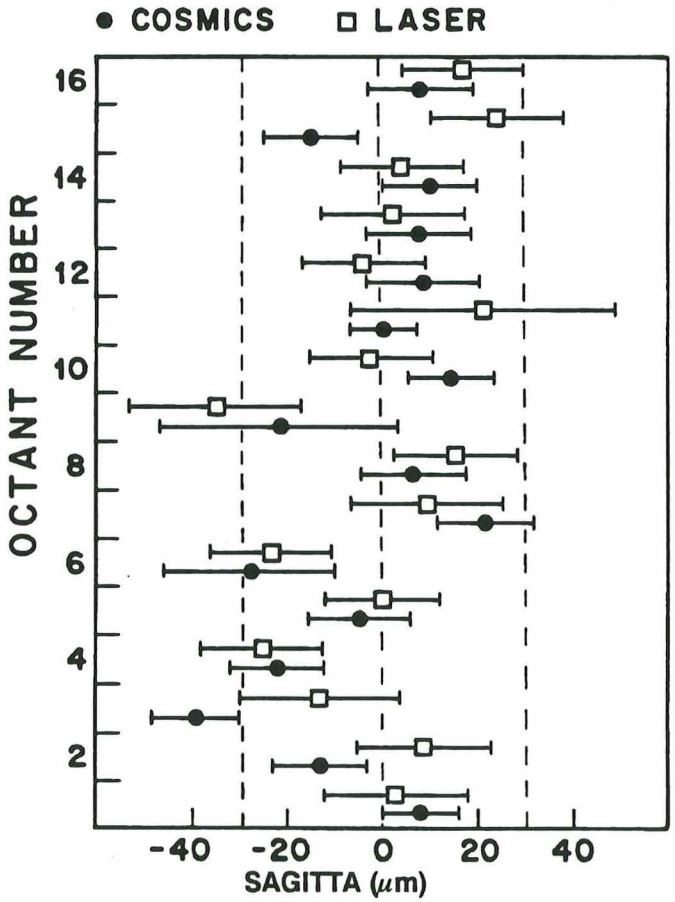

Fig. IV.13. Verification of the 30-μm design tolerances for all 16 octants. The zero line is defined by the vertical straightness monitor system. Square points are UV laser data, and circles are cosmic ray data.

roughly double that of L3. The effects of the size and required precision of the muon detector indicate two main focuses of the engineering: alignment and construction/handling.

More Precise Alignment

The overall increase in the required alignment precision of the L* muon detector compared with that of L3 is a factor of 2 to 5. Adaptation of our alignment tools involves substantial engineering to meet these new goals.

Also with these more stringent alignment requirements comes the need for increased dimensional stability in the chamber support. An example is shown in Fig. IV.14, which shows the mechanical deformations of an L3 module during a 360° rotation. Most notable is that the deformation is elastic and repeatable within the measuring accuracy of 6 μm. Careful planning and design of the elastic nature of the structure, the stability against long term creep, the materials selection, the safety factors, and perturbations in the magnetic environment are crucial to the success of the engineering as it relates to alignment.

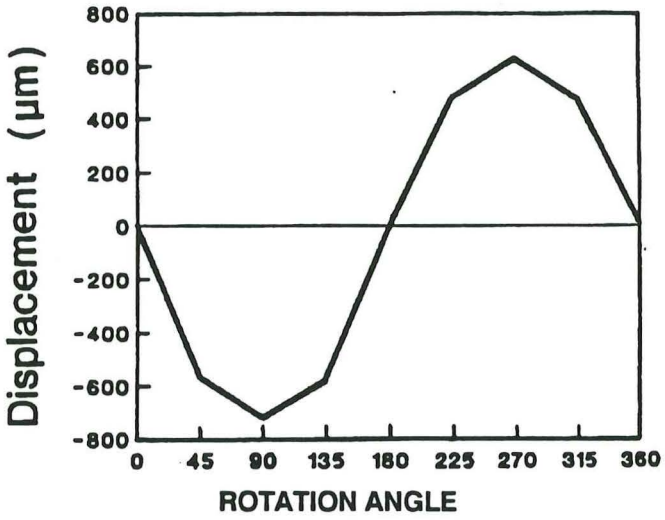

Fig. IV.14. Elastic deformation of a fully operational L3 octant during rotation. It is reproducible to 6 μm in 0°–360°

Manufacturing

The engineering of the muon detector focuses from the beginning on the requirements for the construction and handling. Producing and transporting high-precision detector elements, with these dimensions, create some very unique engineering considerations. Detailed analyses of the reliability and the necessary quality controls for fabrication and assembly of all detector components must be incorporated from the early stages of R&D.

C.2. Design Overview

The three parts of the L* precision muon detector are shown in Figs. II.1 and II.2. "Central" muon chambers are located in the central solenoidal magnet, and cover the region above 33.4°. "Endcap" chambers, also inside the central magnet, cover the region from 7.5° to 31.6°; and small angle "forward" chambers in external forward magnets cover the region from 2° to 7.5°.

This detector is designed to provide sagitta measurements with a precision of 2.4% at 500 GeV. The precision of the momentum measurement rests on the accuracy of the following:

- The chambers 20–30 μm
- The array stand alignment $<20\,\mu$m
- The verification with UV lasers and cosmic rays $<20\,\mu$m

Figure IV.15 shows the principle of sagitta measurement in an L* central region radial module.

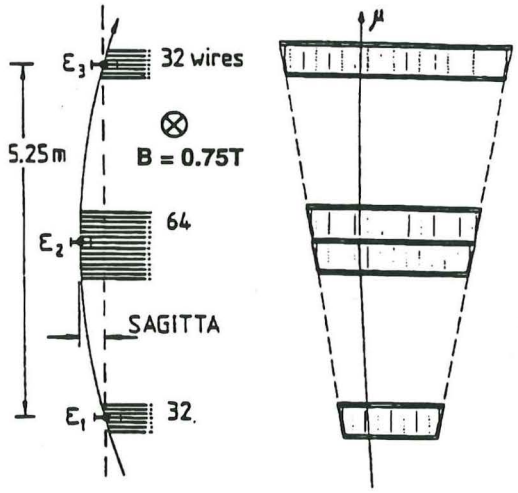

Fig. IV.15. Sagitta measurement in one radial module of the central detector (B = magnetic field).

Each track is measured in three chambers with 32, 64, and 32 wires respectively. With single-wire resolution of 150 μm and 94% of the wires in each chamber used in the fit (6% not used because of inefficiencies and delta rays), the inner and outer chambers measure the track coordinate with a resolution of

$$\varepsilon_1 = \varepsilon_3 = \frac{150\,\mu\text{m}}{\sqrt{0.94\times 32}} = 27\,\mu\text{m}$$

and the middle double chamber with a resolution of

$$\varepsilon_2 = \frac{150\,\mu\text{m}}{\sqrt{0.94\times 64}} = 19\,\mu\text{m}$$

The sagitta error is

$$\Delta s = \sqrt{0.5\,\varepsilon_1^2 + \varepsilon_2^2 + \Delta s_{sys}^2 + \Delta s_{ms}^2}$$

where Δs_{sys} represents all systematic errors and Δs_{ms} represents the effect of multiple scattering in the chambers and air. The systematic errors are kept below 20 μm and, for 500-GeV tracks at 90°, the multiple scattering contributes an additional 15 μm, giving $\Delta s = 37\,\mu$m.

In the central solenoid the magnetic field is 0.75 T directed along the z-axis, parallel to the beam. To cover the angular region above 33.4° there are three layers of central chambers at distances 3.9 m (32 wires), 6.5 m (64 wires) and 9.2 m (32 wires) radially from the beam line. The wires are stretched parallel to the beam line and magnetic field to measure the azimuthal coordinate (bending direction). The centers of the inner and outer chambers are spaced L = 5.25 m apart, such that the sagitta, in millimeters, is given by $s = (BL^2)/(8 \times 0.033 P)$, where B is in kGauss, L in meters, and P in GeV/c. If

P = 500 GeV/c, then s = 1610μm;

this gives $\Delta s/s = \Delta P/P$ = 2.4%.

The resolution shows an improvement as $1/\sin\theta$ as we move away from 90° in the central region.

The endcap chambers in the central magnet cover the region from 7.5° to 31.6°. Momentums are measured in three sets of chambers, each determining x- and y-coordinates. In this way, the sagitta is determined at all ϕ with comparable accuracy. The endcap detector system consists of two parts, which cover 7.5° to 17.6° and 18.8° to 31.6°, respectively. The chamber spacing is increased from Δz = 7.2 m to 8.6 m in the smaller angle range to compensate for the loss in bending power as the angle between the directions of the muon momentum and the magnetic field decreases.

The region from 2° to 7.5° is by covered by chambers in the forward magnets. These also contain three layers of chambers. Wires are strung parallel to the vertical field of 0.3 T in order to measure bending in the horizontal direction. The vertical wire direction eliminates sag and the need for a middle bridge. The chamber spacing of 8 m is chosen to obtain the same resolution as for the central chambers at 90°.

Momentum resolution for 500-GeV/c muons is shown as a function of cos θ in Fig. IV.16. It is better than 2.4% except for the 11% of solid angle between 7.5° and 28.1° covered by the endcap chambers.

The gaps in the resolution curve indicate portions of the solid angle which are not covered or are covered with decreased resolution. This is caused by the central support membrane, the end and side frames of the chambers, and the difficulty in matching chamber geometry at the boundary between central and forward chambers. In a large part of these regions the track is measured, but with less than the full complement of 32 + 64 + 32 wires or with increased multiple scattering in the chamber frames and supports. The preliminary design presented here is very conservative, leaving ample space for chamber mechanics and supports yet covers 85% of 4π. The coverage will improve to about

$$\frac{\Delta\Omega}{\Omega} = 90\%$$

as the design of the chambers and the supports proceeds.

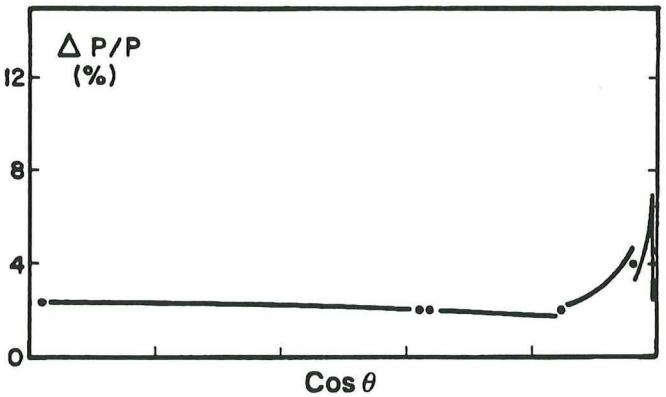

Fig. IV.16. Momentum resolution for 500 GeV/c muons as a function of cosine θ (. . . = partially covered with reduced resolution).

In the bending direction the precision of the momentum measurement requires 20- to 30-μm accuracy of the chambers and better than 20-μm accuracy of the array stand alignment.

The wires within the chamber are aligned with one another to high precision by the glass-carbon fiber bridges developed for the L3 experiment. Three bridges within a chamber are aligned with respect to one another by optoelectronic systems already described in Sect. B. Tolerances of 5 μm can be maintained by the combination of precision bridges and this alignment system. The sense wires of the different chambers within a module are aligned by transferring reference points from the wires near the ends of the support bridges along straight lines by optomechanical systems similar to those within the chambers. The chambers in L* must be aligned in the bending coordinate to 10 μm in order to maintain the overall 20 μm limit on systematic errors.

In the nonbending direction, chamber spacing and alignment are less critical and rely on the mechanical stability of the array structure. The tolerances must be sufficient for measuring the angle with the beam, θ, to determine P from the sagitta (which gives P_T) and for the determination of trigger roads. However, the most strict criterion on alignment of chambers within a module in the nonbending coordinate comes from the need for global alignment between modules. (*Note*: "Global" refers to the alignment of the modules externally with other parts of the detector and the beam. "Local" means the more stringent internal accuracies.) Measurements of a track in the nonbending direction must match the global alignment criteria, which require alignment of chambers to 300 μm. All modules must be aligned to the same spot within the SSC interaction region with a global accuracy determined by the following considerations:

1. To distinguish beam-beam events from cosmic rays and beam gas background.

2. For matching tracks with the central vertex detector.

3. To aid in distinguishing tracks from different beam crossings which originate from points with different z-coordinates.

4. To determine the opening angle of muons pairs.

The alignment tolerances are set by the multiple scattering. There are 12 to 14 interaction lengths in the hadron and electromagnetic calorimeters ($\sim 240\ X_0$), and their mean distance from the interaction point is 2 to 3 m. Hence it is sufficient that the "centerlines" of all modules pass within a common sphere of radius 0.7 mm located at the center of the beam interaction region.

C.3. L* Muon Chambers

Eighty large area precision muon chambers have been designed and constructed for the L3 Experiment. These are the most precise chambers of this size to have been built for any experiment to date. The L* chamber design is based on this design (Fig. IV.17) but will be finalized during the ongoing R&D programs.

The L* chambers fall naturally into three categories as functions of angular coverage and position in the detector: (1) Central, (2) Endcap, and (3) Forward.

1. Central. There are 160 chambers in the "Central" muon detector with 189k signal wires. These chambers are located inside the main solenoid and cover from 33.4° to 88.1° in polar angle. They are arranged in 32 modules with 16-fold symmetry in ϕ. Central chambers are conceptually the most similar to L3; however, on average they are larger and contain more wires. There are five different types of chambers. The outer chamber layer contains two chambers positioned along the beamline, and the inner layer is a single chamber.

The middle chamber layer contains two chambers along the beamline which are thicker than the others because they measure the track with 64 wires. These are divided into 2 layers of 32 wires each, constructed similar to the 32 wire layers in the other chambers. These layers are displaced by one-half cell to offer the following advantages:

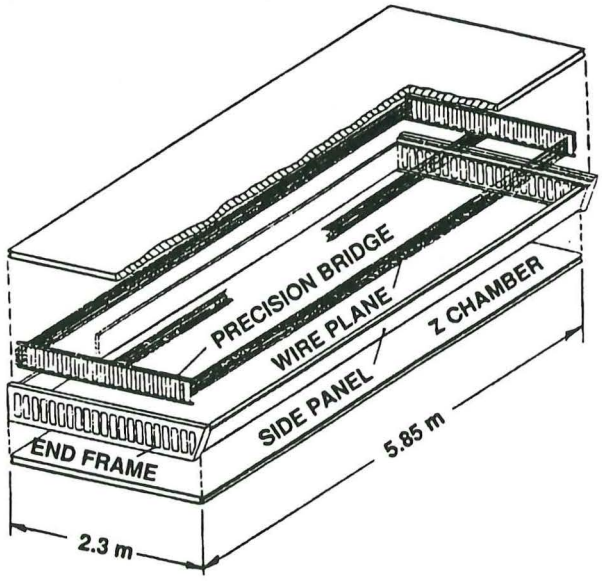

Fig. IV.17. Exploded view of an L3 multisampling outer chamber, showing precision bridges which position the wire planes, and endframes and side panels, carrying the wire tension load.

1. The left-right ambiguity of the chamber is clearly resolved (see the left track in Fig. IV.18).

2. For straight tracks, the sum of drift times, $T_1 + T_2$, must be a constant. This provides self-calibration for the drift velocity, event by event.

3. The relative alignment of the upper and lower layers can be checked by comparing the time sums of tracks that pass to the left of wires in the upper layer and to the right of wires in the lower layer ("left-right") tracks with the time sums for "right-left" tracks.

4. Tracks from previous (or later) beam crossings, $n \times 16$ ns earlier, show the pattern of the right track in Fig. IV.19. The segments are spaced apart by $2 \times v \times n \times 16\ \text{ns} = n \times 1.6$ mm. This allows association of each track with the correct beam crossing.

5. The same method permits rejection of cosmic rays, which pass through the intersection and simulate back-to-back muon pairs. Because the innermost middle chamber is 6.5 m from the interaction point, there is a time difference of 39 ns between ingoing and outgoing tracks at the middle chamber. This results in a 3.9-mm separation between track segments of incoming cosmic rays.

The central outer chambers are 20% longer and 30% wider than the largest L3 chambers. The track is sampled by 32 or 64 sense wires instead of the 16 or 24 used in the L3 design. The basic structural elements of L3 chambers were endframes, side panels, and z-chambers. The L* central chambers will have similar structural elements, but modifications and improvements will be made as a result of our experience with the L3 system. Endframes will be strengthened due to the increased size and wire tension load and will need greater structural stability due

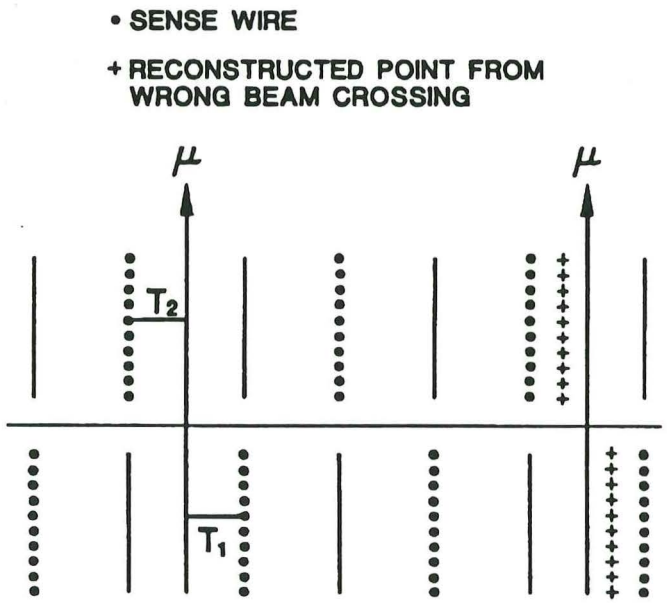

Fig. IV.18. A schematic end view of the central middle chamber which shows the offset cell structure for calibration and resolving left-right ambiguity. The sum of times $T_1 + T_2$ is a constant and is a self- calibration of the chamber. Track segments do not line up when assigned to the wrong beam crossing (right side).

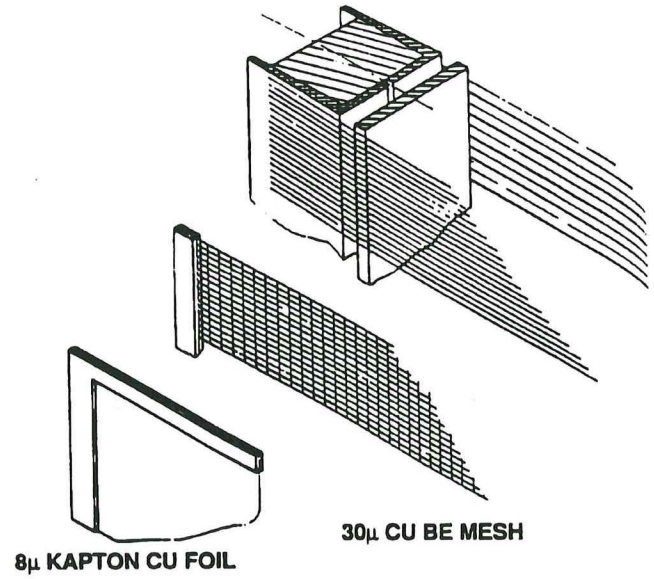

Fig. IV.19. Detail of wire attachment to the precision glass bridges showing a signal plane and a wire cathode plane. Replacement of the wire cathode plane by thin (8- to 30-μm) foil or mesh planes (R&D program) will increase chamber reliability.

to increased accuracy requirements. The L3 outer and middle chambers (Fig. IV.17) were constructed with one angled side panel and one straight side panel. This lack of symmetry has been avoided in L*. The chamber sides are both identical, resulting in improved mechanical stability and predictability. The inner and outer central chambers each have two double covers of z-coordinate measuring chambers installed as their top and bottom covers. These chambers, with a total of 25k wires, are similar to the z-chambers of L3. The middle chambers have no z-layers. They require low multiple scattering covers. Strong lightweight honeycomb panels have been already manufactured as gas covers for the L3 middle chambers. They contribute only 0.9% of a radiation length of material, and thus minimize multiple scattering.

2. Endcap. "Endcap" chambers are located inside the main magnet. They cover from 7.5° to 31.6° in polar angle in two different arrays of three layers each. Each layer measures the track with 32 or 64 sense wires. The innermost array covers from 7.5° to 17.6°, and the second array covers from 18.8° to 31.6°. The inner and outer chamber layers consist of one chamber which measures in the x-direction, and another which measures in the y-direction. The middle layer has a double thickness x-chamber and a double thickness y-chamber, each with two sets of 32-wire bridges. The chambers are all comparatively simple to construct because they are short and either square or rectangular. They will not need middle bridges to decrease wire sag since the chambers are less than 3 m long, and thus they will not require complex internal alignment systems. These chambers contain a total of 215k signal wires.

3. Forward. "Forward" chambers are located inside the external forward magnets and cover from 2° to 7.5° in polar angle. These chambers are also simple and rectangular in design. They have no middle bridges because the momentum measuring wires are vertical and do not sag. Horizontal wires, measuring the other coordinate, are short. There is a total of 55k wires in these chambers.

Due to the large number of chambers in the L* system, parts will be standardized, and produced by industry. Designs will be optimized for mass production. This is realistic and proven. Quality control documentation exists from L3.

Since chamber precision is determined in large part by the positioning accuracy and alignment of sense wires, the wire positioning, wire tensioning, and chamber internal wire alignment must be done with a higher degree of accuracy than was required in L3. The basic concepts will remain similar to those used in L3. The details and exact processes by which wire positioning accuracy is achieved will be determined during the R&D program.

The winding and tensioning systems used to make the L3 wire planes were adequate; however, L* will require more accurately made planes, and many more of them. Processes such as wire attachment and wire tension adjustment will be automated to increase production speed, uniformity, and wire plane quality.

The L3 chamber system contains 250 000 wires, and a direct extrapolation to L* would imply a system of 1.5 million wires in the central detector alone. Field shaping cathode planes account for 67% of the total number of wires. Access for repairs and broken wire removal will be difficult. The system must be designed to be reliable. Large areas of a chamber constructed of only wire planes can be completely disabled by a single broken wire. It is desirable to replace the cathode wire planes by foils or mesh planes (Fig. IV.19) to increase the chamber reliability. These studies are being carried out as part of the R&D program.

After the installation of L*, removal of a chamber for repair will be time consuming. Provisions will be made to give us reasonable access to all critical areas, such as bridges and circuit boards. In this way, most repairs can be made in place, without the need for major interventions. Access ports will be added to the chamber structure and will enable us to make chamber repairs without necessitating major dismantling of the detector. The access ports will be designed for gas safety .

C.4. Gas

The total L* muon detector gas volume of 2800 m^3 necessitates a nonflammable and nontoxic gas.

To achieve the required high accuracies the gas must have a low electron diffusion coefficient ("cool"), have a large electron drift velocity v ("fast"), have a high gain (large free electron yield), and be non-electron-attaching (attachment cross section small for electron energies less than ~5 eV).

We require operation at a safe value of the pressure-reduced electric field (E/P), insensitivity to variations in electric field E, small dependence of v on the magnetic field B (small Lorentz angle, θ). High corona inception voltage is needed to avoid harmful gas decomposition by discharges. In addition, the gas electron transport properties must be insensitive to small variations in temperature, density and composition.

No single gas has all of the above qualities. Therefore, an R&D program was started. The emphasis is on the development of multicomponent gas mixtures with optimal electron transport, gain, and electrical and chemical properties. The radiation and corona induced decomposition byproducts of the gas will be identified. Aging will be measured and considered in the choice of the gas.

Many studies have investigated the basic electron transport (Refs. IV.8–13), the electrical (Refs. IV.14 and IV.15) and other (Refs. IV.13 and IV.16) properties of gases. Good gas mixtures like Ar/CH_4, $Ar/i\text{-}C_4H_{10}$, Ar/CF_4, Ar/C_2H_6, Ar/CO_2, $Ar/CO_2/C_2H_6$ for advanced detectors were identified. But the nonflammable gas that is appropriate in all aspects for use in the L* muon detector must be determined.

To illustrate the information currently available on detector gases, we discuss an Ar/CO_2 mixture as an example. An Ar/CO_2 mixture with specific additives is nonflammable and expected to have low diffusion. However, the gas will need admixtures to improve reliability in a big system like L*.

Figure IV.20 shows the drift velocity (Ref. IV.13) as a function of electric field, E, for Ar/CO_2 mixture. Additives change the basic behavior very little. Working at ~1 atm and E ~1800 V/cm, the drift velocity is insensitive to field variations over a broad range. This is desirable because space charge at high rates can change E. Figure IV.21 gives the deflection angle (Ref. IV.13) due to the Lorentz force at the operational magnetic field of 7.5 kGauss. We note that the angle of 18.7° and the voltage values are similar to L3; therefore, we expect accurate operation.

In Fig. IV.22 the dependence of drift velocity on CO_2 concentration is given. For CO_2 concentrations higher than 16%, the drift velocity is insensitive to small mixture variations. Operational parameters would be

E = 1800 V/cm
v = 5.7 cm/μs
θ = 18.7°
$Ar:CO_2$ = 82:18, 1 bar

However, this gas cannot be used as is. It lacks reliability for a big system due to its tendency to discharge. To keep the good overall features, additives X of a few percent will be examined in a thorough R&D program to provide good gain, suppress corona discharge, and to ensure long lifetime of the chambers. For example, in L3 we observed (Ref. IV.17) that 0.5% water can extend the chamber lifetime up to a factor of 10.

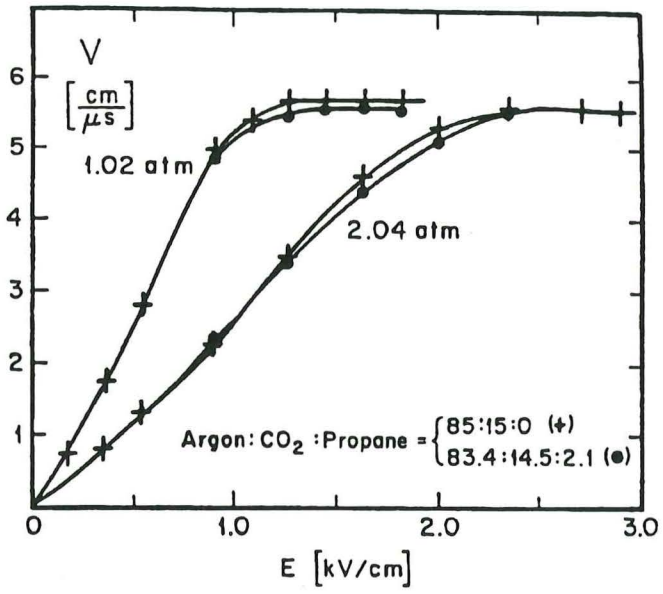

Fig. IV.20. Drift velocity (v) vs electric field (E) for Ar/CO_2, and Ar/CO_2/propane.

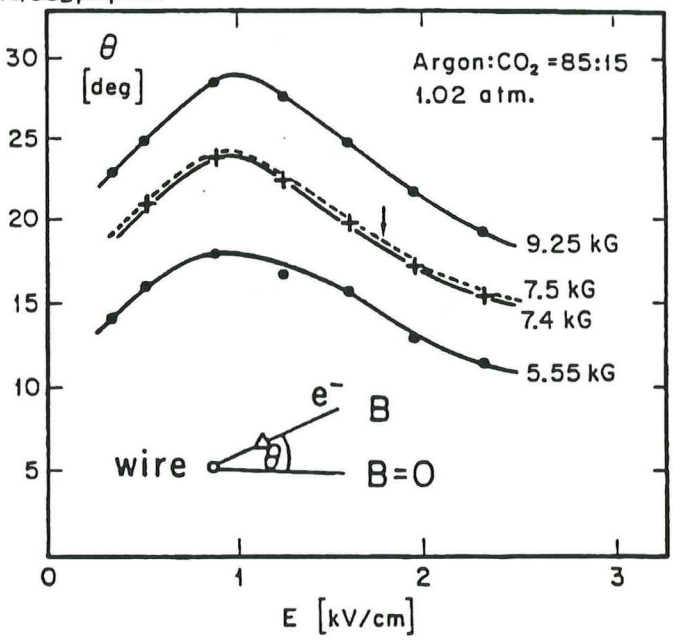

Fig. IV.21. Lorentz angle θ vs electric field E at verious values of magnetic field B. In the main solenoid at L* (B = 7.5 kGauss).

For economical gas consumption, the L* gas system will recycle 95% of the gas, as in L3. The 5% addition of new gas, with the use of purifiers, will maintain the gas quality.

C.5. Electronics

The L* central detector has 127k channels, after linking the wires of two outer and two middle chambers (0.6 reduction). For the endcaps 70k channels are required, after more extensive linking. The forward-backward regions together have a total of 26k channels.

The individual channels consist of amplifier, discriminator, cables, and time digitizing units. The 1-ns recording accuracy of the L3 solution is adequate for L*

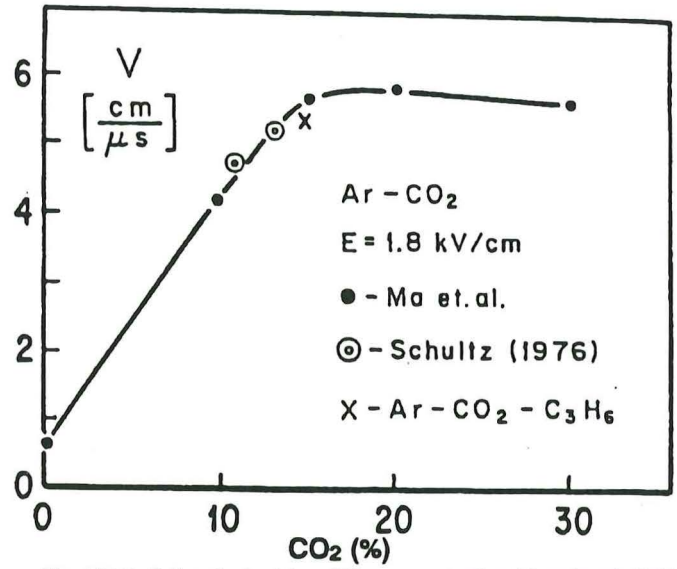

Fig. IV.22. Drift velocity (v) vs CO_2 concentration. The electric field E is 1.8 kV/cm.

resolution requirements and could be used in the central detector. This already operational system of 25k channels cost 190$ per channel, including all cabling, interfacing, readout, and monitors. However, the increase in channel number from L3 to L* is of an order of magnitude. This creates a need for R&D to achieve high component density, cabling reduction, reliability, easy diagnostics and repair, and low cost.

In addition, the complexity of the L* muon spectrometer requires the development of a large number of electronics systems monitoring all the relevant parameters. In particular, the high-voltage system has to be distributed and controlled to react to background conditions in order to avoid wire damage and aging.

C.6. Muon Trigger Generation

The fast level 1 muon trigger will be derived from three coincident layers of Resistive Plate Counters (RPCs) (Ref. IV.18). These devices produce a very fast (10 ns) discharge in a gaseous gap of 2 mm after passage of an ionizing particle. Induced signals are received on external strips and yield a precise timing resolution of 2–3 ns. RPCs and their associated electronics provide a low cost method of instrumenting the very large area required (i.e., 4000 m^2). Three RPC layers will be attached to the muon chambers in the central region. They will be read out by 3-cm strips oriented parallel to the magnetic field. RPC layers with 3-cm radial pick-up strips are also connected to the muon chambers in the endcap regions, and RPCs with 2-cm strips running vertically (parallel to the magnetic field) are placed at three positions in the forward detectors. Fast (i.e., 100 ns) logic searches for tracks pointing to the interaction region along fiducial "roads" in the r-ϕ plane, which specify a particular momentum cut. The precise time resolution of RPCs also enables cosmic ray triggering and flagging.

After the 1-μs maximum drift time has elapsed (i.e., during the level 2 trigger), candidate tracks are also formed using muon chamber hits. A track finder will identify muons within roads that span both bending and nonbending coordinates. These roads point back at the interaction region and are determined by coincident hits (mutually arriving within 1 μs) on selected wires in the outer and inner layers of drift chambers. Roads are assembled for each module in the central region by demanding hits in z-layer wires within narrow (2°) intervals in θ, as implemented at L3. Roads are defined in a similar fashion to detect tracks in the endcap regions, where limits in θ and ϕ will be imposed by requiring hits in orthogonal chamber wires lying within the solid angle defined by each road. In the forward detectors, roads are again subdivided in θ and ϕ by requiring hits in orthogonal chamber wires. Road boundaries will be set more narrow in this region, in order to clearly separate individual tracks and avoid accepting lower momentum particles.

Muon chamber data can be assigned to particular events by linking candidate tracks found in the muon chambers within the 1-μs drift interval to those found in the RPC array and/or hadron calorimeter. In addition, matching of candidate tracks with particular events can be rapidly accomplished by performing time sum calculations for hits in adjacent chamber layers that are offset by half of a cell width (Fig. IV.18). The sum of drift times resulting from the offset chamber layers, plus a correction term proportional to the tangent of the angle between the track and chamber plane (known from the road definition), should always be equal to the maximum drift time, that is, 1 μs. Rapid computation of a time sum for each candidate track will enable every track to be correlated with a particular event, or a range of events in the cases where uncertainties (i.e., in the incident angles) are large.

C.7. Alignment Systems

Throughout the evolution of L3, numerous techniques, instrumentation and test fixtures were employed or developed to obtain the required alignment accuracies. The L3 experience provides a significant knowledge base by which to judge the strengths and drawbacks of proposed alignment techniques or systems and to make specific recommendations of R&D efforts needed for improvements which might otherwise be overlooked or discovered late in the detector's development.

Local Alignment System

The function of the local system is to align chambers within a module. In each of the three muon detector regions (central, endcap, and forward), chambers are grouped into sets of three equidistant layers for the purpose of muon sagitta measurement. The middle layer actually consists of two chambers that are joined one on top of the other and referenced during fabrication such that they may be considered as one chamber for alignment purposes. Each of the three chamber layers measures the particle track precisely in the bending direc-

tion, and from the three combined measurements the sagitta is calculated. The alignment of the wire planes with respect to one another in the three layers in a straight line is the function of the local alignment system. This alignment is termed local because it aligns the three chamber layers to make independent sagitta measurements without concern for the global location of the system with respect to the interaction region or any other local system.

The local alignments are maintained by straightness monitors similar to those in L3 that are described in Sect. B. They are not positioned at the chamber centerlines as in L3 but at each end of the precision bridges that position the wires within each chamber. In this way the local alignment is simplified and made intrinsically more precise.

To reduce the number of straightness monitors, multipoint alignment systems are under study. Under the R&D effort the multipoint alignment system will be researched by a number of institutions such as Draper, MIT, ETH, University of Geneva, and Los Alamos. The Draper approach is shown in Fig. IV.23. The multipoint straightness monitor depicted in this figure is a variant of the three point devices used in L3. The points to be aligned are represented by light sources P_1 through P_6. These light sources are modulated so that they can be individually identified. They are viewed by a quad cell and lens which are held in a rigid tube. The information from the quad cell provides the deviations (in two directions) of light sources P_2 through P_5 from a line connecting P_1 to P_6.

The accuracy demands on the wire plane alignment including straightness monitors are 8 μm vs 15 μm for L3. In addition, path lengths are up to three times longer. The L3 straightness monitors are sensitive enough to recognize 0.1 μm changes and can be adapted to the demands of L*.

It should be noted that in L3 there were two additional systems to accomplish the local alignment, which were required as a function of the chamber geometry. It was necessary to measure and adjust the angle between the centerlines at each end of the detector module and the radial spacing between the chambers. Both of these contributed to the accuracy of the sagitta measurement. The design of the L* muon detector, based on our experience with L3, eliminates the need for these two systems and increases chamber alignment accuracy.

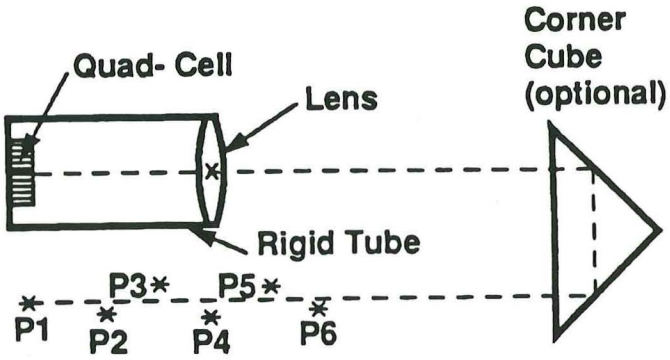

Fig. IV.23. Multipoint (P_1...P_6) alignment system, schematic.

Global Alignment System

To match tracks to one another and to the interaction point, as well as to resolve the momentum of the particle from the sagitta measurement, it is necessary to know the global location of the three chamber layers that have locally determined the sagitta. All muon detector elements must be aligned to a common reference point, close to the intersection point, which must be derived from reference features on the nearest focusing quadrupoles to the interaction region. This global alignment is done with a combination of measurements, which are taken with interferometers, with bubble levels, by survey, and mechanically.

The first step in the global alignment process, referencing between the local and global systems, starts when the chambers are attached to the support structure. The locations of the wire planes within the chambers, as defined by the local alignment systems, are at this point precisely referenced to measurable, global features in the system. Measurements are taken and the consequential shimming and adjustments are made at the support structure attachment points to bring the positions of the chambers into tolerance. All of this is done with the completed detector element at its design orientation. As a result of this referencing, bubble levels and survey targets fixed to the detector elements will permit global alignment of the detector elements in the experimental area.

Since the supports for the muon detectors in all regions are provided by the magnets—which are subject to motion caused by thermal effects, creep, etc.—the global alignment must be continuously monitored. A global alignment system reference structure supports reference elements that operate with the straightness monitors and with survey to the hall benchmarks. This reference structure, supported by isolation mounts, is constructed of lightweight, stable, nonmagnetic composite material and is designed to have very low stresses. It provides a precise common point to link the locations of the muon detector elements with the machine quadrupoles at all times.

Structural Alignment System

The structural alignment process starts when the chambers are attached to the support structure. Precision measurements are taken and compared with the structural analysis computations. Adjustments are made to the support structure attachment points to bring the relative position of the chambers into tolerance. The completed structure will be rotated in its test fixture (Fig. IV.26) to the orientation it will have when installed in the detector. Levels (both single and dual axis), laser interferometers, and precision transfer standards are employed to align the structures and chambers. These

instruments will be constructed according to the same principles as those for L3.

D. CENTRAL REGION MUON DETECTOR

The central region muon detector provides acceptance in each hemisphere over the region of 33.4° to 88.1° from the beam axis. Measurement resolution in this region is equal to or better than $\Delta P/P = 2.4\%$.

D.1. Central Region Arrangement

The central region muon detector is arranged in two basic parts and located in the region between the magnet wall and the calorimeter support tube (Fig. IV.24). Each part extends from the central membrane to 33.4° from the beam axis and is divided into 16 modules that are each supported from the magnet independently of each other.

Each independent module contains five rectangular muon chambers of trapezoidal section. These chambers are arranged into three layers with the wire axis along the z-axis (and parallel to the B field) and wire planes nominally radial. The outer layer contains two chambers each 6.7 m long and 3.3 m wide. The middle layer contains two double-thickness chambers shaped to maximize the acceptance. Chamber lengths for this layer are 5.3 and 5.0 m, and the chamber widths are 2.5 and 2.3 m, respectively. Finally, the inner layer contains one chamber which is 6.4 m long and 1.5 m wide. In addition, both the inner and outer layers will have a less precise chamber layer to determine the z-coordinate of an individual track entering and leaving the measuring module.

D.2. Central Region Structure and Support

The support structure is an aluminum full truss on the sides and both ends of the module. Figure IV.25 illustrates this structure in conjunction with the installed chambers and the magnet support elements. All material is excluded from the active measuring volume and is placed in the regions necessarily obstructed by the mechanics of the muon chamber enclosures. The chambers were arranged to maximize the acceptance, as shown in Fig. IV.24.

This sector support structure is attached to the magnet at three pairs of attachment points distributed along the axis of the magnet. Two pairs of attachment points are near the ends of the truss, and the third pair is near the center of the truss. In order to eliminate support redundancies, the middle two points position the module along the z-axis while the end support points allows motion along this axis. Similarly, all of the points along one side of the module have a tangential degree of freedom. This avoids internal stresses caused by, for example, temperature changes.

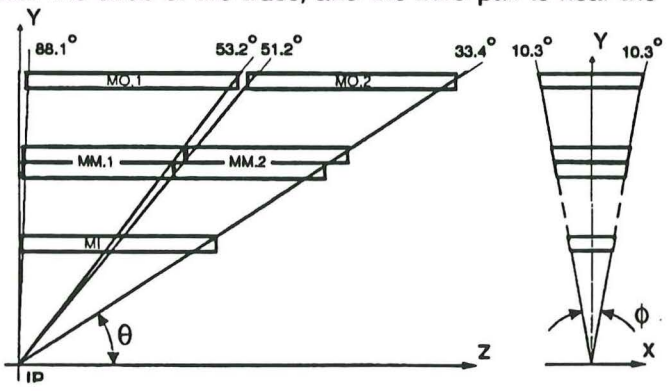

Fig. IV. 24. Central detector, side and end views of 1 of 32 modules. Beam line is along the z-axis (IP = interaction point).

Attachment of the chambers to this support truss is accomplished in a manner proven successful in L3. The chambers are attached to the structure using flexural feet to permit actuated motion for alignment purposes. In order to minimize the forces associated with aligning the chambers, preloaded springs or a constant force device are added to balance the chamber weight at the intended final orientation. Finally, in order to prevent damage to the chambers or the flexure feet while transporting modules between the assembly area and the magnet, elastic stops are used to limit individual chamber motions.

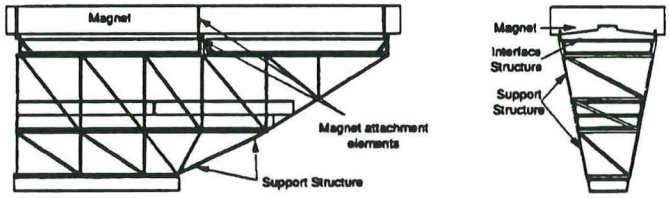

Fig. IV.25. Central region structure and support.

D.3. Central Region Alignment

Alignment of the modules with respect to the beam is achieved with a combination of level monitors and theodolite measurements. The level monitors and survey references are added to the module and calibrated at the design orientation during assembly. Level measurement to 20 microradians and survey to 0.1 mm are sufficient to satisfy the global alignment requirements outlined in Sect. C.2 of this chapter.

The critical alignment of the three chamber layers within a module in the bending plane is done as in L3 with straightness monitors. Each module has eight monitors to perform the alignment. Their locations follow roughly the radial lines indicated Fig. IV.24. These monitors are two-dimensional and are also used to verify z-axis alignment.

The alignment of the chambers within each module is verified with a UV laser system. The lasers, one per module, are mounted on the exterior of the central magnet end plugs for ease of maintenance and repair. The beam is directed by mirrors through the chambers to simulate an infinite momentum particle. Verification is also accomplished with cosmic ray muons.

D.4. Central Region Assembly and Installation

Each central region module is assembled, aligned, and tested in a surface hall. With the support structure

"parked" in a prealigned, stable fixture the muon chambers are installed. The middle layer of chambers must be loaded in through the opening in the top of the frame and the inner and outer layers are fixed to the bottom and top respectively. Test and alignment of each module is accomplished with the aid of a cylindrical cage (Fig. IV.26) which supports the truss structure and permits rotation of the entire module about its longitudinal axis to its design orientation. The modules are also transported in this assembly cage, which has rails inside, similar to those that support the modules during insertion into the magnet. After transport from the assembly to surface areas, each unit is lowered through an access hole to the experimental hall. The entire assembly is then placed on a support structure and elevated to the correct height for insertion into the magnet. After rotation to the correct orientation, the module is rolled off the rails in the cage and onto the permanent nonmagnetic rails in the detector. These permanent rails are attached along their length with insulated mounts to the inside of the coil, and to the magnet near the central membrane and the pole crown. Once inside the magnet, the module is secured at six attachment points to the magnet structure with no contact to the rail system. This arrangement provides isolation of the precision module from the magnet mechanical perturbations as previously described.

E. ENDCAP REGION MUON DETECTOR

The endcap region muon detector provides acceptance over the range of 7.5° to 31.6° and 148.4° to 172.5° from the beam axis.

E.1. Endcap Region Arrangement

The endcap region muon detector is arranged in two basic parts supported by the movable magnet end plugs (pole pieces) at either end of the main solenoid.

Two geometries are under study for the endcap region. One arrangement measures two orthogonal components (x and y) of the track with comparable accuracy (i.e., x and y chambers). Figure IV.27(a) shows an end view of the outermost layer of chambers. This version is described in detail below. The other arrangement measures one track component in the tangential (ϕ) direction (radial chambers) and, with less accuracy, the component in the radial (θ) direction. Figure IV.27(b) shows an end view of the outermost layer of this second arrangement. While it is less conventional, this alternate version is attractive because of potential savings in electronics, the number of chambers, and the ease of support.

In the arrangement described in Fig. IV.27(a), each side of the endcap region consists of 12 layers of square and rectangular chambers arranged in a planar square array. This region provides measurement from 7.5° to 31.6° from the beam axis (Fig. IV.28). Figure IV.27(a) is a view of the outermost layer viewed looking outward from the interaction point. The chambers form a projective geometry providing clear passage through the three layers, maximizing the acceptance. Successive layers alternate from x- to y-chambers, the chamber type designation referring to the orientation of the precise measuring direction of the chamber. No additional cross-axis measuring layers are needed in this array since both x- and y-coordinates of the particle tracks are measured in successive layers.

E.2. Endcap Region Structure and Support

The dominant structural feature of the endcap support is a conical truss that houses the 12 assemblies of cham-

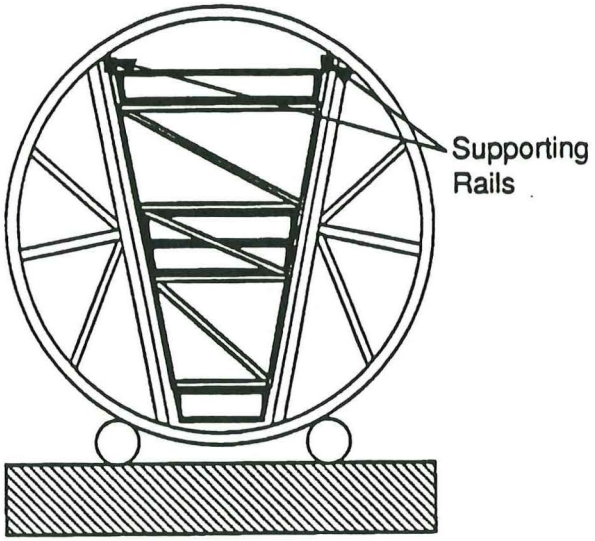

Fig. IV.26. Central region rotation and transport fixture.

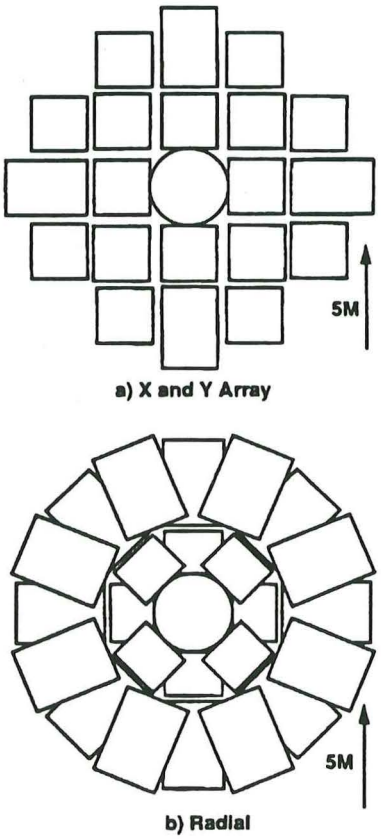

Fig. IV.27. Endcap region layout options.

ber layers. It is composed of 16 tubular elements, which nominally point toward the interaction point. Four of these can be seen in Fig. IV.29, which shows one-quarter of the endcap assembly viewed from outside of the conical structure. In addition, there are numerous diagonal truss elements, which brace the tubular elements to stiffen them. The conical truss is fixed to the magnet end plugs (pole pieces) near their outer edge, where deformations are minimal. This provides a stable mounting for the endcap muon detector array.

Each of the 12 layers of chambers is mounted in a rectilinear grid [as seen in Fig. IV.27(a)]. The structural elements of this grid are placed in the space between the rows of muon chambers and in the shadows of the chamber frame structure. Each layer is assembled in a horizontal position. Truss elements in the spaces between the chambers provide stiffness needed during the assembly process and allow the layers to be mounted inside the conical truss in a manner that isolates them from its mechanical deformations.

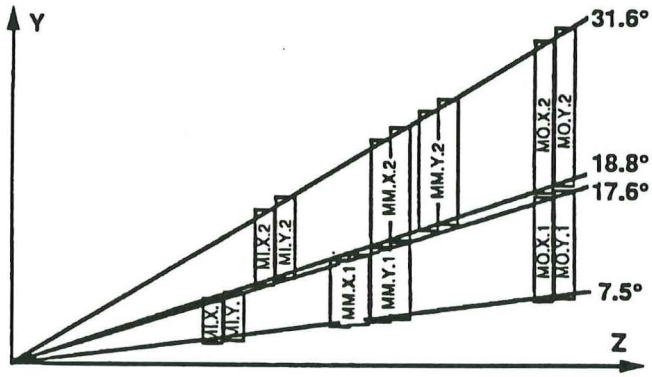

Fig. IV.28. Endcap region layout and acceptances.

E.3. Endcap Region Alignment

Alignment principles, procedures, and verification in the endcap region are similar to those in the central region.

E.4. Endcap Region Assembly and Installation

In the surface hall, a structural cone is built with its large diameter end open on top. The individual chamber layers are assembled in a horizontal plane, lowered into the layer truss structure, and attached in place in the cone. Following assembly of all of the layers into the conical truss, the assembly is moved to a high bay area to permit rotation of the assembly to its final orientation (vertical), followed by final alignments and evaluation of the entire assembly. This assembly, which weighs approximately 125 tons, is then lowered through the access hole to the experimental area, where it is attached to the magnet plug. Finally, the forward region muon detector, magnet plug, and the attached endcap region is slid into its final position in the magnet.

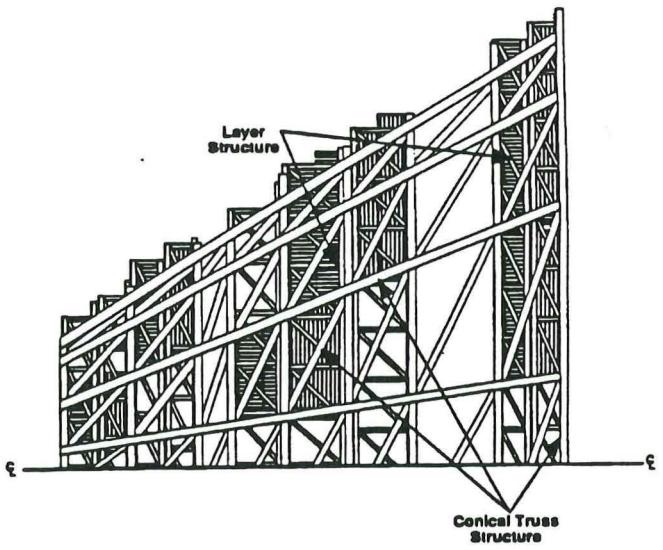

Fig. IV.29. Endcap region support structure.

F. FORWARD REGION MUON DETECTOR

The forward region muon detector provides acceptance over the range of 2° to 7.5° and 172.5° to 178° from the beam axis. Measurement resolution ($\Delta P/P$) in this region is equal to the nominal value of the central region: $\Delta P/P = 2.4\%$.

F.1. Forward Region Arrangement

The forward muon detector measures momenta by three chamber layers—a, b, and c—in a vertical 0.3-T field. The precision measurement of deflection is carried out by 32-64-32 wires, which are vertical and therefore have no sag correction. It is located along the beamline, outside of the main magnet as shown in Fig. II.1. The separate solenoidal magnets contain a vertical field and have an internal clearance of 9.2 × 8.2 × 8.2 m. They also contain a tube of 1 m O.D. to support the machine beamline and quadrupole magnets. The chamber arrangement is shown in Fig. IV.30.

The chambers are assembled into modules for support and alignment. Each forward region contains two side modules and a top and bottom module. The a- and c-layers of the modules each contain two xy-chambers of 3.1 × 4.0 m, mounted one above the other. There are two double-thickness x-chambers in the b-layer with 64 wires mounted in two staggered sets of 32 wire bridges. The a- and b-layers of the top and bottom modules contain an xy-chamber of 2.0 × 3.2 m, and there are two 2.0- × 3.2-m chambers in the b-layer.

The y-coordinate is measured by cells of 16 horizontal wires in the a- and c-layers only. This determines the trajectory angle and allows the formation of trigger roads.

F.2. Forward Region Structure and Support

The structure to support and maintain alignment of these chambers is similar to but less demanding than in the other detector regions since the precision chambers

have only one orientation relative to gravity. The muon chamber support frames and the stabilizing truss structure are fabricated of square aluminum tubing joined into the necessary module support structures. The support

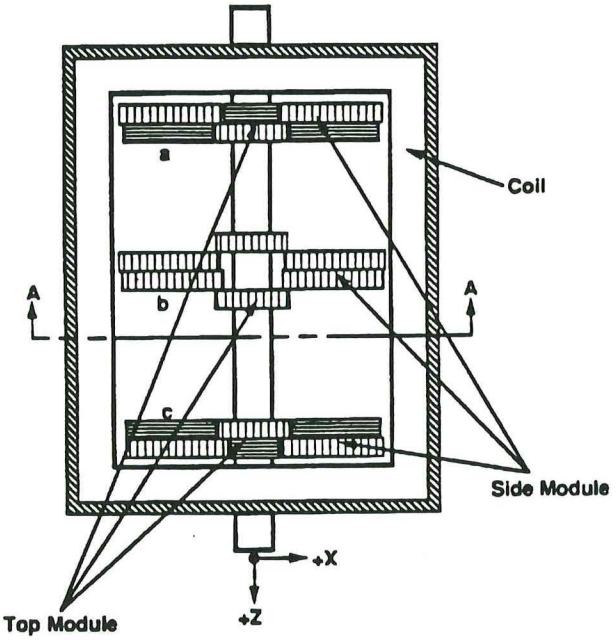

(a) Top view

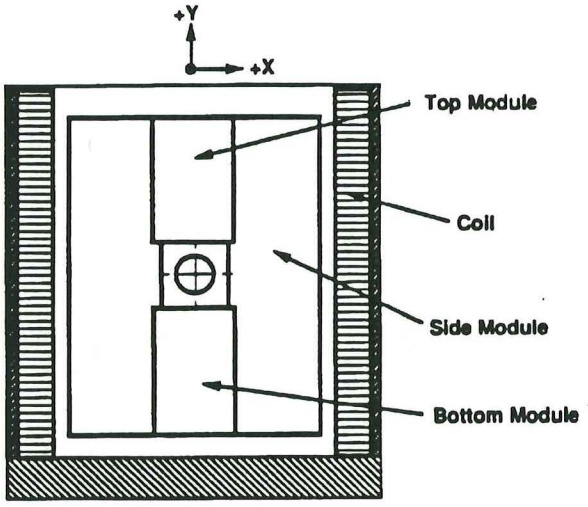

(b) End view (cross section at A-A)

Fig. IV.30. Forward muon detector.

structure for the chambers within a module is designed to allow access during assembly and for subsequent repair and maintenance.

Attachments to the magnet minimize mechanical coupling of the magnet structure with the muon chamber modules. The major rigid attachments are at the bottom magnet plug with additional floating attachments made near the top magnet plug to provide stability to the vertical structure.

F.3. Forward Region Alignment

Alignment principles, procedures, and verification in the forward region are similar to those in the central region.

F.4. Forward Region Assembly and Installation

Assembly of the muon chambers into the support structure is done with the chamber axes vertical so as not to improperly stress the structure, which is designed for vertical mounting. Other aspects of assembly are similar to all of the other muon detector regions.

For assembly in the experimental hall, the bottom module is first lowered into the magnet, translated under the beam, locally aligned to the magnet structure, and secured. The two side modules are similarly installed. Finally, the top module is fitted. This assembly process is straightforward because of easy access.

G. THE L* MUON DETECTOR RESEARCH AND DEVELOPMENT PROGRAM

The physics goals for the L* detector lead to demands on the precision muon system in terms of chamber resolution, alignment, choice of gas, chamber support, and electronics. These can be met after careful studies, plus systematic tests and measurements of full-scale prototypes. In order to ensure the timely completion of the L* precision muon detector, R&D programs are needed and cover the following topics:

1. Chamber design and construction
2. Gas
3. Support structure design
4. Coordination
5. Alignment systems
6. Electronics
7. Data transfer

Programs have been started with detector subsystem R&D funds from the SSC (Refs. IV.19 and IV.20) for (1) chamber design and construction, (2) gas, (3) support structure design, and (4) coordination. Switzerland will undertake R&D on (5) alignment systems, (6) electronics, and (7) data transfer (Refs. IV.21 and IV.22).

G.1. Chamber Design Research and Development

The main goal of the chamber construction R&D project is to design large area drift chambers with good single wire resolution (between 150 and 200 μm). The large number of chambers demands R&D on reliability and design for mass production.

L* chambers will be based on the L3 chamber designs as described in Sect. B. However, the substantial increase in the number of wires means that the chamber structural elements will have to be strengthened. Materials selection is very important. The need for accuracy also leads to greater structural stability requirements.

The chamber precision is determined in large part by the positioning accuracy and alignment of its sense wires. Wire positioning, wire tensioning, and chamber internal wire alignment must now be done with a higher degree of accuracy because of increased chamber lengths.

We are investigating more accurate and more reliable methods of manufacturing the signal wire planes. Part of the program is the development of fully automated production of wire planes with quality control for reliability and uniformity. These portions of the R&D project are important in determining the final chamber precision, and also in increasing chamber reliability.

The L* muon chamber R&D program extends over a 3-year period, after which the full-scale prototypes will be built. Critical design features are tested with smaller prototypes during this program.

Design, alignment, reliability, and manufacturing studies for these large, high-precision chambers will lead to basic structural design concepts during the first year. Feasibility of cathode wire plane replacement by foil or mesh planes to increase chamber reliability will also be determined in the first year.

The foil and mesh studies are in progress at this time. Discussions with industry are under way, informing them of our probable requirements (wire size, spacing, thickness, flatness, material, and precision) and informing us of limitations in standard fabrication techniques. Foils and meshes must be stretched flat and positioned accurately inside the chamber, which is a difficult problem because it must be accomplished without huge support structures and with a minimum of labor-intensive fabrication steps.

We are making trials to improve methods for gluing, supporting, and tensioning foil planes. A foil-tensioning fixture has now been fabricated, and methods to measure tension uniformity across the foil are under investigation for our situation. Several foil plane models have already been constructed and are being tested in this fixture. Material for mesh plane manufacture is on order and will allow us to conduct similar tests with wire meshes.

Conceptual studies of endframe design are proceeding in parallel with foil support mechanisms.

Two chamber simulation programs are now running. They are being compared with each other using known L3 parameters and conditions. Both are being adapted to use available computer graphics and will be used for our drift cell optimization studies.

Chamber structure details will be finalized in the second year. An endframe model will be produced and evaluated, and its stability will be tested. Optimization of wire attachment, wire alignment, and cell design will continue. A model will be constructed to enable verification of the cell structure. Automation of tensioning and alignment techniques will begin, and prototype wire-tensioning and wire-alignment devices will be produced and tested.

The chamber structure design and the production method will be finalized in the third year. Materials and method productions for wire and foil or mesh planes will be determined. A full-length model will be produced and evaluated to test alignment and signal calibration systems.

At the end of this 3-year program, all designs and methods should be finalized, and production of full-scale chambers can start.

G.2. Gas Research and Development

The main goal of the this program is to identify and characterize a suitable gas for the L* muon detector.

Measurement of drift velocity, diffusion coefficient, gain and deflection angle in a 7.5-kGauss field will be conducted. Computation of these parameters will proceed in parallel, however, only as a verification (Refs. IV.13 and IV.14).

Experiments at ORNL and MIT indicate that appropriate binary and ternary gas mixtures of Ar, N_2, CO_2, CH_4, CF_4, and NH_3 have excellent overall characteristics. For these gases reasonably accurate electron-scattering cross sections exist, allowing detailed understanding.

In the first year of R&D the experimental setup to measure drift velocities, diffusion, aging, and gain in magnetic fields up to 7.5 kGauss will be completed. The MIT cyclotron was refurbished to provide the magnetic field. Measurements with UV lasers and X rays have started (Ref. IV.13). In the second year the following specific gas mixtures will be investigated both with and without NH_3 or H_2O admixtures:

Ar/CO_2 CH_4/N_2 CO_2/CH_4 CO_2/CF_4 Ar/TMS

The experimental measurements backed by computations on the mixtures will identify the best candidate gas for the muon chambers. This gas will then undergo additional tests with regard to its overall properties and corona/breakdown decomposition characteristics.

G.3. Structural Support R&D

The R&D program for structural support of the muon chambers is divided into two parts: structural designs and structural analysis.

Part 1. Structural Designs

The structural design of the L* muon detector lends itself easily to a division into three basic areas of emphasis: the central, endcap, and forward regions. Each region is a distinctly different structural design problem, requiring closely coordinated parallel efforts for efficient communication and application of ideas and developed technologies.

The structural design R&D program has as its goal the comprehensive analysis and design of the muon chamber support structure in the three detector regions. In addition, support for the analysis and design of the muon

chambers themselves is foreseen. The development of the structural designs involves three sections which are advancing in parallel.

Section 1: Module Definition. The first task in each region is to define the module boundaries based on stability, assembly, alignment, and maintenance/repair considerations. At this point the basic structural form of the muon chambers, the chamber support structures, the chamber to structure interface, and the alignment schemes are being formulated.

Section 2: Muon Chambers. The development of the muon chamber structural design concentrates on the materials selection, enclosure geometry, and wire supporting and adjusting systems. The development of the chamber structural design is in support of the general muon chamber R&D program.

Section 3: Support Structures. The development of the muon chamber support structures concentrates on the materials selection, main structural element specification, and the designs of the interface between the muon chambers and the support structure, and the support structure to the global supporting elements. Special attention must be given to the installation and maintenance/repair requirements of the muon chambers, as well as to the careful incorporation of alignment systems into the structure.

The R&D on the structural design for the L* muon detector is a 3-year program. The final product of this program will be full-scale, working prototypes which will verify the structural design in every detail before production. We are now concentrating on feasibility studies of different structural design concepts. The results of the current efforts can be seen in Sects. IV.C, IV.D, IV.E, and IV.F of this document. By the end of the first year the designs will be frozen with regard to major conceptual changes such that the detailed designs can be completed in the first half of the second year. At the end of the second year, fabrication of the hardware for prototypes will be complete. The third year will be reserved for the assembly and rigorous assessment of the prototypes.

Part 2. Structural Analysis R&D

Any structural design of the scale and precision proposed necessitates the careful analysis of each mechanical element incorporated into the structure. A detailed finite element analysis of the supporting structures, as well as the drift chambers themselves, is a necessary tool in prototype design and assessment. The models which are currently under development use NASTRAN (NAsa STRuctural ANalysis), which yields critical information on mechanical performance, stress levels, deflection characteristics, temperature effects, and dynamic responses to transient loads. After a final design has been fixed, additional detail can be added to the model in areas of particular structural interest. This makes the finite element model a very useful tool in the alignment of the modules saving time and manpower in the process of aligning the drift chambers.

The proposed scale and nature of the L* muon detector volume makes the application of a detailed structural analysis a necessity in the three basic regions: the central, the endcap, and the forward/backward. The finite element analyses of the structures are needed in three phases of the development of the muon detector.

Phase 1: Initial development of relatively simple models which concentrate on feasibility of different configurations to arrive at a proposed prototype module in each region. This work is in progress.

Phase 2: The second phase will develop one detailed model, integrating chambers and support structures, for each region to be used in the design detailing stage.

Phase 3: In the third phase the refinement of the models will be made to include details necessary for application as an alignment tool and the generation of necessary alignment information.

The structural analysis R&D program is planned to run in parallel with the structural design R&D program, spanning the same time periods. It is foreseen that the 3-year structural analysis effort will evolve from Phase 1 to 3 following the progress of the structural designs. The results of the current efforts can be seen in Sects. IV.D, IV.E, and IV.F of this document. The second year of the structural analysis R&D program will address the work outlined in Phase 2 above.

G.4. Coordination of Engineering

The vast amount of engineering work necessary to support the R&D of a muon detector for the SSC requires a coordinating body to facilitate the effort. The size of the muon detector development program makes division of the work into many subsections unavoidable, and even desirable. Additional groups, which are not specifically muon detector focused, must be simultaneously developing other aspects of the detector. A list of only the major contributors would include:

- Central Tracking
- Calorimeters
- Magnet

As well, there will be other areas of effort in support of the experiment, under direction of the SSC Laboratory, which would include:

- Services
- Experimental Area
- Surface Facilities

These many groups necessary to support the large number of engineering tasks will span at least two continents and most likely involve many different languages. This kind of a multinational collaboration in engineering support makes efficient coordination and communication invaluable.

Generally stated, the main function of this group is to ensure the consistency and quality of all engineering work and promote the flow of information and ideas among the various groups in the muon detector R&D program. In this capacity, this group acts as a communication interface, concerning engineering needs. This includes communication among all groups within the L* muon detector R&D program, and communications from inside the program to all outside groups.

Some specific areas of effort of this group are to assist all L* muon detector R&D programs in the definition of consistent drawing standards, quality control programs, and standards of safety. The emphasis is on the development of consistent engineering practices to promote the efficient development and integration of the various detector elements. The engineering coordination group also assists all R&D programs in the definition of specific test and prototype assessment programs to ensure the engineering integrity of all elements of the detector.

Detailed assembly drawings incorporating all system components and defining the mechanical interfaces will be made at the appropriate time. In addition, a continuous review of all designs for consistency with global objectives is an important, ongoing task.

Coordination of the final, integrated, prototype module assessment program will be handled by this group. The group will compile and control all critical data from the various development groups for prototype assessment.

The engineering coordination group is responsible for generating a global planning for all engineering tasks within the R&D programs. By reviewing the progress of the various programs and identifying problem areas, the coordinator can ensure the compliance of all groups with the global planning.

G.5. Summary of the Muon Detector R&D Program

Table IV.3 summarizes the milestones in the L* muon detector R&D program.

G.6. Request for Support of the Muon Detector R&D

The financial request for R&D funds from the SSC for the FY 1991, the second year of the SSC Muon Detector R&D Program is shown below in Table IV.4. The difference between the requested funding for FY 1990 and what was received is added to the original projected request for FY 1991 to arrive at a revised total of 4645K$ [Refs. IV.19 (page 75) and IV.20]. The request for FY 1992 is 2797K$.

Table IV.4. Financial Request for 1991 R&D (K$)

	Chambers	Gas	Structures	Coordination
Orig. FY 91	410	363	2550	230
ΔFY 90	79	340	550	123
Total FY 91	489	703	3100	353

Table. IV.3. Summary of Milestones for the L* Muon Detector R&D Program

	FY 1990	FY 1991	FY 1992
Muon Chambers	• Determine foil and mesh plane feasibility for manufacture and alignment • Freeze chamber structural designs with regard to conceptual changes	• Evaluate a model of an endframe • Evaluate a model for cell verification • Produce prototype wire alignment device • Produce prototype tension device	• Finalize chamber design and production methods • Choose wire, foil, or mesh plane material and attachment, production, and alignment methods • Construct and evaluate full-length chamber model
Gas	• Complete setup for measurements	• Take measurements of diffusion and establish reliability for 10 gas mixtures	• Construct chamber prototype with accurate cell structure • Test beam measurements
Structural Design and Analysis	• Complete basic structural designs • Freeze drawings with respect to conceptual changes • Complete models (4) of structures and chambers	• Complete detailed designs of structures • Fabricate all prototype parts • Complete finite element models (2) for design details	• Complete assembly and assessment of all prototypes • Complete finite element models for alignment process use
Alignment Systems	• Design system • Construct test stand	• Evaluate prototypes • Integrate global system	• Test and evaluate global system
Electronics and Data Transfer	• Define architecture and system	• Develop chips • Construct prototypes	• Verify performance • Evaluate system

References

IV.1. V. Innocente, SSC Workshop, Berkeley (1987), p. 554.

IV.2. F. Paige and S. Protopopescu in Proceedings of the 1986 Snowmass Study on the Physics of the SSC, Ed. R. Donaldson, FNAL (1987).

IV.3. GEANT version 3.13, September 1989. See R. Brun et al., "GEANT 3," CERN DD/EE/84-1 (Revised; Sept. 1987); GHEISHA, H. Fesefeldt, RWTH Aachen preprint PITHA 85/02 (1985).

IV.4. "L3 Technical Proposal," L3 Collaboration CERN LEPC (March 1983); "The Construction of L3," L3 Collaboration, NIM A289 (1990); "The L3 Muon Detector"; M White et al., ICFA Instrumentation Bulletin (March 4, 1988).

IV.5. W. E. Toth, C. S. Draper Report CSDL-R1885 (Oct. 1987); N. K. Chhabra, C. S. Draper Report CSDL-R2011 (Sept. 1987); P. Bowditch, C. S. Draper Report CSDL-R1597 (Jan. 1983)

IV.6. R. Fabbretti et al., NIM A280 (1989), 13–24

IV.7. F. Hartjes, J. Konijn, and Y. Peng NIM A269, 544 (1988)

IV.8. H.S.W. Massey and E.H.S. Burhop, Clarendon Press, Oxford (1969).

IV.9. L. G. Christophorou, Atomic and Molecular Radiation Physics, Wiley, New York (1971).

IV.10. L. G. Huxley and R. W. Crompton, Wiley, New York (1974).

IV.11. L. G.Christophorou (ed.), Electron-Molecule Interactions and Their Applications, Academic, New York (1984).

IV.12. A. J Fehlmann, G. Viertel, Compilation ETH Zürich IHP (1983); A. Peisert and F. Sauli, CERN 84-08, Geneva (1984).

IV.13. C. M. Ma, U. Becker, D. A. Ma and A. H. Walenta, Drift Velocity and Drift Angle Measurements, MIT Technical Report No. 129 (1982); U. Becker, Y. H. Chang, to be published.

IV.14. L. G. Christophorou et al., NIM 163, 141 (1979); recent results from his group, Oak Ridge National Laboratory.

IV.15. L. G. Christophorou, NIM A268, 424 (1988).

IV.16. T. Ferbel, Experimental Techniques in High Energy Physics, Addison-Wesley Publishing Co, Inc., Menlo Park, Calif. (1987).

IV.17. D. Antreasyan et al., L3 internal report, (1989).

IV.18. R. Cardarelli et al., NIM A263 (1988) 20.

IV.19. "A R&D Program To Continue the Development of Precision Instrumentation for the Study of Muons in the TeV Region." Submitted to the SSC Laboratory (October 1989).

IV.20. Memorandum of Understanding Between the L* Collaboration and the SSC Laboratory (Jan. 12, 1990).

IV.21. "Research and Development Program on High Precision Instrumentation for Industrial and Scientific Applications—Laser Alignment Systems, Fast Electronical Signal Processing and Parallel Optical Data Transmission," Request for Support submitted to Swiss authorities.

IV.22 "R&D Programme in Switzerland for Future Detectors," H. Rykaczewski, to be published in the Proc. of the 1990 International Industrial Symposium on the Super Collider (IISSC), Miami Beach, Florida, March 14–16, 1990.

A. DESIGN CONSIDERATIONS

A.1. Introduction

The design of the calorimeter derives from the general L* concept: The detector is a precision instrument searching for new physics through, first of all, leptonic and photon channels and second quark channels (the measurement of jets). The calorimeter, therefore, should be multifunctional. It provides identification of electrons, muons, and jets and serves as a tracking device by helping to solve pattern recognition problems. It provides capability to separate electrons from hadrons by measuring shower shape and to separate muons from other particles by total absorption of hadronic components. It must detect muon bremsstrahlung and provide corresponding corrections to muon energy measurements.

The electromagnetic calorimeter is a separate dedicated device for precise measurement of electron and photon energy and is discussed in Chapter VI.

A.2. Energy Measurement by Total Absorption.

Devices used to measure energy by total absorption are of two types: (1) homogeneous, where the same medium is used both for particle detection and absorption, and (2) sampling, where different sampling and absorbing media are used. The electromagnetic energy resolution of a homogeneous calorimeter made of scintillating crystals like BGO or BaF_2 is markedly superior to sampling calorimeters. However, the response to electrons exceeds that of hadrons by a factor of ~ 1.5. This means that when a homogeneous calorimeter is introduced to ensure very high-precision electromagnetic energy measurements, the pre cision of jet energy measurements is somewhat compromised since in this case compensation is not likely to be achieved.

In the L*, lepton measurements have the highest priority. The L* calorimeter design goals for energy measurement are as follows: The best possible resolution for photons and electrons (better than 1% at 10 GeV); accurate measurement of muon energy losses, in particular due to bremsstrahlung (10% at 10 GeV); and adequate (better than 10% at 100 GeV) jet energy resolution. As can be seen from Fig. V.1, the very high precision of the L* muon detector can only be achieved if one corrects for muon energy losses in the hadron calorimeter.

A.3. Segmentation, Depth, and Time Resolution

Segmentation is determined by hadronic shower size and bremsstrahlung photon measurement and matches that of the electromagnetic calorimeter. Studies (Ref. V.1) show that an average transverse segmentation of $\Delta\eta \times \Delta\varphi = 0.04 \times 0.04$ is adequate. Longitudinal segmentation is needed both for electron identification and for general tracking and pattern recognition (Ref. V.2). We choose the hadron calorimeter to have an average of nine readout segments (about 1 λ each), which ensures the satisfactory measurement of muon bremsstrahlung energy losses.

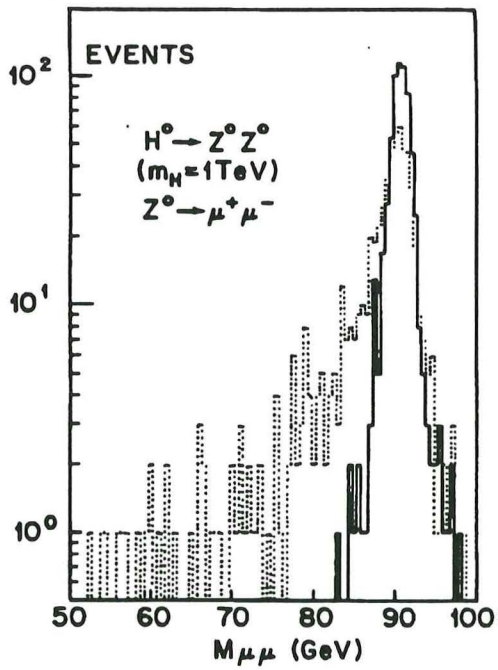

Fig.V.1. An example of deterioration of $Z \rightarrow 2\mu$ mass resolution due to fluctuations of muon energy loss in the 12 λ hadron calorimeter (dotted line). Correction for these fluctuations will be made by calorimeter sampling measurements (solid line). The reaction is pp → H^0 (1 TeV) → ZZ → 4μ.

According to parameterization (Ref. V.3), 98% of the energy of a 1 TeV hadron is contained in 12 λ. It is necessary to keep the flux resulting from hadronic debris of high energy showers at a level that is acceptable for muon detection. For an incident hadron of several hundred GeV, 12 λ are sufficient to keep this flux below 1%. Good time resolution (~ 20 ns) is needed to avoid pile-up (Ref. V.4).

A.4. Radiation Hardness Requirements

Studies (Ref. V.5) show that in the rapidity interval from 0 to 3.5 units a Pb-Fe-Si calorimeter with an inner radius of about 1 m should be able to withstand a total yearly neutron fluence of 10^{12} to 10^{13} neutrons/cm^2. The annual dose due to charged particles is less important.

B. SILICON CALORIMETRY

B.1. Introduction

Silicon calorimetry has become an important feature of modern collider and fixed-target experiments with applications ranging from a fraction of one square meter to a few tens of square meters. To date, silicon has been used primarily in electromagnetic calorimeters and to a lesser extent in position-sensitive devices for improved position resolution in hadron calorimeters. The well-understood properties of silicon as an ionization sampling device, its outstanding potential for meeting many of the most stringent requirements of SSC calorimeters, and its

simplicity of structural support have led us to choose it for the L* detector.

B.2. Advantages of Silicon

The intrinsic advantages of silicon are well known. With respect to almost every technical requirement of SSC calorimetry, silicon as a sampling medium is the equal of, or surpasses, other techniques of sampling calorimetry, with the exception of radiation hardness where liquefied rare gases are a clear choice. We briefly summarize here the properties of silicon and compare them to other techniques.

1. With respect to speed, silicon is rivaled only by scintillator systems. It is by far the fastest of the ionization techniques, with transit (or charge collection) time of 15–30 ns, thereby minimizing pile-up problems.

2. Absolute gain for the sampling medium. Like other ionization charge measuring devices, silicon has a fixed gain determined essentially by the thickness of the silicon wafer.

3. Silicon inherently responds linearly to deposited energy. Electron-hole recombination is not important even for fission fragments. There is no loss of energy sensitivity (saturation) for highly ionizing particles similar to that found in both cryogenic and warm liquids.

4. Transverse segmentation. Here silicon is far superior to other techniques and limited only by practical considerations of channel numbers.

5. Longitudinal segmentation. Silicon is similar to other sampling techniques and channel number considerations dominate the choice of segmentation. Sampling thickness of $\sim 1X_0$ and readout segmentation of $\sim 1\lambda$ are feasible.

6. Silicon operates well at room temperature, although operation at –20° C improves radiation damage noise characteristics by 2 orders of magnitude.

7. Silicon is insensitive to magnetic fields and is very likely the technology that gives the most compact device possible.

8. Monitoring of electronics gain by radioactive sources is possible by simple deposition of low-level activity on silicon surfaces.

9. Because the silicon detector arrays can be easily attached to absorber plates, structural frames in calorimeter construction are almost unaffected by the sampling medium and are determined primarily by mechanical and electrical considerations.

10. Another major advantage of silicon is that only low bias voltages are required ($\approx$100 V), which markedly simplifies design considerations.

B.3. Disadvantages of Silicon

1. The major disadvantage of silicon is the high cost of finished detectors. This situation is improving with time, but designing silicon calorimeters as compactly as possible remains crucial for economic reasons.

2. Electronics for silicon devices are often perceived to be more expensive than those for other techniques. Where this is true, it results from the attempt to design electronics that make full use of the superior characteristics of silicon – particularly segmentation, speed, and pile-up. For a given set of performance characteristics (such as those achievable with liquid argon or warm liquids), the costs per channel for electronics are essentially identical.

3. While computer simulations indicate that it is possible to achieve $e/\pi = 1$, no full silicon calorimeter has yet been built to demonstrate this property experimentally, although the SICAPO collaboration has such tests under way, and the result on e/π ratio will be available (Ref. V.16).

4. The question of radiation damage to silicon detectors requires attention. A clear understanding of the mechanisms of silicon damage and of their effects on detector performance, and an understanding of the SSC environment and the electronic parameters pertinent to SSC operation, are required to judge the potential effects of radiation on silicon performance.

In summary, if one compares silicon calorimetry with other techniques, the general conclusion is that for the same level of performance – that is, speed, segmentation, etc. – the cost of silicon sampling calorimetry exceeds those of other options only through the cost of the silicon. This may be offset to some extent by simpler mechanical construction requirements for the calorimeter. However, the capability of silicon to improve the calorimeter performance makes silicon an attractive solution.

B.4. Radiation Damage

A brief summary of radiation damage to silicon and its effect on calorimeter performance and parameters is given here.

1. In the hadron calorimeter, the neutron and slow hadron ionization will produce (due to displacement threshold) heavier radiation damage to silicon (approximately by a factor of 100) than the electromagnetic ionization.

2. At radiation levels of 10^{12} to 10^{14} n/cm^2 the major effect of radiation damage is the increase of leakage current in the detector. A secondary but important factor is bulk displacement damage, which results in decreased sensitivity and higher resistivity with increase of bias voltage required to maintain full charge collection. Measurements by Lindstrom (Ref. V.6) have indicated that at room temperature leakage current in 500 μm silicon will increase by 30 μA/cm^2 after a neutron exposure of 10^{13} n/cm^2. We assume here that the radiation dose is derived from the SSC environment and is acquired relatively slowly such that self-annealing takes place.

We wish to emphasize two major points, which have a major impact on the utility of silicon in high radiation environments.

1. Radiation damage in silicon is bulk damage due to trap formation and the leakage current increase due to these traps is highly temperature dependent. The simple expedient of operating the detector at –20°C, which can be done with conventional refrigeration techniques, will reduce leakage current by factors of 30 to 80 and thus give a corresponding increase in radiation hardness.

2. The traditional use of silicon in high-resolution nuclear spectroscopy has of necessity required amplifiers with long shaping times and very low noise. For these amplifiers, noise increase due to radiation-damage-induced leakage current at long shaping times is not tolerable. However, with the 10-ns shaping time used in our design of the SSC preamplifiers, the effect of noise due to leakage currents is nearly negligible. Figure V.2 shows noise vs shaping time for three different values of leakage current.

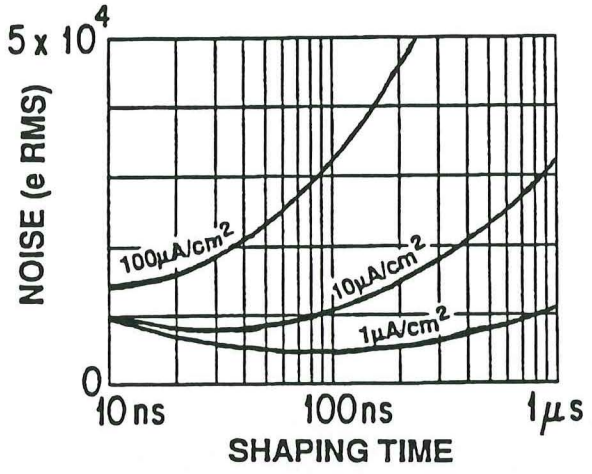

Fig. V.2. Amplifier noise vs shaping time and leakage current for bipolar preamplifier. Calculations are made for 500 μ thick silicon detector with the an area of 3 × 3 cm^2; input capacitance 180 pF at full depletion.

These two factors combine to provide 2 to 3 orders of magnitude improvement in silicon radiation hardness. Extensive calculations indicate neutron doses at the inner face of the L* hadron calorimeter of less than 3×10^{13} neutrons/cm^2/year at $\eta = 3$ for a total 10 years dosage of 3×10^{14} n/cm^2. Without cooling this would lead to a leakage current of 900 μA/cm^2. With cooling to –20°C this is reduced to acceptable level of 12–30 μA/cm^2 with a negligible effect on noise. After 10 years, charge trapping from bulk damage could become important and perhaps require annealing or replacement of a significant fraction of the silicon.

B.5. Silicon Procurement

We are requesting the silicon wafers from the Soviet Union. The Joint Institute of Nuclear Research (Dubna) is coordinating this effort. The total surface required is approximately 5×10^7 cm^2. The Titanium-Magnesium Factory at Zaporozhye, Ukraine, Soviet Union, can produce float-zone refined silicon crystals of either n- or p-type of high resistivity. The monocrystals are currently produced in ingots of up to 76 mm in diameter and more than 10 cm long. Assuming that the wafer thickness will be 0.5 mm and that the waste will be 0.4 mm, the total weight of material required is about 24 tons, including a 20% contingency. The factory can produce 5–6 tons of material annually. Thus, the required amount of silicon can be produced in about 4–5 years.

The required number of wafers is about 3×10^6. This production will be performed primarily in Minsk, Byelorussia, Soviet Union, by the Research Center associated with the University of Byelorussia and by subcontractors. Slicing, lapping, polishing, thermal oxidation, multiple photolithography, ion implantation, and metal (aluminum) deposition will be performed by them. The fabrication of wafers is estimated to be about 7×10^5 wafers per year and can proceed in parallel with silicon ingot production.

The total cost of the raw silicon ingots is estimated to be about 60M Roubles plus 5M$ needed for the purchase of quality control equipment. The estimate of wafer production cost includes cost of labor as well as the purchase of needed equipment. Provided that an R&D program is implemented, the production is estimated to cost 40M Roubles plus 5M$.

C. CENTRAL AND ENDCAP REGIONS

C.1. General Layout and Energy Resolution

Figures V.3 and V.4(a) show the layout for the L* calorimeter hadronic sections. In the hadron calorimeter the passive medium consists of lead and stainless steel layered plates with relative thickness chosen to reduce the electron response of the calorimeter so that e/h remains close to 1 in the hadronic part. There is experimental evidence that particular combinations of calo-

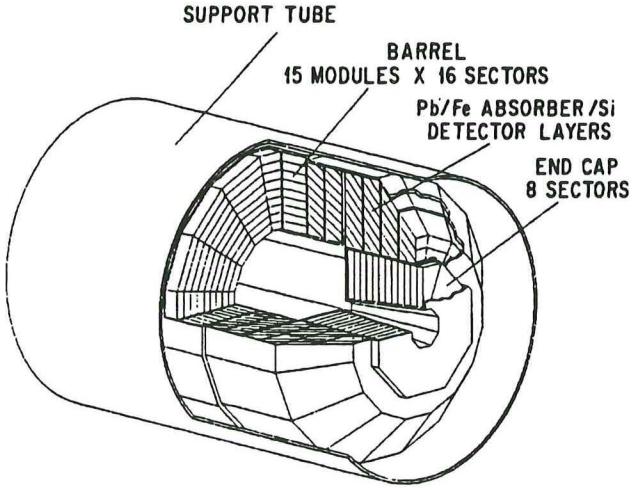

Fig. V.3. The central hadron calorimeter.

rimeter materials will be compensating (Ref. V.7). It is suggested that a Pb-Fe-Si calorimeter should consist of a mixture such that Pb/(Pb+Fe) = 0.25, in length, to ensure that e/h = 1. However, the BaF_2 electromagnetic calorimeter, which is 1.67 λ deep, prevents the entire calorimeter from exhibiting full compensation.

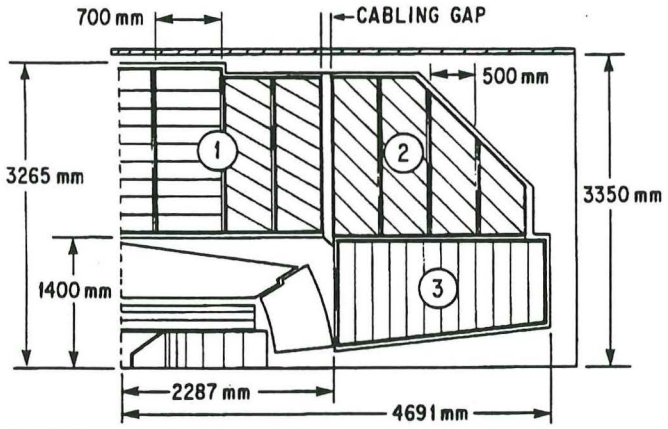

(a) BaF_2 e-m calorimeter in front.

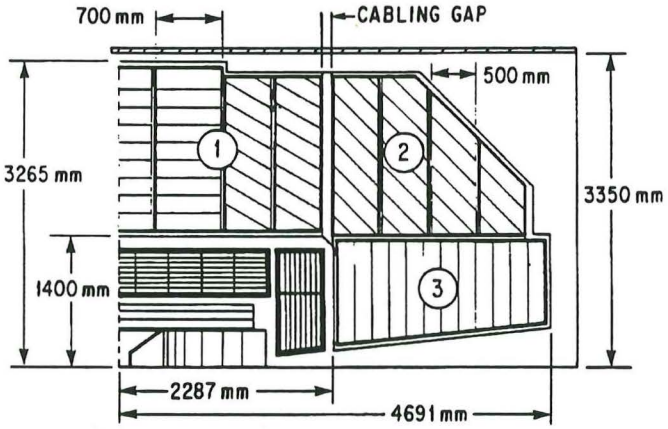

(b) Fine sampling Fe-Pb-Si e-m calorimeter in front.

Fig. V.4. Side quarter section of the central hadron calorimeter. Three out of five assemblies are shown. Absorber layers are shown schematically at correct orientation.

From our experience with the L3 calorimeter, we expect the hadron energy resolution of the BaF_2 (e-m) and Pb-Fe-Si (hadron) calorimeter system to be

$$\frac{\sigma_h}{E} = \frac{50\%}{\sqrt{E}} + 4\%$$

with an e-m resolution of

$$\frac{\sigma_{em}}{E} = \frac{1.3\%}{\sqrt{E}} + 0.5\%$$

Based on indication that liquid xenon is likely to be compensating, the overall resolution involving a liquid xenon e-m section is estimated to be

$$\frac{\sigma_h}{E} = \frac{50\%}{\sqrt{E}} + 2\%$$

As described in Chapter II, the mechanical support for the e-m calorimeter is designed in a way that it can be replaced by a fine sampling (0.5 X_0) silicon section. In this case, the entire calorimeter should be compensating, and the hadron resolution will be

$$\frac{\sigma_h}{E} = \frac{50\%}{\sqrt{E}} + 1\%$$

where the 1% constant term is defined by systematic uncertaintites of calibration, uniformity, stability, etc. The e-m resolution for this fine sampling section will be

$$\frac{\sigma_{em}}{E} = \frac{15\%}{\sqrt{E}} + 1\%$$

(1% due to systematics mentioned above). Figure V.4(b) shows the layout of the fine sampling Pb-Fe-Si section. The amount of silicon required for such upgrade is 30% of that required for the central calorimeter.

C.2. Segmentation

A unique requirement of the hadron calorimeter is that it should preserve the excellent muon momentum precision of the L* detector by accurate measurement of the bremsstrahlung photons, as well as other muon energy losses. To achieve the precision of (30–40%)/$\sqrt{E}$ in these measurements, it is necessary to maintain 2 to 4 X_0 sampling throughout the entire calorimeter with good longitudinal segmentation.

The basic silicon pad size will be approximately 3×3 cm^2 (or 2.5×2.5 cm^2) and 500 μm in thickness. Smaller pad sizes, while feasible, are not required because the L* hadron calorimeter segmentation does not need to exceed the segmentation of the BaF_2 electromagnetic section that precedes it (see Chapter VI). We assume that hadronic towers are constructed by summing preamplifier outputs from the basic 3×3 cm^2 units, although some variation in pad size is required to provide full coverage. Towers at small angles at the inner calorimeter edge are 3×3 cm^2, whereas at the 90° outer edge they are as large as 12×12 cm^2. With the average readout longitudinal segmentation of 9, it leads to a channel count of 180 000 in the hadronic calorimeter.

C.3. Structure

As can be seen in Fig. V.4, the calorimeter begins at r = 1.40 m and extends to r = 3.33 m. In the endcap region, it begins at 2.287 m and extends to 4.691 m from the crossing point along the beam direction. Angular coverage of above 5.7° is provided. The central hadron calorimeter consists of five assemblies weighing between 100 and 800 tons, which in turn are composed of a total of 17 structural modules (15 barrel rings and 2 endcaps). Each of these modules is subdivided into 16 (8 for endcaps) azimuthal segments with 51 to 60 layers of absorber and silicon sense layers. Figure V.5 shows one segment. The mechanical structure of these modules, as well as the assembly procedure, is similar to that of the L3 hadron calorimeter. Structural framing for the modules

consists of two 20-mm-thick stainless-steel membranes between which the absorber plates are installed. Separator/support walls between azimuthal segments run at small angles to radial directions to minimize the dead-region effect. The maximum stress applied to the side membranes is calculated to be ~30 kg/cm^2.

The description of the absorber structure follows (see Fig. V.5). A 2 X_0 layer is 27 mm thick. Absorber plates consist of 18 mm of austenitic stainless steel and 6 mm of lead. A sense layer is bonded to the stainless steel. Thus each layer is a mechanically self-contained unit, and fabrication and testing of the individual layers are performed prior to installation in the modules. The 3-mm space between absorbing plates contains silicon, preamplifiers, and signal-routing circuitry. A 4 X_0 layer consists of a double thickness of lead and stainless steel with a total thickness of 51 mm. The entire calorimeter is 11.7 λ deep at 90 ° and 13.9 λ at 5.7°. At 90° the hadron calorimeter will consist of 35 layers of 2 X_0 thickness and 16 layers of 4 X_0 thickness. Thermal control of the central hadron calorimeter is achieved by liquid cooling of the entire assembly to –20°C. A stainless steel shroud on the exposed surfaces of the calorimeter provides for the containment of both the cooled surfaces and the coolant. Compensation for thermal expansion is provided by the use of similar materials and compliant attachments where necessary. The entire calorimeter weighs 1710 tons.

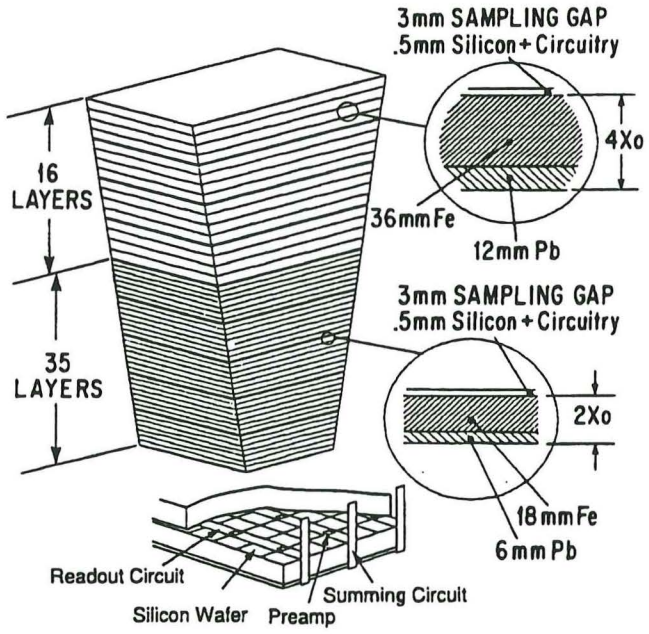

Fig. V.5. The calorimeter absorber/detector structure at 90°.

C.4. Electronics

Preamplifiers

The estimated total area of silicon required is 5200 m^2, yielding approximately 5.8 million 3 ×3 cm^{2}detector elements. For 500 μm silicon, the pad capacitance will be approximately 180 pF. Larger pad sizes will be formed by area summing these pads within layers. This minimizes signal-to-noise problems and simplifies the system by requiring only a single ASIC (application-specific integrated circuits) preamplifier design throughout. Oak Ridge National Laboratory (ORNL) has produced a preamplifier under generic R&D funding for a detector capacitance of 100 pF with a power dissipation of 2.5 mW, a rise time of 14 ns, and a signal-to-noise ratio of 6:1 for minimum ionizing particles. Studies indicate that at 180 pF we can achieve a signal-to-noise ratio of 4:1. Power dissipation could be traded off for more speed and lower noise. A conservative power dissipation of 10 mW per channel is assumed. The ASIC preamplifier will be configured into quad preamplifiers and located at the intersection of silicon pads. Packaged amplifiers of this type can be produced at a cost of about 1.15$ per amplifier in the quantities needed for this detector. The ability to design and produce these elements cheaply is an essential factor in favor of using silicon.

Signal Routing

Within a given layer, signals from individual preamplifiers are combined to form larger-area layer signals which are then routed to the edge of the absorber where summing amplifiers are located (Fig. V.5). Signals from several consecutive layers are then summed together to create a signal for an individual channel. On average, nine longitudinal segments will be formed in this way. All the signals are routed to the outer rim of the calorimeter assembly, where pipelined storage and digitization, as well as trigger-formation circuitry, are housed.

Trigger Considerations

It is clear that the major responsibility for the first level trigger will fall to the electromagnetic and hadron calorimeters. Not only will tower sums provide an energy trigger, but it also seems feasible to provide a very fast isolated muon trigger. With an average longitudinal segmentation of 9, tracking of isolated muons is certainly achievable and highly desirable. Such segmentation also improves the bremsstrahlung corrections to the muon momentum measurements.

Additional summing amplifiers for triggering purposes will be located at the perimeter of the calorimeter, where appropriate segment sums can be made and sent to the trigger electronics. Coarser sums may be developed for the first level trigger and finer sums for the second level trigger. While the first level trigger is likely to be formed from thresholds on analog sums, the data may be digitized, with flash ADCs, for computing second level triggers. The digitization rate depends heavily on the design of the triggering system. After the first level trigger, the rate should be below 1 MHz. After the second level

trigger, the rate should be below 10 kHz. In any case, pipelined storage will be required to hold the data for trigger decision. While data acquisition will involve all 180 000 channels, the first and second level trigger will work with coarser resolution by summing together many segments.

Power Dissipation and Cooling

Heat generated within the calorimeter is primarily from two sources: electronics and detector leakage current. The predominant source of heat for the electronics comes from the preamplifiers. A conservative estimate yields electronic power consumption within the calorimeter of 67 kW, where 10 kW is due to detector dark current. Dark current will be increased with radiation exposure. We estimate conservatively a maximum leakage current of 40 μA/cm^2, which would be localized to high-radiation areas. If we assume that the entire calorimeter exhibits such a high current, the maximum power generated is 200 kW at the end of 10 years, leading to a power load for the entire calorimeter of less than 300 kW.

C.5. Specifications and Performance

Central Calorimeter	
Inner radius	140.0 cm
Outer radius	333.0 cm
Support tube inner radius	335.0 cm
Ring modules	15
Azimuthal segmentation	16
Total weight	1506 tons
Endcaps	
Length along beam	230.0 cm
Azimuthal segmentation	8
Inner radius (minimum)	20.3 cm
Outer radius	138 cm
Total weight (two modules)	204 tons
Absorber	
Material	Pb + Fe (stainless steel)
$2X_0$ layer	0.6 cm Pb + 1.8 cm Fe
Layers ($2X_0$)	35
$4X_0$ layer	1.2 cm Pb + 3.6 cm Fe
Layers ($4X_0$)	16 at 90°; 25 at 5.7°
Depth	
With BaF_2 and support tube	11.7λ at 90°
With BaF_2	13.9λ at 5.7°
Segmentation	
$\Delta\eta \times \Delta\varphi$(average)	0.04 × 0.04
Longitudinal (average)	9
Number of channels	180,000
Readout and Performance	
High resistivity silicon pads:	
Area	3 × 3 cm^2
Thickness	500 μm
Charge collection time	15 ns
MIP signal (mean)	54K electrons
Preamplifier noise (at 180 pF, 10 ns shaping)	13K electrons
Estimated e-m energy res.:	
In $2X_0$ section	28%/$\sqrt{E}$
In $4X_0$ section	40%/$\sqrt{E}$
Estimated hadron energy res.:	
With BaF_2 e-m calorimeter	50%/$\sqrt{E}$ + 4%
With fine sampling silicon e-m calorimeter	50%/$\sqrt{E}$ + 1%

D. FORWARD CALORIMETER SYSTEMS

D.1. Forward Acceptance

The forward electromagnetic and hadronic calorimetry covers the angular region from 6.7° down to 0.3°.

D.2. Choice of Detector Technology

The anticipated high-radiation environment in the forward region places severe constraints on the choice of detector technology. At a distance of 10.5 m from the primary interaction vertex, the expected neutron fluency at 2.0° (η = 4.05) is 10^{14} neutrons/cm^2/year while the corresponding gamma ray dose at the same position is 10 Mrad (Ref. V.5). This ensures operation at radiation levels comparable or less than in the endcap region of the central calorimeter. Below this angle the radiation levels rise rapidly and can seriously reduce the operational lifetime of most detector technologies.

For the angular region above 2.0° BaF_2 is chosen as the electromagnetic detector medium, followed by a silicon sampling medium for the hadron calorimeter. Below 2.0°, we choose a radiation-hardened warm liquid technology both for electromagnetic and hadronic sections, which will go down as far as 0.3° (η = 5.95). To maintain better hermeticity over the transition region at 2°, we prefer warm liquid technology over cryogenic technology (LAr). As a backup solution for the choice of BaF_2 and silicon, we propose a warm liquid technology for the total forward calorimeter.

D.3. Forward Calorimeter Layout

The forward calorimeter shown in Fig. II.1 covers the angular region from 6.7° (η = 2.84) down to 0.3° (η = 5.95) and extends between 10.5 and 13.5 m from the interaction point. The detector is divided into an inner and outer sections, separated at 2.0° (Fig. V.6).

The outer forward calorimeter consists of a (25 X_0, 1.7λ) BaF_2 electromagnetic section followed by a 12 λ lead–stainless steel hadron calorimeter with silicon sampling media. This outer silicon hadron calorimeter consists of a 6 λ front section composed of 42 layers of 6 mm of lead, 18 mm of stainless steel, a 3-mm detector gap,

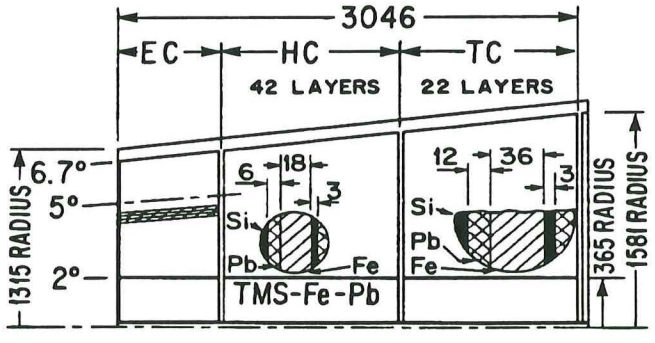

Fig. V.6. Longitudinal view of the forward calorimeter system showing the outer electromagnetic calorimeter (BaF2), the outer hadron calorimeter (Si), and the inner calorimeter (TMS) below $\phi = 2°$.

and a 6-λ tail section composed of 22 layers of double-thickness absorber layers and 3-mm gap. The expected energy resolution for this device is $\sigma/E = 0.013/\sqrt{(E)} + 0.5\%$ (electromagnetic) and $50\%/\sqrt{(E)} + 4\%$ (hadronic).

The inner forward calorimeter (plug) consists of a sampling TMS calorimeter. The two back sections have the similar absorber structure as the outer forward calorimeter with dual 3-mm-gap TMS ionization chambers. The front section consists of 25 absorber layers (each of 1 X_0) providing a total of 1.8 λ.

The total weight of the forward calorimeter unit is 260 tons for the hadronic section and 20 tons for the electromagnetic section.

D.4. Outer Forward Electromagnetic Calorimeter

For the outer forward electromagnetic calorimeter we choose a similar transverse segmentation of $\Delta\eta = \Delta\phi \leq 0.04$ (on average) as in the central calorimeter. There are in total 7610 crystals in the outer forward electromagnetic calorimeter.

The photosensors and the DAQ chain for the BaF_2 crystals are identical to those used in the central electromagnetic calorimeter (see Chapter VI). Also, the mechanical support of the crystals will use similar techniques as in the central region.

The BaF_2 calorimeter forms a ring mounted against the forward hadron calorimeter sitting in the support tube (see Figs. II.1 and V.6).

D.5. Outer Forward Hadron Calorimeter

The outer forward hadron calorimeter uses for ease of fabrication and hermeticity two sizes of silicon detectors providing a segmentation of $\Delta\eta = \Delta\phi \leq 0.04$ (on average) thus matching the BaF_2 crystals. The detector sizes (see Fig. V.7) for two regions are 20×20 mm^2 ($2° \leq \theta < 4°$) and 40×40 mm^2 ($4° \leq \theta \leq 6.7°$).

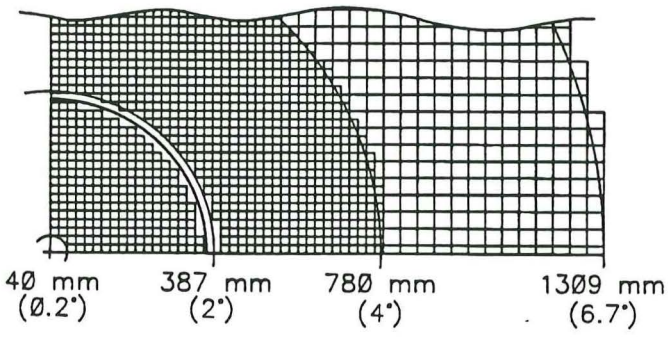

Fig. V.7. Cross section of the outer hadron calorimeter showing the Si detector arrangement (above 2°) and the inner calorimeter (TMS) with its subdivision of the electrodes.

The corresponding number of silicon detector elements in these two regions is 3544 and 2228 per layer, respectively. Detector elements are grouped into tower segments.

The silicon detectors will be mounted against the absorber slices, which form rings around the beam tube. For installation and service reasons the rings are grouped into two longitudinally separated assemblies. Radiation-hard variants of the central calorimeter electronics will be used for the front end electronics of this detector. Later stages of the DAQ chain will be modified for the much larger occupancy in the forward direction.

D.6. Inner Forward Calorimeter

Below 2.0°, the choice of technology for the inner (plug) forward calorimeter is warm liquid [tetramethylsilane (TMS)] with Pb-Fe radiator material. Equal detector response (compensation) for the measurement of electromagnetic and hadronic energy can be expected (Ref. V.8). Warm liquid hydrocarbon and silane media such as TMS and tetramethylpentane (TMP) can satisfy the detector requirements for radiation hardness (Ref. V.9). The TMS ionization chambers will be mounted in containers allowing for the pressure build-up due to chemical disintegration.

The electrodes of the ionization chambers are segmented in the following way: each of the 89 planes is subdivided into 940 cells of 20×20 mm^2. By summing five consecutive layers 33464 tower segments are formed (see Fig. V.7).

With the development of fast, radiation-hard charge preamplifiers for warm liquid calorimetry (Refs. V.10 and V.11), fast detector response is possible despite the relatively slow drift velocities in these liquids. In response to the repetition rate of the SSC only the very front spike (16 ns) of the ionization signal will be used. Under these conditions only moderately severe purity requirements need to be met: Free electron lifetimes of $\geq 1\ \mu$s are more than sufficient for adequate charge collection efficiency.

To maintain the intrinsically fast response of the front-end electronics (less than 10 ns), the preamplifier must be mounted directly on the detector. Detector capacitance, in turn, must be kept as low as possible, either by the choice of small electrode size or by series connection of larger electrodes. For the pad size of 20×20 mm^2 and 3-mm gap proposed for this calorimeter, the corresponding source capacitance will easily guarantee an amplifier risetime between 5 ns and 10 ns on the basis of previous design considerations for fast, front-end electronics (Ref. V.10).

D.7. Electronics

A monolithic front-end charge preamplifier manufactured in an industrial radiation-hardened (D-I) BiFET technology has recently been developed for warm liquid calorimetry (Ref. V.11) with <500 rms electrons of noise.

This same design can also be applied to a silicon ionization medium which meets and exceeds the corresponding requirements for speed, sensitivity, and radiation hardness. Fast output rise times can be achieved for the pad size of 20 × 20 mm^2 and 3-mm gap foreseen in the TMS calorimeter from the low input source capacitance (3 pF). For the larger pads of 40 × 40-mm^2 (340 pF), the same amplifier rise time can be maintained by raising the noise specifications from this preamplifier (see Sect. C.4). In a recent design upgrade, the rise time of this device is now faster than 10 ns with typically < 10 mW of power dissipation. The radiation hardness measured for this new polysilicon technology is 4×10^{14} neutrons/cm^2 and roughly an order of magnitude higher in radiation hardness to γ ray exposure than previous BiFET technologies. This latter design compensates for changes in transistor β values and the corresponding increase in low-frequency noise that would otherwise occur after exposure to radiation (Ref. V.1.2).

E. ALTERNATIVE TECHNOLOGY

Our alternative for the central and endcap regions uses liquid scintillator sampling. ITEP, Moscow, together with ORNL will be responsible for this option. Sampling calorimeters with plastic scintillator readout are well developed and are not risky from technological point of view. By introducing liquid scintillator (which is also a well-established technique), we can avoid any potential difficulties with respect to radiation hardness of a scintillator since it can be exchanged.

An alternative technique for the forward calorimeter system was discussed above in Sect. D.2 of this chapter.

E.1. Liquid Scintillator Calorimeter

The mechanical design and readout segmentation for a liquid scintillator calorimeter are the same as for the silicon option, except for the detector gap (5 mm) and optimization of absorber/detector thickness.

The liquid scintillator detectors are placed between the absorber plates in sealed leak-tight stainless steel containers, with the possibility to exchange the liquid in the entire calorimeter. The inside surfaces of the containers are painted with a reflecting paint, and the inside volume is divided internally by thin reflecting separators into cells with typical size of 6 × 6 cm^2, with a thickness of 5 mm. The light readout of each cell is made through a wavelength shifting (WLS) fiber that spirals inside the liquid scintillator cell (shown in Fig. V.8). The fibers pass through container walls and run along the module sides, reaching photodetectors mounted at the back of the modules. Several fibers are connected to each photodetector.

Mineral-oil-based liquid scintillator will be used because of its high hydrogen content. Physical properties of a typical scintillator are light yield 66% of anthracene, light attenuation length 4 m, decay time 2 ns, and maximum emission wavelength 423 nm.

The fiber has a diameter of 1 mm and consists of a WLS core and of a cladding of about 30 μm thickness, with refractive index lower than that in the core. The scintillation light is absorbed by the WLS in the fiber core and is then reemitted with the longer wavelength. A fraction of reemitted light (6–7%) is trapped inside the fiber and travels to the photodetectors. Only the part of the fiber contained inside the liquid scintillator cell has the WLS in its core. Outside the cell, the fiber core is clear. This improves the light transmission and reduces Cherenkov light conversion in the fibers. Modern scintillating fibers are known to be radiation resistant up to 10 Mrad. Radiation resistance of WLS fibers should be better. Monte Carlo simulation of the light collection efficiency for a minimum ionizing particle in the cell of 6 × 6 cm^2 with liquid scintillator thickness of 5 mm with realistic geometry and absorption/reflection coefficients shows that the number of photons at the photodetector input is 80/MIP/detector layer. A photodector with a gain of 1000 will allow the detection of minimum ionizing particles above the noise level of room temperature electronics. A possible candidate for such a photodetector is a hybrid photodiode with a silicon anode, which is presently being developed by Hamamatsu. In this device photoelectrons are accelerated in vacuum by applying a voltage of 10–15 kV before entering the silicon anode where a few thousand electron-hole pairs are created. This device can be segmented with cathode-anode pads of 3 × 3 mm^2, and a vacuum tube can house as many as 100 of these segments. The signals are fast, with a rise and fall time of 3 and 8 ns, respectively.

The R&D issues for this technique are the following. The light collection system clearly needs optimization and careful experimental study. The type of scintillator should be optimized for the optical fiber used. It should match the absorption spectrum of the fiber and it should not attack the fiber chemically. Fiber gluing and sealing tech-

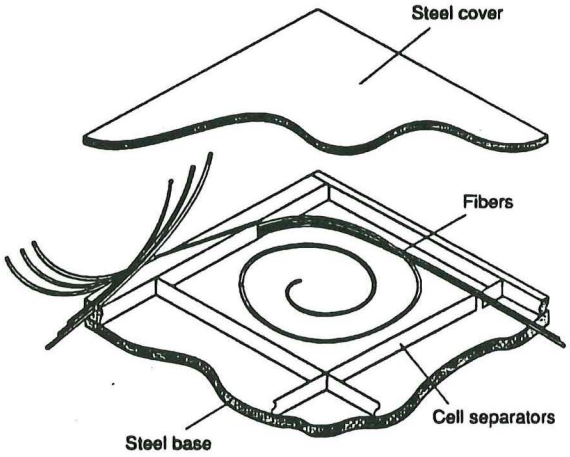

Fig. V.8. A cell of liquid scintillating calorimeter with WLS fiber readout.

niques should also be developed as well as corresponding photodetectors. They have to be fast, compact, stable, tolerant to magnetic field and cost-effective. Radiation damage tests on WLS fibers should be performed, as well.

F. SIMULATION

A major simulation effort is needed during the design phase to optimize detector performances and cost. It is imperative that during this phase computer models be continually checked with test beam data at each step.

The initial studies will focus on a BaF_2 electromagnetic, Pb-Fe-Si and Pb-Fe-TMS hadron calorimeters, as well as on the alternative choices. Presently, CALOR89 contains the most detailed representation of the physics necessary for good simulation and is used for this work. GEANT will be used for ray tracing.

Simulation studies will include studies of resolution and compensation, including time-dependent effects due to neutron moderation time or radiation damage; position-sensitive effects; determination of the best particle separation (i.e., discrimination between electrons and hadrons) as a function of longitudinal sampling frequency, transverse cell size and tower structures; investigation of hermeticity based on realistic engineering; investigation of albedo corrections to the e/π ratio; and radiation field mapping. In addition, handling of muon bremsstrahlung in CALOR89 will be improved, and remaining discrepancies between experimental results and simulation calculations will be reconciled.

This work will be jointly carried out by ITEP, IHEP (Serpukhov), Dubna from the Soviet Union, RWTH (Aachen) in Germany and by the University of Mississippi (UMiss), Los Alamos National Laboratory (LANL), ORNL, and the University of Tennessee (UTenn), with ITEP, UMiss, and RWTH (Aachen) being the coordinating centers in each country. To ensure adequate computing resources, a program to adapt CALOR89 to the parallel computing environment of a Unix-based microprocessor farm has been initiated by UMiss. To facilitate the use of geometry profiles which can be extracted from engineering design studies ORNL and UMiss are participating in a program to incorporate certain CAD/CAM packages into the geometry package of CALOR89.

The UMiss-ORNL-UTenn group presently is benchmarking CALOR89 using experimental results reported by the ZEUS, HELIOS, and SICAPO collaborations.

G. RESEARCH AND DEVELOPMENT

G.1. Past and Ongoing Projects

The L* hadron calorimeter R&D program includes the following detector techniques: Si detectors, liquid scintillator, planar gas proportional counters (PPC), and warm liquid TMS. The relative merits of these techniques are compared in Table V.1. The program is the joint effort of the following institutes and research centers:

- Silicon Detector Project: Dubna, ORNL, ITEP (Moscow), UTenn, UMiss, University of Alabama (Ulabama), University and INFN of Milano and Florence, and RWTH Aachen 1 Physics Institute (FRG).
- Liquid Scintillator Project: ITEP, ORNL, LANL, UMiss, and TIFR (Bombay).
- Planar Proportional Chamber PPC Project: ITEP, IHEP (Serpukhov), and IHEP (Beijing, China).
- TMS Project: ITEP, RWTH Aachen 1, and UAlabama.
- Radiation Damage Studies: IAE (Kurchatov Institute, Moscow), ORNL, RWTH Aachen 1, UAlabama, UTenn, and TIFR (Bombay).
- Simulation Studies: ITEP, IHEP (Serpuhkov), Dubna, ORNL, LANL, UMiss, UTenn, RWTH Aachen 1 Physics Institute, and TIFR (Bombay).

The L* R&D program at ITEP (Moscow) was started in 1988. The work is performed by a group of 40 physicists, engineers, and technicians who for the last few years worked on the construction and testing of the L3 hadron calorimeter. Test beam facilities at the ITEP 10-GeV proton synchrotron are used and test beam facilities at Serpukhov 70-GeV proton synchrotron can also be made available.

The liquid scintillator project described in Sect. E is the result of this R&D effort. Other projects are described below.

Silicon Detector Project

Within the USSR the program is being undertaken by JINR Dubna in collaboration with the TMF at Zaporozhye and the University of Byelorussia (Minsk), USSR to

Table V.1. Comparison of Hadron Calorimeter Detector Techniques

Detector technique	Fast response (ns)	Radiation longevity per year	Signal/noise for m.i.p. per cell	R&D issues
Silicon pads (3 × 3 cm^2)	20	10^6 rad, 10^{13} n/cm^2	4	Cost, electronics, compensation
Liquid scintillator	10	10^7 rad, 10^{14} n/cm^2	10	Readout, mechanical design
Gas PPC	10	High	> 10	Mechanical tolerances, compensation
TMS (readout pads 2 × 2 cm^2)	100	10^7 rad, 10^{14} n/cm^2	5	Low signals, purity, and electronics

develop a cost-effective technology for large scale production of radiation-hard silicon pad detectors. A specialized research laboratory is being constructed to carry out this research. It will include clean areas and detector tooling facilities.

In addition, a joint silicon detector project will be undertaken by the collaboration of ITEP, Dubna, ORNL, and the UTenn to build a plane of silicon detectors with a total area of 50 × 50 cm^2 in order to perform a test-beam scan of hadron and electron showers and to measure the pion to electron response ratio for various absorbers and absorber compositions. The silicon pads used by ITEP have an area of 5 × 5 cm^2, have a thickness of 400 μm, and are made by the planar process from 5 Kohm-cm n-type silicon (Ref. V.14). The detectors have a small leakage current (average 10 nA/cm^2) and a capacitance of 600–800 pF at a total depletion voltage of 100 V. Few pads have been tested recently to check the quality of the detectors and to find an appropriate match to the multichannel slow readout electronics existing at ITEP. Two detector planes will be produced soon. Beam tests of a silicon detector plane, with fast electronic readout (now being developed by ORNL and UTenn), are scheduled for the end of 1990.

The SICAPO collaboration started the development of silicon calorimetry in 1983 at CERN, building and testing silicon-tungsten and silicon-uranium electromagnetic calorimeters between 4 and 50 GeV (Ref. V.15). In previous years the SICAPO collaboration showed that a silicon hadron calorimeter for both silicon-uranium (Ref. V.16) and silicon (iron and lead) (Ref. V.7) can be made compensating by reducing its response to the electromagnetic component of the hadronic shower. At present SICAPO is building the first prototype of a Si/(Fe + Pb) hadron calorimeter, about 5 λ deep, equipped with about 20 000 silicon detectors; measurements on the lateral hadronic shower development are being carried out currently at CERN. The Si/(Fe + Pb) hadron calorimeter will be tested at CERN by summer 1991. To date the first two mosaics, each made of 480 silicon detectors with a total area of 0.2 m^2, have been put into operation. The use of these mosaics as active medium of a calorimeter with both Fe and Fe + Pb (thicknesses of Pb = 0.25 thickness of Fe) as absorber has allowed the measurements of lateral and longitudinal shower development for 12-GeV protons. A BiCMOS preamplifier with a rise time of 7.5 ns and a maximum voltage swing of 7 V, optimized for the operation of a detector capacitance of 150 pF, has been developed (Ref. V.17).

The Aachen research work on silicon detectors will be carried out together with other German physics institutes and industry. The goal is to develop ultra radiation-hard large-area silicon detectors particularly suited for the forward region. Radiation damage tests will be carried out and annealing procedures will be developed. As an intermediate prototype test, a calorimeter system consisting of 10 layers of a 5 × 5 matrix of 50 × 50 mm^2 silicon pad detectors together with a radiation-hard ASIC electronics system will be built and tested in 1991.

UTenn and ORNL have been heavily involved in silicon calorimetry. Tennessee has built a set of four silicon tungsten electromagnetic calorimeters for the SLD detector with a total area of 2 m^2 (Refs. V.3 and V.13). A beam test of these modules was conducted in April 1989 and the results were in agreement with design specifications. Tennessee also has received SSC generic R&D funds to develop low cost sources of silicon detectors and to participate in the SICAPO collaboration study of silicon hadron calorimetry. ORNL received similar funds to design ASIC fast amplifiers for silicon detectors. Along with UMiss both participate in the Silicon Electromagnetic Calorimeter Collaboration to construct a 3-m^2 electromagnetic calorimeter to SSC specifications.

Planar Proportional Chamber (PPC) Project

Planar Proportional Chambers and their application to the fast radiation resistant calorimetry are being studied by ITEP (Moscow), IHEP (Serpukhov), and IHEP (Beijing). PPC is a gaseous detector with planar metallic electrodes. The gap between the electrodes is small (1 mm) and is maintained with high precision (10 μm). At a sufficiently high voltage, the electric field is sufficiently large for avalanches to occur. The gain of about 10 000 – 100 000 at 55–60 kV/cm was measured with a 5 × 5 cm^2 prototype detector (see Fig. V.9) filled with isobutane gas. The response is very fast (7 ns). The high-voltage dependence of the PPC response is shown in Fig. V.10.

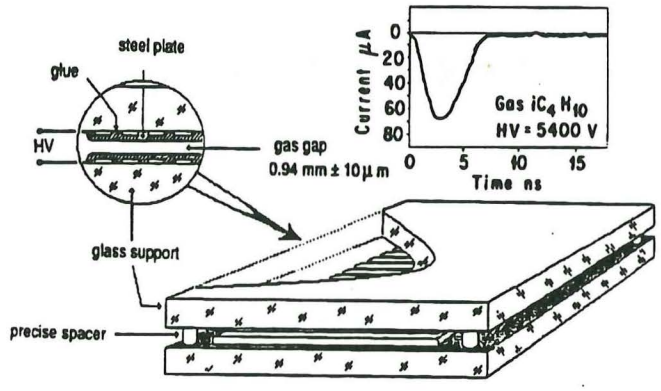

Fig. V.9. Planar proportional chamber (PPC) prototype and typical chamber response to MIP.

PPCs can work with intense particle beams because the space-charge effects normally causing saturation and aging effects are minimal for planar electrodes. The working gas for PPCs should not be transparent to its own UV light to prevent the development of secondary avalanches. Beam tests with a larger prototype of 50 × 50 cm^2 made of 64 PPC cells are scheduled for

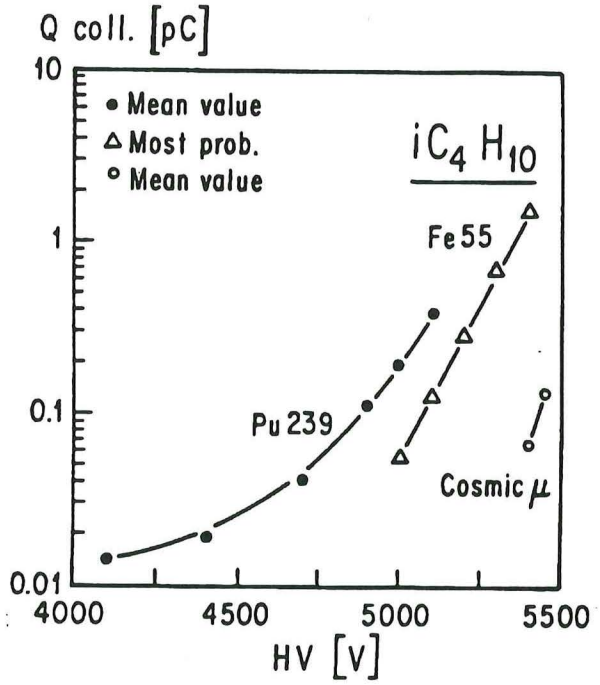

Fig. V.10. HV dependence of the PPC response to different radiation sources.

1990. R&D issues to be addressed include the rate dependence of PPC efficiency and aging effects. Nonflammable gas mixtures with the same properties as isobutane need to be identified. In the beam tests the pion-to-electron ratio has to be measured. Mass production technology of large-area PPCs is being studied.

TMS Project

The Aachen group has instrumented the forward regions of the L3 and TASSO detectors. A major effort has been invested in the simulation of these detectors using the GHEISHA package now being widely used at major laboratories. The current activities focus on warm liquid ionization chambers and silicon detector research work. Special programs have been set up to investigate the radioaction damage to TMP and TMS. Two stainless steel containers housing the ionization media and an electrode system have been built in Aachen. They will be exposed during the next months at a high radiation area of the SPS and will allow detailed measurements of the drift velocity, lifetime, pressure build-up, and gas decomposition as a function of the radiation dose. Together with industry the Aachen group has set up a program to develop ultra clean stainless steel containers for TMS particularly in view of mass fabrication. Several techniques like laser welding and high temperature soldering will be pursued.

After these investigations the activities will be focused in designing and building a radiation-hard prototype calorimeter, where a system engineering approach to the construction of a large calorimeter will play a dominant role. Beam tests which will be carried out in early 1992, will allow the absorber structure to be finalized in order to obtain full compensation.

A total of 100 TMS chambers of 50 × 50 cm^2 will be built in ITEP. About 30 are operational now. These chambers have a liquid gap size of 3 + 3 mm and 4 + 4 mm. The readout electrodes have an area of 6 × 50 cm^2. A purification/filling system for the TMS liquid has been built. Techniques for cleaning and degassing the chamber surfaces have been developed. Free electron life times as large as 8 μs were obtained in a fully operational chamber. (Electron drift time is about 300 ns at 10 kV/cm). Multiple measurements confirmed that the purity of TMS inside the sealed chamber does not change over the period of six months. The scan of hadron and electron showers inside the uranium and lead absorbers with a single TMS chamber was performed in the ITEP test beam. A typical result is shown in Fig. V.11. Another set of measurements was performed with 11 TMS chambers behind uranium and iron absorbers. Electromagnetic resolution of 25%/√E was measured with 5 mm uranium and with 25 mm iron absorbers in the energy range of 2–6 GeV.

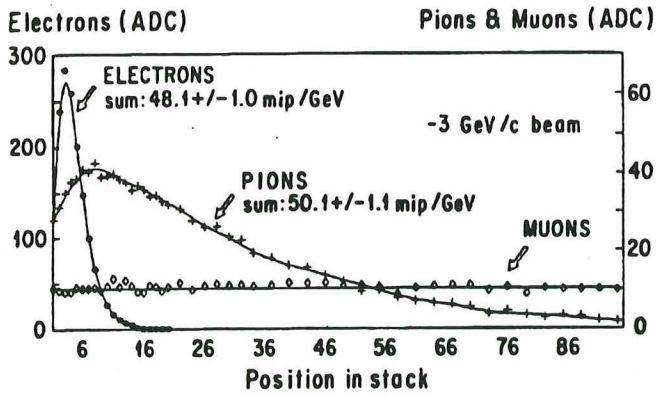

Fig. V.11. Shower curves for 3-GeV electrons, pions, and muons measured with a single TMS chamber inside a stack of 5-mm uranium plates.

The Warm Liquid Calorimetry Collaboration is presently investigating fundamental properties of warm liquid technology for calorimetry at the SSC. UAlabama, which is a member of this collaboration, is presently funded by the SSC Laboratory for research on this warm liquid sybsystem. Test beam measurements are presently under way at Fermilab to measure compensation of electromagnetic and hadronic energy response expected with this technology, the feasibility of integrated swimming pool detector configurations, and general materials compatibility issues. UAlabama began work in warm liquid calorimetry through the SSC generic detector R&D program with the development of fast forward calorimetry for the SSC and is now developing fast, ultra-sensitive, radiation-hardened electronics for this

technology. A distinguishing feature of this approach is the ability to extract a fast detector signal, despite the relatively long drift times in these fluids. The UAlabama group has already designed and built fast, radiation-hard charge preamplifiers for this technology and is now developing and testing faster designs with high radiation hardness.

The UAlabama group is also working closely with United States industry to develop warm liquid vessels with highly integrated electrode designs. In collaboration with Coors Ceramics and other ceramic manufacturers, this group is developing an integrated ceramic electrode with a flexible metalized anode pattern, similar to printed circuit board technology. Feedthrough connections in this scheme are then routed through a common multichannel tab on the same ceramic substrate. A laser welded outer stainless steel vessel for this electrode is presently being developed by Hutchinson Technologies.

For the TMS option the Tata Institute in Bombay is fabricating steel containers made by electron/laser welding thin steel plates on both sides of steel spacer bars. Performance tests will be carried out.

Simulation

To carry out simulations for the detector design and physics studies, as a part of the R&D program, the CALOR89 code package must be adapted to run on a parallel processing computing system. This system will be based on a series of RISC processors, following L3's extensive experience. The UMiss, ORNL, and LANL will be actively involved in this work. Close collaboration with SSCL will be maintained.

At the RWTH Aachen the successfully used GHEISHA code is continuously improved and speeded up.

At TIFR (Bombay), a GEANT has been set up with a segmented BaF_2 in front of an absorber/scintillator hadron calorimeter. A dual processor Apollo DN1000 (25 MIPs) will be used for detailed simulation studies.

G.2. R&D Requirements to the SSC

There are 40 physicists and engineers from ITEP and 30 physicists and engineers from Dubna working on the R&D effort for the L* collaboration supported by the Soviet government. In this section we list our requests to SSC for FY 1991 and FY 1992.

Silicon Procurement in the Soviet Union

The issue of silicon supply in the quantities required and on the time scale necessary is one of crucial importance. The main considerations have been addressed in Chapter V, Sect. B.1. A considerable R&D effort in the Soviet Union is required and is described below.

At Dubna, R&D will be aimed at developing the cost-optimized technology required for the large-scale production of radiation-hard silicon detectors. In efforts related directly to an interface with industry, Dubna will develop technology that will be applicable to industrial mass production and involve quality control at each production step. The collaboration between Dubna and USSR industry should result in cost-reducing measures. R&D associated with this activity is needed. Specific steps include the definition of specifications for silicon monocrystals; production of test samples and test evaluations; definition of final specifications for production steps by the end of 1992; and design of equipment for quality control. Institutions involved in this integrated effort are JINR (Dubna), the University of Byelorussia, ZTMF (Zaporozhye), ITEP (Moscow), ORNL, UTenn, and RWTH Aachen.

The work at Dubna will be carried out from 1991 on. It will involve facilities having a total area of 350 m^2 and a clean area of 70 m^2. A deionized water installation will be available together with slicing, lapping, and polishing machines. Thermodiffusion, thermal oxidation growth, photolithography, and metal deposition will be carried out. In the second phase, additional tools will be installed for the examination and evaluation of silicon properties, together with equipment needed for the design and fabrication of photolithography masks. The total anticipated cost is 6900K roubles and 1150K$.

Silicon Calorimetry in the United States

The Silicon Electromagnetic Calorimeter Collaboration subsystem proposal to the SSC laboratory will be expanded to include hadron calorimeter elements. Presently, the proposal has partial funding for the first year. In the following discussion, it is assumed that the SECC proposal will be fully funded. The L* collaboration proposed to build a full azimuthal segment ($2\pi/16$) of a 90° L* calorimeter module including cabling, signal routing, mounting boards, colling, and full electronics through tower sums for the first level trigger with pipeline storage and digitization. We envision a 2-year program beginning in January 1991. A few planes of the calorimeter will be instrumented with silicon obtained from commercial suppliers; and the remainder, with detectors from the production facilities in the Soviet Union as the silicon becomes available.

A program of radiation damage studies will be initiated immediately to study effects of radiation-induced energy resolution and rise-time characteristics. These effects are expected to be very dependent on the particular silicon used. Therefore, tests will be performed with detectors made from TopSil, Wacker, Hamamatsu, and Soviet material, as well as from high-resistivity silicon produced by technologies other than float zone. A matter of particular significance that must be studied is that low temperatures introduced to reduce effects of leakage current may well increase the signal degradation effects by inhibiting self annealing of cluster vacancies.

Design and production of radiation hardened electronics (both bipolar and CMOS) will be pursued, including preamplifiers suitable for hadronic pads, summing amplifiers, pipeline storage elements and digitization circuitry.

A silicon plane with an area of $0.5 \times 0.5\ m^2$ is under construction for tests at ITEP to establish parameters necessary for compensation and verify the SICAPO results on compensation. Preamplifiers developed at ORNL for the SECC system will be used in these tests.

Milestones are June 1992 for the final decision on radiation hardness and June 1993 for the final decision on Soviet capability to provide finished detectors. Our requests for silicon hadron calorimetry R&D are presented in Table V.2.

Table. V.2. Budget Request for Silicon Calorimetry R&D

		FY 91 (K$)	FY 92 (K$)
Electronics	Design	200	100
	ASIC rad-hardened bipolar run	100	
	ASIC rad-hardened CMOS run	100	100
	Packaging, cables	20	150
	Fast DAQ system		75
Mechanical design, construction, and refrigeration		75	
Radiation damage studies		50	50
Silicon purchase		60	
Silicon Calorimetry R&D Total		605	475

Liquid Scintillating Calorimeter

ORNL will proceed with the development of a liquid scintillator technique as the main backup option of the L* hadron calorimeter. The hadron calorimeter prototype 6λ long module with 60 liquid scintillator readout planes is to be constructed and tested by ORNL in collaboration with ITEP (Moscow).

Lawrence Livermore National Laboratory (LLNL) will construct a prototype liquid scintillator cell containing a spiral of wavelength shifting fiber for characterizing its performance using fast readout electronic schemes and new photodetectors.

We are requesting 350K$ for these activities in FY 1991 and FY 1992.

Simulation Studies

The simulation studies will be intense during the design phase of the L* calorimeter construction and prototype beam tests. The engineering simulation studies required to support the design, construction, and testing of the L* calorimeter are estimated to cost 575K$ per year.

Warm Liquid Calorimeter for the Forward Region

We propose to build the prototype warm liquid calorimeter for the L* forward region. Requested funds are to support an engineering design of the calorimeter prototype to cover travel expenses to meet with collaborators in Europe and Asia and to purchase prototype vessels, the fluid purification system, and electronics. We are requesting support from home institutes (e.g.,the annual request from UAlabama is 200K$ for operational funds and 200$K for capital equipment).

R&D Budget Request

Our requests to SSC for R&D of hadron calorimeter detector techniques and simulation are presented in Table V.3.

As stated in this chapter, there have been many efforts at Dubna, ITEP, and other USSR laboratories on R&D for hadron calorimeter. We request the SSC to invite 10 Soviet physicists and engineers to integrate the ideas and experience to the SSC standards. We request travel and per diem support per person of 32K$, or 320K$ total per year.

Table V.3. L* Hadron Calorimeter R&D Budget Request (K$)

Activity	FY 1991	FY 1992
Silicon procurement in the U.S.S.R.	750	400
Support of Soviet scientists at SSCL	320	320
Silicon calorimetry R&D in the U.S.	605	475
Liquid scintillator project R&D	350	350
TMS R&D for forward region	400	400
Simulation studies	575	575
Hadron Calorimeter R&D Total	3000	2520

References

V.1. G. Brandenburg et al., Proc. of the 1986 Snowmass Study, p.420; R. Partridge., Proc. of the 1984 Snowmass Study, p. 567; T. Akesson et al., Proc. at the Workshop on Physics at Future Accelerators, CERN 87-07 vol. 1, p. 174.

V.2. B. Adeva et al., "The Construction of the L3 Experiment," NIM A289 (1990), 35.

V.3. Yu Galaktionov et al., to be published.

V.4. Proc. of the Workshop on Calorimetry for the SSC, Tuscaloosa, Alabama, March 13–17, 1989.

V.5. D. Groom, Proc. of the Snowmass Study ,1988, p. 711.

V.6. G. Lindstrom et al., in Proc. of Tuscaloosa Workshop on Calorimetry, 1989; C. Bertrand et al., Silicon Calorimetry for SSC, Summary Report of the Silicon Calorimetry Working Group, OREXP-89-0902.

V.7. SICAPO Collaboration, E. Borchi et al., Phys. Lett. B222 (1989), 525.

V.8. R. Wigmans, NIM A259 (1987), 389; M. G. Albrow et al., NIM A265 (1988), 303; K. Ankoviak et al., NIM A279 (1989), 83.

V.9. R. Holroyd, "Effects of Radiation Damage to TMP, TMS, and Liquid Argon Solutions," SSC-SR-1035 (June 1988), p. 335,; R. Holroyd and D. Anderson, NIM A236 (1985), 294.

V.10. D. DiBitonto et al., NIM A279 (1989), 100.

V.11. D. DiBitonto et al., "Fast, Radiation-Hard Charge Preamplifier for Warm Liquid Calorimetry," Proc. of the Workshop on Calorimetry for the SSC, Tuscaloosa, Alabama, March 13–17, 1989.

V.12. P. M. Van Peteghem et al., Proc. of the ESSCIRC, San Francisco, September 1989.

V.13. S. Berridge et al., "The Small Angle E-M Calorimeter at SLD: A 2 m^2 Application of Silicon Detector Diodes. Trans. on Nuc. Sci, vol. 36, No.1 (1988), 339.

V.14. E. Fretwurst, G. Lindstrom et al., Technical Progress Report for the Development of the Plug Calorimeter, H1-TR110, Sept. 1987; E. Fretwurst et al., and R. Wunstorf et al., in ECFA Study Week on Instrumentation Technology for High-Luminosity Hadron Colliders, CERN 89-10, vol. (1989), 319 and 321.

V.15. SICAPO Collaboration, G. Barbiellini et al., NIM A235 (1985), 55.

V.16. SICAPO Collaboration, F. Lemeilleur et al., Phys. Lett. B222 (1989), 518; A. L. Angelis et al., to be published in Phys. Lett. B.

V.17. A. Gola, G. Pessina, and P. G. Rancoita, "Fast Front-End Electronics for Experiments Using Silicon Calorimeters at SSC/LHC Colliders," to be published in NIM (1990).

A. INTRODUCTION

We propose a very high resolution electromagnetic calorimeter for the L* experiment. Two options will be pursued. The first one uses barium fluoride (BaF_2) crystals; the second uses liquid xenon (LXe). Both options have radiation resistance up to at least 10^7 rad; an energy resolution of $1.3\%/\sqrt{E} + 0.5\%$, comparable to the 12 000 BGO crystals L3 electromagnetic calorimeter; and π/e suppression ratio of $\approx 10^{-4}$.

The physics motivation is to make precise energy measurements of photons and electrons. The unique capability of this detector is shown, for example, in its ability to detect Higgs particles in a mass region of 80 to 180 GeV (Ref. VI.1). See also Chapter X.

There exists a gap between the upper limit for Higgs detection at LEP Phase II ($\approx M_Z$) and the lower limit for Higgs detection at the SSC using the four lepton final state ($\approx$200 GeV). This gap will be covered by a precision electromagnetic detector, measuring the Higgs in its $\gamma\gamma$ and 4 lepton decay channels with $\Delta M/M < 0.5\%$.

The high-resolution calorimeter also will be used to search for new massive gauge bosons through their decays into e^+e^-. This will allow us to explore the energy regime where high-energy symmetries, such as superstring inspired E_6, break down to form the gauge structure observed at low energies.

B. THE BaF_2 ELECTROMAGNETIC CALORIMETER OPTION

The BaF_2 electromagnetic calorimeter consists of 26 000 large size (50 cm long, 24.5 radiation length) crystals. The calorimeter has the following three parts:

- A central barrel calorimeter with an inner radius of 75 cm and an outer radius of 140 cm. It covers the rapidity range of $|\eta| < 1.45$.
- Two endcaps, located at $z = \pm 150$ cm, which cover the rapidity range of $1.45 \leq |\eta| \leq 3.0$.
- The forward and backward calorimeters are located at $z = \pm 10.5$ m. They cover the rapidity range $3.0 \leq |\eta| \leq 3.8$ as discussed in Chapter V.

The crystals are approximately square in cross section, with sizes ranging from 2×2 cm^2 in the front for the smallest crystal to 5.2×5.2 cm^2 in the back of the largest crystal. The typical crystal covers a $\Delta\eta \times \Delta\varphi$ interval of 0.04×0.04. The total volume of crystals is 17.2 m^3 (83.6 tons), as summarized in Table VI.1.

The BaF_2 calorimeter has the following features:

- 3 ns peaking time of the scintillation light readout, i.e., gating in a single beam crossing;
- Bipolar signal output with residual tail of less than 10^{-4} after 35 ns;
- Radiation resistance up to at least 10^7 rad;
- Energy resolution of $1.3\%/\sqrt{E} + 0.5\%$, comparable to the L3 electromagnetic calorimeter.

Table VI.1. BaF_2 Crystals

Detector	Number	Volume (m^3)	Weight (ton)
Barrel	11 304	10.4	50.5
Endcaps	7100	2.7	13.1
Forward	7610	4.1	20.0
Total	26 014	17.2	83.6

B.1. BaF_2 Readout

BaF_2 is the fastest scintillation material known. Table VI.2 lists the properties of BaF_2, liquid xenon (LXe), and KRS-6, a fast Cherenkov radiator (discussed below).

Table VI.2. Properties of Some Fast Detectors

	BaF_2	LXe	KRS-6
Density (g/cm^3)	4.88	3.05	7.2
X_{rad} (cm)	2.04	2.77	0.94
X_{int} (cm)	29.9	55	23.0
X_{rad}/X_{int}	0.068	0.050	0.041
$R_{Moliere}$ (cm)	4.4	5.6	2.4
Ref. Index	1.49	NA	2.2
Hygroscopic	No	NA	No
Luminescence (nm) (slow)	320		NA
(fast)	210	170	
τ Decay (ns) (slow)	630	45 (e)	NA
(fast)	0.9	2 (α)	
Light output (γ/MeV) (slow)	5000	40 000 (e)	
(fast)	1000	50 000 (α)	1500

(e): Response to electrons $\beta \approx 1$.

(α): Response to a particle $\beta << 1$.

Figure VI.1a shows the emission spectra for pure BaF_2 and BaF_2 doped with 1% of lanthanum (Refs. VI.2, VI.3). The peak intensity of the slow component (300 nm) from the lanthanum-doped BaF_2 crystals is reduced by a factor of about five with little change to the fast components (195 and 220 nm). It is also known that the intensity of the fast components has no temperature dependence, although the slow component decreases with increasing temperature at a rate of $-2.4\%/°C$ (Ref. VI.4).

Figure VI.1a also shows the quantum efficiencies of two photomultipliers (PMT): (1) a special UV-sensitive, solar-blind PMT with a cesium telluride (Cs-Te) photocathode and a synthetic silica (quartz) window (Hamamatsu R3197), and (2) a PMT with a bi-alkali photocathode and a quartz window (Hamamatsu R2059). By using the solar-blind photocathode (Cs-Te), one would be able to collect only the fast scintillation light.

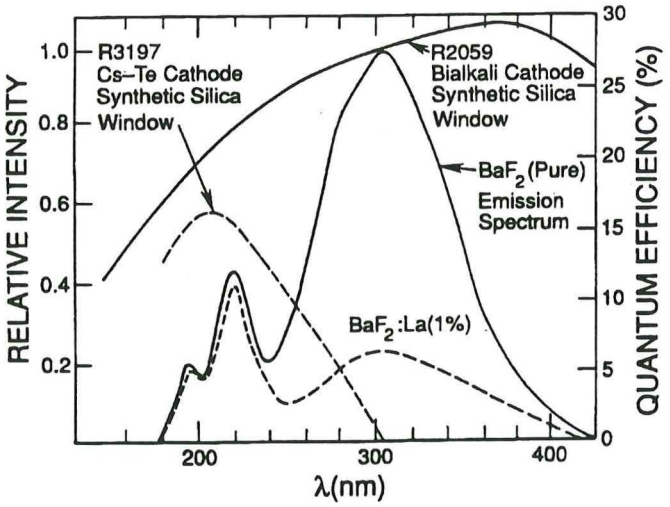

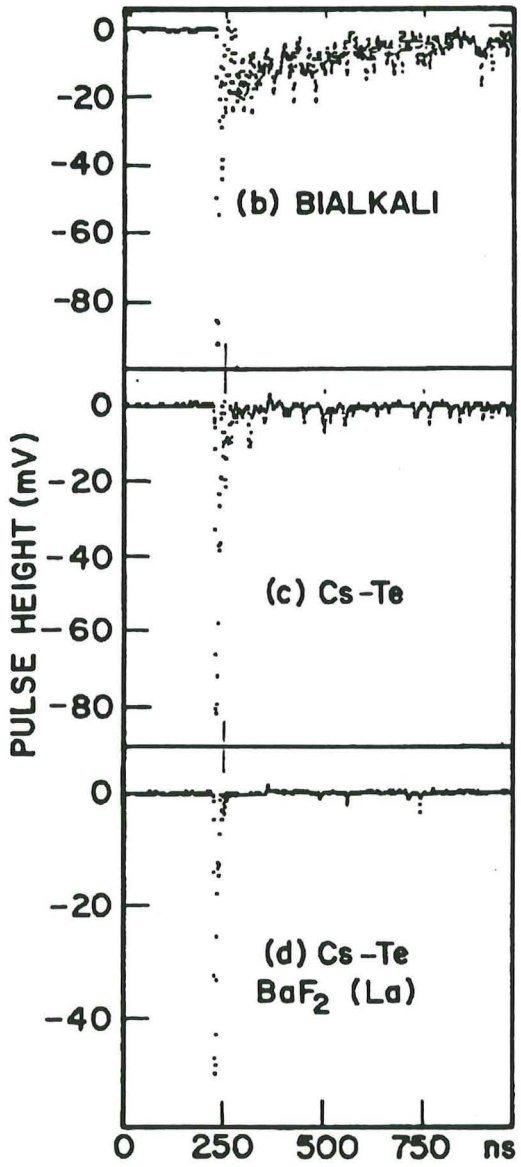

Fig. VI.1. (a) BaF_2 scintillation spectrum. (b,c,d) BaF_2 scintillation pulses observed with a digital scope with (b) bi-alkali photocathode, (c) Cs-Te photocathode, and (d) Cs-Te photocathode and La-doped Baf_2 crystal. The rise time for the fast signal is 3 ns.

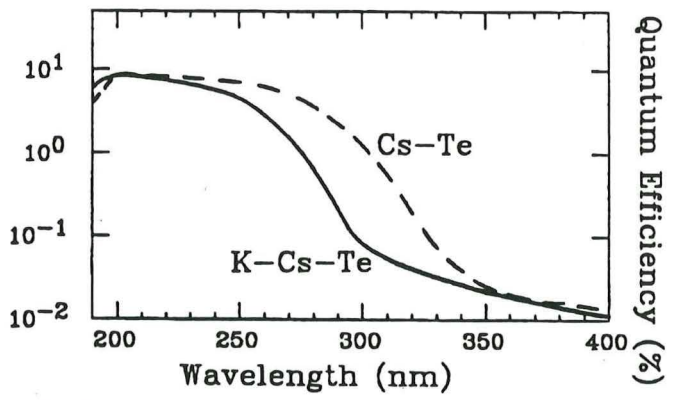

Fig. VI.2. New K-Cs-Te photocathode compared with the Cs-Te cathode. The new cathode will supress the slow component by a factor of 50 without La doping.

Figure VI.1b, c, and d shows the BaF_2 pulse height observed with a digital scope, with (b) bi-alkali cathode, (c) Cs-Te cathode, and (d) Cs-Te cathode and La-doped BaF_2. Figure VI.2 shows the quantum efficiency curves from a K-Cs-Te photocathode recently developed by the Hamamatsu Company (Ref. VI.5). This new photocathode is expected to suppress the slow component by a factor of ~50 without using lanthanum-doped BaF_2.

With the existing very fast scintillation light, we are carrying out extensive R&D work to design the BaF_2 readout system as follows:

- Hamamatsu R2148-type vacuum photodiode with K-Cs-Te photocathode and quartz window as the photosensitive device, working in a magnetic field.
- A preamplifier mounted on the base of the photodiode has a gain of 100 μV/1000 electrons and 45-ns decay time. The typical noise of this preamplifier together with the photodiode is 1000 electrons for a few ns peaking time.
- A fast shaper with 3-ns peaking time and two-pole zero cancellation: one for the residual slow component (594 ns) and the other for the preamplifier decay (45 ns). It has two outputs: (1) a bipolar output for the signal and (2) a unipolar output for RFQ calibration. The residual signal of the bipolar output after 35 ns is less than 10^{-4}. Combining the optical and electrical suppression, we are safe from the slow component contamination.

Figure VI.3 shows the input and output pulse shape simulated with a PSPICE program for the designed circuit. The input signal, which has a 3-ns rise time and a fast/slow ratio equal to one, is an average of digitized BaF_2 scintillation pulses obtained from a solar-blind PMT with a Cs-Te photocathode.

Also shown in Fig. VI.3 is the output from the preamplifier. Both bipolar and unipolar output pulses are shown in Fig. VI.3. This fast readout will enable us to operate the detector in a single beam crossing, thus reducing pile-up to a minimum. This is demonstrated in Fig. VI.1c, where we use Cs-Te crystals without lan-

thanum dopant. With use of the new KCs-Te, the slow component decreases by a further factor of ~20.

B.2. BaF_2 Energy Resolution

We have measured the photoelectron yield of BaF_2 to be 80 000 per GeV by using a solar-blind PMT with a Cs-Te photocathode. This light yield is more than enough to provide $1\%/\sqrt{E}$ resolution. The contribution of electronics noise to the total energy resolution is also negligible for particles of a few GeV.

A GEANT simulation was carried out to calculate the resolution of the BaF_2 calorimeter. The simulation includes a shower leakage fiber wall and 30% radiation length of dead materials at the front of the BaF_2. Table VI.3 lists the result of this calculation together with other contributions. With a 0.4% precision calibration, it is clear that the BaF_2 calorimeter will provide the design goal of $1.3\%/\sqrt{E} + 0.5\%$ resolution.

B.3. Calibration

After many years of working on precision measurement of electrons, we have learned that precise, frequent calibration in situ is vital in maintaining the high resolution of any electromagnetic calorimeter. Our main calibration will use a Radio Frequency Quadrupole accelerator (RFQ) that has been developed by Caltech and AccSys

Table VI.3. Energy resolution.

E (GeV)	5	10	100	500
Photo electrons	0.2	0.1	0.04	0.02
Noise	0.8	0.4	0.04	0.08
Calibration	0.4	0.4	0.4	0.4
GEANT	0.61	0.56	0.37	0.37
Total	1.10	0.80	0.55	0.55

Technology (Ref. VI.6). The first calibration RFQ will be installed in L3 soon. A fluoride crystal target bombarded with a pulsed proton beam from the RFQ, $^{19}F(p,\alpha)^{16}O^*$ (Ref. VI.7), and the subsequent decay of the excited oxygen nucleus $^{16}O^*$ produces hundreds to thousands of 6-MeV photons per millisteradian per beam pulse. These photons, functioning as a synchronized equivalent high-energy photon of up to 40 GeV per calorimeter cell will serve as a calibration source for our electromagnetic calorimeters. The BaF_2 readout has been designed to accomodate this pile-up mode with a unipolar output. This technique provides a relative calibration with precision of 0.4% in a few minutes. The feasibility of this calibration mode has been proven in an experiment with four BaF_2 counters and a 7×7 L3 BGO crystal array at an RFQ facility at AccSys in September 1988 (Ref. VI.6).

Complementary to the RFQ calibration, we will also use minimum ionizing particles (MIPs) produced by the

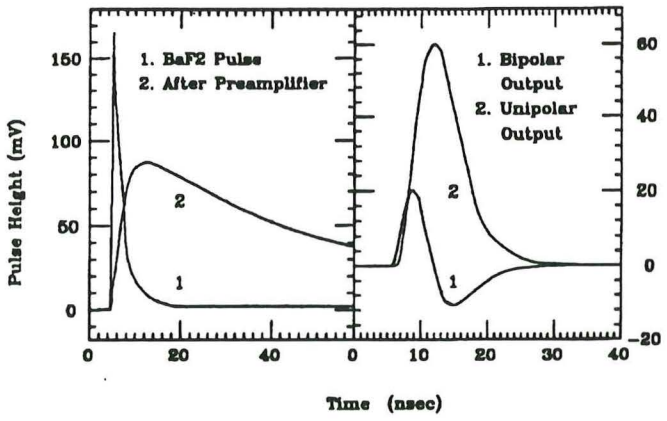

Fig. VI.3. BaF_2 readout pulse shape simulated with a PSPICE program: (a) input and after preamplifier, and (b) outputs.

collider as a calibration source. A MIP passing through a BaF_2 crystal longitudinally would deposit 0.33 GeV energy in the crystal, which would be read out by the crystal with a few percent resolution. With a few hundred tracks, the peak position (that is the calibration point) can be determined to 0.4%. The multiplicity of high-energy charged hadrons is large enough to provide a calibration within 12 h during SSC running.

The daily calibrations with these techniques will be confirmed by the measurement and invariant mass reconstruction of inclusive Z^0, Υ, and J production, where the vector bosons decay into e^+e^-. With a P_T cut of 10 GeV on the vector boson, a typical crystal in the central calorimeter will see 20 e^+ or e^- from Z^0 decay and 200 from Υ decay (Ref. VI.8) for each week of running.

B.4. Mechanical Support Structure

We have chosen to follow the proven design concept of the L3 BGO calorimeter. The structural material is confined to thin cell walls around the crystals, and to a cylindrical inner tube that carries the weight and is attached to a conical funnel that transmits the load to support flanges. This results in the best solid angle coverage and energy resolution. Figure VI.4 is a schematic showing the central BaF_2 calorimeter consisting of the barrel and the endcaps.

Crystals are located in cells composed of thin walls made by a carbon-fiber composite. The carbon-fiber cavities are bonded together to form a rigid honeycomb with a wall thickness of 250 μm.

The carbon-fiber cells in the barrel are bonded to an inner cylindrical sandwich shell with an acrylic foam core and thin carbon-fiber composite skins.

Initial studies show that it should be possible to achieve the same cell wall thickness (250 μm) and assembly tolerances (100-300 μm) between the crystals, as we used for the L3 BGO calorimeter.

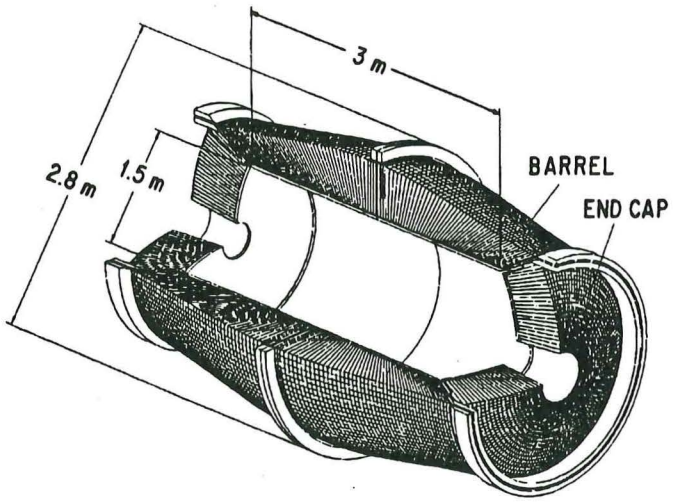

Fig. VI.4. A schematic showing central BaF_2 calorimeter.

B.5. BaF_2 Crystal Production – R&D at SIC

Production of 26 000 large pieces of BaF_2 over a period of three years will require a monthly yield of 750 pieces. The Shanghai Institute of Ceramics (SIC) has accumulated six years of experience on the research, development, and production of BGO crystals, and was able to deliver 400 finished crystals per month in collaboration with LAPP (Annecy, France), CERN, and Caltech. Since October 1989, SIC has been working on BaF_2 scintillator crystal research. SIC has grown small, pure, and doped BaF_2 crystals for tests at Caltech, and explored the making of large size crystals.

In a collaboration with the Beijing Glass Research Institute (BGRI), SIC has delivered a 40-mm-diameter crystal 220 mm long to Caltech. SIC has also installed a new large furnace facility. Adding contributions in other equipment, raw materials, and labor, SIC invested an equivalent value in excess of 250K$ in 1989.

The research and development program at SIC will extend to three years (from 1 January 1990 to 31 December 1992) and will focus on the following three areas:

- Development of a mass production method of growing large, highly transparent, radiation resistant crystals using BaF_2 and doped BaF_2 as the pilot crystals.
- Systematic study of rare-earth doped BaF_2 crystals, especially lanthanum-doped BaF_2 crystals.
- Systematic study of new fluoride system scintillator crystals with emphasis on CeF_3, LaF_3. and other rare earth fluoride crystals.

Studies (Refs. VI.2, VI.3) indicated to SIC that La-doped BaF_2 single crystals would be the important material for use in the electromagnetic calorimeter for the SSC. The effects of other rare-earth doping on the scintillating properties of the BaF_2 will also be explored.

China is rich in oxides, chlorides, fluorides, and other compounds of rare-earth metals that are available for research and development. Thus, a more systematic study of rare-earth fluoride crystals at SIC, with focus on the exploration of new scintillation materials for the SSC, is necessary. This work will be carried out on CeF_3 and LaF_3 crystals because these compounds are less expensive than other rare-earth compounds.

The manpower devoted to this research and development program will total 25 to 30 full-time equivalents each year for three years. In addition, the program will involve technical personnel and workers at SIC. Based on past experience, we expect an average of 8 to 10 additional full-time employees to be working on the program at any time.

B.6. Research and Development Program

The R&D program for the BaF_2 detector is a follow-on of the generic R&D program on BaF_2 crystal properties, production, and calibration in progress at Caltech and the Shanghai Institute of Ceramics (Ref. VI.9). The detector development will be carried out over three years (1990 – 1993), and will focus on the following issues:

- mass production and quality control of large crystals
- uniform light collection from crystals
- doped crystals
- crystal radiation hardness tests
- basic crystal research
- fast UV photodevice insensitive to the magnetic field
- fast shaping electronics
- digital electronic readout and trigger
- prototype crystal array
- precision calibration methods

B.7. Other Materials

Although at present BaF_2 represents the favored option for a crystal electromagnetic calorimeter, we are also keeping abreast of other developments.

For example, another approach is the use of Cherenkov radiation. As an example, the properties of KRS-6 (70% TlCl + 30% TlBr) are shown in Table VI.2. The transmission of the KRS-6 crystals, which have properties similar to lead glass, is reduced by less than 2.5% as a function of wave-length (400 to 800 nm) after irradiation with 100 Mrad of γ-rays.

Because of the low photoelectron yield (about 1500 photoelectrons/GeV), amplification is needed. Hence, the readout method in a magnetic field must be developed. An R&D program for KRS-6 is in progress at ITEP to answer these questions. The first application of KRS-6 in high energy physics will occur at HERA. The luminosity monitor and electron tagger at H-1 will use KRS-6 for an electromagnetic shower detector. The behavior of KRS-6 under realistic experimental conditions will be followed closely.

C. LIQUID XENON OPTION

C.1. Overview

The liquid xenon electromagnetic calorimeter uses layers of photodiodes to read out the scintillation light. Photons and electrons with an energy above a few GeV can be detected with better than 0.5% energy resolution and better than 2 mm spatial resolution. Also, accurate measurement of the three-dimensional shower profile can be used to distinguish a single γ from γ's originating from π^0 decay. The photodetector and electronics can be calibrated using 5.5 MeV α particles.

A common concern about using a homogeneous electromagnetic calorimeter is that it may spoil the jet energy resolution, mainly due to the large fluctuation of the neutral pion content inside a jet. Monte Carlo results show that due to the behavior of scintillating liquid xenon at high-ionization densities (Table VI.6), the relative response to electrons and pions (e/π ratio) can be adjusted close to 1. The properties of xenon as an absorber for high-resolution electromagnetic showers have been demonstrated recently with a 40-liter ionization detector (Ref. VI.10) and liter size scintillating detectors (Ref. VI.11).

C.2. Description of the LXe Calorimeter

The main components of the xenon detector are:

- 15 m^3 detector absorber/radiator ellipsoid, covering $|\eta| \leq 3.0$ with 22 radiation lengths of LXe,
- 72 000 photodiode-DAQ chains, and
- a cryogenic system.

Figure VI.5 is a schematic view of the xenon calorimeter, which consists of a hollow ellipsoid filled with 2.4×10^4 cells. Layers of UV photodiodes will measure the longitudinal and transverse shower development. The full detector is composed of two independent half shells bolted to a vertical plate located at the midplane. The overall dimensions are 5.2 m in length and 2.8 m in diameter. The very large heat capacity coupled with good thermal insulation provides for an inherently stable system. A breakdown of the external support systems triggers the pressure-assisted, gravitationally driven transfer of xenon to a LN-cooled storage tank.

Each cell of the xenon counter (Ref. VI.12) includes photosensors, UV reflectors, preamplifiers, and cables; a schematic of one cell is shown in Fig. VI.6.

The UV photosensors measure the UV light signals from xenon (170 nm). The photodiodes currently used for the prototype studies by the LXe detector R&D group (Ref. VI.13) are either 1×1 cm^2 prototypes from Hamamatsu (Refs. VI.14,VI.15) or 5-cm-diameter laboratory models made at Waseda University (Ref. VI.16). Both have rise times of about 10 ns, a quantum efficiency of about 70% at 170 nm, and work directly in the xenon liquid. The photodetectors are inherently insensitive to the value and the direction of the magnetic

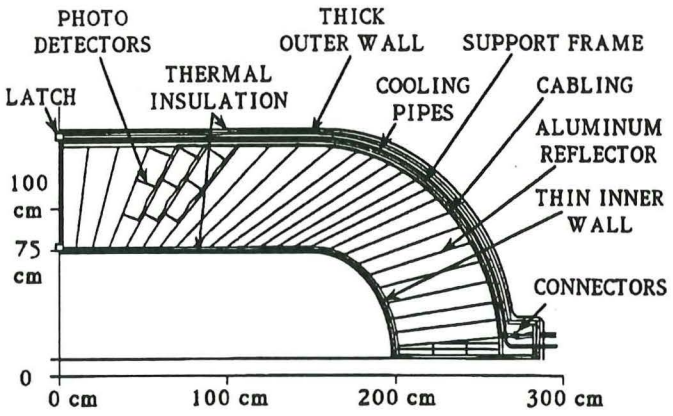

Fig. VI.5. One quarter of the olive shaped scintillating Xenon Calorimeter System.

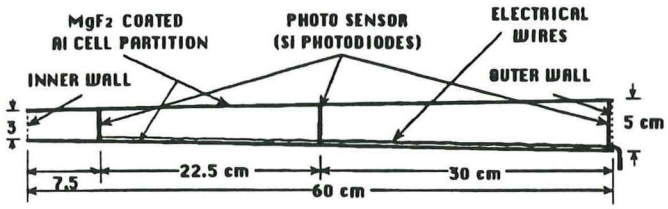

Fig. VI.6. Schematic of a single cell showing 3 photo detectors for longitudinal shower measurement.

fields. The signal from the scintillation light of electromagnetic showers exceeds that from direct ionization by more than two orders of magnitude. This allows for a direct sampling of the longitudinal shower development.

The UV reflecting cell partition functions as the optical insulators of the towers whose sizes are determined by the angular resolution (160 ϕ and 150 η intervals). The cell walls are completely transparent to the shower development (i.e., unobtrusive to the energy measurement) yet reflect UV light uniformly. There are no cracks for particles to sneak through. Ultraviolet reflectors made of 100-μm kapton foil coated with Al and MgF_2 with a reflectivity of about 85% (Ref. VI.11a) have been tested. As with tapered crystalline absorbers, a homogeneous longitudinal response can be expected by a modulation of the reflective properties of the walls.

C.3. Status of Prototype Work

The present development program (Ref. VI.13) aims at measurement of fully contained 100 GeV electron showers with high precision and reproducibility using a 5×5 matrix of cells, as shown in Fig. VI.6. From experiments on 1000-cm^3 liquid xenon detectors (Refs. VI.11, VI.14, VI.16) (Fig. VI.7) with heavy ions and radioactive sources, we conclude that energy loss in liquid xenon is transferred up to extreme ionization densities with high efficiency into scintillation light. The photoelectron yield in LXe is 50 000 for 5.5 MeV α particles or 10^7/GeV (Refs. VI.14, VI.15). A typical spectrum has a width of 6 to 8%

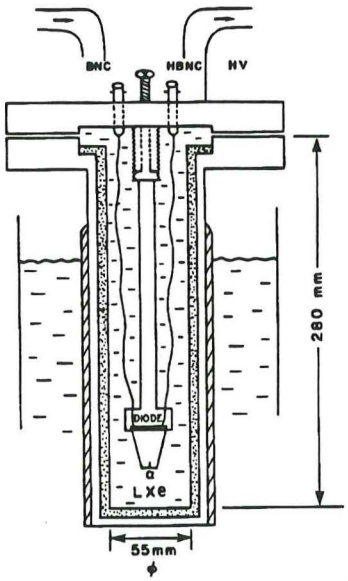

Fig. VI.7. A typical test cell used by M. Miyajima, S. Sugimoto and M.P.J. Gaudreau [Refs. VI.14, VI.15]. The distance between the diode and α can be varied up to 26 cm.

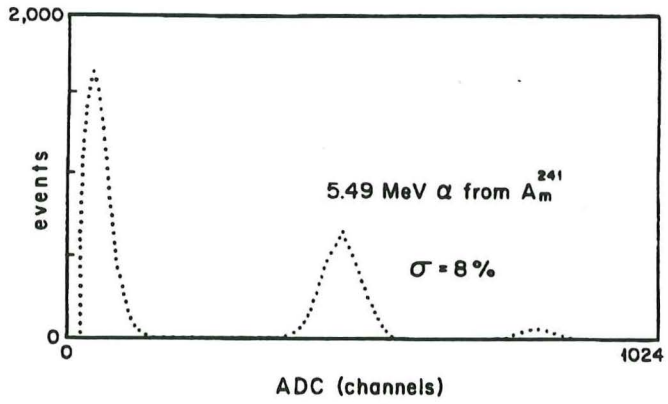

Fig. VI.8. Scintillating LXe signal (middle), pedestal (left) and a test pulse (right) using 5.49 MeV α source by T. Doke et al [Ref. VI.16].

(Refs. VI.14, VI.15, VI.16) and is very stable (Fig. VI.8); therefore, it can serve as a reliable calibration for the experiment. There is no indication of any light attenuation in liquid xenon over a distance of 7 cm in a prototype cell (Fig. VI.7). The data are consistent with the variation expected from light acceptance and 85% random reflection effects (Ref. VI.11a, VI.14).

When α particles are stopped in the diode in vacuum, the measured output pulse height equals that theoretically expected. The half width of the leading edge (high-energy side) of the spectrum is only limited by electronic noise, whereas the half width for the low-energy side is increased by the energy levels of the ^{241}Am source and the straggling of the α particles through the material. The energy resolution determined by the leading edge of the pulse height distribution is 0.5% with 3 μs and 1.5% for 20 ns (Ref. VI.14) gate time. This serves as a precision calibration for the diodes, electronics, and absolute energy scale.

C.4. Jet Energy Resolution

LXe saturates at the level of dE/dx about 10 GeV/g cm^2. In LXe, the light output per unit energy loss, dL/dE, for relativistic heavy ions, is much larger than dL/dE of electrons because of the higher density of electron-ion pairs and thus more light from recombination. These effects compensate well the nuclear energy loss due to hadron nuclear energy loss and make the e/π of LXe close to 1 (Ref. VI.12). This was checked using the GEANT Monte Carlo code to compute the excess energy deposited (within 15 ns) by slow nuclear fragments produced from 10, 50, and 100 GeV pions incident in a 3×3 matrix of 60-cm-long LXe cells. We plan to experimentally confirm this by beam testing a prototype detector together with a compensating calorimeter.

C.5. Xenon availability

Liquid xenon is principally produced as a by-product of the cryogenic liquefaction of air. Other methods include absorption-mesh, nuclear, and combined techniques. One liquid liter equals 518 gaseous liters at standard temperature and pressure (STP). Current xenon production capacity is limited by demand, not by production. Based on the number of large liquid oxygen production facilities in the United States and worldwide that can be adapted to produce xenon, there is plenty of production capacity available for our needs. However, as the xenon production schedule is quite long, advance planning is required, and R&D is needed to find the best xenon production method: air separation, membrane, absorption, and nuclear, or a combination of several methods.

C.6. Summary

Experimentally, the data on a xenon electromagnetic detector show that:

- Large signals and good resolution (10^7 photoelectrons/GeV) are achievable.
- Xenon is homogenous and radiation resistant.
- α sources can be used for calibration.
- 3-D shower measurement is possible.
- e/π can be adjusted.
- There are no cracks and little dead space.

However, more R&D is still needed on the following:

- The attenuation length for UV scintillation light with UV light source.
- Uniform light collection efficiency.
- Radiation resistance of diodes.
- Low noise, wider dynamic range, faster amplifiers.
- Signal shape is different for electrons and α particles, (requires an inexpensive flash analog to digital conversion with ten 5-ns bins (50 ns) to measure pedestals, pile-up, and e/π)

- Liquid temperature control: ± 1°C.
- New production methods for xenon, e.g., nuclear, absorption, cryogenic or combined. Currently, xenon is expensive, with a long production schedule.
- Purification system to be scaled from 0.1 to 45 tons.

C.7. Milestones

The major milestones in our R&D program are:

- September, 1990: Beam test of full size prototype cells.
- Third Quarter 1991: Beam test of a 5×5 prototype with a compensated hadron calorimeter to show $e/\pi = 1$.
- Third Quarter 1992: Beam test of 10×10 prototype.

To conclude, the superior intrinsic physical properties of scintillating liquid Xe encourage us to take the technical challenge, and it may be a promising option for a precision electromagnetic calorimeter at the SSC.

R&D Funding Request

The goal of the R&D program is to develop arrays of BaF_2 and LXe and their fast readout, to test and calibrate the arrays at high-energy electron/pion beams together with an L* hadron calorimeter prototype. We will also test the arrays at the calibration RFQ facility to be built. The detailed breakdown of the budget is listed in Table VI.4

Table VI.4. Cost of the L* EMC R&D Program

Item	FY 1991 (K$)	FY 1992 (K$)
BaF_2 Crystal Array Components	**513**	**458**
160 Production-size BaF_2 crystals ($3.5/cm^3)	239	239
160 Hamamatsu phototubes	53	53
160 Analog electronics channels	48	48
160 Digital readout (VME) channels	103	48
Carbon fiber support structure	70	70
LXe Array Components	**375**	**540**
LXe (5k$/liter)	100	200
400 Silicon diodes	35	105
400 Analog readout channels	60	60
400 Digital readout channels	105	85
Mechanical structure	75	90
Materials and Service	**582**	**704**
Crystal cutting, polishing, uv reflector	85	60
Crystal array, temperature control and monitoring	75	75
BaF_2 Radiation damage test and runs	40	40
BaF_2 Cosmic ray and gain monitoring setups	27	9
BaF_2 Test beam setups and runs	45	95
LXe Purifier	75	90
LXe Support structure and extractor	100	200
LXe Test beam runs	50	50
RFQ: Target parts, assemblies, accelerator setup	85	85
Equipment	**750**	**665**
BaF_2 UV/VIS photospectrometer	30	
BaF_2 Fast scopes, pusle generator	55	
BaF_2 High and low voltage pwr supplies	40	40
RFQ Accerlerator calibration system	625	625
Personnel (FTEs)	**600**	**600**
BaF_2 1 Mech. eng. and 3 technicians	300	300
LXe 1 Mech. eng. and 3 technicians	300	300
Travel	**125**	**135**
ANNUAL TOTALS	**2945**	**3102**

References

[VI.1] J. Gunion et al., in "The Higgs Hunter's Guide", UCD Preprint, 89-4 (1989). M. Chen et al., in Proc. of the Summer Study on High Energy Physics, Snowmass, 1988, p.806.

[VI.2] P. Schotanus et al., **IEEE-NS34** (1987) 272 and NIM,. **A281** (1989) 162.

[VI.3] C.L. Woody et al., **IEEE–NS 36** (1989) 536.

[VI.4] P. Schotanus et al., **Nucl. .Instr. and Meth. A238** (1985) 564; and Kobayashi et al., **Nucl. Instr. and Meth. A270** (1988) 106.

[VI.6] R.Y. Zhu et al., Super Collider I, Plenum Press, (1989), 587; H. Ma et al., NIM, **A281** (1989) 469 and **A274** (1989) 113.

[VI.7] F. Ajzenberg-Selove, Nucl. Phys. A475 (1987) 1; H.B. Willard et al., Phys. Rev. 85 (1952) 849, and G. Gorodetzky et al., Nucl. Phys. A91 (1967) 113.

[VI.8] H. Bergstroem et al., Penn State, PSV/TH/63, March 1990.

[VI.9] H. Ma et al., "Development and Precise Calibration of a High Energy Barium Fluoride Crystal Array", Caltech, **CALT–68–1517**, 1988.

[VI.10] A. Baranov et al., CERN-EP/90-03.

[VI.11] (a) M. Miyajima et al., (b) T. Doke et al., etc., Japanese Physical Society Meeting at Osaka, Japan, March, 1990, and Liquid Ar and Xe Conf. at Waseda, April, 1990.

[VI.12] M. Chen et al., CERN 89-10, ECFA 89-124.

[VI.13] M. Chen et al., SSC Detector Subsystem Proposal, 1989.

[VI.14] M.P.J. Gaudreau, M. Miyajima, S. Sugimoto. et al., Osaka Univ. Ouins, Rep., 90-01, May 8, 1990..

[VI.15] S. Sugimoto et al., Osaka University, Rep. 90-02, May 1990.

[VI.16] T. Doke et al., MITLNS Tech. Rep. no. 175, May 1990.

A. INTRODUCTION

The L* central tracker (Fig. VII.1) will measure charged-particle momenta and the coordinates of the event vertex. It is made of silicon microstrip detectors from 10- to 40-cm radius and drift tubes plus scintillating fibers from 40- to 75-cm radius. The angular coverage is 5°–175°. The momentum resolution is $\Delta P/P$ = 50% at P = 400 GeV at 90° as shown in Fig. VII.2. The vertex resolution is 20 μm(r-ϕ) and 1 mm (z).

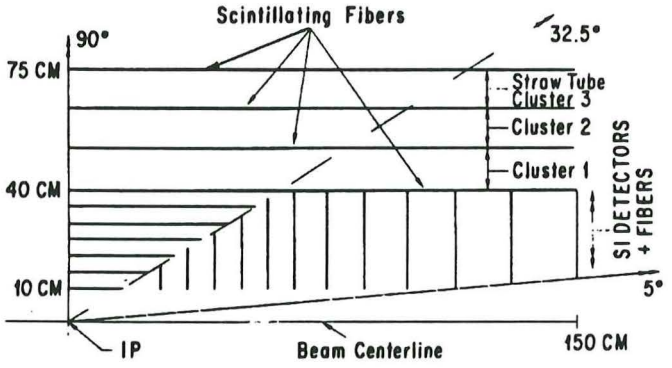

Fig. VII.1. Central tracker layout.

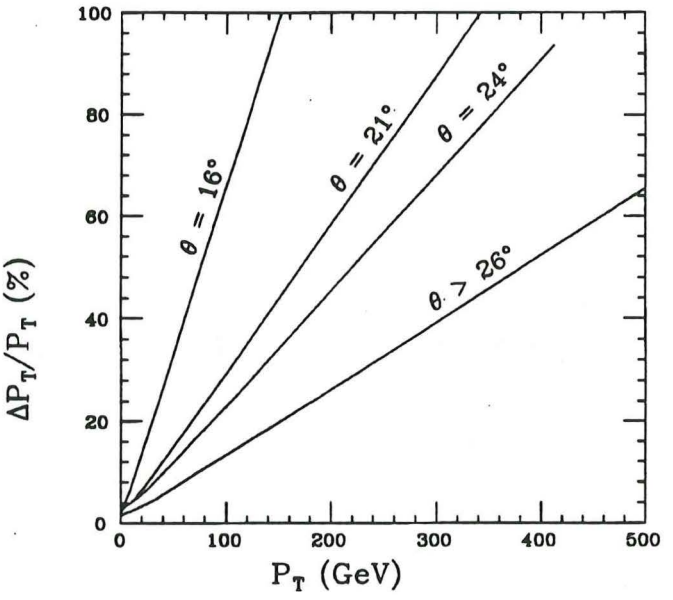

Fig. VII.2. Momentum resolution of the central tracker. The straw tubes cover $\theta > 26°$ all layers.

The central tracker is necessary to identify muons, electrons, and photons, as well as to separate a new source of leptons or photons from QCD. Central tracker data will be used for muon identification by momentum and angle matching with data from the outer muon detector, and for electron identification by momentum and position matching with the electromagnetic calorimeter data. Tracker data will also be used to measure the charge-sign of the electron and distinguish electrons from photons. In order to measure lepton isolation from hadronic clusters (Ref. VII.1), the central tracker is also designed to have good pattern recognition.

The ability to resolve individual beam bunch crossings in time together with the measurement of the z-coordinate of the event vertex will determine the number of collisions occurring in a triggered beam crossing and which collision produced the individual charged particles. For events that contain more than one lepton, it is crucial to know that they came from the same pp collision.

To optimize the design parameters, we performed Monte Carlo calculations of physics signatures of

$$pp \rightarrow ZZ + X,\ WW + X,\ W' + X,\ Z' + X,\ \text{Higgs} + X$$

and backgrounds

$$pp \rightarrow q \text{ or } g + X,\ t\bar{t} + X,\ b\bar{b} + X,\ W + X,\ Z + X$$

These calculations have been performed with ISAJET and GEANT. About 3×10^6 events were generated in total. Some of the results are listed in Chapter X.

B. RADIATION CALCULATIONS

The neutron flux in the electromagnetic and hadron calorimeter has been calculated for the L* detector geometry and the return neutron flux into the central detector volume from the calorimeters (using the BaF_2 option for the electromagnetic calorimeter) has been determined. The L* geometry was simulated in two stages. We used the GEANT code with ISAJET to produce minimum bias events from which we determined the angular and energy distributions of the hadrons entering the calorimeters. For these calculations we were concerned with the typical collision events since the neutron flux in the detector will be the time average of a number of collider events. The LAHET code (Ref. VII.2) was used to follow the hadrons through the calorimeter. All secondaries produced were transported until they fell below some threshold (usually 0.1 to 1 MeV for charged particles or to 20 MeV for neutrons). Neutrons produced as a result of the intranuclear cascade were then transported by the MCNP code (Ref. VII.3) to thermal energies or until capture. With this procedure we were able to understand the time variation of the neutron energy distribution. The equilibrium flux of neutrons in the detector was then determined by adding the neutrons produced at each event to the flux that remained from previous events.

In general, the neutron flux in the calorimeters and central volume is due to hadrons with momenta less than 5 GeV/c. Of all hadrons, 85% are pions. The neutron flux distributions as a function of the incident hadron momentum was calculated for the L* detector assuming the central tracker extended to the boundary of the electromagnetic calorimeter. However, it was anticipated that a soft neutron shield in front of the calorimeters might

be necessary. A composite shield of boron and polyethylene [0.13 radiation length (i.e., 5 cm thick)] in front of the calorimeter was also investigated. We determined the flux distributions for all neutrons above 1 eV and above 100 keV. The cross section for dislocations in silicon exhibits a sharp increase above 100 keV (see Fig. VII.3) so the flux above 100 keV is a more appropriate indicator for damage to these devices.

A typical time spectrum for the neutrons in the central volume is shown in Fig. VII.4. This distribution measures the neutron flux crossing an annular disk perpendicular to the beam direction and 125 cm downstream of the interaction point for a 2.5 GeV pion entering the calorimeter in the rapidity interval 2–3. The maximum neutron flux occurs 30–40 ns after the interaction time. The curve for all neutron energies exhibits a long tail while the curve for those neutrons with energies greater than 100 keV falls more sharply with time. This is a consequence of the softening of the neutron energy spectrum as the neutron undergoes repeated inelastic scattering events in the BaF_2. Also plotted is the curve for the detector with the 5-cm absorber between the central detector and the electromagnetic calorimeter. There is a factor of three reduction in the flux maximum and a pronounced decrease in the tail of the distribution. The hydrogen in the polyethylene is very efficient in reducing the neutrons energies to below 100 keV.

The total neutron flux per event is obtained by folding the hadron spectra with the neutron flux per hadron.

To get the final equilibrium neutron flux in the central volume one must add the neutron flux that remains from previous SSC events. The result is shown in Fig. VII.5.

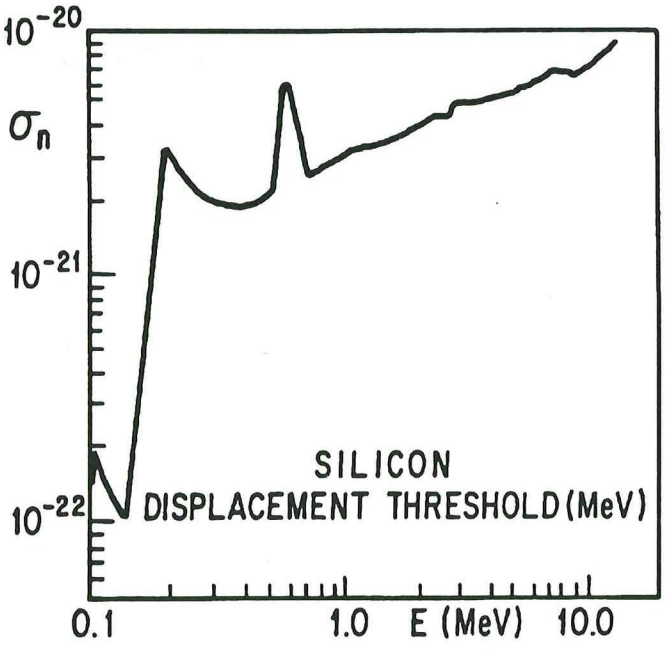

Fig. VII.3. Displacement cross sections as a function of neutron energy for silicon.

The calculations of the neutron fluence in the central tracker volume show that levels less than $10^{12}/cm^2$ per year can be achieved if a moderate amount of polyethylene or similar material is placed at the outside boundary of the central tracker. These levels set the development goals for the radiation resistance of the selected detector and electronics components. The same procedure was used to predict the neutron current in the calorimeters in the rapidity interval 2–3. The total neutron

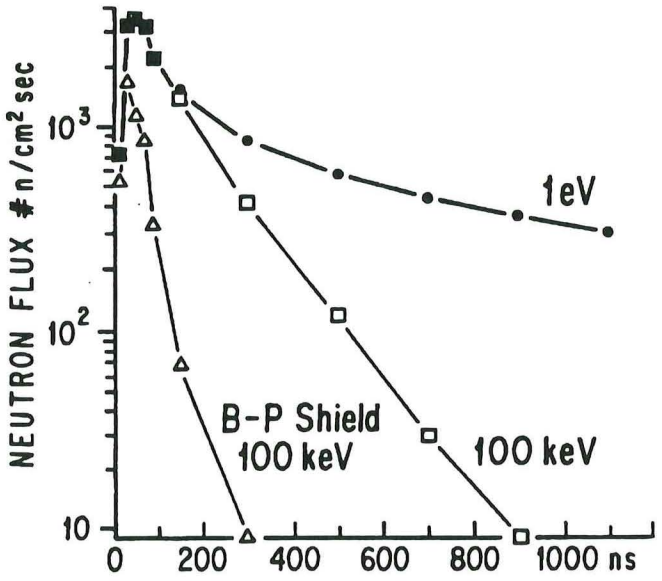

Fig. VII.4. Typical time spectrum of neutrons from one collision in the central volume for an annular disk at 125 cm downstream of the interaction point.

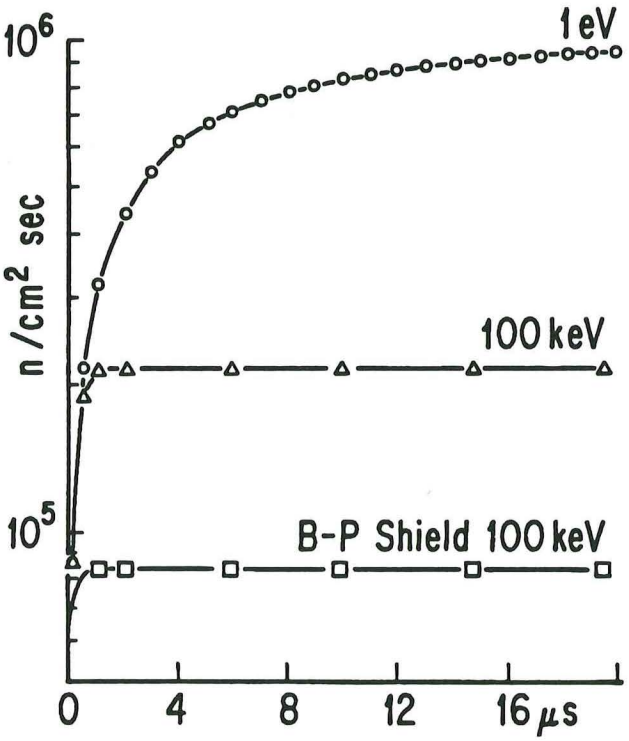

Fig. VII.5. The time evolution of the equilibrium neutron flux in the central volume. The first interaction occurs at time zero.

flux/cm^2 per SSC year with energies greater than 100 keV at depth of 12.5 cm in the BaF_2 varied from 2.6×10^{13} to 3.8×10^{13} across the rapidity interval.

C. SILICON DETECTOR

The silicon detectors are reverse-biased diodes finely divided into strips. The strips provide a high-precision position measurement (hit/no hit) in the direction orthogonal to their long axis. The use of double sided detectors (readout strips on both surfaces of the detector) will give two dimensional position information. On one side of the detectors, the strips will run parallel to the z (beam)-axis for the central detector, and radially for the endcap detector. These strips will provide the very high resolution φ measurement needed for the momentum measurement. The strips on the second surface of the detector are canted at a small angle with respect to the strips which determine φ. The less precise position information for the second dimension (z for the central detectors, and r for the endcap detectors) is determined by the strips on both sides of the detector.

The design properties of the silicon microstrip detectors are

- Thickness = 300 μm = 0.0032 radiation length
- Signal collection time ~ 10 ns
- Full depletion operating voltage typically 25–200 V
- 32k electron-hole pairs for a minimum ionizing particle
- Typical rms electronics noise < 1000 electrons
- Strip pitch: 25 μm for inner layers, 50 μm for outer layers
- Wafers covering 30–40 cm^2, cut from 4-in.-diameter ingot
- Wafers mechanically and electrically bonded end-to-end to make a detector 15–20 cm long
- The detectors will be double-sided with 5-mr stereo angle
- High radiation resistance to fluences of 10^{14} neutrons/cm^2 (E > 100 keV), several times higher fluences of minimum ionizing particles, and electronics with comparable or superior resistance
- Front-end electronics mounted on the detectors

C.1. Electronics for Silicon Detectors

The electronics for each strip will consist of a preamplifier, pulse shaper-discriminator, some data processing, local buffering sufficient to cover the second level trigger decision time, and a multiplexed fiber optic readout.

To reduce the interconnection problems, the electronics will consist of either VLSI circuits bonded directly to the silicon detector wafer or the detectors and electronics will be implemented as a monolithic device. First successes in doing this with high-resistivity detector-grade silicon have been reported (Ref. VII.4).

C.2. Radiation Damage in Silicon Devices

Upon exposure of a silicon detector to radiation, some of the incident particles create lattice dislocations in the silicon crystal. Defects found uniformly throughout the entire volume are called bulk effects. There are also effects involving the silicon–silicon dioxide surface layer. At present surface effects are not the limiting factor in the radiation tolerance of one-sided detectors. Double-sided detectors involve more intricate processing and structures, and therefore they may be more prone to surface effects than the single-sided devices. Double-sided detectors are produced like VLSI devices, which degrade dominantly because of surface effects. Radiation-hard versions of VLSI are capable of withstanding fluences of 10^{15} neutrons/cm^2 (Ref. VII.5).

Bulk damage has several major components. Degradation in carrier lifetime results in the reduction of the signal amplitude. Increased thermal generation of electron-hole pairs results in a large increase in the leakage current and noise in the detector. Finally, the creation of additional acceptor states in the silicon can slowly change n-type silicon into p-type silicon.

At the charged particle doses expected at the innermost layers of the L* central tracker, we have measured the effect of bulk radiation damage on candidate detectors.

Leakage current increases linearly with the radiation dose (Ref. VII.6). This leakage current shows a very strong temperature dependence. The measurements performed at Los Alamos show about a factor of 2 reduction in the leakage current for every 7°C drop in temperature (Fig. VII.6 and Ref. VII.7).

Figure VII.7 shows electronics damage reflected in the change in threshold voltage after a proton irradiation at Los Alamos of radiation-hardened transistors produced by UTMC (of Colorado Springs).

D. THE STRAW DRIFT TUBES

There will be 80 layers of thin-wall, small-diameter drift tubes in the barrel part of the L* central tracker, from 40- to 75-cm radius.

The drift tubes to be used in L* are based on technology which has evolved over the past several years in experiments at colliding beam facilities and on balloon payloads. They are very simple detectors, being proportional tubes with walls made of aluminized plastic film. The idea of using multiple layers of small cylindrical tubes for precision trajectory measurements was originally conceived for metallic tubes (Ref. VII.8). It was then recognized that the aluminum wall could be replaced with aluminized mylar (Ref. VII.9).

Drift tubes with very thin walls have been developed within the past few years to reduce the hard single scattering, multiple scattering, and photon/electron conver-

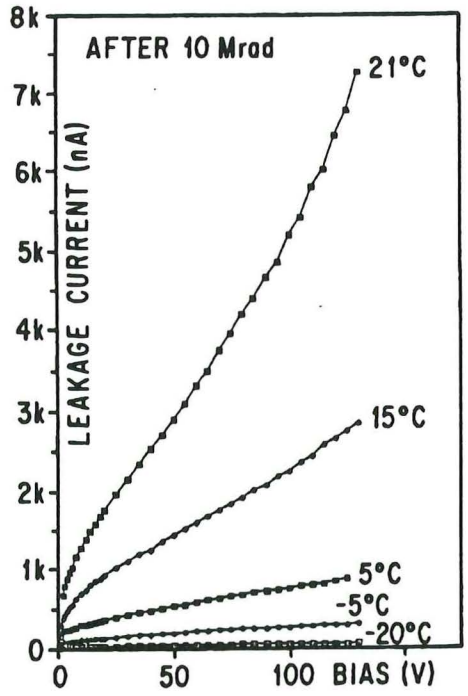

Fig. VII.6. Leakage current in silicon detectors after a 10 megarad exposure to 800 MeV/c protons, as a function of detector temperature.

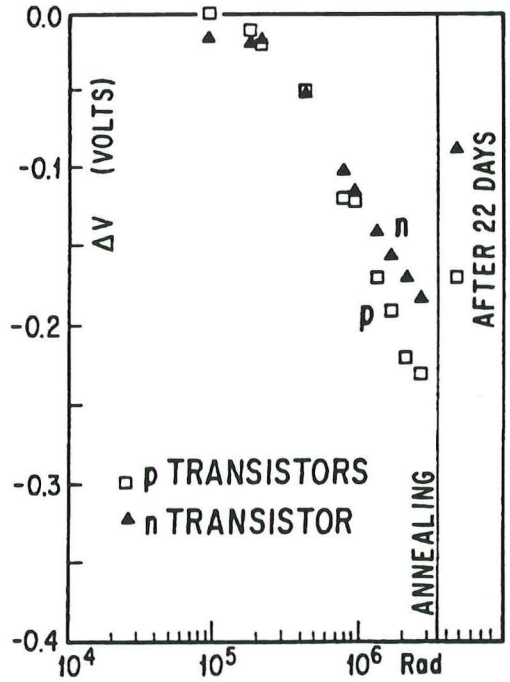

Fig. VII.7. Effect on threshold voltage of transistors after proton irradiation and room temperature annealing.

sion problems associated with excess material. The group at Boston University (Refs. VII.10–11) chose a wall material having a thickness of 25 μm (12.5 μm of mylar, over a 12.5-μm layer of conducting polycarbonate coated with 1000 Å of aluminum) after having experimented with even thinner walls, which were susceptible to wrinkling effects. The Boston drift tubes were used in a balloon experiment (PBAR) to measure antiproton abundances, and achieved 84-μm resolution on the bench, and 109-μm resolution during an actual flight with a nonuniform magnetic field of order 10 kG, in an environment which had large variations in temperature and gas density. The gas used was a 50-50 mix of argon and ethane at 1 atm absolute pressure.

D.1. Straw Tube Tests

We have made several SSC prototype detectors with small-diameter (3.8-mm), thin-wall straw drift tubes using 20-μm-diameter gold-plated tungsten wires tensioned at 50 g. In tests with cosmic rays through five rows of tubes the standard deviation of the residuals was found to be 69 μm (Fig. VII.8), implying a single tube resolution of 89 μm, using Ar-ethane (50/50).

A number of gases satisfy the speed requirements of the SSC, most of which have CF_4 as a principal component (Ref. VII.12). Speeds of the order of 100 μ/ns are readily attainable, implying drift times for a 3-mm-diameter straw of about 15 ns. Good resolution has been achieved in 4-mm-diameter straws with CF_4 + 20% isobutane (105 μm for 1 atm pressure (Ref. VII.13).

We have explored the issues involved with the use of thin straws and CF_4 in an SSC radiation environment (Ref. VII.14). The prototype for these studies used straws which were 30 cm in length. They were operated in the Fast Spectrum Facility at the MITR-II Research Nuclear Reactor at MIT. We exposed our tubes to 4×10^{14}

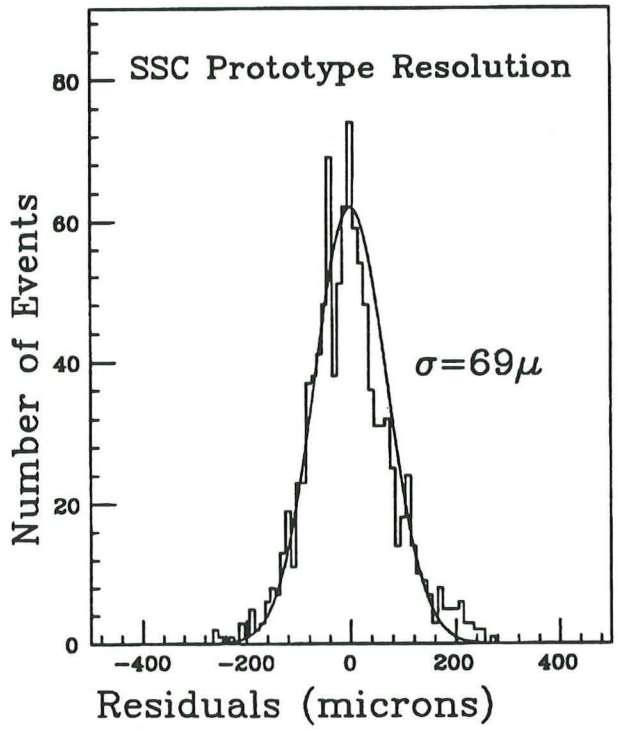

Fig. VII.8. Track residuals from a prototype straw tube array tested with cosmic rays.

neutrons/cm^2 (fission spectrum) at the MITR-II and found the performance of the tubes to be stable. We monitored singles rates (5 MHz per tube), coincidence rates (2 MHz per tube), tube currents (15 μA per tube for 2200 V in pure CF_4), and pulse heights from Compton electrons. Figure VII.9 shows ^{55}Fe pulse height spectra taken before, during, and after the run. It is seen that gain shifts do not exceed the 1% level. A prototype detector with 1-m-long straw has been constructed and operated to study electrostatic stability and mechanical alignment.

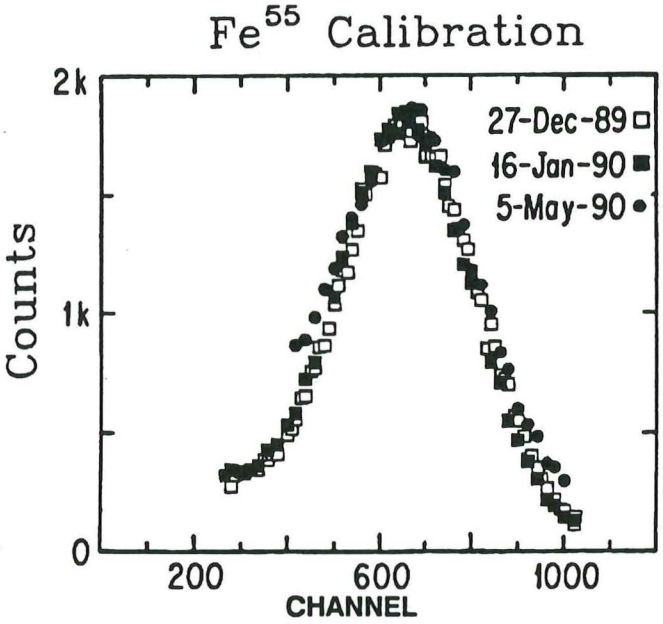

Fig. VII. 9. Fe-55 pulse height spectra from straw tubes taken before, during, and after exposure to 4 $\times$ 10^{14} neutrons per cm^2.

E. SCINTILLATING FIBER DETECTOR

Spiral-wound scintillating fibers are placed at the outer radius boundaries of each straw tube cluster. These fibers provide z-coordinate information. The fiber system totals approximately 50 000 channels. For mechanical stability the layers of scintillating fibers will be mounted into the carbon fiber composite supports described in Sect. F. To avoid cross-talk, the fibers will be covered with an external absorber. The four layers of fibers will have stereo angles of $-10°$, 0°, and 0°, $+10°$. The z resolution at the vertex is $\sim$1 mm (see Fig. VII.10). It is estimated that this configuration will be able to resolve tracks of about 2 mr separation and to determine the z position of over 98% of tracks entering the detector.

We have identified the Hamamatsu venetian blind multichannel photomultiplier as the most promising readout option. The high light output of the 1- to 2-mm fibers makes less developed and more costly technology such as avalanche photodiodes and solid state photomultipliers unnecessary. Solid state photomultipliers would require cryogenic hardware, which cannot be easily accommodated in the compact design of the central tracker. The multichannel photomultiplier is currently being studied at UCLA (Ref. VII.15). Together with the UCLA group, we plan to carry out necessary three-dimensional electrostatic modeling and develop a more compact tube suitable for the L* design.

The speed of the scintillating fiber system permits its use as a tracking system, even at SSC luminosities of 10^{34} cm^{-2}s^{-1}.

Optimization of the central tracking detector configuration will be studied during the next year.

F. ENGINEERING AND MECHANICAL DESIGN ISSUES

Figure VII.11 displays an elevation view of the silicon and straw tube detectors and the basic support structures.

Since the silicon detectors have fine segmentation and high precision, the mechanical design concentrates on positional accuracy and extreme stability under experimental conditions. The main issues are achieving 5-μm wafer positional stability with no periodic adjustments, selecting support materials which meet all design considerations while remaining below 2% radiation length in radial density, managing waste heat from wafer electronics with no compromise of the position accuracy of the system, achieving alignment and manufacturing feasibility, and satisfying the requirement of radiation resistance in structural strength and dimensional stability.

The positional stability of the intricate wafer array may be influenced by many factors such as creep, distortion

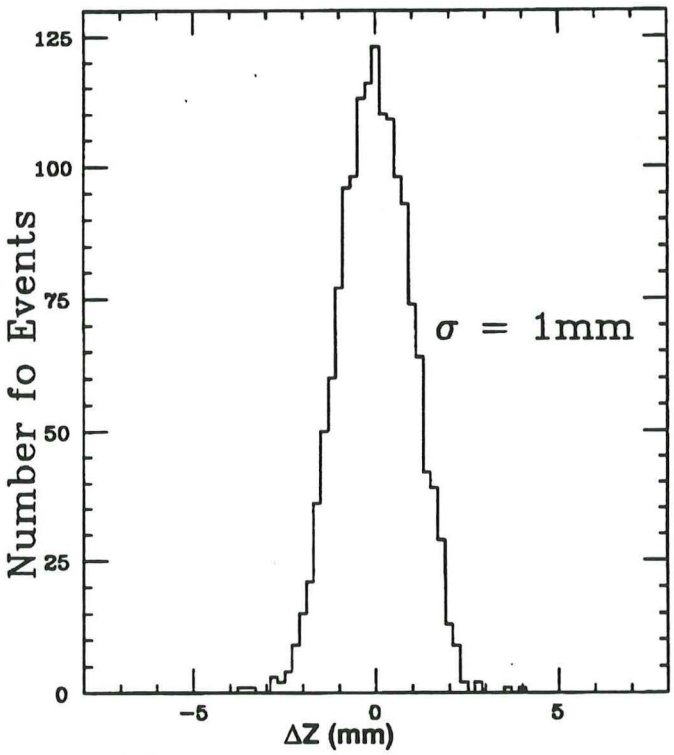

Fig. VII.10. Vertex z-resolution from the silicon and scintillating fibers.

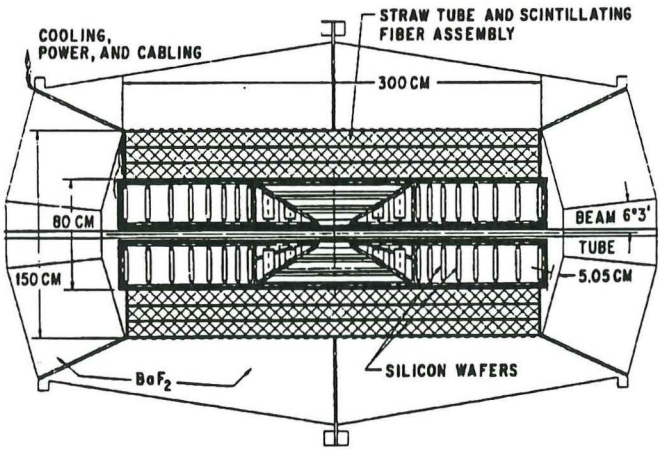

Fig. VII.11. Elevation view of the design of the central tracker with support structures.

of the support structure from thermal gradients, and material property changes over time. Many materials lack the radiation resistance to fulfill the stability requirements. Traditionally, radiation exposure testing has focused on effects associated with material strength, not molecular structural changes that may lead to creep and reduction in stiffness.

The silicon detector is designed to operate at a temperature between –20°C and +10°C. The detector electronic heat load is 1 mW/channel. The heat flux is 2.5 W/cm^2. The radiation exposure is expected to be 10 Mrads over a 10-year service life. Structures total 2% of a radiation length except in limited regions.

F.1. Silicon Subsystem Conceptual Design

The silicon wafers in the central and forward regions are edge-bonded into 16-cm-long strips. Electronics for power and signal processing are mounted at each end of the long strip. The silicon layers in the central and forward region are supported at discrete points between the end supports. The ends of the silicon layers are bonded to rings at each end. The rings provide support and passage for an internal heat pipe. Cooling fluid is wicked to an area directly beneath the electronic package. Heat flows through this thin walled area and evaporates the cooling medium. This technology has been employed extensively in Los Alamos space and reactor projects. It simplifies the process of cooling the large number of individual wafers. By minimizing the conductive path, the ~2.5 W/cm^2 heat load associated with the electronics package can be effectively dissipated with a minimal temperature gradient. Distortions in the silicon layer sandwich are avoided by minimizing the thermal gradient and through an appropriate material choice for the cooling ring. Since the silicon subassembly will likely be operated at temperatures well below room temperature, coefficients of thermal expansion for materials comprising this assembly must be carefully selected and in some cases tailored to specific values.

The long strip wafer technology imposes a substantial local heat load, possibly as high as 20 kW. The system will be cooled with an integrated network of heat pipes. The heat pipe network is capable of thermally equilibrating the entire silicon detector array. Our design goal for structure temperature uniformity is 0.25°C.

The rings are mounted onto the support structure of the central region. These units are supported on kinematic supports to avoid introducing distortions. Consideration will be given to using a support structure material that has a zero coefficient of thermal expansion, for example, graphite epoxy or a metal matrix composite.

The central and forward detector regions must be supported by a frame that is highly stable throughout the life of the detector. The frame network would be assembled in subsections to provide a jigging fixture when assembling the silicon modules. We plan to assemble the central detector region first, and then add the adjacent forward regions.

The entire silicon tracking subsystem must be enclosed in a pressure vessel capable of confining the heat-pipe working fluid. Kinematic supports will be used to isolate the silicon tracking subsystem from the vessel external pressure load. To ensure the 5-μm stability, these external loads must be isolated. The internal operating pressure of this enclosure will track the vapor pressure of the heat pipe coolant. Once the heat pipe working fluid and cooling system operational scheme has been established, uncertainties in the design pressure will be eliminated. The baseline design approach for the external enclosures is a lightweight honeycomb graphite composite. The condenser for the integrated heat pipe system will be part of a heat pump system with sensitive temperature control. The heat pump will reject up to 20 kW and must be capable of stabilizing the condenser sink temperature against cyclic thermal drifts greater than 0.1°C.

F.2. Material Options

The material selection is driven by three primary factors, 5-μm material stability, 2% radiation length restriction, and radiation resistance in the presence of chemical agents. To achieve these goals, application of the latest composites and high stiffness-to-weight ratio construction techniques will be required. Our reference design draws upon all these possibilities. Candidate composites will have their coefficient of thermal expansion tailored to either match the thermal expansion of silicon or set to zero, as the case requires. The ultimate material selection and the general structural arrangement will be driven most by the radiation length restriction.

F.3. Engineering Program Plan

The first phase comprises a 3-year development effort culminating in testing of a full operational tracking system module. Full integration tests of the powered module will be completed and the stringent stability requirements verified. Phase 2 consists of the engineering design and fabrication activities throughout the construction phase. Considerable emphasis will be placed on completing the detailed design of the system, and incorporating design changes as needed to interface appropriately with adjacent detectors. The engineering emphasis will then shift to manufacturing liaison and quality control activities. Test and evaluation of the entire system will be completed in the last program year, Phase 3. Qualification tests will be performed in a laboratory environment, and individual component systems will be thoroughly tested. Design adjustments will be made if needed during this test phase. Subsequent to these acceptance tests the silicon subsystem will be disassembled into manageable subassemblies for transport to the SSC site.

F.4. Straw Tube and Fiber Engineering Design

The straw tube and scintillating fiber detector assembly is composed of three clusters approximately 3 m in length. Overall there are approximately 75 000 straw tubes nested together in a close packed array. To maximize stiffness and maintain exacting dimensional control, the entire array will be constructed as one unitized structure. We plan to separate the three clusters of tubes with very thin but stiff graphite/epoxy composite shells. These shells will have a nominally zero coefficient of thermal expansion and will provide the detector transverse structural stiffness and serve to oppose the compressive load created by the 75 000 tensioned wires.

The 3-m-long wires will be supported at two points along their span, resulting in 1-m-long unsupported lengths. Prestressing the wires to a 50-g tension will minimize wire sag.

Terminating the wires on the external face of a honeycomb sandwich end cover, while making electrical connections to the electronic circuits, also serves to transfer the combined 3750-kg load to the stiff graphite composite shells. Our analysis shows that the shell deflection under this load is nominally 300 μm, with 375-μm sandwich facings. The sandwich end plate and shells preclude inducing any strain on the straw tubes, while enhancing the dimensional stability of the overall detector.

Precision can be built into the straw tube bundle array by utilizing advanced composite construction techniques and conventional manual composite fabrication procedures. An important aspect of the procedure will be the construction of a precision tubular mandrel 3 m long. The axial dimensional control of the straws and the circumferential pattern will be strongly influenced by the inherent accuracy of the mandrel tooling.

The first step in constructing the straw tube bundle array is to apply the innermost graphite epoxy shell around the precision mandrel. Onto this cured shell surface one would build the straw tube array. The external surfaces of the straw tubes will be bonded with low-density adhesive. Fillers may be used to reduce the radiation length associated with the adhesive, as well as to serve to strengthen the composite bundle. Chopped graphite fiber filler is one candidate that also has the advantage of reducing the thermal expansion coefficient of the epoxy matrix.

After completing the first tube cluster, the next step would be fabrication of the first intermediate graphite/epoxy shell. At this juncture, the shell would be made in two layers, and in between the two shell layers we would sandwich the 4-mm-thick scintillating fiber mesh. This step would positively locate and hold the fiber mesh throughout the detector life. A low temperature curing adhesive would be used so as not to damage the fibers. Successive layers would complete the straw tube graphite shell composite array. A dimensionally stable, stiff structure would be the desired end result. Experimentation would be used to determine if one final curing cycle can be used to achieve the overall assembly. An alternative would be to cure after each successive tube bundle array is completed.

The unitized straw tube detector assembly would be mounted onto the silicon tracking subsystem shell enclosure. The straw tube detector will be optically aligned within 25 μm to the silicon tracker as a single unit. Implementation of this single composite straw tube assembly design concept will avoid alignment of three separate concentric straw tube arrays to the inner silicon tracking subsystem.

G. INITIAL R&D

Los Alamos National Laboratory has been participating in the silicon tracker and the straw tube major subsystem research program. As part of this program preliminary and generic studies of structural design and materials and cooling concepts are under way. This work has provided major guidance to the design described here. As part of other Los Alamos efforts, radiation damage studies of candidate silicon detectors and electronics are under way at the Los Alamos Meson Physics Facility, and silicon arrays are in use in high-intensity research as part of Fermilab experiment 789. Boston University has an extensive program in straw tube development and physics research. ITEP Moscow is engaged in scintillating fiber studies as part of research at ITEP and CERN. UCLA physicists are engaged in scintillating fiber and multichannel photomultiplier development in collaboration with Japanese industry. Studies of neutron transport, physics simulations, and pattern recognition and data compaction using general adaptive methods and parallel methods are in progress

at Los Alamos. University of New Mexico and Indiana University will be joining in the central tracker work.

During the first 3 years of R&D for L*, in addition to the current major subsystem R&D, we request support for L* specific development activities as follows in Tables VII.1 and VII.2.

These estimates represent the program for the FY 1991 year. For FY 1992 and FY 1993, we will submit revised requests based upon the detailed technical progress and insights. The end of the 3-year period should result in full-scale prototypes and stability and performance tests (see Table VII.1).

Table VII.1. Summary of Milestones for the L* Central Detector R&D Program

	FY 1991	FY 1992	FY 1993
Si Detectors	• Evaluate detectors	• Select strip length • Test at 10^{14} neutrons/cm^2	• Select final detector characteristics
Si Electronics	• Evaluate front end	• Test prototype front-end and optical link	• Finalize front-end and optical link
Si Structure	• Evaluate materials	• Stability and cooling test of full-scale prototype assemblies	• Finalize manufacturing plan
Straw Detectors	• Select gas • Measure drift velocity and Lorentz angle in 0.75-T field	• Complete tests at 10^{14} neutrons/cm^2 and 1 Coulomb/cm • Finalize design of 3-m-long straws	• Finalize manufacturing plan
Straw Electronics	• Evaluate front end	• Select front-end amplifiers	• Select optical link
Straw Structures	• Evaluate materials	• Complete stability and mechanical design	• Finalize manufacturing plan
Scint. Fiber Detectors	• Evaluate fibers	• Select fibers • Test at 10^{14} neutrons/cm^2	
Scint. Fiber Readout	• 3-D model of photo tube	• Prototype and test compact tube	• Test production tube
Scint. Fiber Structures		• Stability and mechanical tests	• Finalize manufacturing plan
Radiation Damage	• Prototype structure materials	• Complete tests on structural materials and detectors	
Simulations	• Complete code revision for neutron simulation	• Complete high-luminosity (10^{34}) design option	
System Integration	• Complete conceptual design of mounting, cabling, and alignment	• Finalize mounting and alignment	• Finalize installation plan

Table VII.2. L* Specific Development Activities

	Cost (K$/year)
Integrated Mechanical Engineering	**800**
Structural design and analysis and stability tests of the hybrid silicon, straw tube, and scintillating fiber system (engineering in LANL MEE-12, including overhead, travel, fringes, etc.)	400
System integration of the central tracker cabling, cooling, mounting, alignment, and assembly with respect to external L* systems (engineering as above)	200
Prototype structures, materials, fabrication of straw tube and scintillating fiber support structures	200
Silicon:	**525**
Silicon detector engineering (engineering in LANL MEE-Division as above)	200
Readout electronics and optoelectronics engineering for readout of silicon detectors in L* configuration (engineering as above)	200
Technician support of electronic engineering	100
Silicon detector purchases for test and evaluation in electronic and radiation damage studies	25
Straw Tube:	**500**
Straw tube mechanical engineering studies of detectors, fittings, wire alignment, and assembly (engineering and technical support at Boston University, including materials)	150
Electrical engineering for straw tube readout (engineering and technical support, Boston University, including materials)	150
Gas studies	100
Radiation damage studies (50 days at MIT Research Reactor, including technical support)	100
Scintillating Fibers:	**100**
3-D electrostatic modeling and prototypes of compact multichannel photomultiplier tube with UCLA and Hamamatsu	100
Monte Carlo:	**280**
APOLLO DN10000 system for event simulations for central tracker design	100
Neutron code modifications and code support and validation for design of geometric and absorptive neutron mitigation (work coordinated with ORNL and Mississippi and Tennessee) and performed by LANL groups X-6 and T-2)	180
Total	**2205**

References

VII.1. G. Arnison et al., Zeit. Phys. C37, (1988), 505

VII.2. R. E. Prael and H. Lichtenstein, Los Alamos National Laboratory Report LA-UR-89-3014 (September 1988).

VII.3. Los Alamos National Laboratory Report LA-7396-M (revised April 1981).

VII.4. H. Spieler et al., to be published, Proc. IEEE Nuclear Science Symposium (Jan. 1990).

VII.5. W. R. Dawes, Jr., Nucl. Instr. and Meth. in Physics Research A288, (1990), 54.

VII.6. H. J. Ziock et al., to be published in Proc. IEEE Nuclear Science Symposium (Jan. 1990).

VII.7. J. Kapustinsky, Los Alamos National Laboratory, private communication.

VII.8. U. Becker et al., NIM 180 (1981), 61.

VII.9. P. Baringer et al., NIM A254, (1987), 542.

VII.10. S. Ahlen et al., Phys. Rev. Lett. 61, (1988), 148.

VII.11. B. Zhou et al., NIM A287, (1990), 439.

VII.12. L. Chrisophorou et al., NIM 163, (1979), 141.

VII.13. H. Ogren, private communication (1990).

VII.14. B. Zhou et al., submitted to IEEE Trans. Nucl. Sci.

VII.15. K. Arisaka, private communication (1990).

A. DETECTOR INSTALLATION SEQUENCE

The experimental hall is assumed fully equipped with two 200-ton cranes, a large open central main shaft and two auxiliary shafts situated in optimized positions for detector installation. Above the main shaft is a 1000-ton mobile gantry crane, installed temporarily, that is required for handling major components of the magnets and some heavy detector elements (Fig. VIII.1).

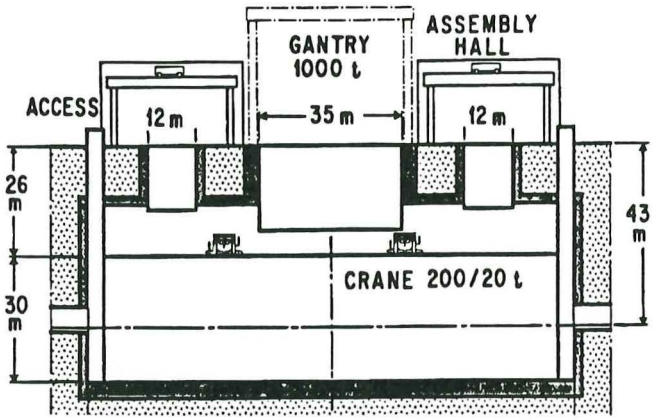

Fig. VIII.1. Collision hall parameters, longitudinal section.

The L* detector assembly starts with the lowering and mounting of the three magnets where the collision hall large shaft is initially open directly to the surface and preassembled subunits created on the surface are installed, using the 1000 t temporary gantry crane. After the magnet tests, the detector units are installed with the forward magnets and the central magnet pole plugs placed at the far end of the hall (Fig. VIII.2).

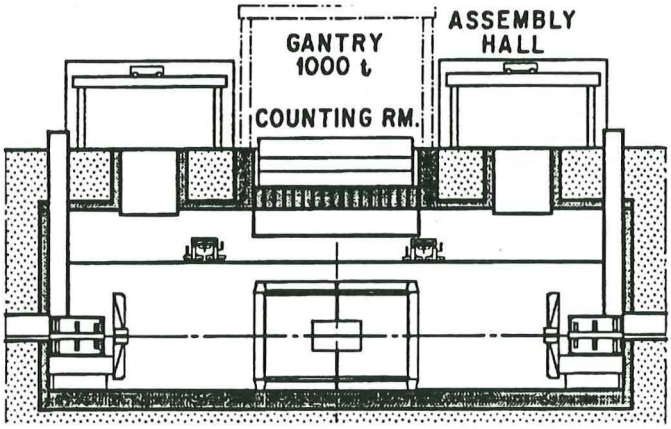

Fig. VIII.2. Magnet complete, ready for detector assembly.

The first component is the hadron calorimeter barrel where modular rings weighing up to 190 ton are assembled in three independent groups on a common track and placed inside the central magnet (Fig. VIII.3).

The electromagnetic calorimeter barrel and central tracking detector with the central vacuum chamber of the beam line is preassembled at the surface then lowered and inserted as one unit, followed by the connection of the services before the electromagnetic calorimeter end

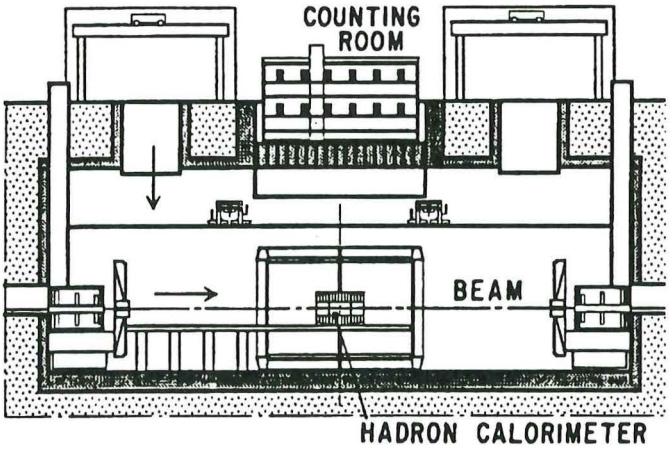

Fig. VIII.3. Hadron and electromagnetic calorimeter barrel installed.

caps are fitted. The hadron calorimeter end caps complete the installation inside the support tube (Fig. VIII.4).

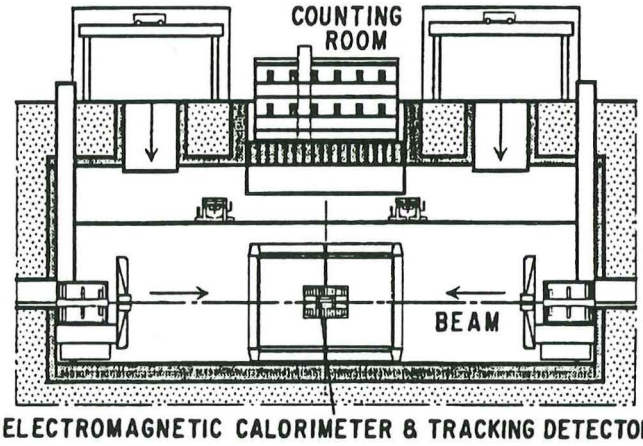

Fig. VIII.4. Central tracker and calorimeter endcaps installed.

Once the major operation of installing the hadron calorimeter barrel is completed, the muon chamber central section assembly equipment is lowered and placed in position in front of the magnet openings, followed by the lowering of the muon central chamber units. They are placed vertically into a cylindrical rotating device, lowered an placed on a mobile scissor table. Once aligned with one of the 16 predetermined positions the unit is then displaced inside the magnet. The process continues until the 16 units on one side of the magnet are installed aligned and connected. The services from the calorimeter are then brought out along the slope of the muon central section structures passing through the fixed outer ring part of the magnet pole. Whilst the central units on the other side of the magnet are being inserted, one of the two preassembled muon chamber endcap groups is lowered directly adjacent to the pole plug of the central magnet where they are secured and aligned (Fig. VIII.5).

With the upper poles open, the forward muon chambers are lowered inside the forward magnets. The machine elements are then lowered with their structures and installed thus completing the detector layout ready for beam, giving an overall installation period of 3.5 years

after the completion of the basic experimental hall (Fig. VIII.6). Experience of L3 has shown that a main task force of 50 support technicians rising to 100 at peak periods should be sufficient to maintain the time schedule of the total detector installation over the 3-year period 1995–1998. This is assuming that only normal hours are worked and that shift and weekend work is kept as a contingency.

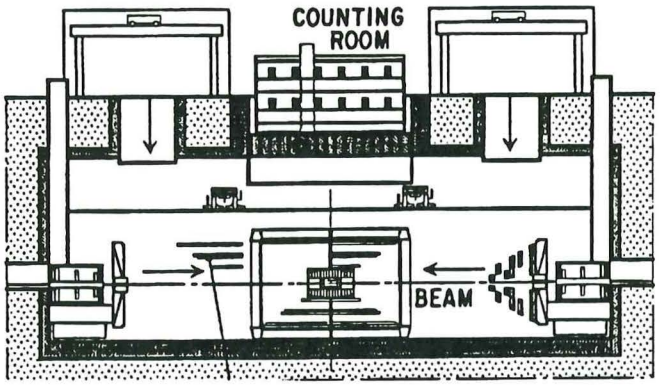

Fig. VIII.5. Muon chambers assembly.

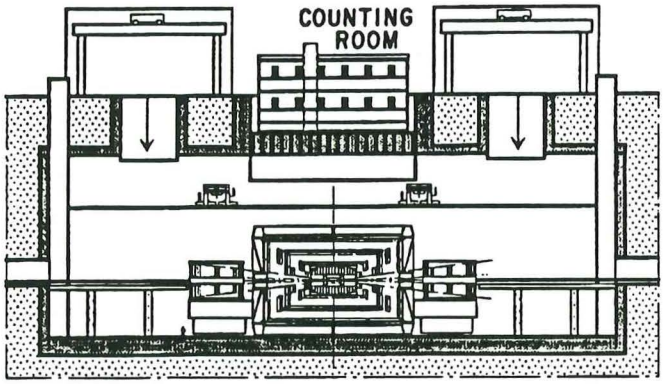

Fig. VIII.6. Detector complete and machine elements installed.

Since the L3 installation was completed on time and kept within the installation budget, it is used as a model for the L* detector assembly where many sequences and techniques are identical. The provisional planning table (Fig.VII.7) demonstrates that the installation time sequence is feasible and within a reasonable extrapolation of the L3 experience.

B. SURFACE FACILITIES

The facilities that will be defined in the Resources and Requirements Report are governed mainly by the magnet manufacturing and surface assembly requirements where the coil halls are needed at a very early stage of the site development.

C. ACCESS AND SAFETY

The L3 detector is selected as a model for the access and safety requirements where the use of multiple scaffold arrays, hydraulic elevators and manipulators for personnel and equipment is integrated with permanent gangways around the experimental hall. For maintenance when the access time is limited, the forward detectors inside the conical support tube fixed to the magnet pole plug are removed and a lightweight bridge structure installed that will permit access to equipment located on the hadron calorimeter end faces. During major machine shutdowns, the forward magnet with the central pole plug can be displaced 6 m without disconnecting thus permitting access throughout the magnet volume by using specially adapted fixtures that can be attached to the muon chamber support structures to carry out minor repairs and inspections. Major dismantling of the detector elements inside the central magnet requires the displacement of the pole plug and forward magnet units to the far end of the experimental hall.

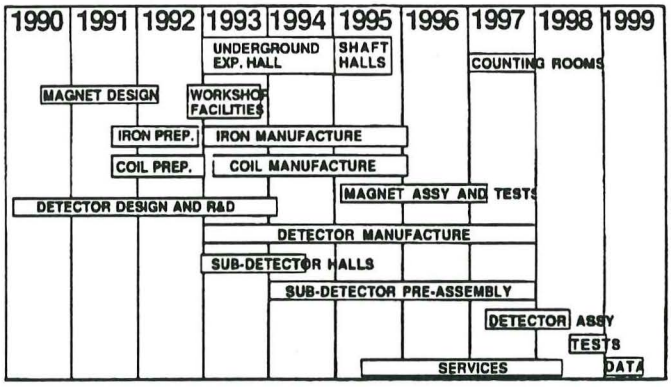

Fig.VIII.7 L* planning.

D. ENGINEERING SUPPORT

The L* Collaboration has defined the initial detector engineering coordinating design responsibilities and is starting the organization of an information exchange network where the detector parameters, planning and technical coordination can be monitored. Engineering support is also expected from the SSC Laboratory for detector design and manufacturing contract assistance including the supply of the detector facilities, counting rooms and installation participation.

E. EXPERIMENTAL RUNS WITH DIFFERENT INNER DETECTORS

To perform runs for jet physics and muon physics either at 10^{33} $cm^{-2}s^{-1}$ to 10^{34} $cm^{-2}s^{-1}$, the inner detector region can be opened up and the electromagnetic and tracking detectors extracted to be replaced by an additional hadron calorimeter. The operational sequence would involve the withdrawal of the forward-backward magnets, the reinstallation of the rail systems and the extraction of the calorimeter end caps. This is followed by withdrawing the electromagnetic barrel and replacing it with the hadron calorimeter unit, using the same rails and technique. After testing, the rails are removed and the detector closed. The whole operation should be accomplished during a normal, few months long shutdown.

A. INTRODUCTION

The interaction rate at the SSC is of the order of 10^8 events per second. Further, since the probability of having more than one interaction per crossing is significant, the triggering and readout systems must take into account overlapping events. The total number of channels in the L* experiment is of the order of 10^6.

These requirements mandate several general guidelines used in designing the L* detector. One aspect of the large event rate which is new to the HEP detector is the requirement for radiation resistant electronics. The large number of channels will require reliable and even fault-tolerant electronics designs.

B. DATA ACQUISITION

B. 1. Introduction

The design of the data acquisition and triggering tasks for L* must take into account the following:

- Adaptability to new, unexpected physics
- Ability to adopt new technologies
- Accessibility, fault tolerance, and redundancy
- Radiation damage to electronics
- Power consumption and heat dissipation
- Cable volume, weight, and installation effort
- Manufacturing, installation, and maintenance costs
- Ground loop problems

Two general consequences of these issues are that on-detector electronics must be minimized and that fiber optics use must be maximized. Keeping as much of the electronics off the detector as possible is the best way to ensure adaptability to new technologies as well as to minimize the number of radiation-hardened electronic devices. This adaptability and the radiation hardness issue are particularly crucial given the expected 10-year operational lifetime of L*. Fiber optics permits digital signals to be carried off the detector without the intolerable bulk of coaxial cable. It is the only technique that effectively addresses the problem of ground loops.

Detector-mounted electronics include preamplifiers, discriminators, ADCs, and drivers for optical data links. This set of the electronics is essentially the minimum required to transmit data out of the detector volume.

The time required for data from a given event to exit the various L* subdetectors varies greatly. The calorimeter data must be resolved within 16 ns of the occurrence of an event, whereas the muon chambers will continue to output data for the same event for the next 1000 ns. Meanwhile, no fewer than 60 additional events will have occurred. Clearly sophisticated buffering is required to match up data from various subdetectors regarding a particular event identified by the trigger.

B. 2. Muon Spectrometer

Chapter IV outlines the precision muon spectrometer system. The acquisition system accepts drift data for time-to-digital conversion from about 250 000 channels and 20 000 channels of binary information from resistive plate chambers (RPCs), primarily for triggering.

Wire chambers produce signals with characteristic times of a few tens of nanoseconds. The drift times are typically hundreds of nanoseconds, so the signal may actually appear only many beam crossings after the interaction. The timing measurement requires a multihit pipeline TDC, with resolution of the order of 1 ns. This is readily accomplished with currently available digital technology.

Data from the muon spectrometer must be accepted more or less on a continuous basis, since the event to which the data belongs has not yet been identified. Fortunately, the anticipated data rates are relatively low, only 0.03 track/μs in the barrel detectors and 11 tracks/μs in the forward detectors. With these boundaries, several front-end configurations can be considered.

The simplest system just amplifies and discriminates the data before sending them on to the counting house. This requires only amplifiers, discriminators, and transmitters to be mounted near the sense wires. All time-to-digital conversions and trigger calculations are then deferred to the counting house. This configuration has the following advantages:

- The majority of the electronics are accessible, which allows upgrading in responses to changing needs and technologies.
- Optical fibers can be used to relieve the cabling volume.
- Only small amounts of electronics must be made radiation resistant and fault tolerant.
- No global time reference is required at the detector.
- No location reference is required at the detector. These data may be added in the counting house.

The other extreme is to mount the majority of the electronics on the detectors. Time-to-digital conversions are then performed on the detector. Location identifiers are appended to each data word and then sent via a LAN to the counting house. This configuration also has advantages:

- Cable volume is insignificant.
- Transmitted data are truly digital and include error correction codes for extreme fault tolerance

The best solution, based on cost and performance, exists between these two extremes of integration. Future developments in electronics and digital optical technologies and the interface with other detector systems will mold the details of the final solution.

B. 3. Calorimeter System

The calorimeter system described in Chapters V and VI has about 26 000 channels in the BaF_2 electromagnetic calorimeter and 300 000 in the hadron calorimeter.

Calorimeters produce a range of signals. The fastest can resolve interactions in successive beam crossings.

In the slowest, the signal pulse spans several beam crossings, but the leading edge can resolve the individual beam crossing. The interaction rate demands a pipelining to store the signal while the trigger decision is being made.

Very fast detectors (e.g., BaF_2), which can resolve signals in successive beam crossings are necessary for the high rate portions of the detector. There are several possible methods for pipelining these signals:

- Electronic analog delays such as CCDs or switched capacitor delay lines can provide high-quality delay.
- Digital electronic delay systems are the most desirable because they are easily controllable and exact.

To realize a digital delay system, the data must, of course, be digitized. Only two devices appear to approach this problem: the Flash ADC and the Sigma Delta ADC. The Flash ADC has problems meeting cost requirements because of its inherent complexity. The Sigma Delta ADCs have not been demonstrated at the required speeds yet, although the basic design shows the potential for large-scale integration and higher speeds.

B. 4. Central Tracking Detector

The central tracking detector, described in Chapter VII, has three sections: the silicon microvertex detector with 76 000 channels, the straw tube tracker with 75 000 channels, and the scintillating fiber tracker with 50 000 channels.

Data generated by the silicon microvertex detector and the scintillating fiber tracker are basically digital and very prompt. Data paths to the counting house can effectively be created by multiplexing data from several detector elements to digital optical fibers.

B. 5. Detector Electronics

Table IX.1 shows a summary of the subdetectors and their associated electronics requirements. The silicon microvertex detector requires a preamplifier, shaper-discriminator, some data processing, local buffering to cover the first and second level trigger decision time, and a multiplexed fiber optic readout.

The scintillating fiber tracker will require a system based on microchannel plate photomultipliers servicing many fibers with timing resolution better than 16 ns.

The straw tubes and muon drift chambers both require timing resolution of better than 1 ns, with a conventional amplifier/discriminator/pipeline TDC configuration.

The resistive plate chambers are used only in the trigger and will probably need no more than a simple discriminator, with a timing resolution of better than 16 ns.

The silicon pad detectors in the hadron calorimeter require either a fast ADC located on the detector, with digital pipelining to the first and second level triggers, or analog pipelining followed by a slower ADC after the second level trigger. The ADC requires 12 bits of dynamic range and 2% resolution. A possible candidate is a Sigma Delta ADC, which may also be most applicable to a liquid ionization detector, such as TMS.

For the BaF_2 detectors in the electromagnetic calorimeter, a dynamic range of as much as 22 bits may be necessary. Analog pipelining of such signals is a real challenge, and a single Sigma Delta ADC is not usable for this dynamic range. One possible solution, which gives all the advantages of digital pipelining and digital trigger, is to use two or three Sigma Delta ADCs per channel in a weighted multilinear parallel system.

Sigma Delta ADC

One fundamental feature of the Sigma Delta ADC is that it operates continuously, generating a single-bit stream of binary data. Within a selected bandwidth, the original waveform can be completely reconstructed from these binary data by means of a digital filter. These digital filters can be designed to extract various quantities from the bit stream, such as timing or integrated charge, at speeds and resolutions useful for all levels of the triggering system.

Figure IX.1 shows a block diagram of a basic Sigma Delta ADC. Its distinguishing features are the feedback around the ADC, the cascaded integrators in series with the input, the single-bit output, and the digital filtration.

The basic channel (see Fig. IX.2) consists of a Sigma Delta converter with a sampling frequency of 500 MHz. The one-bit output stream is fed into a dynamic shift register. A low-pass digital filter processes the first N cells in the pipeline. The output of this filter is summed with the similarly filtered output of the other channels in the trigger. The result is compared with a digital reference, which is programmable and can form part of the first level trigger. The filtering essentially reconstructs the digitized signal, and the width of the filter defines the accuracy with which the reconstruction is done. Short filters may be used in the prompt trigger.

Table IX.1. Subdetectors and Associated Electronics Requirements

Subdetector	Signal	Resolution	Dynamic Range	Electronics
Si microvertex	Hit	16 ns		Special
Scintillating fiber tracker	Hit	5 ns		MCP tube Discrim.
Straw tubes	Timing	< 1 ns	0.1 μs	Discrim. TDC
Drift chambers	Timing	< 1 ns	1 μs	Discrim. TDC
RPC	Hit	16 ns		Discrim. TDC
Hadron; Si pads, TMS	Ampli.	1.8%	12 bits	ADC
EM calorimeter; BaF_2	Ampli.	0.5%	22 bits	ADC

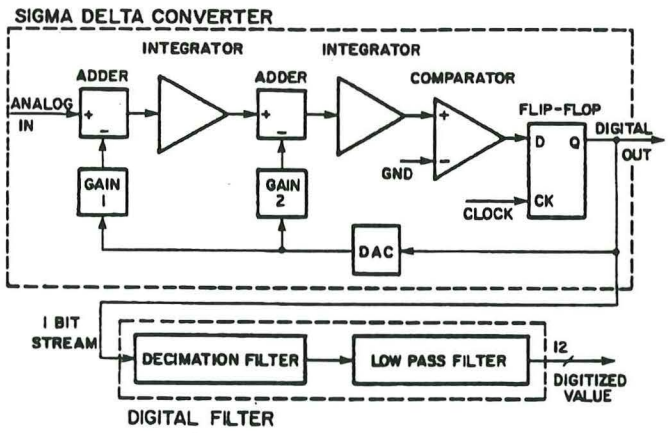

Fig. IX.1. Basic Sigma Delta converter.

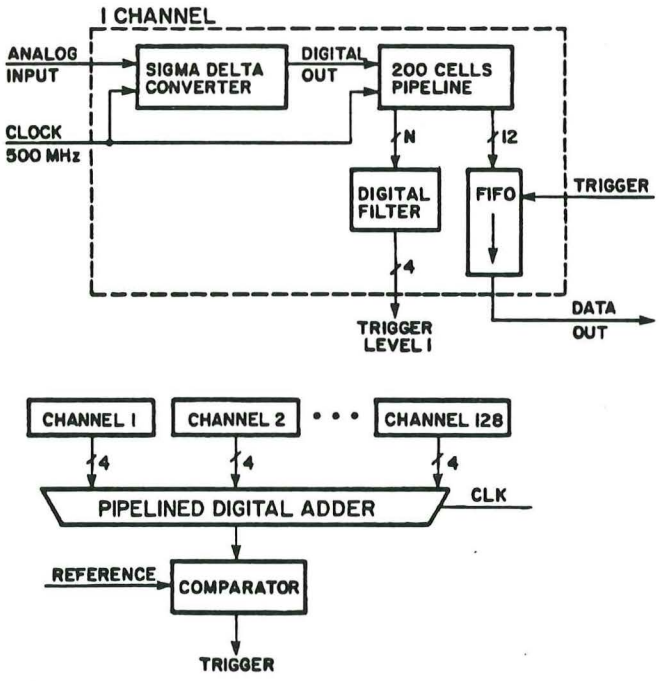

Fig. IX.2. Possible calorimeter level 1 trigger solution.

C. TRIGGERING

C. 1. Introduction

At the SSC, events are generated at the rate of 10^8 per second. Only about 10 events per second can be recorded to permanent storage media.

Because of the buffering requirements, the trigger system is composed of several layers of decision making (see Fig. IX.3.). The first level trigger will select only 1 in 500 events to be retained for further study. The second level trigger now has 500 times longer to make a decision on the remaining events, while using the same amount of buffering as the first level trigger. With the additional time, the second level trigger uses more information to make a more accurate decision.

C. 2. First Level Trigger

The first level trigger computes 10^8 decisions per second. A nominal 400 ns is assigned to this decision. Clearly these computations are pipelined. Consequently, the data of the 25 events also must be pipelined.

Because of the short time scale for the trigger decision, only a few thousand channels of information—consisting largely of coarse tower sums from the hadronic and electromagnetic calorimeters and rough tracks from auxiliary, fast muon detectors—will participate. This time scale also restricts the hardware configurations possible to implement the trigger decision. Areas of consideration and development include:

- Programmable and hardwired gate arrays
- Digital filters and digital signal processors
- Associative memories and neural networks
- Optical and electro-optical computing elements

C. 3. Second Level Trigger

Another 200:1 reduction of background events is needed in a second level trigger to bring the data rate from 200 kHz to 1 kHz. If 10 μs are allocated for this level trigger process, an additional memory for only five elements is required for the front-end data. Finer tower sums from the electromagnetic and hadronic calorimeters can be used to make finer cuts. Information should be available from the precision muon spectrometer on the number and momentum of muon particles. Cut algorithms at this level will stress the detection and inclusion of interesting events. The required rejection factor and the short time available for a decision will call for the use of state-of-the-art electronics and software.

The second level trigger will be fed with pipelined event data at the 60-MHz beam clock rate but process only the events accepted by the first level trigger. The granularity of the calorimeter will be important in pattern recognition. Such pattern recognition could be used for isolation cuts on interesting events.

C. 4. Third Level Trigger

Filtering of events at the third level requires event reconstruction with fully digitized data. The task is to assemble the entire event and transmit it to the memory of one of the event processors. Thus the muon spectrometer and central trackers contribute fully at this level. Assuming a 1-kHz input rate and 1 Mbyte per event, the event builder must have a bandwidth substantially larger than 1 Gbyte/s. We expect to follow substantive developments in parallel computing and telecommunication technologies.

D. R&D EFFORTS

The R&D activities, milestones, and funding requests are summarized in Table IX.2.

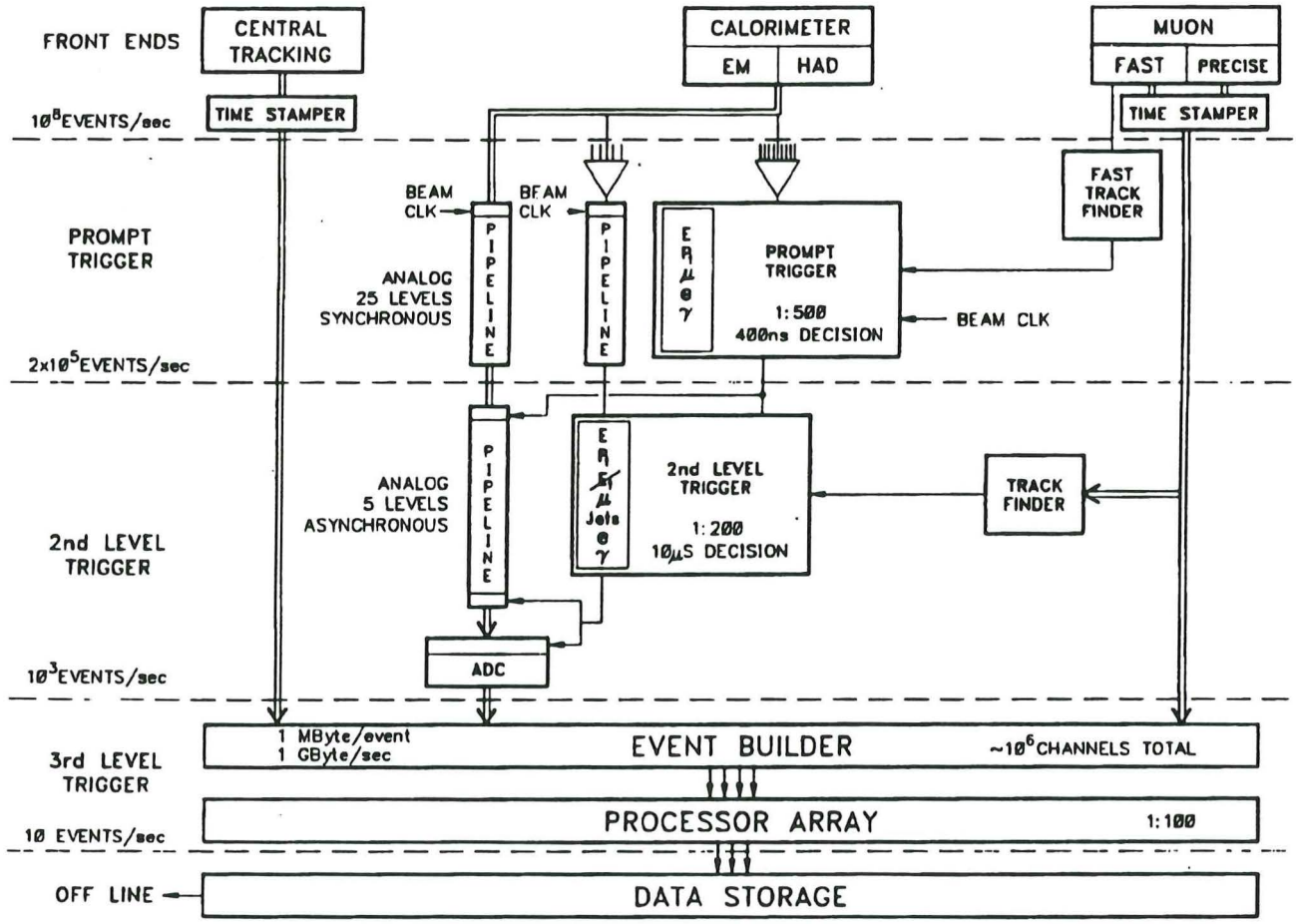

Fig. IX.3. Trigger architecture.

Table IX.2. Milestones and Funding Request for R&D (K$)

Activity	Milestones		Funding Request	
	FY 1991	FY 1992	FY 1991	FY 1992
Front-end electronics, data buffering and conversion, trigger interface (ORNL)	• Design quad preamplifier for the Si calorimeter • Design analog summers for 1st level trigger • Develop analog pipeline chip	• Radiation-hardness tests • Produce prototype amplifier, summer and pipeline chips	100	100
System simulation software (ORNL)			50	50
Associative memories (UMiss)	• Determine associative memory feasibility for 2nd level trigger	• Build model muon track finder for the hadron calorimeter	200	200
L* ADCs and TDCs (LeCroy)	• Determine Sigma Delta ADC feasibility for L* subdetectors • Develop chips for ADC and TDC	• Produce model ADC/TDC for L* muon chambers • Radiation- hardness tests	1600	2300
Electro-optics and fiber optics (LeCroy)	• Perform electro-optics component modeling	• Design and produce prototype optical network	300	600
System integration (LeCroy)	• Define L* DAQ and trigger project • Define electronics parameters	• Finalize trigger concept and demonstrate its feasibility	600	900
		Data Acquisition and Trigger R&D Total	2850	4150

A. INTRODUCTION

The L* experiment is an international collaboration. We are requesting nearly equal amounts of support from the United States, the Soviet Union, Europe, and Asia, and we are organizing the L* experiment's management structure to reflect the different levels of participation and support. This chapter describes preliminary ideas concerning the organization of L* (see Fig. X.1). We discuss the structure and functions of the different committees of the L* group. Our ideas derive mostly from experience gained with the L3 experiment, which brings together 500 physicists from 13 nations and 36 institutions, with major support from the Soviet Union, the United States, Europe, and Asia. The L* management structure will also remain in effect after the approval stage.

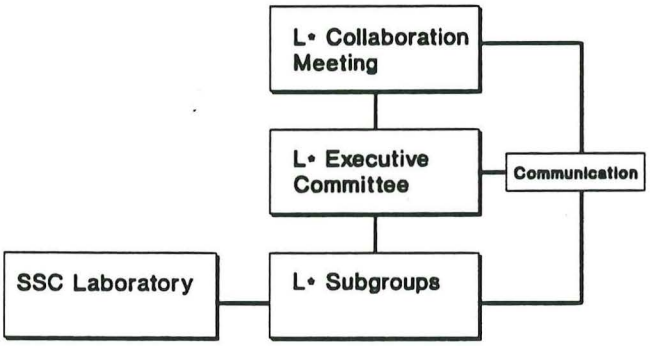

Fig. X.1. Organization of L*.

B. COLLABORATION MEETINGS

The L* Collaboration meeting is a forum at which every member is invited to participate. It is chaired by the Spokesperson. Questions on scientific, technical, financial, and organizational matters will be discussed. The results of Executive Committee meetings will also be presented. As with L3, the opinions of all members of the Collaboration (including graduate students) will be heard. In particular, no closed meetings will be held. L* Collaboration meetings will occur four times a year.

C. L* EXECUTIVE COMMITTEE

The L* Executive Committee will recruit its members from representatives of participating laboratories and universities. Each member will have one vote. A partial list of members is included in Table X.1; this list will be completed during the first meetings of the Executive Committee, which will be headed by the Spokesperson. Executive Committee meetings will be open to all members of the Collaboration. The responsibilities of the committee are as follows:

1. Select new members for the L* Collaboration.
2. Discuss in detail financial and managerial issues.
3. Resolve conflicts. If no common agreement can be found, the Spokesperson may suggest a vote.

Table X.1. Partial List of Members of the L* Executive Committee

Nations	Members
United States	U. Becker, J.Branson, W. Bugg, D. DiBitonto, A.Engler, O. Fackler, R. Heinz, H.Newan, A.Pevsner, P.Piroue, F. Plasil, J. Reidy, J Rohlf, G. Sanders, & others
Soviet Union	Y. Galaktionov, A. Lebedev, I. Savin, N. Tchernoplekov, and others
Europe	B. Borgia, M. Bourquin, K. Lubelsmeyer, P. Rancoita, C. Sciacca, and others
Asia	S. X. Fang, Z. W. Yin, A. Gurtu, Y.Y.Lee, D.Son and others

The Executive Committee usually meets during Collaboration meetings. Additional meetings will be arranged, if necessary.

D. L* SUBGROUPS

The L* Subgroups are individually organized (see Tables X.2 and 3). They have an executive committee and are chaired by a coordinator. The members of the subgroup executive committees are chosen on the basis of participating institutes. They are approved by the L* Executive Committee. The decisions of the coordinator and the subgroup executive committees are reported at Collaboration meetings for suggestions and approval. A partial list of members of the subgroup executive committees is detailed in Table X.3.

Table X.2. Organization of the Subgroups

Subgroup Executive Committee
Subgroup Coordinator
Coordinator for Finances
Coordinator for Services

E. RESPONSIBILITIES OF THE SPOKESPERSON

To manage a large international group efficiently, the Spokesperson must be able to interact on all levels of the collaboration. In particular, the spokesperson has the responsibility to make immediate technical decisions when necessary. The Spokesperson should report his or her decisions to the Executive Committee and the Collaboration.

F. SELECTION OF NEW MEMBERS OF THE COLLABORATION

1. During 1990, the L* Collaboration invites all interested groups to join without specific rules or procedures.

2. From 1991, the following procedures are discussed:

a. The interested new group discusses joining the Collaboration with the Spokesperson.

b. The Spokesperson appoints an ad hoc membership committee of five L* physicists. The membership committee holds in-depth discussions with the new group on matters of mutual interest and compatibility.

Table X.3. Partial List of Members of Subgroup Executive Committees

A		PHYSICS GOALS AND NEW IDEAS	S. Kunszt, L. Okun, R. Slansky, G. West, and others
B	B1	MAGNET	H.Britt, C. Henning, I. Horvath, P. Marston, N. Martovetsky, N. Tchernoplekov, and others
	B2	EXPERIMENTAL AREA AND INSTALLATION	Not yet defined
C		MUON DETECTOR	U. Becker, J. Burger, O. Fackler, C. Grinnell, H. Hofer, G.Viertel, M. White, L. Wilk, and others
D		HADRON CALORIMETER	B. Bugg, Y. Galaktionov, I. Golutvin, F. Plasil, M. Rennich, I. Savin, and others
E		ELECTROMAGNETIC CALORIMETER	M. Chen, H. Newman, P.Piroue, D.Stickland, Z. W. Yin, & others
F		CENTRAL TRACKER	R. Heinz, J. Rohlf, G. Sanders, and others
G		FORWARD CALORIMETER SYSTEMS	D. DiBitonto, A. Gurtu, K. Luebelsmeyer, and others
H		TRIGGER AND ONLINE COMPUTERS	B. Borgia, H. R. Brashear, M. Fukushima, A.Lebedev, P.Lecomte and others
I		OFFLINE COMPUTERS	H. Newman, R.Mount, H.Rykaczewski and others
J		ANALYSIS AND MONTE CARLO SIMULATION	H. Newman, M. Pohl, J. Reidy, and others
K		PARAMETERS AND ASSEMBLY	T. Shannon and others
L		FINANCES AND REVIEWING	F. J. Eppling, M. Jongmanns, S.M.Ting and others
M		SERVICES: Operation, Communications, Administration, SSC logistics	F. J. Eppling and others

SSC Laboratory

SSC Laboratory

c. The chairman of the membership committee reports the committee's findings at the L* Executive Committee.

d. The L* Executive Committee makes its decisions by a closed vote. If the new group receives two-thirds support, the case is presented to the L* Collaboration meeting, and the new group is introduced to the members of the Collaboration.

e. In a meeting of all the representatives of the participating institutes and universities called by the Spokesperson, a closed vote is taken. The new group is welcomed into the L* Collaboration if it receives two-thirds support of all the representatives.

G. L* NETWORK

A network is necessary for the coordination of the detector design, mechanical engineering, and analysis of test data.The L* network is based on the experience with the LEP3NET (see Fig. X.2). We anticipate expanding LEP3NET to all institutions collaborating in L*.

The L* network link requirements are currently 64 kbits/s to all sites and at least 256 kbits/s to major sites in the Collaboration. These requirements will increase to the 1.5-Mbit/s range to all sites and to the 10-Mbit/s range for the principal sites by 1995. The first major step will be the LEP3NET upgrade of the transatlantic link to the 384 kbits/s.

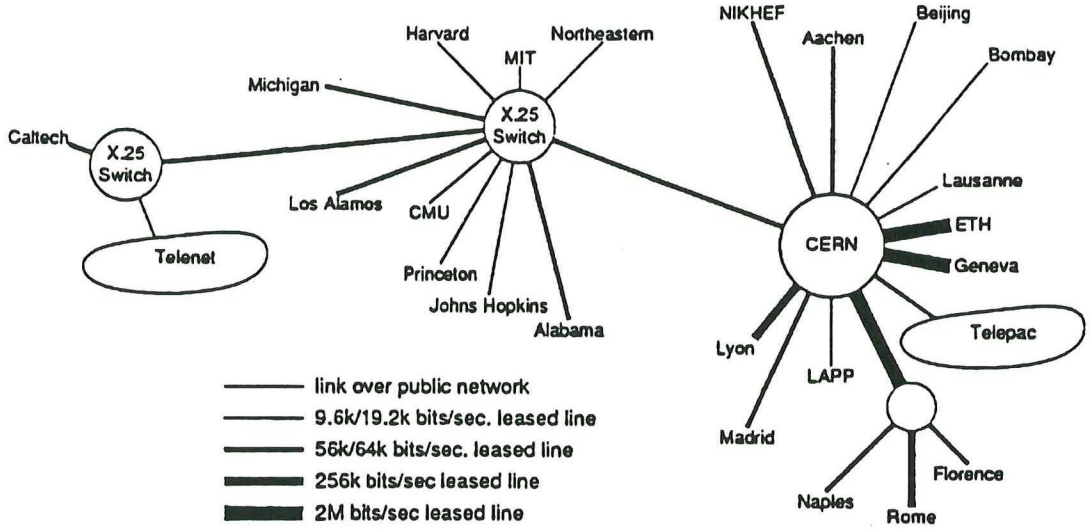

Fig. X.2. Network lines serving L3.

A. MILESTONES

The milestones and a description of key events that must occur to define the detailed design of the detector are integrated in the individual chapters describing the components of the L* experiment. In particular, they can be found in this document on the pages as listed below:

B. COST

As in the case of L3, with substantial non-US requests for the construction of the L* detector and due to the very different accounting systems (salaries, infrastructure, overhead,...) in the participating countries and currency exchange uncertainties, a cost estimate is not possible nor meaningful until a detailed distribution of responsibilities has been assigned.Once a decision has been made about the responsibilities on detector elements, the L* subgroup on Finance and Reviewing will account the non-US contributions in equivalent US dollars in order to obtain a total cost estimate of the L* experiment.

C. FUNDING OF R&D

The detailed funding requests for R&D are presented at the end of each chapter describing the various subdetectors. Table XI.1 summarizes our R&D request to the SSC laboratory.

Table XI.1 US Funding Request for R&D [M$]

	FY90	FY91	FY92	TOTAL
MAGNET		0.5	0.5	1.0
MUON DETECTOR	1.0	4.6	2.8	8.4
HADRON CALORIMETER		2.6	2.1	4.7
EM CALORIMETER		2.9	3.1	6.0
CENTRAL TRACKER		2.2	2.2	4.4
FORWARD CALORIMETER		0.4	0.4	0.8
DAQ + TRIGGER		2.9	4.2	7.1
COORDINATION		0.5	0.5	1.0
TOTAL	**1.0**	**16.6**	**15.8**	33.4

Additional R&D efforts at similar levels are carried out by non-US institutions of L*.

D. FUNDING OF L* CONSTRUCTION

The responsibility for funding of L* is distributed between the USA, USSR and Europe/Asia. In table XI.2, a possible sharing of responsibilities for the different subdetectors is summarized. The US part is shown in FY90 dollars. The US contribution as mentioned below assumes the warm coil magnet option, a silicon hadron calorimeter and a BaF_2 electromagnetic calorimeter. Table XI.3 shows a more detailed breakdown of a possible US contribution for the various subdetector options of L*.

Table XI.2 Sharing of responsibility and US funding proposal for construction of the L* detector.

Subdetector	USA [M$]	USSR	Europe + Asia
MAGNET (Warm Coil)	68.3	*	
MUON DETECTOR	110.0		*
HADRON CALORIMETER (Si)	50.8	*	
EM CALORIMETER (BaF2)	2.0	*	*
CENTRAL TRACKER	40.0	*	*
FORWARD CALORIMETER	2.0	*	*
EDIA (10%)	27.3	*	*
TOTAL	**300.4**	*	*

* Contribution in material, manpower and detector systems.

Table XI.3 Proposed US funding contribution for the various L* subdetector options [M$]

MAGNET		
CENTRAL MAGNET (Warm Coil):		
COIL + POWER SUPPLY	29.8	
RETURN FRAME + ASSEMBLY	31.9	
FORWARD-BACKWARD MAGNETS:		
COIL + POWER SUPPLY	3.1	
RETURN FRAME + ASSEMBLY	3.5	
TOTAL	**68.3**	
MUON DETECTOR: Central + Forward Detector		
MUON CHAMBERS	48.0	
ARRAY STRUCTURES	20.0	
ELECTRONICS	36.0	
ALIGNMENT + CALIBRATION SYSTEM	3.0	
GAS SYSTEM	3.0	
TOTAL	**110.0**	
HADRON CALORIMETER		
	Silicon Option	Liquid Scintillator
DESIGN,STRUCTURE,TOOLING	9.0	9.0
ELECTRONICS	25.0	21.0
DETECTOR ASSEMBLY	3.8	3.8
PRODUCTION CONTROL EQUIPMENT	10.0	
COOLING SYSTEM	3.0	
DETECTORS: Scintillators,Fibers,...		16.0
TOTAL	**50.8**	**49.8**
EM CALORIMETER		
	BaF2	LXe
ELECTRONICS	2.0	
TOTAL	**2.0**	To be studied
CENTRAL TRACKER		
SILICON DETECTORS AND ELECTRONICS	17.0	
STRAW TUBES AND ELECTRONICS	11.0	
SCINTILLATING FIBERS, READOUT AND ELECTRONICS	3.0	
STRUCTURES, COOLING	9.0	
TOTAL	**40.0**	
FORWARD CALORIMETER SYSTEM		
ELECTRONICS	2.0	
TOTAL	**2.0**	

A. UNIQUE PROPERTIES

The L* experiment has the following properties:

1. A large magnet constructed like a building (but with more iron than concrete) providing $BL^2 = 69\ Tm^2$.
2. A precision muon system in a volume with $BL^2 = 20.7\ Tm^2$, $2° < \theta < 178°$, with resolution $\Delta P/P \approx 2.4\%$ at $P = 0.5$ TeV.
3. A fast calorimeter with a rise time of 2–5 ns and fine longitudinal segmentation that has two alternatives:

(a) An electromagnetic calorimeter in front with a resolution $\Delta E/E = (1.3/\sqrt{E} + 0.5)\%$ and $\Delta\theta = 0.2°$, $\Delta\phi = 0.2°$, followed by a hadron calorimeter made of Fe-Pb with Si or liquid scintillator readout, with $\Delta\eta\Delta\phi = 0.04\times0.04$ and with a combined jet resolution $\Delta E/E = 50\%/\sqrt{E} + C$, with $C = 4\%$ for BaF_2 and $C = 2\%$ for a liquid xenon electromagnetic calorimeter; or

(b) A complete compensating hadron calorimeter that measures jets with energy resolution $\Delta E/E = (50/\sqrt{E} + 1.0)\%$. This is made possible because the size of the magnet permits the installation of special handling equipment to exchange the electromagnetic and central vertex detectors for different experimental runs.

4. A fast central tracking detector with timing information from silicon strips and plastic scintillation fiber and pattern recognition from straw tubes. The central tracker provides $\Delta P/P = 50\%$ at $P = 0.4$ TeV and the event vertex to 1 mm.

B. PHYSICS EXAMPLES

We now present a few physics examples. We also present examples of detector responses for luminosity of $10^{34}cm^{-2}\ sec^{-1}$. The resolution of L* enables us to search for Higgs from 80 GeV continuously to 1 TeV. In particular, we will be able to cover the most important mass region from 80 GeV to 200 GeV. This is a continuation of current L3 efforts, which cover the region of Higgs mass up to M_Z.

B. 1. Search for the Higgs with 80 GeV < M_H < $2M_Z$

A great effort is underway at LEP to search for the Higgs. As summarized in Table XII.1, the mass of the Higgs has profound implications for the determination of the correct fundamental theory (Ref. XII.1). By measuring e, μ, and γ, L3 will be able to explore the Higgs mass range $M_H < 50$ GeV at LEP Phase I by 1992, and $M_H <$ 80 GeV at LEP Phase II by 1996.

The detection of a Higgs in the mass range 80 GeV < $M_H < 2M_Z$ can only be done at the SSC using high-resolution measurements of photons and leptons in the decays $H^0 \Rightarrow \gamma\gamma$ and $H^0 \Rightarrow ZZ^* \Rightarrow e^+e^-e^+e^-$ or $\mu^+\mu^-\mu^+\mu^-$ or $e^+e^-\mu^+\mu^-$. The great importance of this mass range stems from the fact that:

If $M_H > M_{Z^0}$ for the lightest Higgs, then the minimal supersymmetric extension to the Standard Model is ruled out.

Table XII.1. The Higgs Mass: Implications for Physics

Experiment	M_H Range	Implications
L3 at LEP I (1992)	$M_H < 50$ GeV	Minimal SUSY
L3 at LEP II (1996)	$M_H < M_Z$	Required by minimal SUSY
L* at SSC	$M_H < 200$ GeV	Required by nonminimal SUSY. If not: new physics below M Planck
L* at SSC	$200 < M_H < 1$ TeV	Standard Model
L* at SSC	No Higgs	New physics with WW, Z^0Z^0 rates increase

Nonminimal supersymmetric theories require $M_H <$ 200 GeV. If $M_H >$ 200 GeV, then SUSY is ruled out.

Most importantly, if no Higgs exists with $M_H <$ 200 GeV, then there **must** be new physics below the Planck scale.

$H^0 \to \gamma\gamma$, 80 GeV < M_H < 160 GeV

In this section we demonstrate the ability of the L* electromagnetic detector to search for the Higgs in the $\gamma\gamma$ decay mode. The study was done by Monte Carlo program PYTHIA version 5.3 (Ref. XII.2), and has been checked with ISAJET version 6.28 (Ref. XII.3).

Figure XII.1 shows a lego plot of transverse energies in the $\eta-\varphi$ plane for a 150 GeV Higgs that decays into two photons together with associated QCD jets. The distinctive feature of isolated photons in the Higgs decay can be used to reject the QCD background.

Photon Backgrounds

The main background in the $H^0 \to \gamma\gamma$ search is direct production: $q\bar{q} \to \gamma\gamma$ (59 pb) and $gg \to \gamma\gamma$ (493 pb) (Ref. XII.4). This background will be reduced by event selection cuts on photon rapidity (η_γ), photon transverse energy (E_T^γ), rapidity of the 2-photon system ($\eta_{\gamma\gamma}$) and $\cos\theta^*$, where θ^* is the polar angle of photons in the $\gamma\gamma$ rest frame. The cuts used in the event selection are (Fig. XII.2):

$|\eta_\gamma| < 2.8$

$E_T^\gamma > 20$ GeV

$|\eta_{\gamma\gamma}| < 3$ (to reduce $q\bar{q} \to \gamma\gamma$)

$|\cos\theta^*| < 0.8$ (to reduce $gg \to \gamma\gamma$).

The background cross sections after event selection cuts are reduced to 91 pb for $gg \to \gamma\gamma$ and 14 pb for $q\bar{q} \to \gamma\gamma$. Because the Higgs width in this mass region is very narrow ($\approx$10 MeV), a very high resolution electromagnetic calorimeter is needed to detect the 0.3 pb signal (Ref. XII.5) from $H^0 \to \gamma\gamma$.

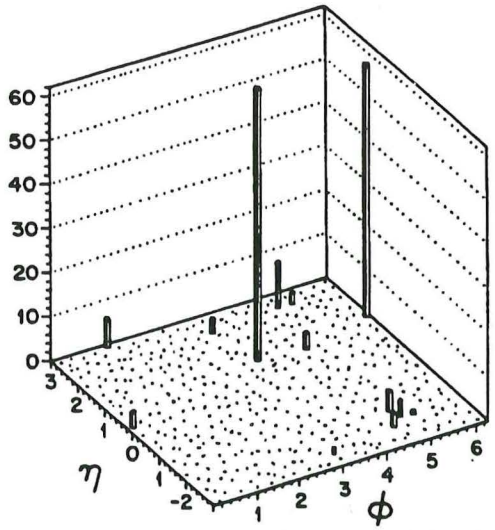

Fig. XII.1. Transverse energy distribution of the $H^0 \to \gamma\gamma$ in the η - ϕ plane.

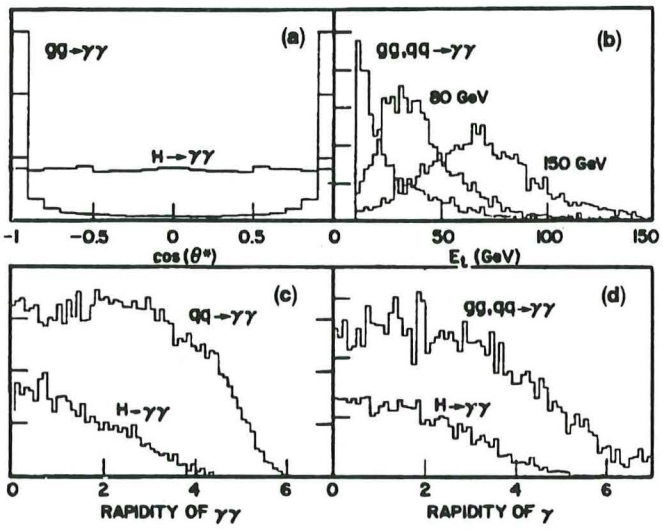

Fig. XII.2. Distributions of (a) $\cos\theta^*_\gamma$, (b) E^γ_T, (c) $\eta_{\gamma\gamma}$, and (d)η_γ.

There are copious π^0, and thus photons, produced at the SSC. The QCD two-jet cross section is 1.2 mb for $P_T >$ 20 GeV and $|\eta| < 2.8$. There are also processes producing one real photon and a QCD jet, such as $qg \to q\gamma$ (119 nb) and $q\bar{q} \to g\gamma$ (6 nb), which will fake a two-isolated-photon final state with a higher probability. Using the fact that in $H^0 \to \gamma\gamma$ decay there is very little energy around the γ rays (Fig. XII.1), an isolation cut is used to reject photons produced from fluctuations in jet fragmentation. The cut requires that the sum of the transverse energy in a cone of radius R=0.6, $(R = \sqrt{\Delta\eta^2+\Delta\varphi^2})$, excluding the transverse energy of the photon itself, is less than 10% of the transverse energy of the photon plus 5 GeV, $\Sigma E_T <$ (5 GeV + $E_T^\gamma/10$). By using this cut, the rate of one isolated photon from a jet is reduced by a factor of 10^4, and the rate of two isolated photons from two jets is thus reduced by a factor of 10^8.

Signals

Figure XII.3 shows the signal/background ratios of 5σ, 9σ, 15σ, and 27σ for Higgs mass of 80, 100, 120 and 150 GeV, respectively. Note that the central tracker information is used only to detect the presence of charge particles and the event vertex. This can be done with the scintillating fibers alone.

Remarks: In using the R cut by requiring $\Sigma E_T <$ (5 GeV + $E_T^\gamma/10$), we have assumed a perfect Monte Carlo program and that pile-up problems, beam gas problems, etc., can all be solved ideally. As often happens in experiments, the real situation is quite different. For example, in the search for the t-quark at hadron colliders, the QCD background was not accurately predicted until the data on b-quark production at CERN were used to tune the Monte Carlo programs (Ref. XII.6). To study our ability to detect $H^0 \to \gamma\gamma$, we have made different R cuts. Assume there are more backgrounds and pile-up so the energy in the R < 0.6 cone is much larger, and we must cut at much higher energy.

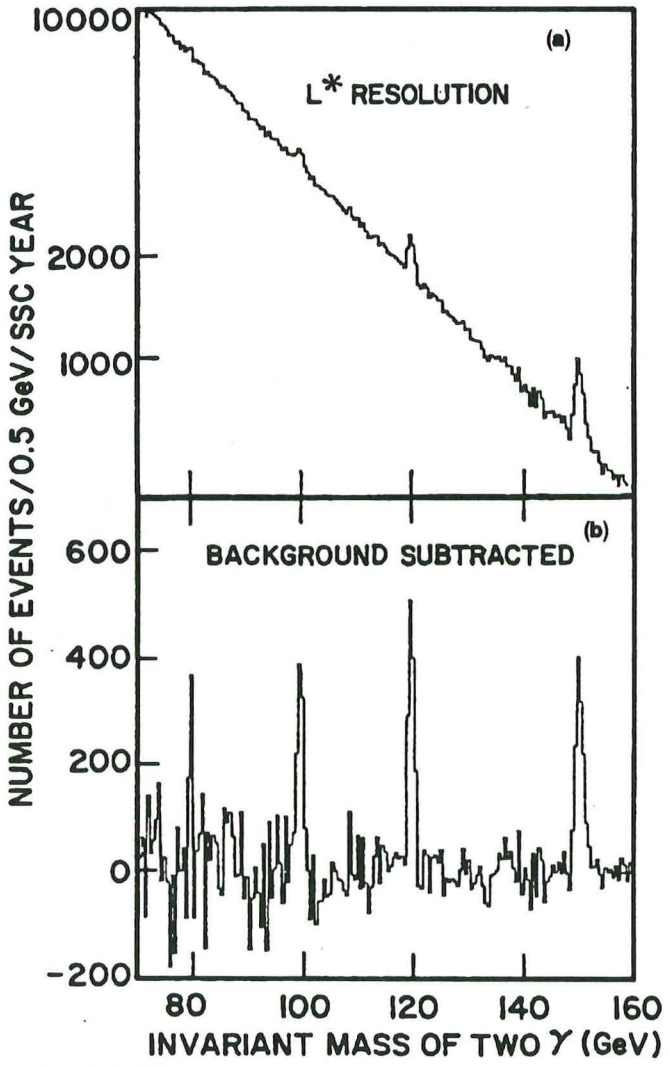

Fig. XII.3. $H^0 \to \gamma\gamma$ detection for L* electromagnetic calorimeters with (a) signal together with direct photon background, (b) signals after background subtraction.

(a)If $\Sigma E_T < (10\ GeV + E_T^{\gamma}/10)$,

then the 100 GeV $H^0 \to \gamma\gamma$ signal/background ratio will change from 9σ to 6σ.

(b) If $\Sigma E_T < (15\ GeV + E_T^{\gamma}/10)$

then the 100 GeV $H^0 \to \gamma\gamma$ signal/background ratio will be 4.1σ.

The results of (a) and (b) indicate that indeed we will be able to study $H^0 \to \gamma\gamma$.

$H^0 \to$ 4 Leptons, 140 GeV < M_H < $2M_Z$

The best signal for the Higgs in this mass range is the four lepton channel via the ZZ* intermediate state

$$p + p \to H^0 + X \to ZZ^* + X \to 4\ \text{leptons} + X,$$

where the Z* is virtual with mass $< (M_{Higgs} - M_Z)$. We generate events using ISAJET and select those leptons for which $P_T > 5$ GeV and $5 < \theta < 175°$. In addition, we require that the total visible energy, excluding leptons, be less than $(5\ GeV + E_\ell/10)$ within a cone of $R = 0.3$ around the lepton direction. The overall acceptance for Higgs is 58% after the above cuts. QCD events are rejected by this isolation cut and requirement $M_{\ell\ell} > 10$ GeV when applied to all four leptons.

The remaining background comes from the associated production of a Z^0 with a pair of heavy quarks, such as top quarks, where both decay semi-leptonically. The leptons from heavy quarks have little hadronic energy around them and thus are similar to the leptons from the virtual Z^*. Because the second pair of leptons comes from a real Z^0, one cannot use the Z^0 mass as constraints for either pair of leptons to reduce the heavy quark background.

The expected Higgs signal together with this background is shown in Fig. XII.4 for the L* resolution. As seen, the energy resolution is crucial in detecting the Higgs. No other experimental method, SSC or LHC, can detect the Higgs in this mass range.

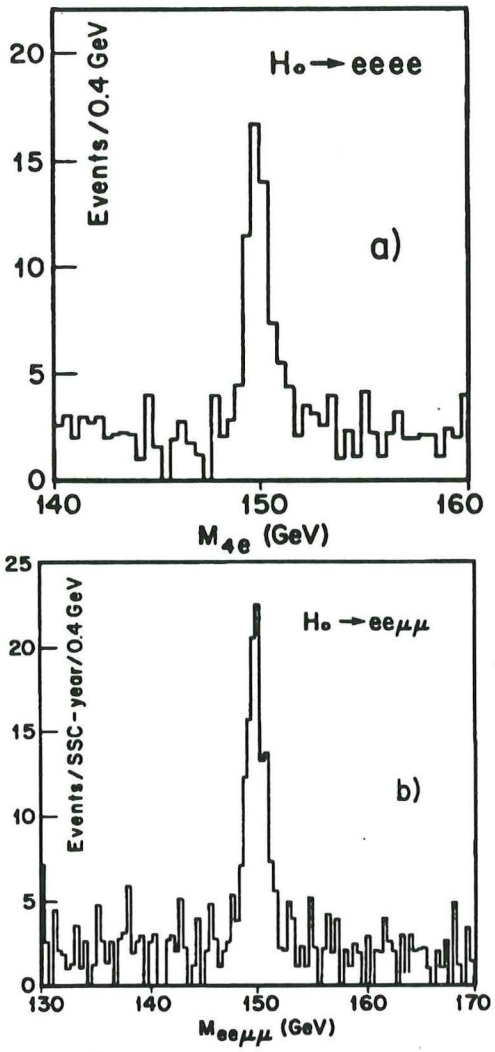

Fig. XII.4. $H^0 \to ZZ^* \to$ 4 leptons together with backgrounds.

B. 2. Search for the Higgs with $2M_Z < M_H < 800$ GeV

This is the mass region where the reaction $H^0 \Rightarrow$ 4 leptons is the cleanest channel to detect. The backgrounds are muons and electrons from QCD and electroweak processes.

Muon Backgrounds

Muons are from the following sources: (a) decays of c, b, and t quarks, (b) decay in flight of pions and kaons, (c) punchthrough, and (d) W and Z (or Drell-Yan) production.

The hadronic punchthrough was calculated for hadrons of various incident momentums with the GEANT Monte Carlo code. The probability of a particle exiting the electromagnetic + iron–silicon calorimeter (12 interaction lengths at 90°) was calculated, parametrized, and entered into the ISAJET Monte Carlo code. The punchthrough probability of about 10^{-4} for $p_{out}/p_{in} > 0.5$ is dominated by pion decay before interaction in the calorimeter and cannot be reduced by increasing the number of interaction lengths.

The single-muon inclusive rate, dN/dP_T (events per 5 GeV per SSC year) is shown in Fig. XII.5. It is dominated by prompt muons from heavy quark decays for $P_T >$ 25 GeV. The spectrum at large P_T is dominated by t-quark decays and is insensitive to the exact value of the t mass in the range of 100–200 GeV (we used $m_t = 140$ GeV). If the t-quark does not exist, then the single inclusive muon spectrum is about an order of magnitude lower.

The dimuon rate (muon $P_T > 5$ GeV) from QCD backgrounds (first three processes above) is 4×10^9 events per year. The 4-μ rate from QCD backgrounds is 6×10^6 events per year.

We have defined the following cuts to reject muon backgrounds:

(1) $P_T > 5$ GeV and momentum matching with the muon spectrometer, within two standard deviations and

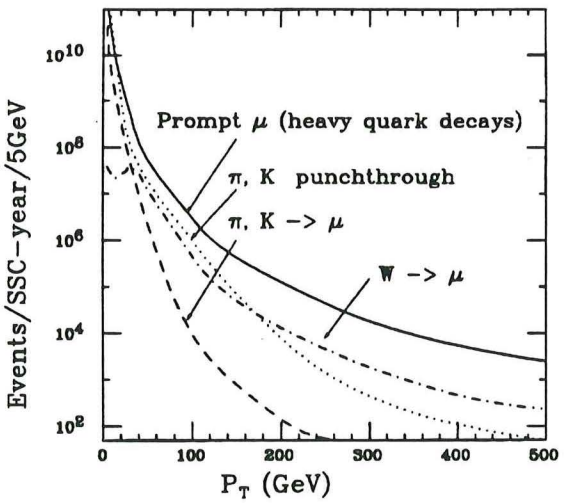

Fig. XII.5. Single muon rates and their origins.

(2) vertex matching, within three standard deviations. Momentum matching reduces the single-muon rate from punchthrough and decays by a factor of 20. Vertex matching reduces the single-muon rate from heavy quark decays by a factor of three.

(3) muon isolation, which reduces the single muon rate by about 20. We define a cone (R) about the muon axis in pseudorapidity (η) azimuthal-angle (φ) space as $R = \sqrt{(\Delta\eta^2 + \Delta\varphi^2)}$. We construct ΣP_T of all charged particles in the cone and have studied this variable ΣP_T as a function of the cone size. Events in which the muons arise from quark decays have a large value of ΣP_T because of the decay chain: $q \Rightarrow q' \mu\nu$. We have found that the optimum value of cone size for tagging quark decays is about $R = 0.3$. In this cone, we accept μ candidates with the condition $\Sigma P_T < [5\ \text{GeV} + P_T(\mu)/10]$. The isolation cut will reject the single muon background by a factor of 20 while removing only a few percent of the muons from Higgs decays for $200\ \text{GeV} < M_H < 800\ \text{GeV}$.

Electron Backgrounds

The prompt electron rates are the same as the prompt muon rates; however, the rate of misidentified (fake) electrons differs from the rate of muon backgrounds. The major source of fake electrons is from a π° and charged particle entering the same BaF_2 crystal. After the hadron calorimeter veto ($E_{had} < 0.1\ E_{em}$), the rate of fake electrons is comparable to the prompt electron rate.

The central tracker rejects the fake electrons by a factor of 10^2 from momentum-energy matching and an isolation cut will reject electrons from quark decays by a factor of 20.

Examples of Higgs Production

Fig. XII.6 shows the $H^0 \to 4\mu$ spectrum at Higgs mass of 400 GeV, with the backgrounds calculated from:

$$p\,p \to q\bar{q} + X \to 4\mu + X$$
$$\to Z^0 Z^0 + X \to 4\mu + X$$
$$\to Z^0 + X \to 4\mu + X.$$

We have selected the $H^0 \to 4\mu$ from the R cut requiring in $R = 0.3$ cone we have (excluding the transverse momentum of μ):

$$\Sigma P_T < [5\ \text{GeV} + P_T(\mu)/10]$$

Requiring all four muons to be isolated rejects the QCD background to a level well below ZZ continuum.

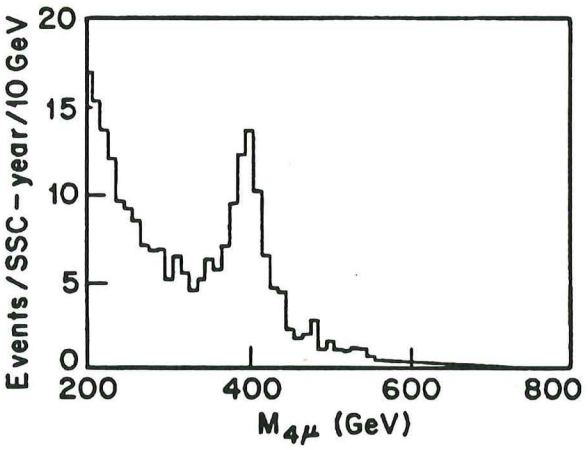

Fig. XII.6. $H^0 \to 4\mu$ with backgrounds rejected with muon isolation cuts.

Remarks: There are two distinct advantages of good μ resolution in this mass region: (1) It will enable us to measure the width of $H^0 \to 4\mu$ precisely. (2) More importantly, good μ resolution will enable us to control the background. To properly use the R cut experimentally, the following backgrounds in the R cone must be small:

(1) hadron spray from beam gas,

(2) muon spray from upstream of the intersection region,

(3) pile-up of events.

There is no reliable way before the start of the experiment to check this.

Indeed, our experience in the past at ISR with luminosity 10^{31} has indicated that these are difficult problems to solve for clean lepton experiments.

In the case the energy background and pile-up in the R cone is much larger than predicted, we must depend on the L* ability to select muon events in the Z^0 mass peak to observe the $H^0 \to Z^0 Z^0 \to 4\mu$ signal.

In Fig. XII.7a, we assumed the $H^0 \to 4\mu$ signal of Fig. XII.6 with a background that is 10 times worse than the ideal Monte Carlo prediction, and we used a cut

$$\Sigma P_T < [50\ \text{GeV} + P_T(\mu)/10]$$

and in this way we select $\mu\mu$ events by requiring they come from $M_{Z^0} \pm 2$ GeV (at $P_\mu = 100$ GeV the momentum resolution is $\Delta P\mu/P\mu \leq 0.5\%$). Compared with Fig.

XII.6, the low mass background in Fig. XII.7a is still higher than in Fig. XII.6, but the background above 300 GeV is essentially unchanged. Figure XII.7b shows that if we only have a muon momentum resolution of ≈10% and can only select $\mu\mu$ in the mass region $M_{Z^0} \pm 20$ GeV, we will not be able to see the $H^0 \to 4\mu$ signal.

Remarks: We have studied the case of collecting more events for the reaction $H^0 \to 4\ell$ by performing the experiment at $10^{34}cm^{-2}sec^{-1}$. In this case, we will use only the scintillating fiber information in the central tracker to locate the vertex. The signal/background ratio shown in Fig. XII.7a is essentially unchanged. The yield will increase 10 times.

B. 3. If Mass of H^0 > 1 TeV or There Is No Higgs

If there is no Higgs with mass <1 TeV, then the production of

$$pp \to Z^0(\mu\mu)\, Z^0(\mu\mu) + \ldots \quad (1a)$$

$$pp \to Z^0(\mu\mu)\, Z^0(q\bar{q}) + \ldots \quad (1b)$$

$$pp \to W^{\pm}(q\bar{q})\, Z^0(\mu^+\mu^-) + \ldots \quad (2)$$

$$pp \to W^{\pm}(\mu\nu)\, Z^0(\mu^+\mu^-) + \ldots \quad (3)$$

$$pp \to W^+(q\bar{q})\, W^-(\mu\nu) + \ldots \quad (4)$$

will increase with $M_{Z^0Z^0}$, $M_{W^{\pm}W^{\pm}}$, or $M_{ZW^{\pm}}$, and the longitudinal polarization of the weak bosons will also increase with the invariant masses. At mass region larger than 1 TeV, calculations of both the signal and background may be even less reliable. Nevertheless, the following properties of L* are important for the success of this type of experiment:

1. Speed of the detector response. At this mass, the yields of reaction (1)–(4) are small, so an experiment at $10^{34}cm^{-2}sec^{-1}$ may be neccesary. To do this, we will run the experiment only with the scintillating fibers in the central tracker, which have a typical response time of < 5 ns and provide the z coordinate accuracy of 1 cm. The speed of the calorimeter typically 10–15 ns may permit us to study hadron jets together with precision measurements of leptons up to the luminosity of $10^{34}cm^{-2}sec^{-1}$.
2. Identification of $Z^0 \to \ell\ell$. The best way to identify Z^0 is to isolate the Z^0 peak with a resolution comparable to the Z^0 natural line width, Γ. Therefore the measurement of the muon momenta P_1 and P_2 with opening angle ϑ must satisfy:

$$\frac{\Delta m}{m} \cong \frac{1}{2}\left[\left(\frac{\Delta P_1}{P_1}\right)^2 + \left(\frac{\Delta P_2}{P_2}\right)^2 + \left(\frac{\Delta\vartheta}{\tan\frac{\vartheta}{2}}\right)^2\right]^{1/2}$$

$$< \frac{\Gamma_{/2.3}}{m_z} \cong 1.22\%$$

The two muons from 500 GeV Z^0 decay form an opening angle typically $\vartheta = 21°$. From multiple scattering in the calorimeter, we have $\Delta\vartheta/\tan\vartheta/2 \cong 0.7\%$ at $\vartheta = 21°$. We conservatively require $\Delta P/P \cong 1.2\%$ at 250 GeV (or $\Delta P/P = 2.4\%$ at 500 GeV), which is our design goal.

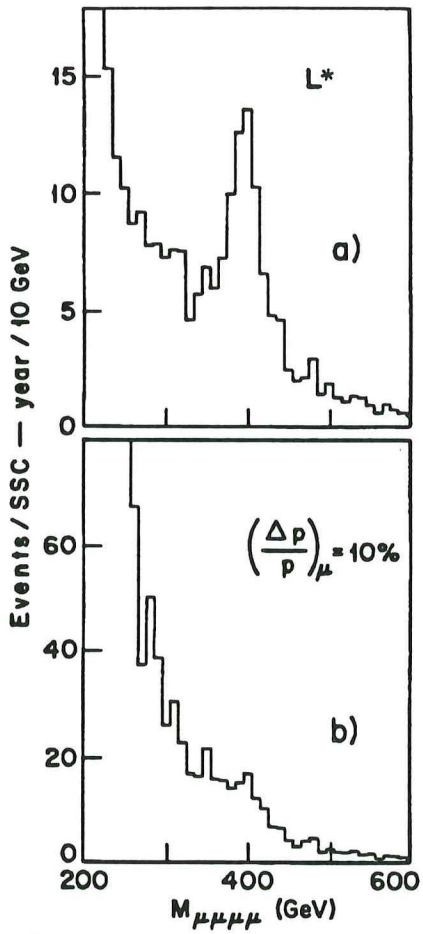

Fig. XII.7. $H^0 \to 4\mu$ together with backgrounds rejected by requiring μ pairs to have the Z-mass for (a) L* and (b) poorer resolution for one SSC year at 10^{33} $cm^{-2}sec^{-1}$.

3. Identification of $Z^0 \to q\bar{q}$ and $W^{\pm} \to q\bar{q}$. To obtain the best jet resolution comparable with the width of $W^{\pm}$ and Z^0 (≈2.5 GeV), the design of L* permits us to do the following:

(a) Remove BaF_2 and replace it with a fine sampling silicon or liquid scintillator calorimeter so that the entire hadron calorimeter is made from the same media. We have jet resolution $\Delta E/E = (50/\sqrt{E} + 1.0)\%$.

(b) Continue the experiment without modifications, if we have decided to use the LXe as electromagnetic calorimeter and tests show that we have obtained $e/\pi = 1$, and we have jet resolution $\Delta E/E = (50/\sqrt{E} + 1)\%$.

Because the detector is 4π this will enable us to reconstruct the $Z^0 \to q\bar{q}$ and $W^{\pm} \to q\bar{q}$ decays with mass resolution of ≈2 GeV. We can also reconstruct the $W^{\pm} \to \mu\nu$ decay by measuring the missing energy to locate the neutrino P_T.

Properties 1, 2, and 3 above give us the best arrangement to study reactions (1)–(4), as well as longitudinal polarization of Zs and Ws.

B. 4. Search for Narrow Dilepton Resonances

There are models (such as E_6, see Ref. XII.7) predicting the existence of Z′ with a very narrow width typically $\Gamma_{Z'/M'} = 0.65\%$ to 3.8%.

Using the electromagnetic detector (1% resolution), we can measure the width of $Z' \rightarrow e^+e^-$. Because at P = 7.5 TeV our muon detector provides $\Delta P/P = 36\%$, we can measure the forward-backward charge asymmetry for $Z' \rightarrow \mu^-\mu^+$ up to $M_{Z'} = 15$ TeV.

Remarks: It is important to remember that physics changes quickly. In ten years, the examples presented here will most likely no longer be considered relevant. These examples only serve as an illustration of the detector capability to search for new phenomena at the SSC.

References

[XII.1] J. Ellis, T. Sjostrand, and J. Zwirner, discussion at CERN, May 16, 1990.
[XII.2] H. Benson and T. Sjostrand, A Manual to the Lund Monte Carlo for Hadronic Processes, PYTHIA version 5.3, November, 1989.
[XII.3] F. Paige and S.D. Protopopescu, ISAJET 6.28 A Monte Carlo Event Generator for PP and $\bar{P}P$ Reactions, April, 1990.
[XII.4] D. Dicus and S. Willenbrock, Phys. Rev. D37 (1988) 1801.
[XII.5] The cross-section of $H^0 \rightarrow \gamma\gamma$ is scaled up by a factor of two according to J. Stirling (private communication).
[XII.6] C. Albajar et al., Zeit. Phys. C37, 489 and 505 (1988).
[XII.7] F. del Aquila et al., Nucl. Phys. B287, 419 (1987).

Conclusion:

Taste, experience, and judgement in experimental physics come slowly with time. After working for the last 25 years on electrons, muons, and photons at the electron synchroton (DESY), proton synchroton (BNL); high luminosity proton-proton collider (ISR), and electron-positron collider (LEP) we express our interest to continue this type of experiment at the SSC, mainly to explore the unknown.

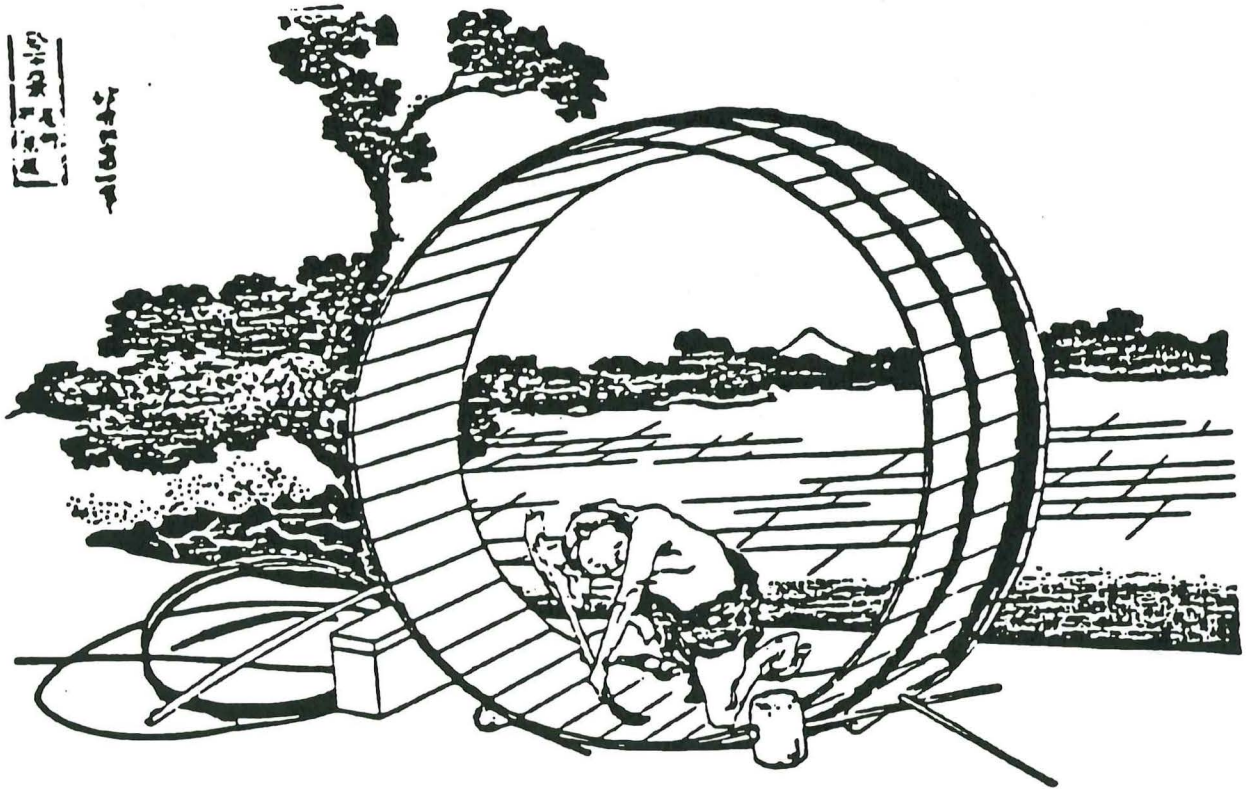

Expression of Interest to the

Superconducting Super Collider Laboratory

by the

L★ COLLABORATION

May 1990

Expression of Interest

to the Superconducting Super Collider Laboratory by the L* Collaboration

May 1990

The University of Alabama, Tuscaloosa, Alabama, USA
L.Baksay, J.Bussenitz, D.DiBitonto, L.Jurkins, X.Liu, T.Pennington, M.Timko, D.Whitcomb, L.Wurtz, Y.Yu

The University of South Alabama, Mobile, Alabama, USA
K.Clark, M.Jenkins

The University of Alabama, Huntsville, Alabama, USA
J.Gregory, Y.Takahashi

The University of Alabama, Birmingham, Alabama, USA
J.Harrison, E.Robinson

Auburn University, Auburn, Alabama, USA
J.Williams

The University of Central Arkansas, Conway, Arkansas, USA
H.Woolverton

Lawrence Livermore National Laboratory, Livermore, California, USA
E.Ables, R.Bionta, H.Britt, A.Chargin, G.Dale, O.Edwards, O.Facklar, J.Helm, C.Herring, D.Matlowicki, J.Miller, M.Mugge, W.Nail, H.S.Park, S.Shen, S.Sierakowski, K.Skulina, D.Stack, W.Stolz, R.Vidal

California Institute of Technology, Pasadena, California, USA
M.Chen, G.Gratta, D.Kirkby, R.Mount, H.Newman, R.Y.Zhu

University of California, San Diego, California, USA
J.S.Branson, M.Hebert, E.Shaer, X.Sopczak

Purdue University, Lafayette, Indiana, USA
A.Bujak, L.Gutay, T.McMahon

Indiana University, Indiana, USA
M.Gebhard, R.Heinz, A.Komives, L.Miller, S.Mutson, J.Musser, G.Spiczak, G.Turner

Johns Hopkins University, Baltimore, Maryland, USA
H.Akbari, J.Bao, C-Y.Chien, G.Feldman, T.Fulton, C.W.Kim, J.F.Kitmanis, J.D.Orndorff, A.Pevsner, W.J.Spencer, C.Spetsios, A.Szalay

Boston University, Boston, Massachusetts, USA
S.Ahlen, G.Bauer, J.Beatty, J.Brooks, T.Coan, M.Felcini, J.Hu, D.Levin, W.Lu, A.Marin, S.Otwinowski, D.Osborne, J.Rohlf, D.Warner, B.Zhou

Harvard University, Cambridge, Massachusetts, USA
K.Kamer, P.McBride, J.Schuessa, K.Strauch

Massachusetts Institute of Technology, Cambridge, Massachusetts, USA
A.L.Anderson, U.Becker, P.Berges, J.D.Burger, Y.H.Cheng, M.Chen, I.Clare, R.Clare, T.S.Dai, F.J.Eppling, M.Fukushima, M.P.J.Gaudreau, K.Ghoni, C.Grimm, E.S.Hafen, P.Hertzog, G.Herten, A.Kerman, T.Kramer, T.Lanius, D.Luckey, P.Marsden, D.B.Montgomery, I.A.Pless, J.M.Qian, M.Saraiznov, S.M.Shobbin, M.Stauer, J.D.Sullivan, K.Sumorok, J.Tang, Samuel C.C. Ting, S.M.Ting, T.J.Wenaus, M.White, S.X.Wu, S.Wynhoff, C.H.Ye

The Charles Stark Draper Laboratory, Cambridge, Massachusetts, USA
R.Arruda, J.Barry, E.Bart, M.Fury, M.Hanebery, T.Hines, G.Holden, F.Nimblett, J.Paradiso, W.Toth, L.Wilk

University of Mississippi, University, Mississippi, USA
L.Cremaldi, J.Furgeson, S.Harper, J.Reidy, J.Zhang

Mississippi State University, Starkville, Mississippi, USA
L.Craft, S.Flerchy

Jackson State University, Jackson, Mississippi, USA
F Lee

Princeton University, Princeton, New Jersey, USA
J.Bakken, M.Convery, P.Derwa, D.Lee, P. Proust, K.Read, H.Sucoka, D.Suckland, R.Sumner, D Wright

Los Alamos National Laboratory, New Mexico, USA
D Ables, R Barber, J Bosseveen, D.Carrasco, T.Carey, G.Dransfield, R.Ferber, P.Ferguson, V.Gavron, D.Giovanelli, R.Gupta, J Hanlon, S.Hecker, C.Hosford, J.Kapustinsky, W.W.Kinnison, E.Knapp, B.Konegsaard, R.Kruger, K.Lackner, A.Lapedes, D M.Lee, M Leitch, R.Lemons, R.Little, T Lopez, M.Matta, M.Merrigan, D.Metzger, W.O.Miller, G.Mills, F.A.Morse, J.M.Moss, E.Mottola, M.Merrigan, S.Newfield, R.Perkins, R.Prael, W.Rodriguez, S.P.Rosen, C.Sadler, V.D.Sandberg, G.H.Sanders, D.Sharp, R.Stanley, B.Smith, W.Sommer, G.Stephenson, D.Strottman, J.Sunier, T.Thompson, G.T.West, D.H.White, J.Williams, W.Wilson, K.Wolcestun, H.J.Zook

University of New Mexico, New Mexico, USA
J.Ellison, D.Finley, S.Humphries, R.H.Wiedemann

Columbia University, New York, USA
E.Aprile, Reshmi Mukherjee

LeCroy Corporation, Chestnut Ridge, New York, USA
M.Gorski, S.Maher, R.Sumner,

Carnegie Mellon University, Pittsburgh, Pennsylvania, USA
I.Brock, A.Engler, T.Ferguson, R.W.Kraemer, F.Lindo, C.Rippien, J.Smith, R.Sutton, H.Vogel

Brown University, Providence Rhode Island, USA
M.Aryal, A.De Silva, D.Rossi, M.Widgoff

University of Tennessee, Knoxville, Tennessee, USA
S.C.Berridge, W.M.Bugg, G.T.Condo, Y.C.Du, T.Handler, H.J.Hargis, E.L.Hart, R.Kroeger, A.Weidemann

Memphis State University, Memphis, Tennessee, USA
D.Franceschetti, S.Jahan, W.Jones

Vanderbilt University, Nashville, Tennessee, USA
S.Csorna

Oak Ridge National Laboratory, Oak Ridge, Tennessee, USA
D.J.Alexander, B.R.Appleton, P.E.Arakawa, J.B.Bell, F.E.Barnes, J.M.Barnes, M.L.Bauer, R.L.Beatty, J.A.Blank, L.A.Boatner, C.Bottcher, H.A.Brashear, C.R.Brinkman, T.J.Burns, J.G.Carter, S.C.Chakoumakos, M.M.Chiles, J.E.Chosta, L.G.Christophorou, F.E.Close, H.O.Cohn, R.I.Crutcher, F.C.Davis, R.E.DePew, J.H.DeVan, T.H.Dunigan, M.S.Emery, H.Felcias, T.A.Gabriel, T.A.Herrick, M.J.Hollis, D.T.Ingersoll, J.O.Johnson, J.W.Johnson, H.E.Knee, D.F.Kuban, R.J.Lauf, D.L.McCorkle, S.A.McElhaney, D.L.McElroy, J.W.Moore, F.Plasil, R.T.Primm II, M.J.Rennich, R.T.Santoro, T.E.Shannon, B.H.Singletary, V.K.Sikka, T.P.Skreen, M.S.Smith, J.W.Stapleton, M.R.Strayer, R.W.Swindeman, A.W.Trivelpiece, J.R.Tuck, J.F.Wendelken, D.M.Williams, A.C.Williamson, A.Wrenberg, C.Y.Wong, K.G.Young

University of Utah, Salt Lake City, Utah, USA
H.Bergeson, M.Solomon

Howard University, Washington DC, USA
R.M.Catchings, J.Lindesay

University of Geneva, Geneva, Switzerland
M.Bourquin

Swiss Federal Institute of Technology, Zürich, Switzerland
H.Anderhub, J.Behrens, A.Biland, M.Dhina, G.Faber, M.Fabre, R.Fabbretti, K.Freudenreich, M.Hasinoff, H.Hofer, U.Horvath, E.Isiksal, M.Jongmanns, H.Jung, J.Lecoq, P.Lecomte, P.LeCoultre, L.Li, X.Lue, M.MacDermott, M.Maolinbay, O.McNally, M.Pohl, G.Rahal-Callot, P.Razis, H.Rykaczewski, D.Ren, S.Spiess, H.Suter, J.Ulbricht, G.Viertel, H.VonGunten, S.Waldmeier, J.Weber, L.Zehnder

LAPP, Annecy, France
J.J.Blaising, R.Morand, M.Schneegans, M.Vivargent

Physics Institute, RWTH Aachen, Germany
P.Blömeke, M.Buchholz, E.Couig, H.Hesn, K.Hilgers, W.Karpinski, H- H.Kleinmanns, O.Kornet, W.Kranz, T.Lehmann, K.L.Löbestemeyer, T.Meinholz, D.Pandoulas, J.Y.Pei, M.Pohlmer, R.Siedling, D.Schmitz, K.Schmiemann, M.Schöntag, A.Schultz von Dratzig, J.Schwenke, G.Schwering, M.Topporowsky, W.Wallraff, W.Xiao, Y.Zang, J.Zhou

Central Research Institute for Physics of the Hungarian Academy of Sciences, Budapest, Hungary
Gy.Barczo, E.Dénes, E.Nagy, J.Tóth, L.Urbán

INFN and University of Florence, Florence, Italy
A.Baldini, M.Boccaleri, M.Bruzzi, A.Cartacci, G.Ciancaglini, C.Civinini, R.D'Alessandro, E.Gallo, M.Meschini, M.Pieri, P.Spillantini, J.F.Wang

INFN and University of Milan, Milan, Italy
E. Borchi, A. Penzo, P. G. Rancoita, L. Riccati, A. Villari, L. Viarani

INFN, Naples and University of Naples, Naples, Italy
A. Alocco, M. G. Alviggi, E. Brambati, G. Chiefari, R. De Asmundis, E. Drago, V.Innocente, S. Lanzano, L. Merola, M. Napolitano, S. Patricelli, C. Sciacca

University of Rome, Rome, Italy
L. Barone, S. Borgia, F. Ceseroni, F. De Notaristefani, E. Longo, G. Mirabelli, S. Morganti

Tata Institute of Fundamental Research, Bombay, India
T.Aziz, S.Banerjee, S.R.Chendvankar, S.N.Ganguli, S.K.Gupta, A.Gurtu, A.K.Jain, P.K.Malhotra, K.Mazumdar, R.Raghavan, K.Shankar, K.Sudhakar, S.C.Tonwar

Joint Institute for Nuclear Research (JINR), Dubna, USSR
E.Belyakova, A.Chepistov, A.Cheremukhin, S.Dolya, V.Dumin, Yu.Ershov, N.Fedeev, A.Feshchenko, V.Genchev, L.Gershtein, I.Golutvin, N.Gorbunov, L.Gramenitsky, I.Ivanchenko, M.Kadykov, V.Kalegin, A.Karev, V.Kartvelishvili, M.Kazarinov, S.Khabarov, V.Khabarov, Yu.Kiryushin, D.Klein, V.Krivokhizhin, V.Kukhtin, R.Lednicky, I.Lukyanov, V.Lysyakov, A.Malakhov, V.Mikhailov, N.Nogaytsev, V.Ochkurov, V.Peresypkin, D.Peshekhonov, V.Peshekhonov, D.Pose, V.Prichodko, A.Prokesch, A.Rashevsky, I.Savin, S.Sergeev, M.Shabratov, L.Shipatz, A.Skvorets, G.Smirnov, D.Smolin, V.Sviridov, G.Sukhanov, A.Vishnevsky, Yu.Yazlovetsky, O.Zaimidoroga, M.Zamyatin, A.Zarubin, V.Zhiltsov, E.Zubarev

Leningrad Nuclear Physics Institute, Leningrad, USSR
V.Andreev, A.Denisov, Y.Dolushkin, V.Ivochkin, V.Jenovsky, A.Kaschuk, V.Khoze, A.Krivshich, P.Levchenko, V.Mayorov, A.Nadtochy, V.Razmyslovich, Y.Ryabov, V.Samsonov, A.Semenov, V.Schegelsky, A.Schastovsky, Y.Solomonov, A.Sheverdyaev, N.Smirnov, E.Spiridenkov, V.Suvorov, A.Tsaregorodtsev, G.Velichko, S.Volkov, A.Vorobyov, An.Vorobyov, Y.Zaitsev

Institute of Theoretical and Experimental Physics, ITEP, Moscow, USSR
A.Arefiev, A.Artamonov, A.Babaev, V.Bocharov, S.Burov, N.Byerov, M.Chumakov, A.Dolgolenko, V.Dolgoshein, V.Ehrenfeld, V.Eichenin, A.Epifantsev, A.Fedotov, Yu.Gaponenkov, V.Gemanov, P.Gorbunov, A.Gordeev, S.Gordeev, P.Gorichev, Yu.Gorodkov, E.Grigoriev, R.Gurin, Yu.Kamyshkov, V.Khovansky, Yu.Kirillov, A.Klimentov, Yu.Komaritsyn, V.Kouznetsov, A.Kovalenko, S.Krutchinin, M.Kubantsev, A.Kuchinskiy, A.Kurilin, V.Lebedenko, I.Matchanova, A.Malinin, S.Marmonov, A.Mastbaumov, V.Morgunov, A.Nikitin, N.Penkin, V.Pismenov, V.Ryasnin, V.Pojidaev, A.Rozkov, M.Ryabinin, I.Sadisky, A.Savin, M.Savitsky, A.Selivanov, V.Semachkin, V.Shamanov, P.Shagin, S.Shevchenko, V.Shevchenko, K.Shmakov, V.Shoutko, E.Shumilov, A.Smirnov, M.Solovov, S.Solomentsev, E.Tarkovsky, V.Tchudakov, I.Vasilyev, V.A.Vinogradov, V.S.Vinogradov, I.Vorobiev, V.Zaitsev, O.Zaitsovich, S.Zaitsovich, N.Zhvatov

Kurchatov Atomic Institute, Moscow, USSR
S.Baranov, A.Barkov, S.Belyaev, L.Bragin, N.Cherepistov, T.Chunyaeva, T.Devoyan, G.Dorofeev, V.Drozdov, V.Evdokimov, S.Frolov, E.Golubov, E.Grishin, A.Imanov, V.Karpov, I.Karpushov, E.Klimenko, A.Kochergin, V.Krugov, V.Kulyasov, Yu.Kuropatov, A.Kuznetsov, S.Lebedev, O.Lukyanov, Yu.Lukyanov, A.Matchejev, V.Martin, V.Martemyanov, N.Marovskiy, V.Martynenko, A.Matveyev, V.Matchmudov, E.Mukhina, A.Myagchilov, S. Novikov, A.Ogloblin, I.Ovchinnikov, S.Osetrov, V.Pavlyukov, V.Pobedinskiy, K.Polukeyich, V.Porugovsky, G.Rasserenov, N.Rodina, V.Ryabov, A.Saranov, M.Secov, V.Selivanov, B.Seregin, E.Shelaev, M.Solovyev, S.Sverchkov, S.Terentyev, E.Vasilchov, P.Volkov, A.Voropaev, P.Vorobiev, T.Vorobieva, M.Vyrodov, E.Vyscovsky, I.Zotov

Institute for High Energy Physics, Serpukhov, USSR
N.Fedyakin, A.Kozelov, R.Krasnokutsky, A.Lebedev, S.Medved, Yu.Mikhailov, E.Razuvaev, R.Shuvalov, E.Slobodyuk, A.Vasiliev

Institute of Nuclear Physics, Novosibirsk, USSR
L.Barkov, A.Skrinsky, E.Solodov

Yerevan Physics Institute, Yerevan, Armenia, USSR
N.Akopov, A.Amatuni, Ts.Amatuni, R.Avakyan, R.Avetyan, A.Avetisyan, G.Bayatyan, P.Gaburyan, A.Hagopyan, R.Kavlov, S.Kazaryan, S.Matinyan, G.Mkrtchyan, A.Oganesyan, J.Percyan, V.Pogosov, K.Shakhyarov, A.Shirinyan, S.Taroyan, N.Ter-Antonyan, G.Vartapetyan

Institute of Physics, Academy of Sciences of the Georgian SSR, Tbilisi
D.Chkareuli, G.Dvali, N.Mamaladze, G.Lezhava, P.Peiman, T.Lomtadze, A.Djavrishvili, E.Zadeidze, I.Iashvili, K.Aheladze, M.Sveradze, E.Ioramashvili, N.Roinishvili, L.Gabunya, L.Hvaniashvili

Institute of Physics, Academy of Sciences of the Estonian SSR, Tartu
L.Oja, H.Ulbo

Institute of High Energy Physics, Beijing, China
C.Chen, G.M.Chen, H.S.Chen, S.X.Feng, S.G.Gao, W.X.Gu, Y.F.Gu, Y.N.Guo, Y.Han, J.He, J.T.He, B.N.Jin, H.T.Li, J.Li, P.Q.Li, W.G.Li, X.G.Li, S.Z.Lin, Q.Liu, Y.S.Liu, Z.P.Mao, L.J.Pan, Z.M.Qian, G.Rong, Y.Y.Shun, X.W.Tang, K.L.Tung, J.H.Wang, L.Z.Wang, R.J.Wu, Y.G.Wu, Z.D.Wu, R.S.Xu, Y.D.Xu, S.T.Xue, C.G.Yang, C.Y.Yang, K.S.Yang, Q.Y.Yang, Z.Q.Yu, B.Y.Zhang, C.C.Zhang, D.H.Zhang, L.S.Zhang, S.Q.Zhang, D.X.Zhao, M.Zhao, Z.P.Zheng, G.Y.Zhu, Q.M.Zhu, Y.C.Zhu, Y.S.Zhu, H.L.Zhuang

Chinese University of Science and Technology, Hefei, China
H.F.Chen, Z.F.Gong, C.H.Gu, C.Li, Z.Y.Lin, W.G.Ma, C.R.Wang, X.L.Wang, Z.M.Wang, Z.Z.Xu, B.Z.Yang, J.B.Ye, X.Q.Yu, Z.P.Zheng

Shanghai Institute of Ceramics, Shanghai, China
X.L.Fang, P.X.Gu, J.K.Guo, C.F.He, G.Q.Hu, S.K.Hua, H.J.Li, J.L.Li, P.J.Li, Q.Z.Li, Z.L.Pan, D.Z.Shen, G.S.Shen, E.W.Shi, W.T.Su, X.X.Wang, Z.Y.Wei, Y.Y.Xia, L.Xu, Z.L.Xue, D.S.Yan, Z.W.Yin, X.L.Yuan, Y.F.Zhang, G.M.Zhao, Y.L.Zhao, W.Z.Zhong, R.M.Zhou

High Energy Physics Group, Taiwan, China
C.Chang, A.Chen, W.Y.Chen, H.Y.Cheng, Y.C.Gau, S.S.Gau, Y.Y.Lee, W.T.Lin, W.T.Ni, Y.D.Tsai, S.C.Yeh

Waseda University, Science and Engineering Research Laboratory, Tokyo, Japan
T.Doke, J.Kikuchi

Saitama College of Health, Saitama, Japan
K.Masuda

Kyungpook National University, Taegu, Korea
D.Son, S.K.Cha, J.K.Ko

Gyeongsang National University, Jinju, Korea
J.S.Song, I-G.Park, S-K.Choi, K.S.Chung

Chungnam National University, Daejeon, Korea
H.Y.Lee

Chonnam National University, Kwangju, Korea
J.Kim

Kangreung National College, Kangreung, Korea
D.W.Kim, G.S.Kang

Korea University, Seoul, Korea
J.S.Kang

Seoul National University, Seoul, Korea
J.Kim

Sangji College, Wonju, Korea
Y.Y.Keum

Taegu University, Taegu, Korea
D.S.Kim

Spokesperson:
Samuel C.C.Ting
MIT-LNS, Bldg.44
81 Vassar Street
Cambridge, MA02139, USA

Precision Lepton Detectors in the TeV region

dla

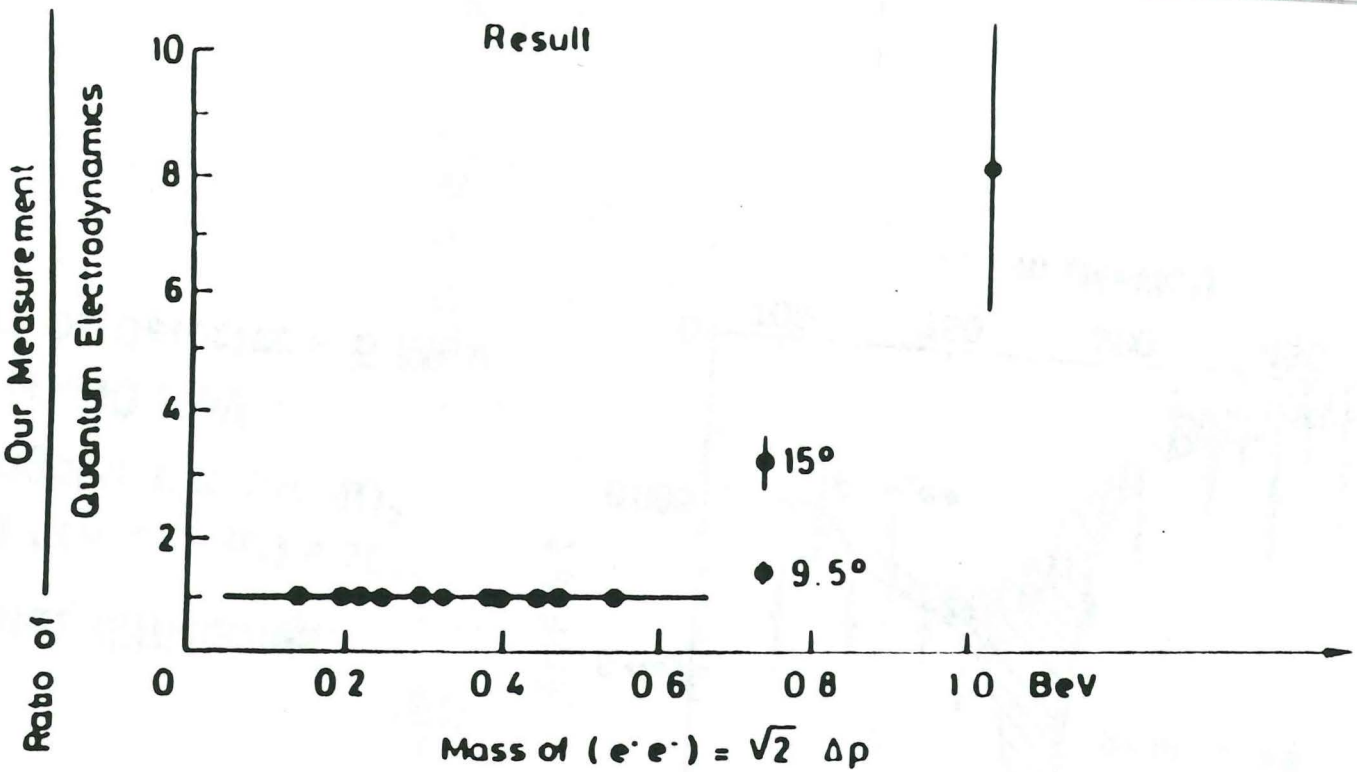
Result
Ratio of Our Measurement / Quantum Electrodynamics
10
8
6
4
2
0
15°
9.5°
0 2
0 4
0 6
0 8
1 0 BeV
Mass of (e⁺e⁻) = √2 Δp

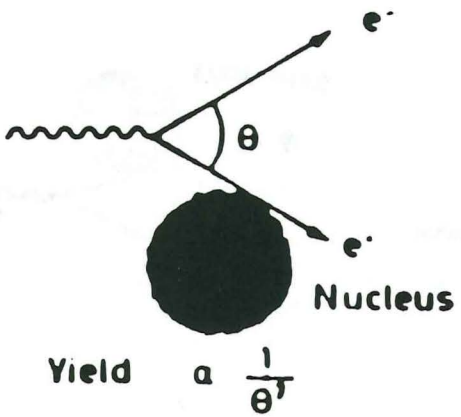
e⁻
θ
e⁻
Nucleus
Yield a 1/θ⁴

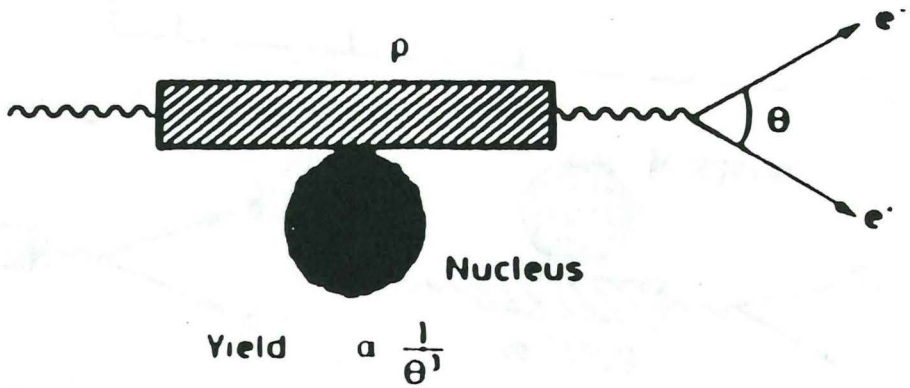
ρ
e⁻
θ
e⁻
Nucleus
Yield a 1/θ⁴

Interferences in Leptonic Decays.

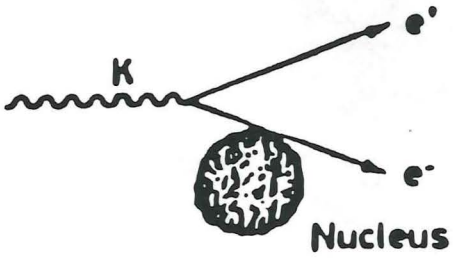

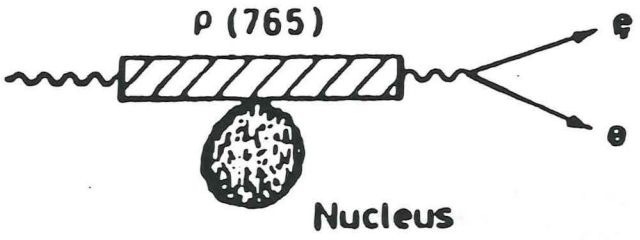

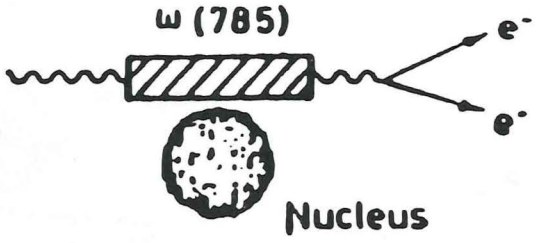

Experimental difficullies

1. $(\rho \rightarrow e^- e^+) / (\rho \rightarrow \pi^- \pi^+) \approx 10^{-5}$
   Rejection againt $\pi\pi >> 10^8$
2. Width of $\omega \sim 10$ MeV
   Resolution of delector ~ 5 MeV

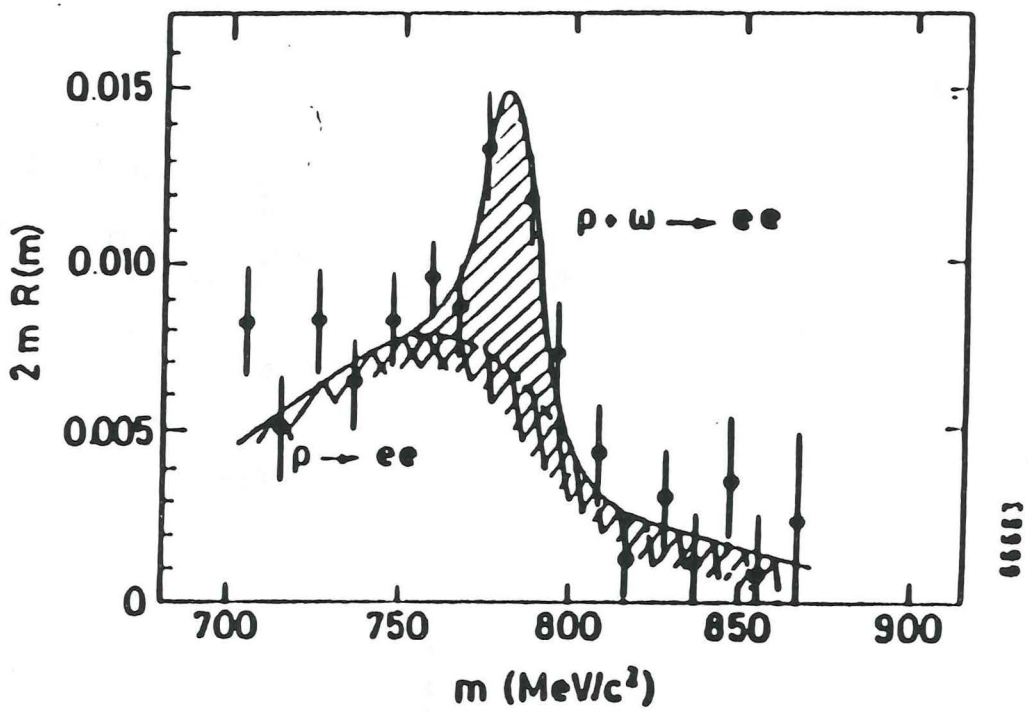

DESY

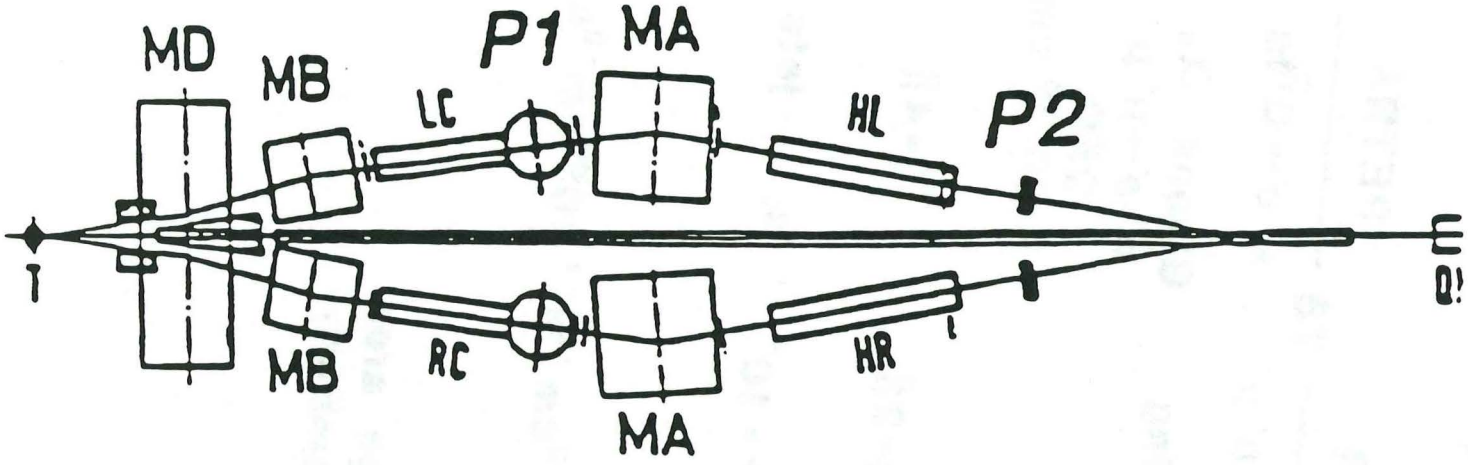

$P1 = P2$

25 Years of Electrons, Muons and Photons

64	DESY 72	BNL 74	ISR 78	PETRA 83	LEP 90
	$\gamma \to e^+ e^-$	$J \to e^+ e^-$	$p\ p \to \mu^+ \mu^-$	$e^+ e^- \to Q\bar{Q}g$	$Z^0 \to l^+ l^-, Q\bar{Q}$
	QED $R < 10^{-14}$ cm $\rho, \omega, \Phi \to e^+ e^-$ SU3	New Quarks	Scaling	Gluons - α_s $e^+ e^- \to \mu^+ \mu^-$ QED $R < 10^{-16}$ cm	3 Families g_A, g_V $B \to \mu + X$
	$\frac{\Delta M}{M} = 1\%$	$\frac{\Delta M}{M} = 0.1\%$	$\Omega = 2\pi$	$\Omega = 4\pi$	$\Omega = 4\pi$
	$\frac{ee}{hh} = 10^{-8}$	$\frac{ee}{hh} = 10^{-10}$	$\frac{\mu\mu}{hh} = 10^{-6}$	e, μ, jets	e, μ, γ $\frac{\Delta p}{p} = 1\%$
	$10^{35} cm^{-2} s^{-1}$	$10^{36} cm^{-2} s^{-1}$	$10^{32} cm^{-2} s^{-1}$	$10^{30} cm^{-2} s^{-1}$	$10^{31} cm^{-2} s^{-1}$
	$p_1 = p_2$	$p_1 = p_2$ high rate chambers	large area chambers		$p_1 = p_2$ (e, γ) $p_1 = p_2 + \Delta E$ (μ)

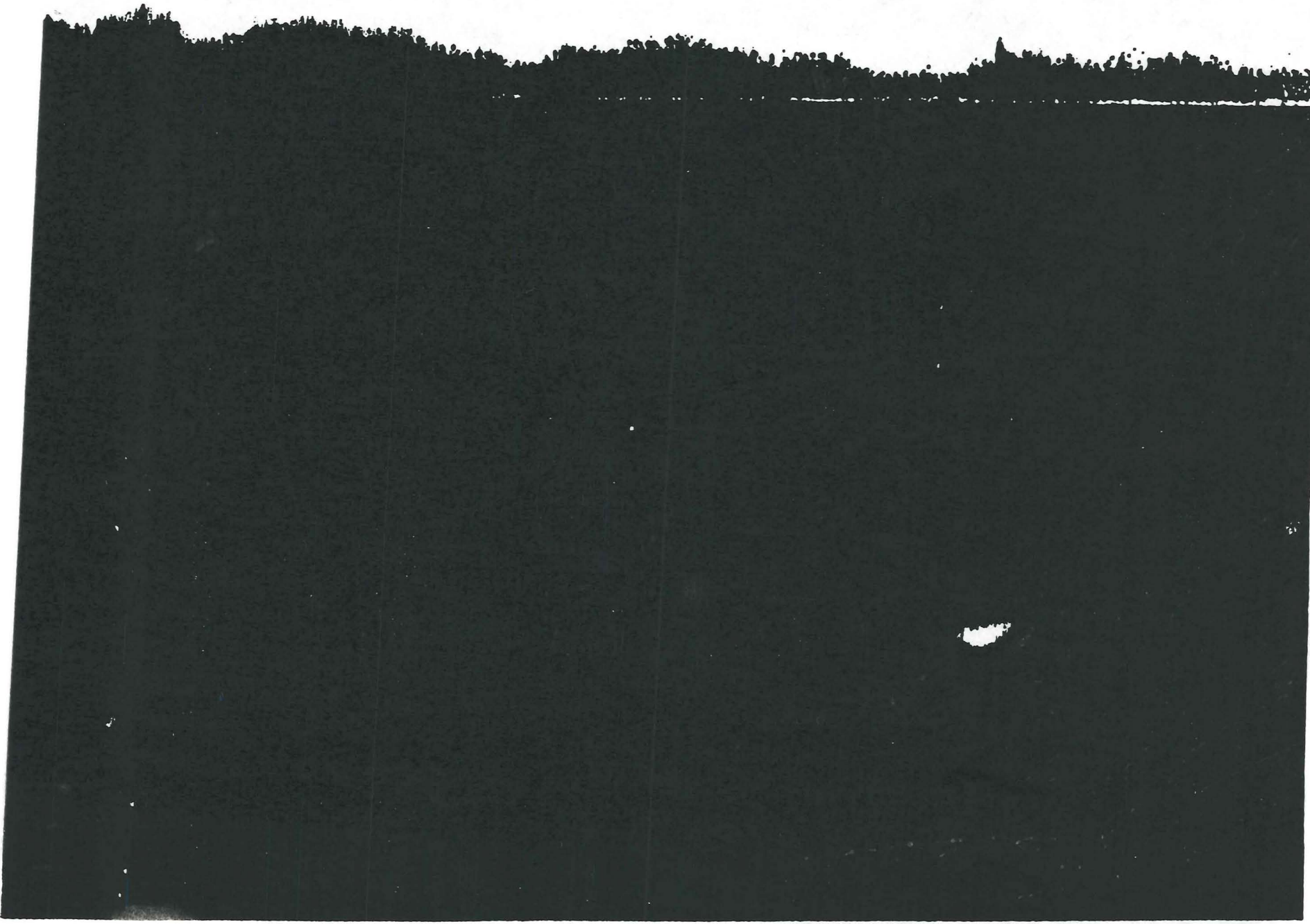

View of events

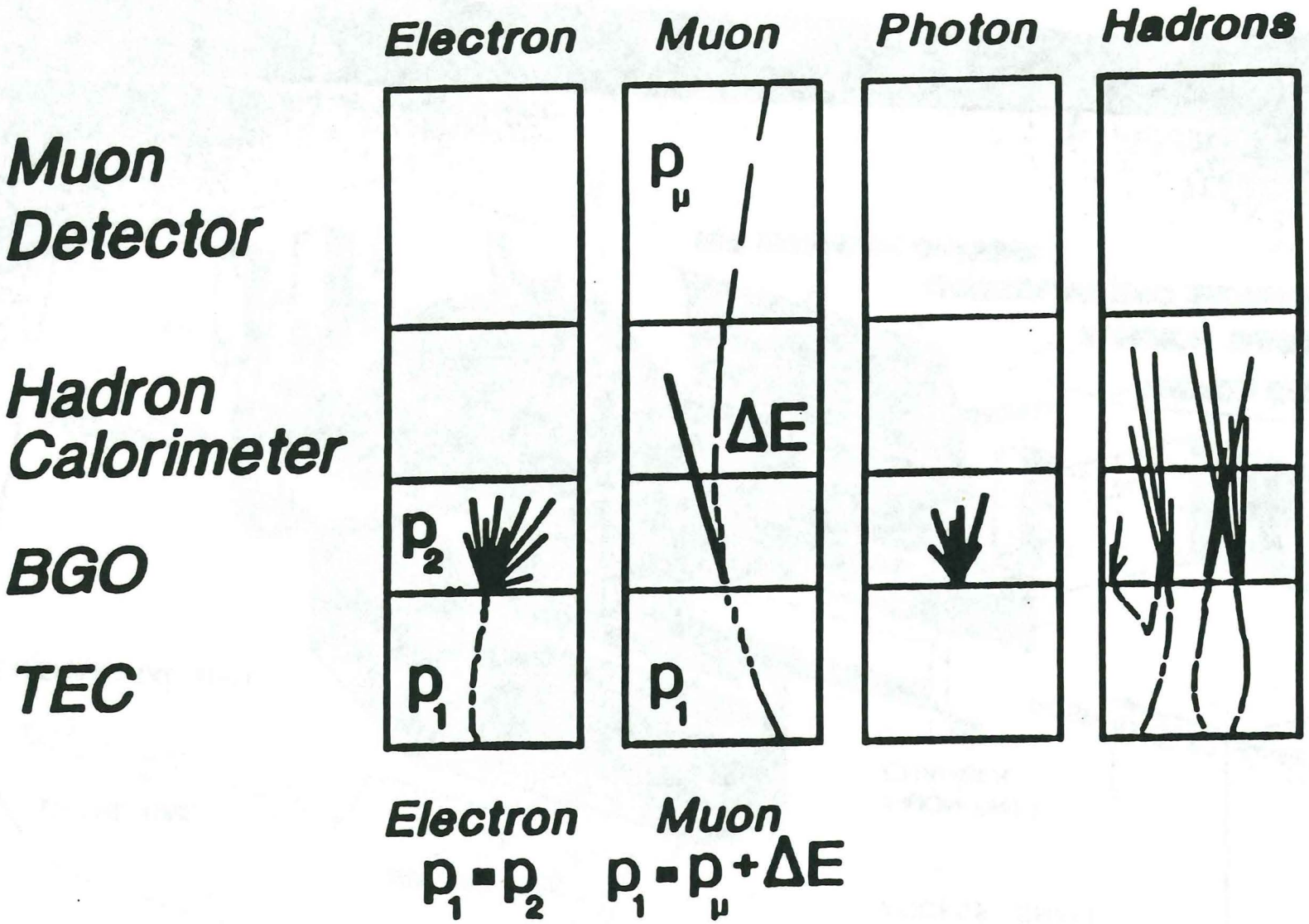

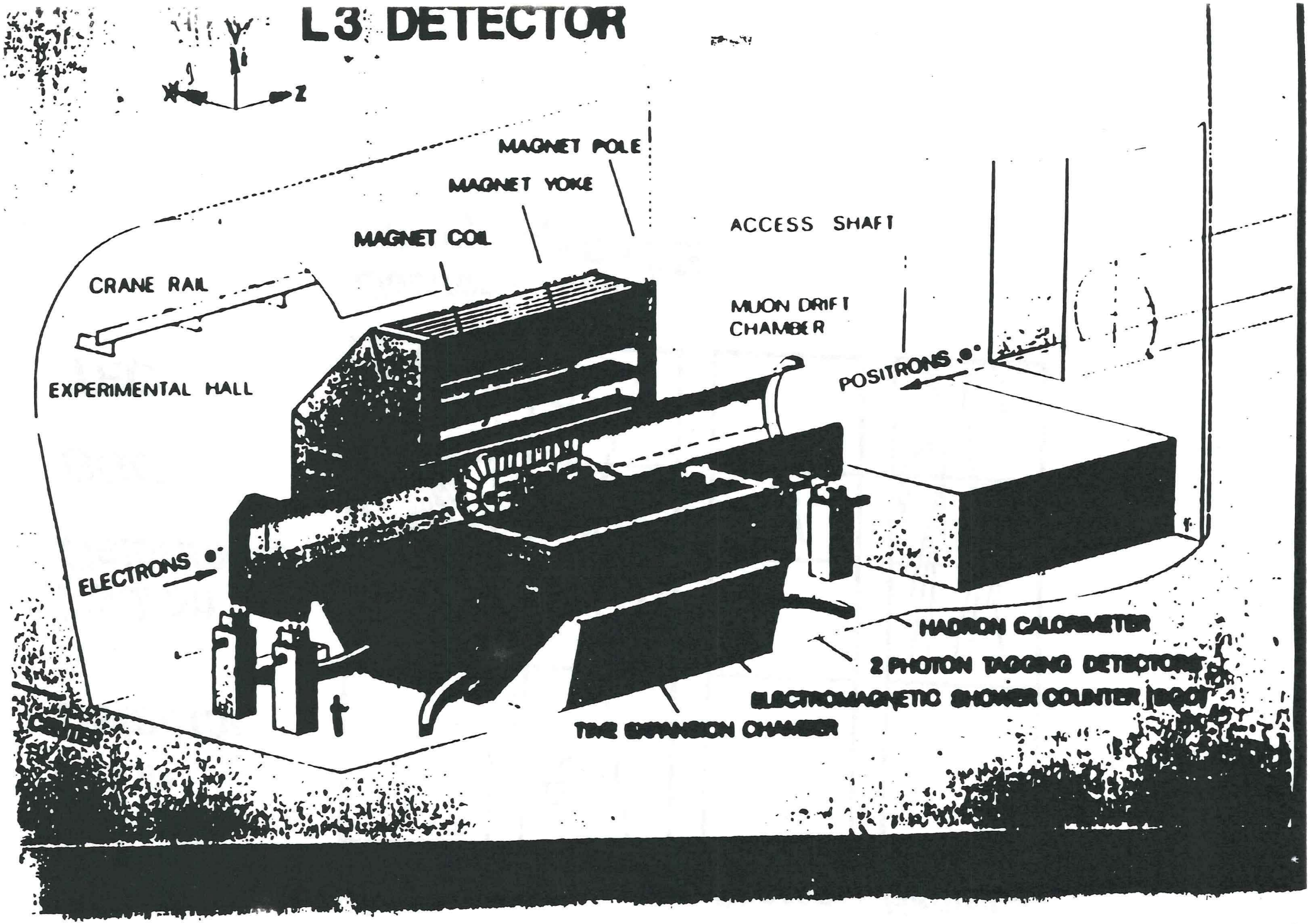
L3 DETECTOR
Z
MAGNET POLE
MAGNET YOKE
MAGNET COIL
ACCESS SHAFT
CRANE RAIL
MUON DRIFT CHAMBER
EXPERIMENTAL HALL
POSITRONS
ELECTRONS
HADRON CALORIMETER
2 PHOTON TAGGING DETECTORS
ELECTROMAGNETIC SHOWER COUNTER
TIME EXPANSION CHAMBER

L3

581 scientists.....40 institutes

L★

850 scientists.....70 institutes

$Z^0 \rightarrow$ hadrons

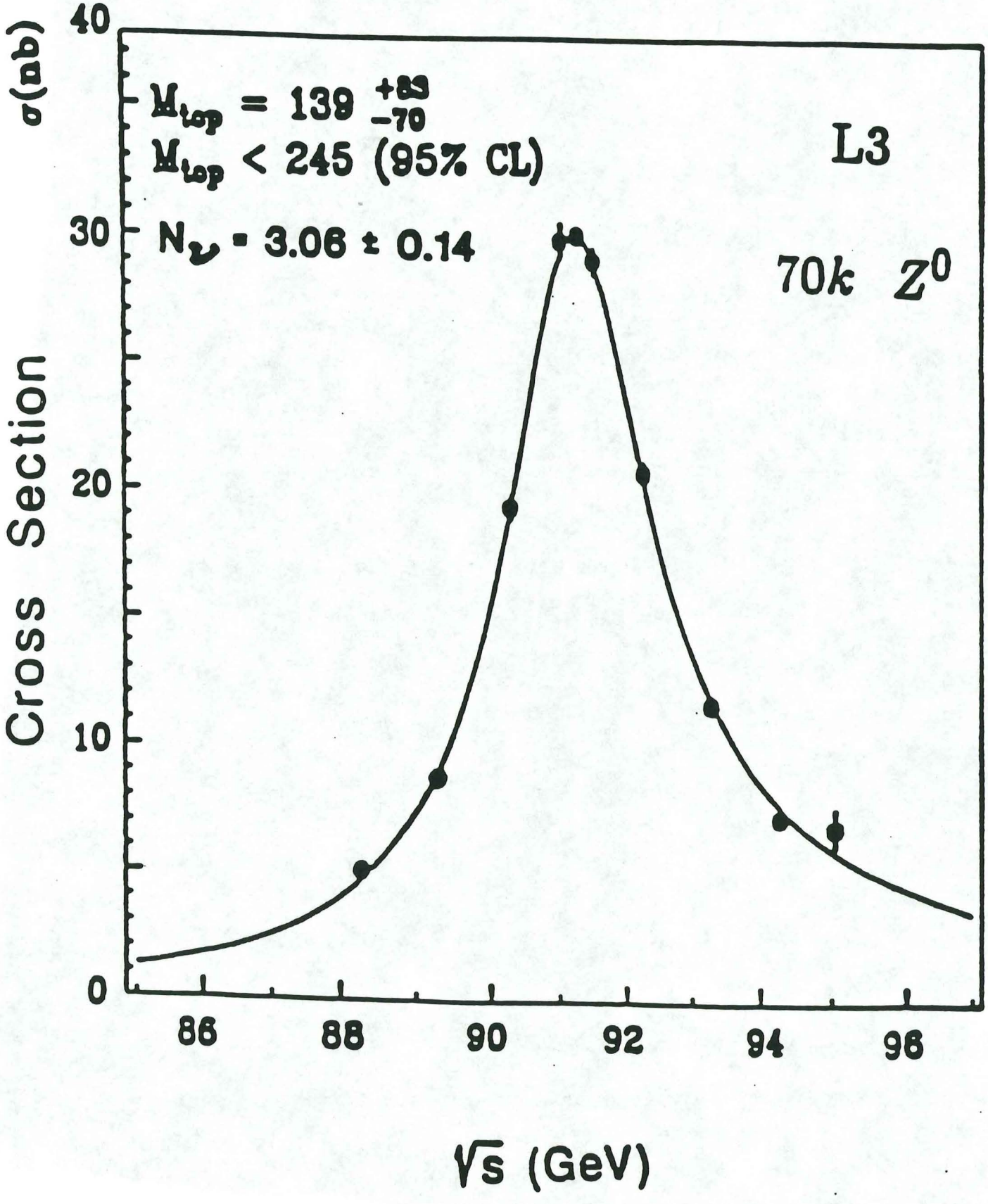

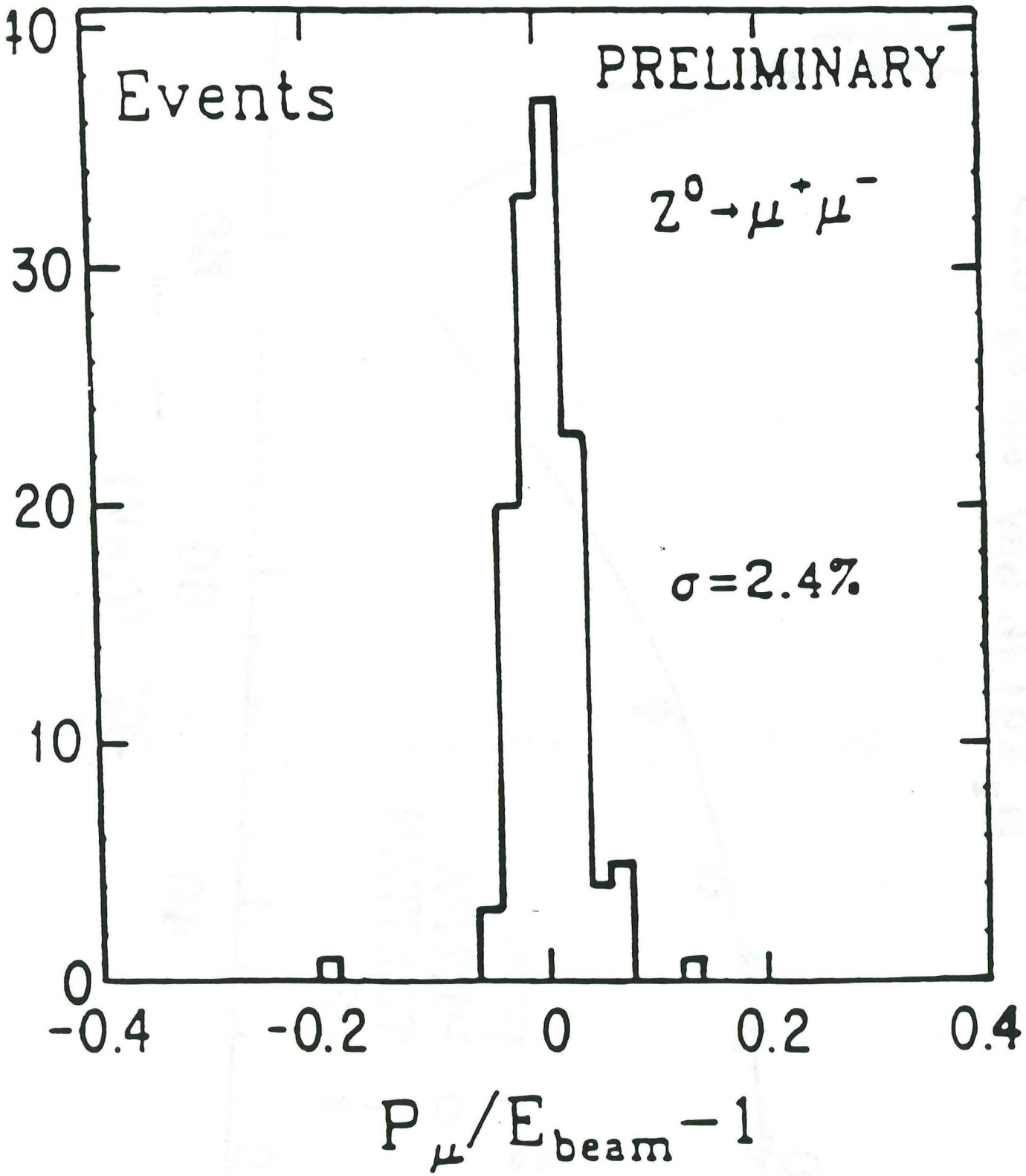
Events
PRELIMINARY
$Z^0 \to \mu^+\mu^-$
$\sigma = 2.4\%$
40
30
20
10
0
-0.4
-0.2
0
0.2
0.4
$P_\mu / E_{beam} - 1$

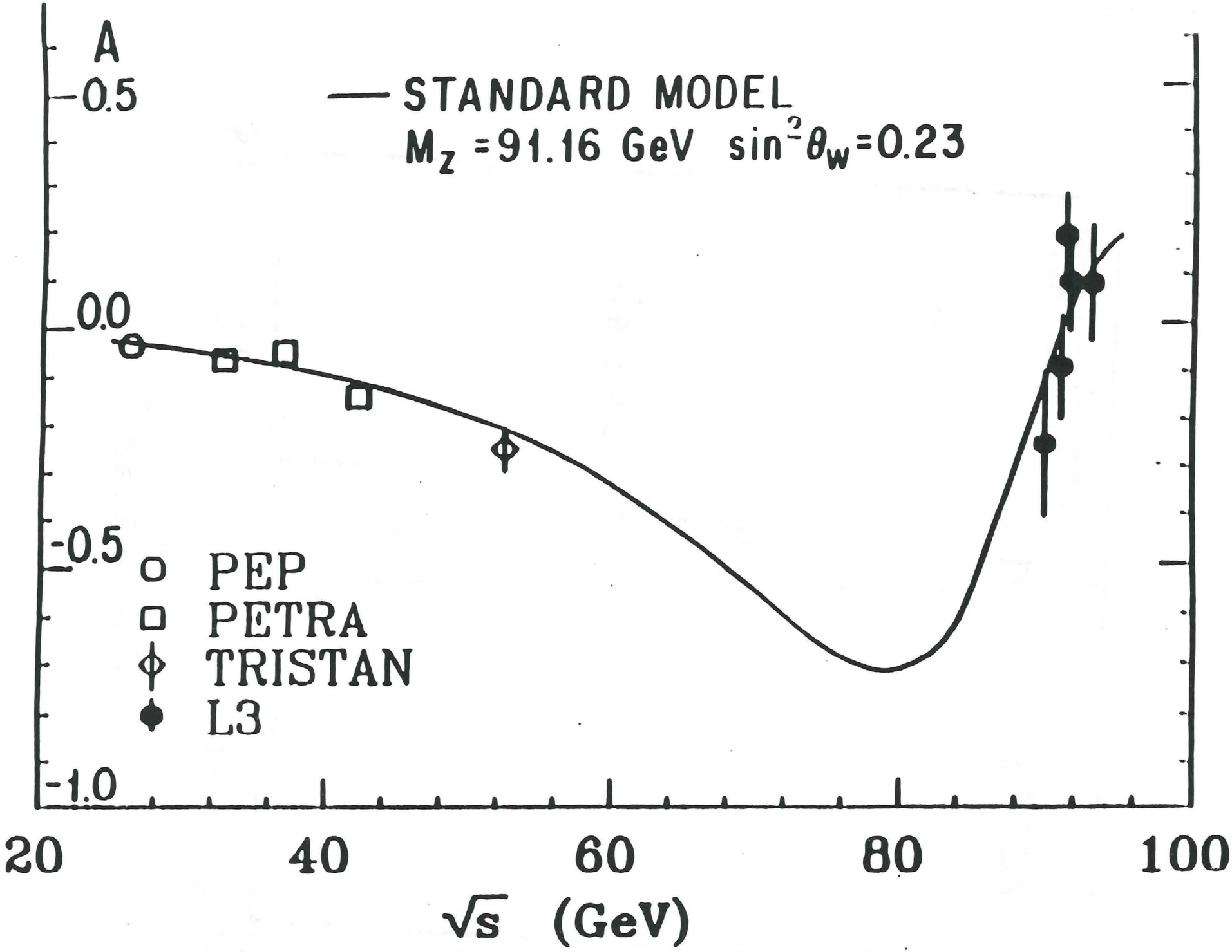
A
0.5
0.0
-0.5
-1.0
— STANDARD MODEL
M_Z = 91.16 GeV $\sin^2\theta_W$ = 0.23
PEP
PETRA
TRISTAN
L3
20
40
60
80
100
$\sqrt{s}$ (GeV)

$|_{\parallel}$ = 84.0 ± 2.0 MeV

$g_A = 0.499 \pm 0.007$

$g_V = -0.064^{+0.027}_{-0.019}$

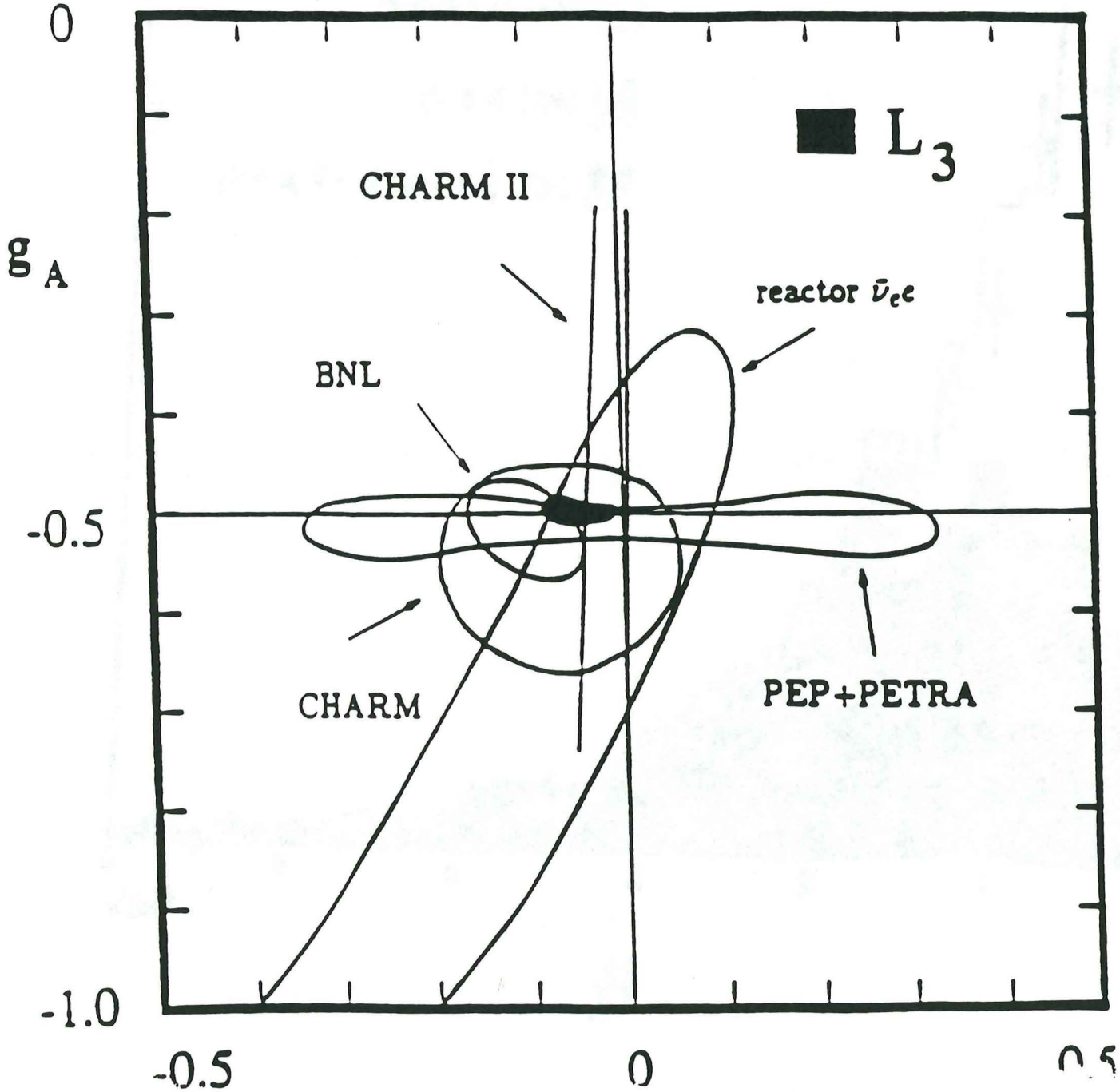

$A_{b\bar{b}}^{FB}$ = 13.5 % ± 5.4 %

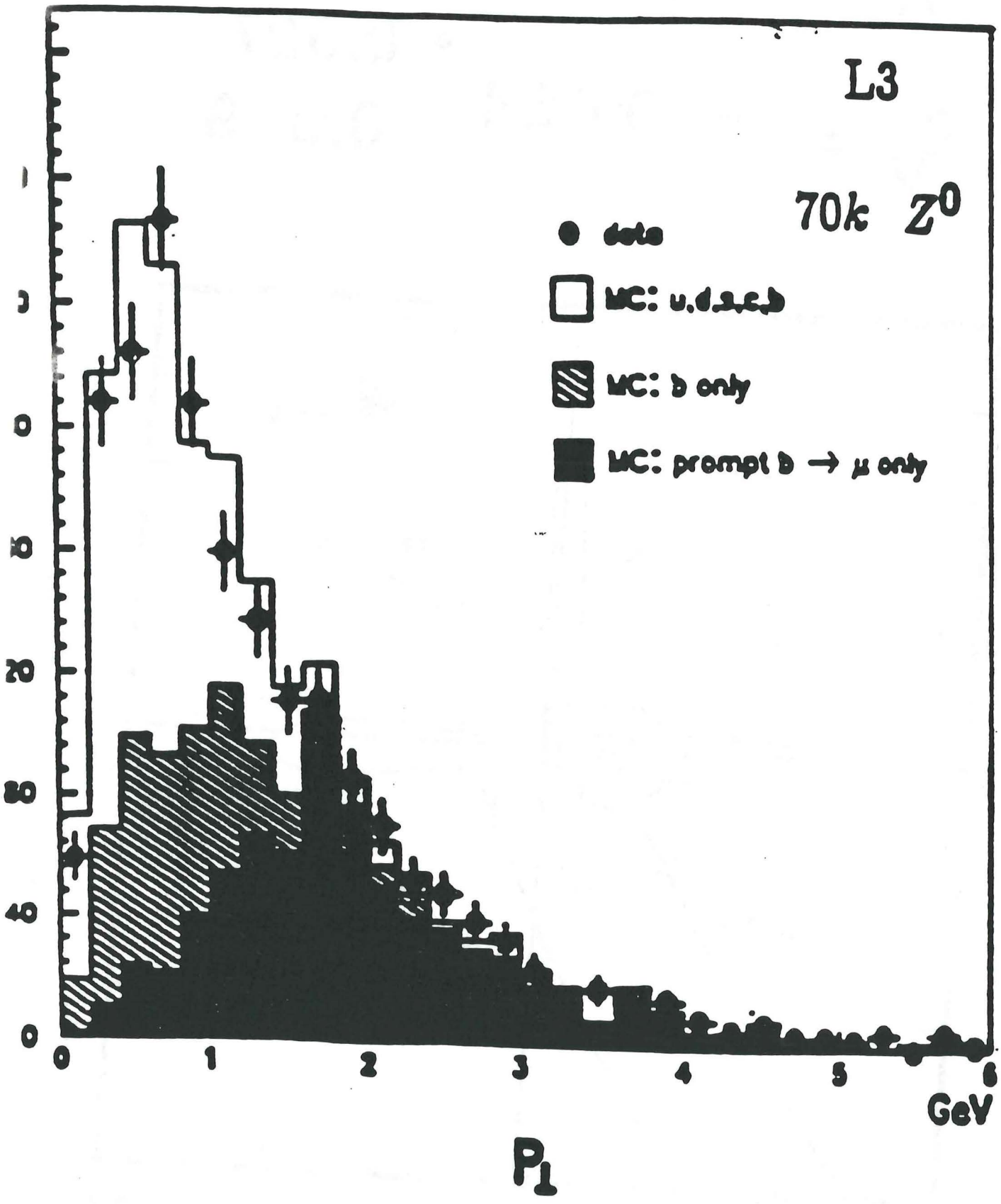

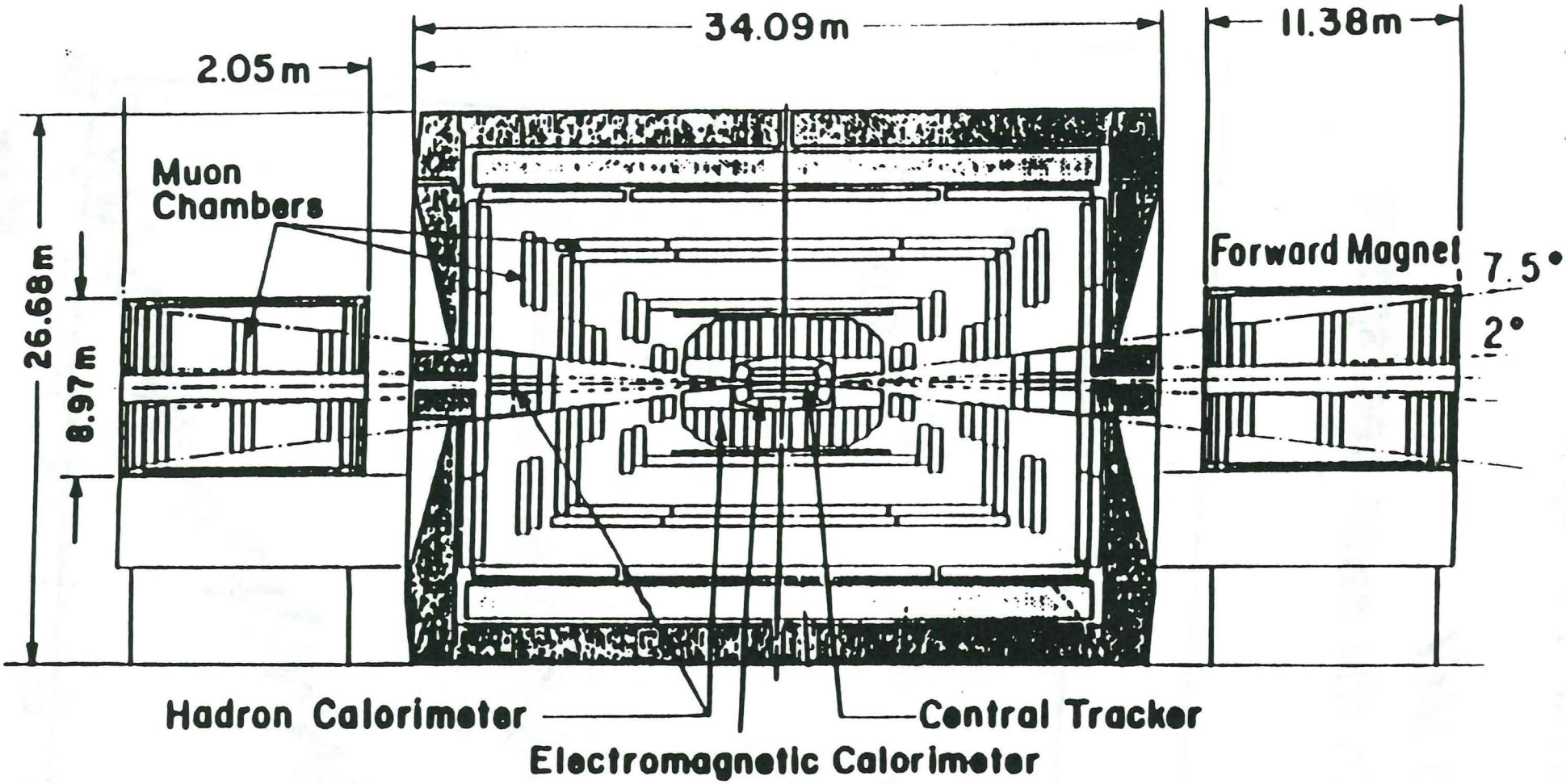
34.09m
11.38m
2.05m
Muon
Chambers
26.68m
8.97m
Forward Magnet
7.5°
2°
Hadron Calorimeter
Central Tracker
Electromagnetic Calorimeter

L*

Inclusive $\gamma\gamma$ spectrum

- E_γ > 700 MeV
- Both γ's in the same hemisphere

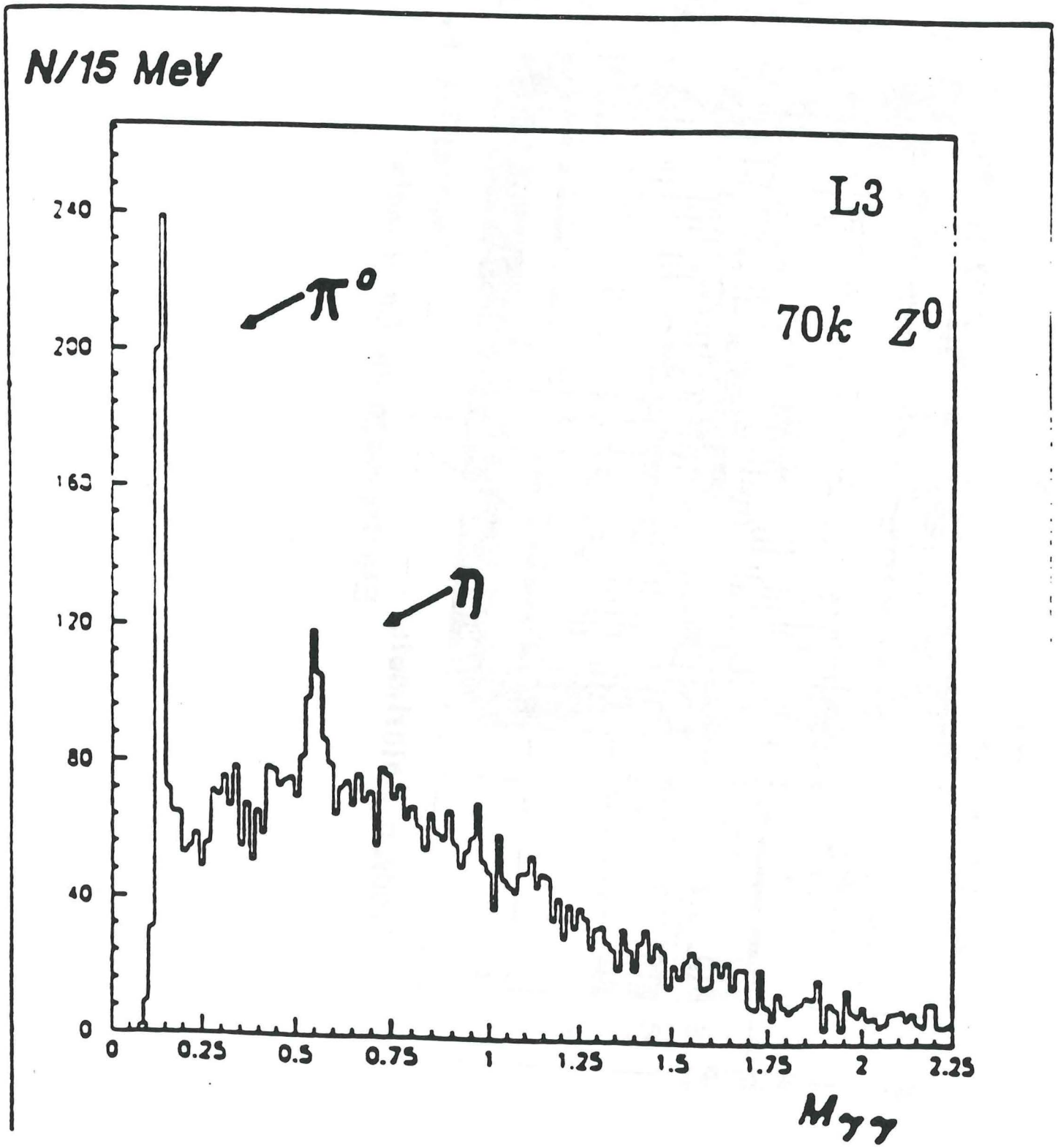

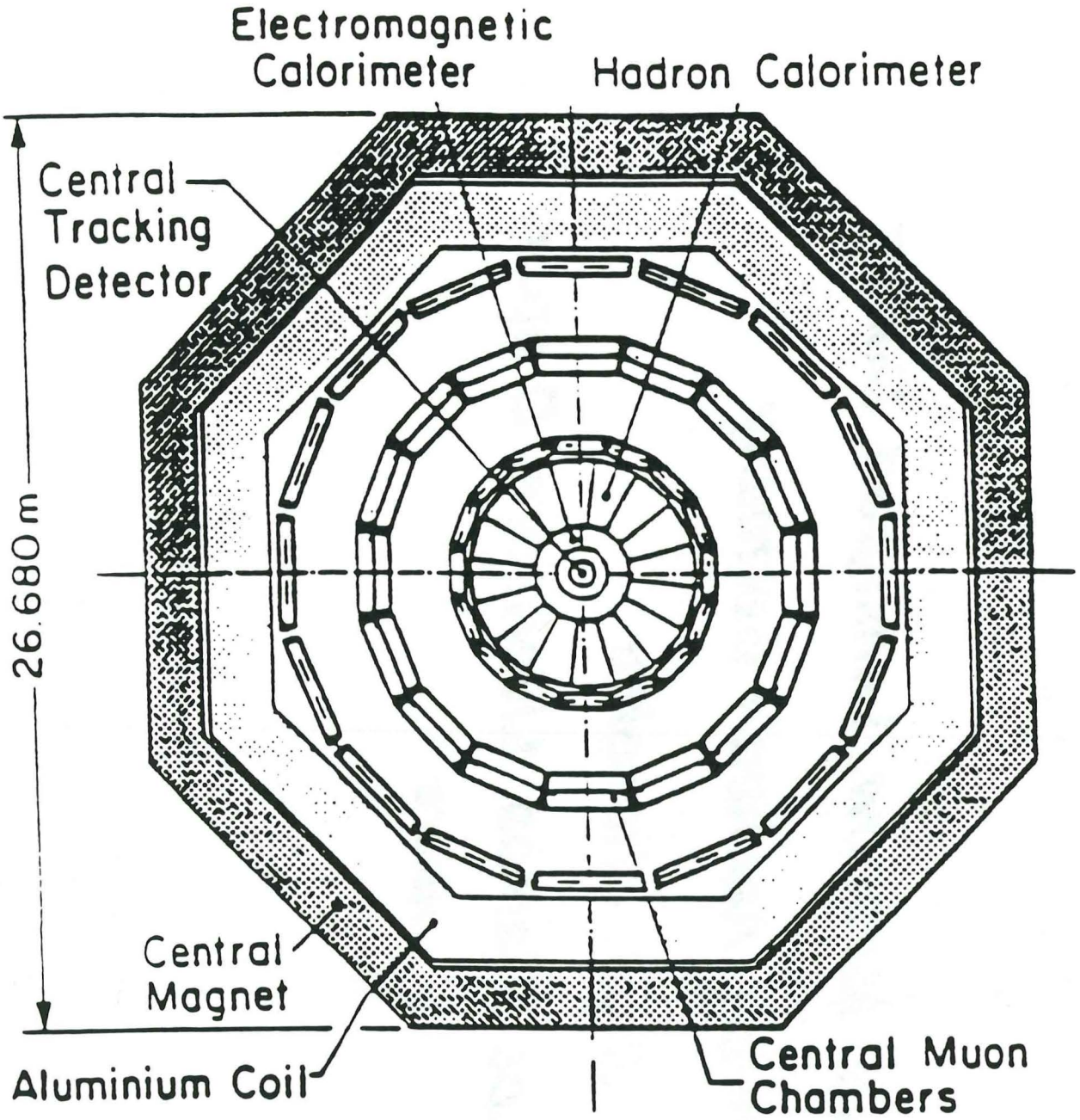
Electromagnetic
Calorimeter
Hadron Calorimeter
Central
Tracking
Detector
26.680 m
Central
Magnet
Aluminium Coil
Central Muon
Chambers

L*

L* Engineering Centers

Examples **:**

Kurchatov, ITEP Moscow, Leningrad, Dubna

ETH Zürich, Aachen I Germany

S.I.C. Shanghai

Oak Ridge, Los Alamos, Livermore, Draper

others

Magnet System

consists of a Central Magnet
providing a field of 0.75T
& forward-backward magnets
with field of 0.3T

Central magnet design :

either conventional with aluminium coil
or
superconducting coil with iron return
or
superconducting coil with a superconducting
return coil to replace iron

Coil Options for the Central Solenoid

Parameter	Aluminium Coil	SC Coil	Double SC Coil	Unit
Field	0.75	0.75	0.75	Tesla
Power Consumption	22	2	2	MW
Outer Diameter	26.7	25.0	30.0	m
Mass of Iron	48 200	41 350	-	ton
Mass of Coil(s)	7 700	1 103‡	4 000‡	ton
Operating Current	66	23	25	kA

‡ Including structure and vacuum vessel

L3 MAGNET

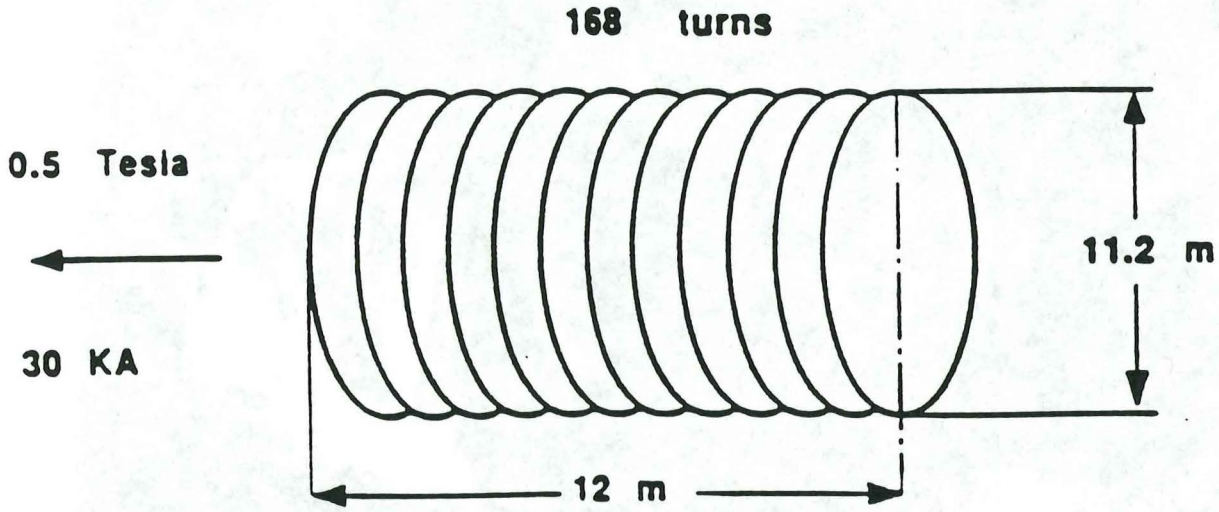

Total stored energy 160 MJ
Power consumption 4 MW

L* MAGNET

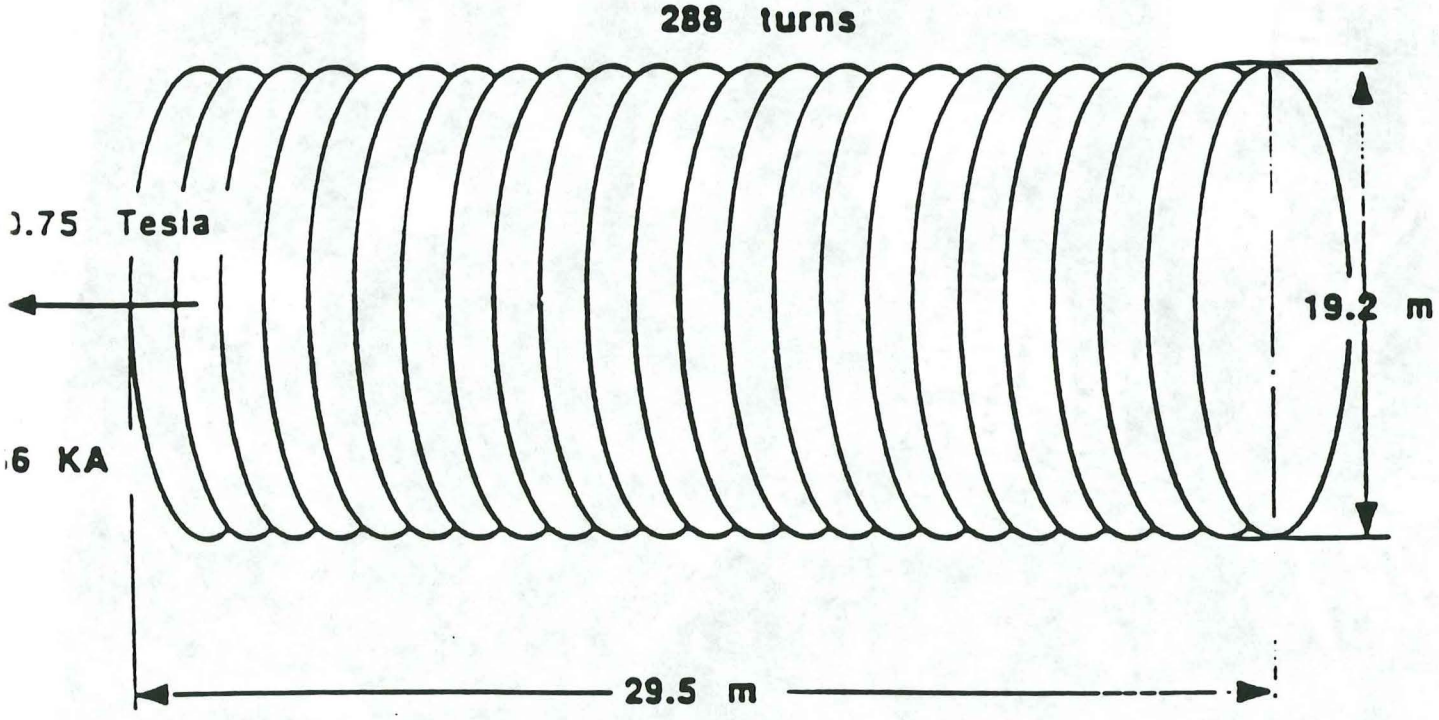

Total stored energy 2660 MJ
Power consumption 20 MW

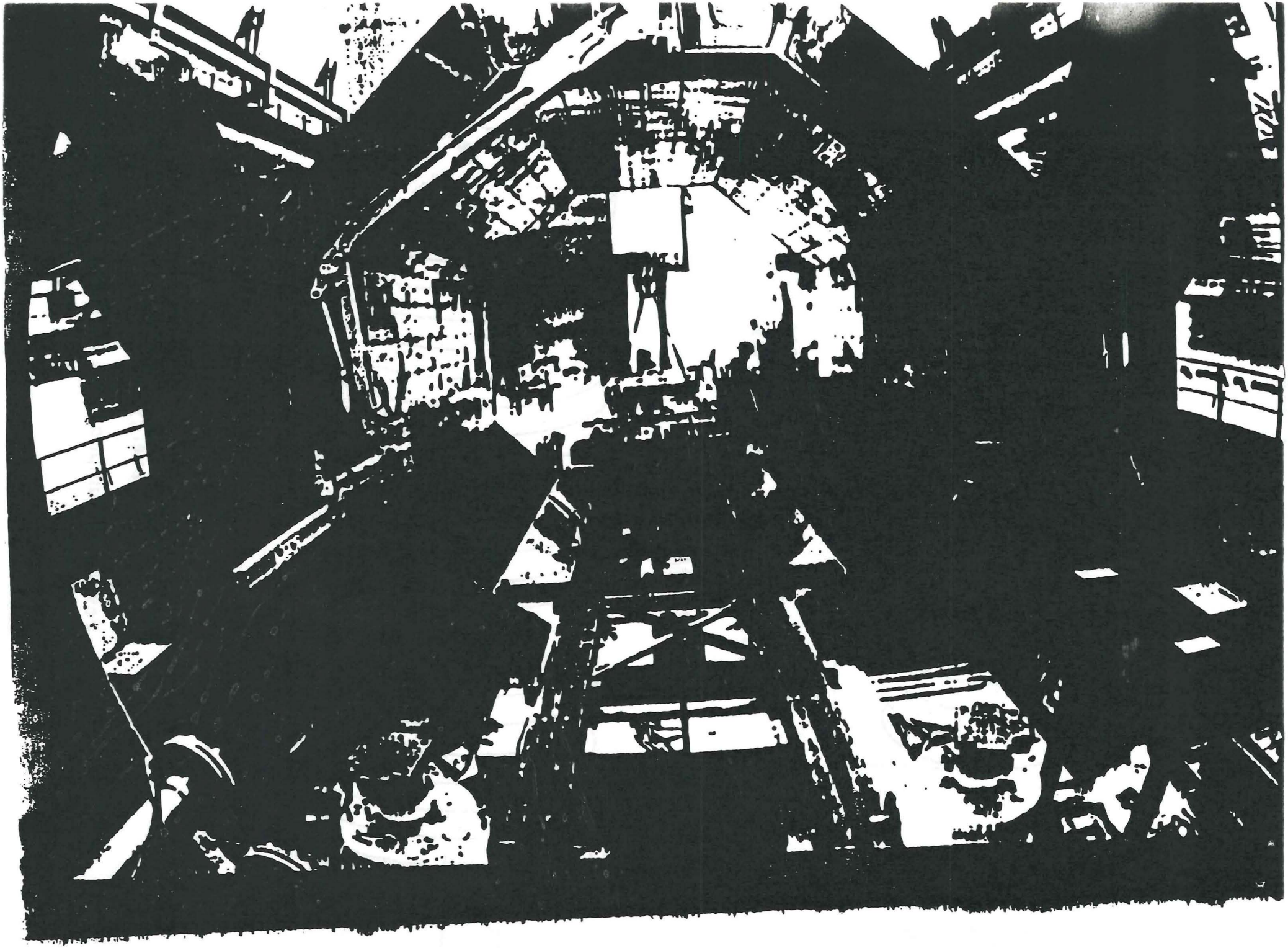

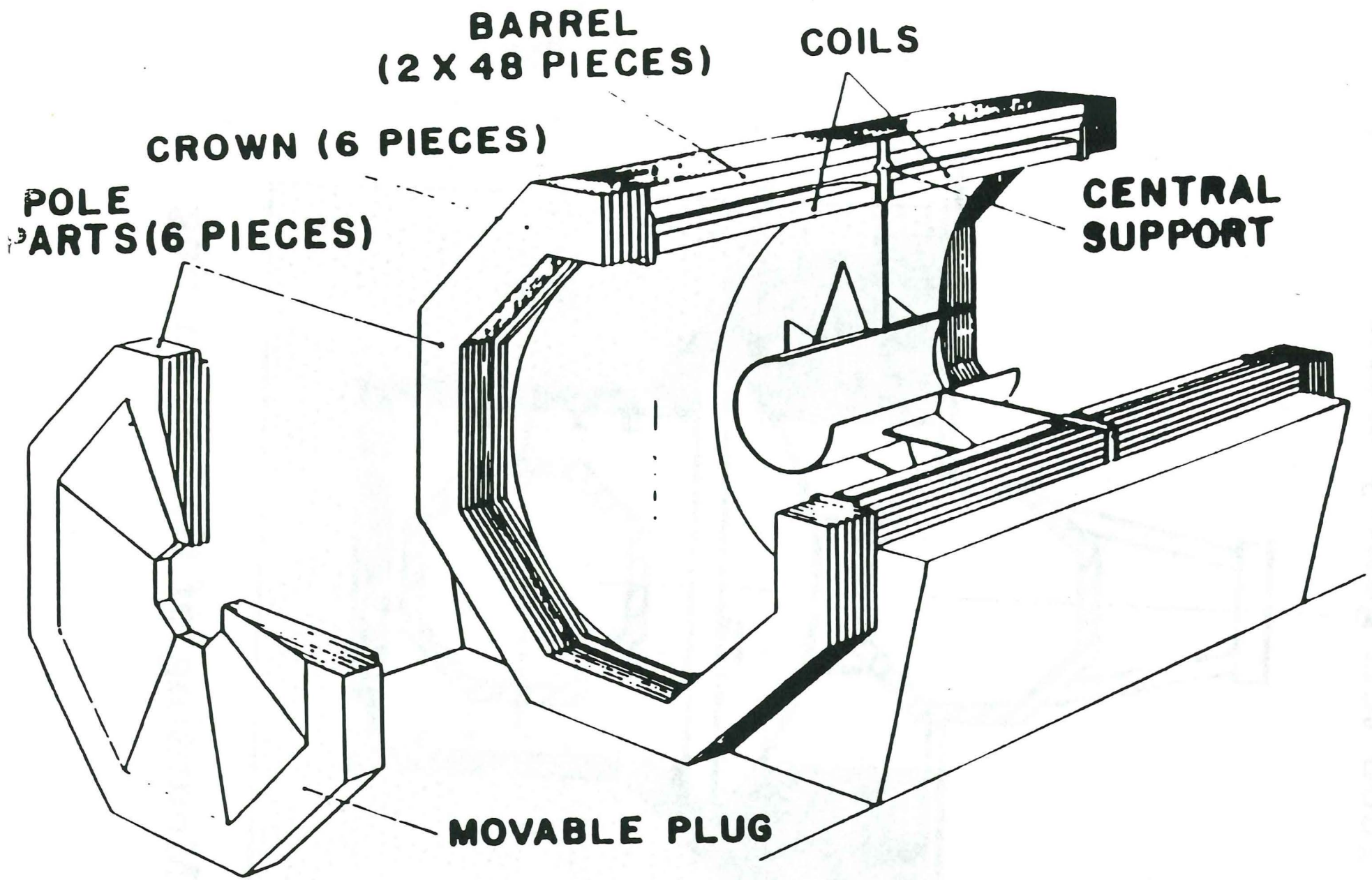
BARREL
(2 X 48 PIECES)
COILS
CROWN (6 PIECES)
POLE
PARTS (6 PIECES)
CENTRAL
SUPPORT
MOVABLE PLUG

1000 ton gantry crane

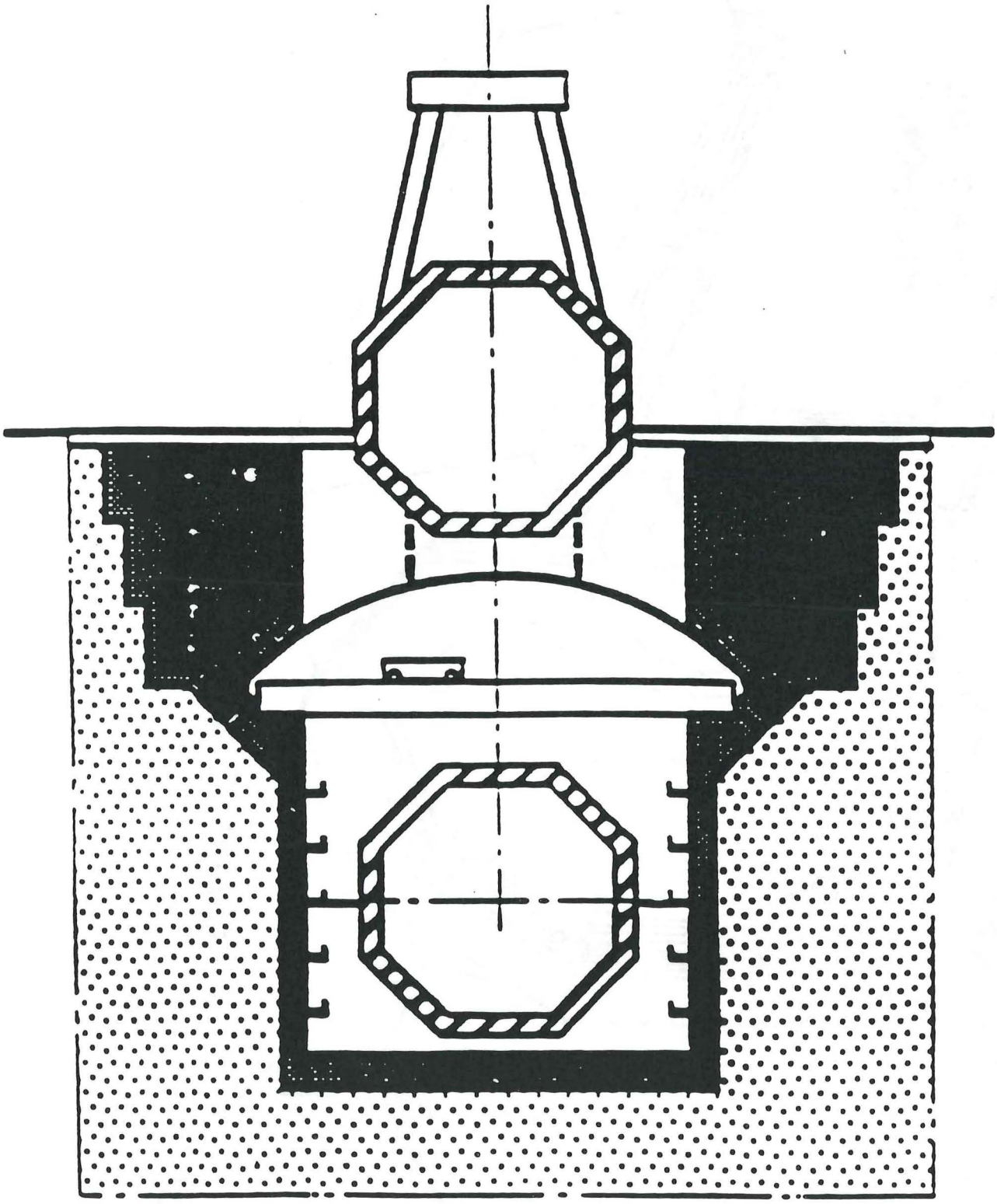

Mounting of the crown ring

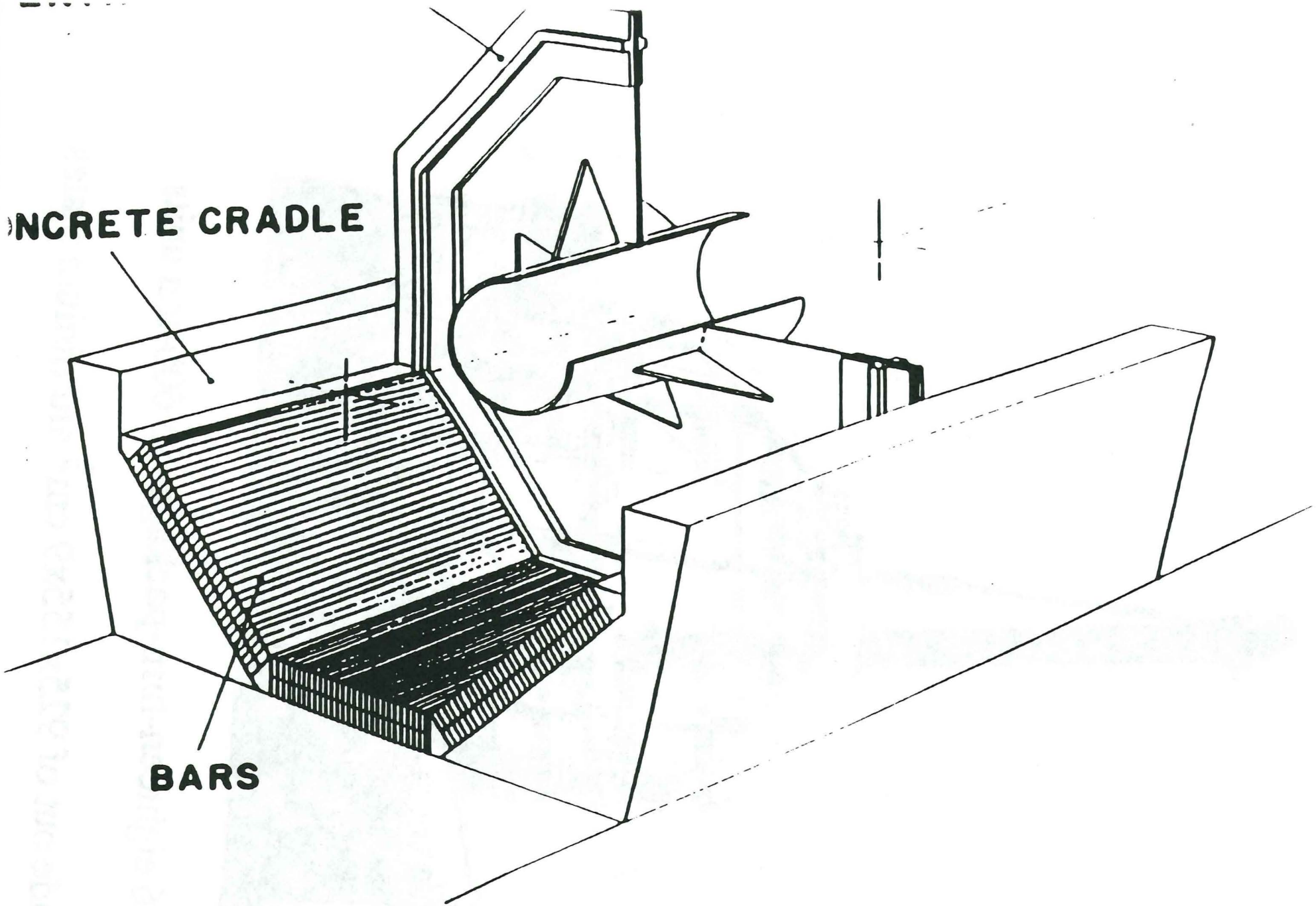
NCRETE CRADLE
BARS

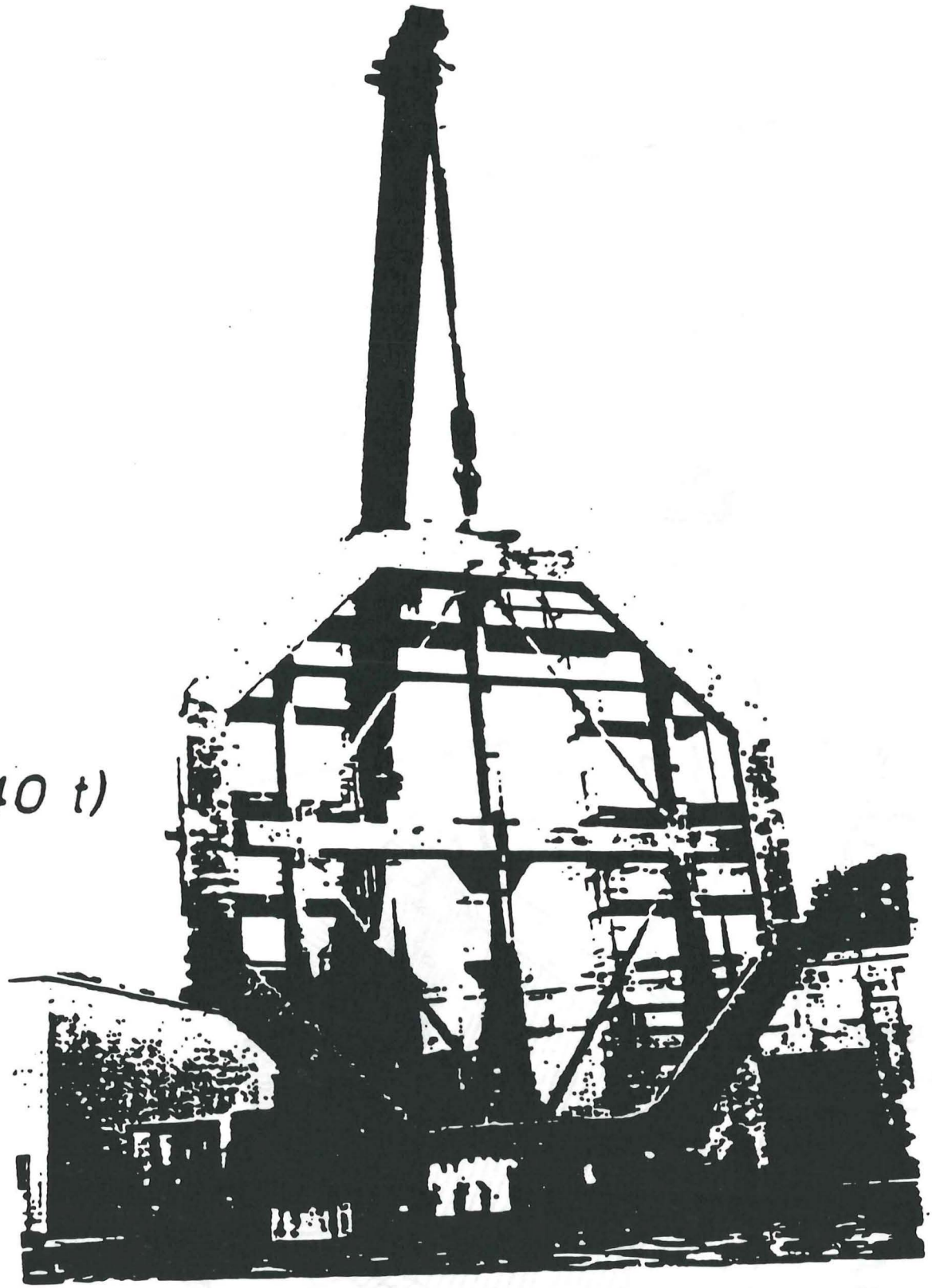

3
x 40 t)

16 eighteen-turn-packages in 600-ton units

*

made out of 925x155x9 cm^3 aluminium plates

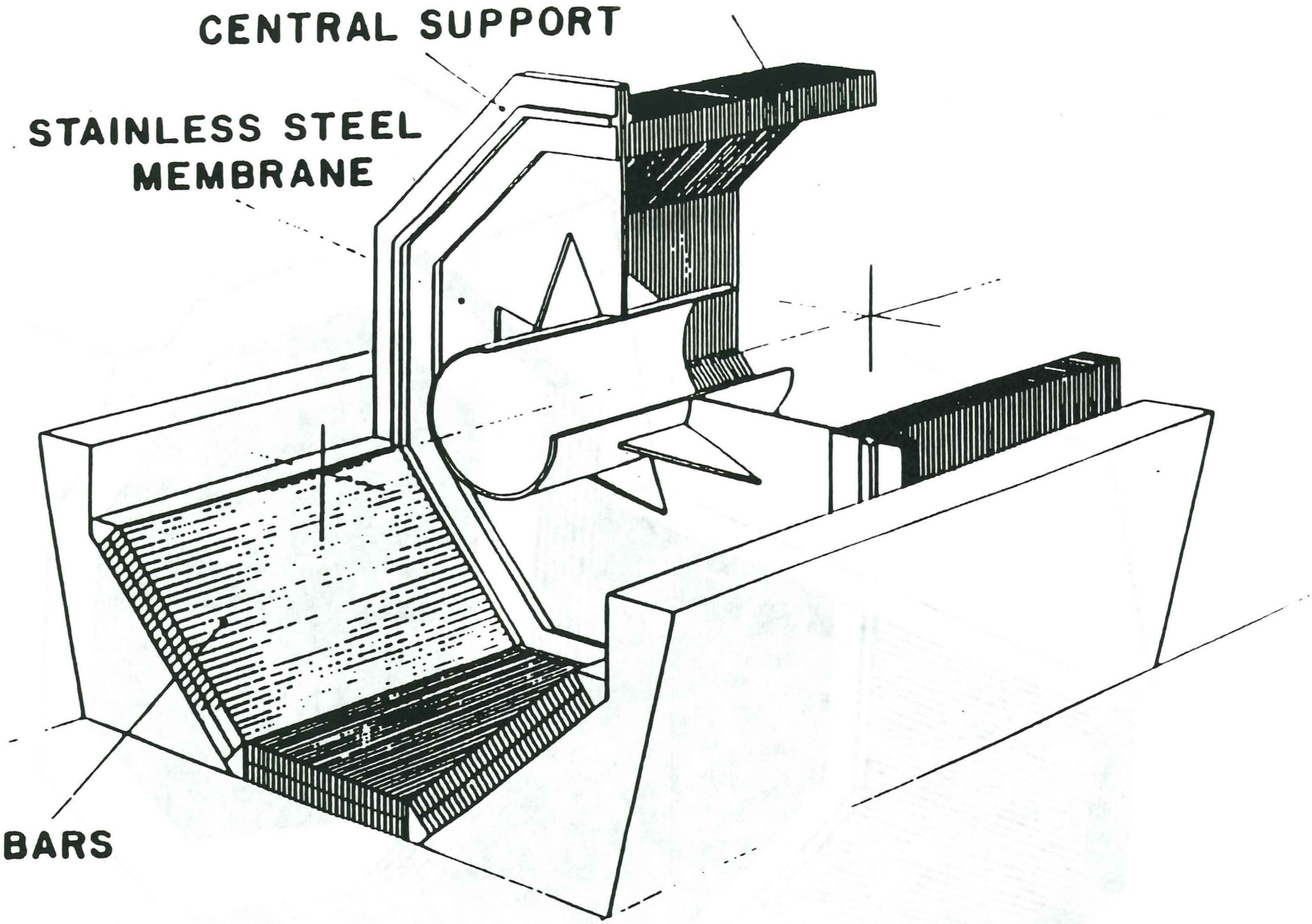
CENTRAL SUPPORT
STAINLESS STEEL MEMBRANE
BARS

HIGH PRESSURE COLLECTION

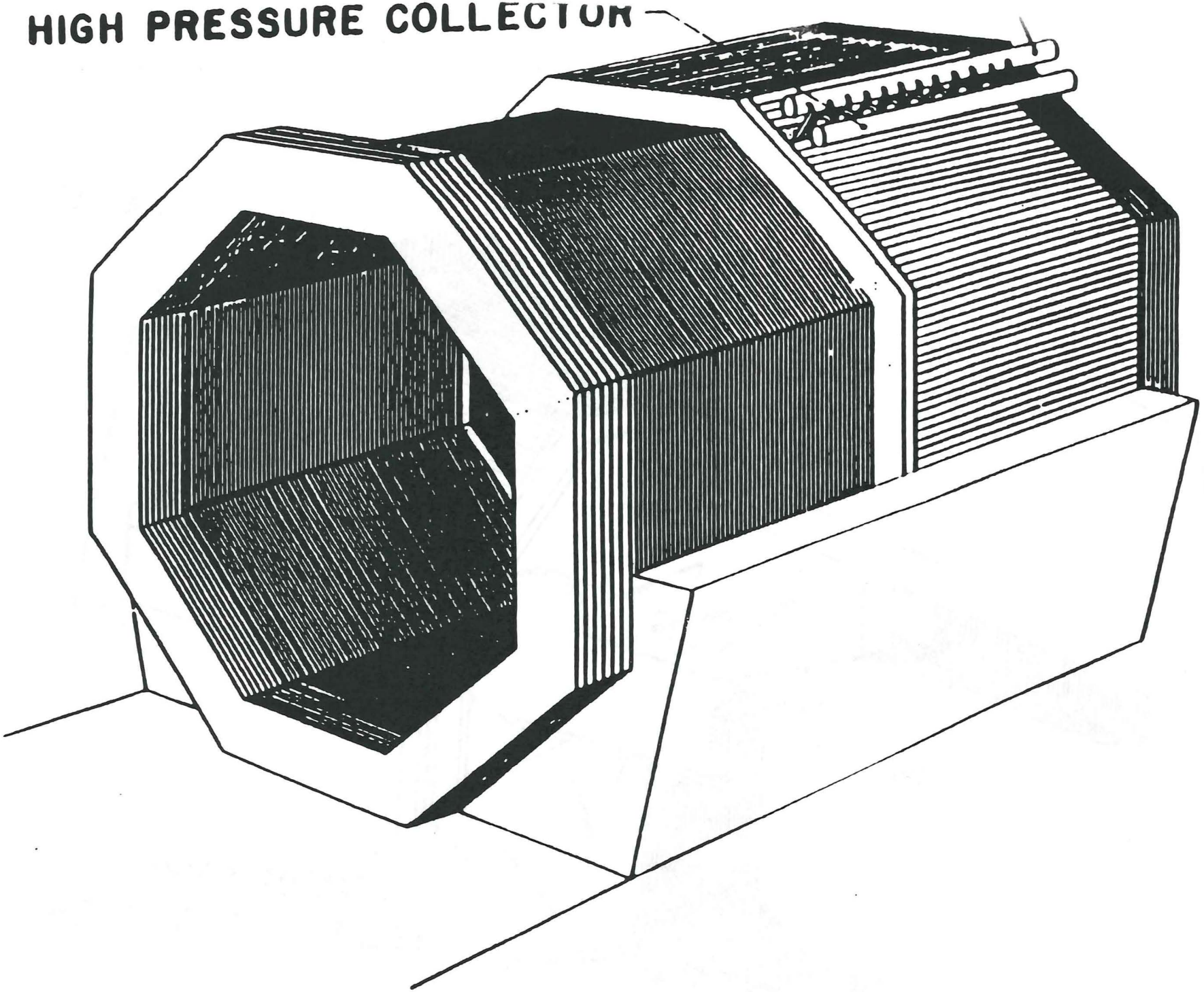

For Al coil magnet

L3 is ~ half scale prototype

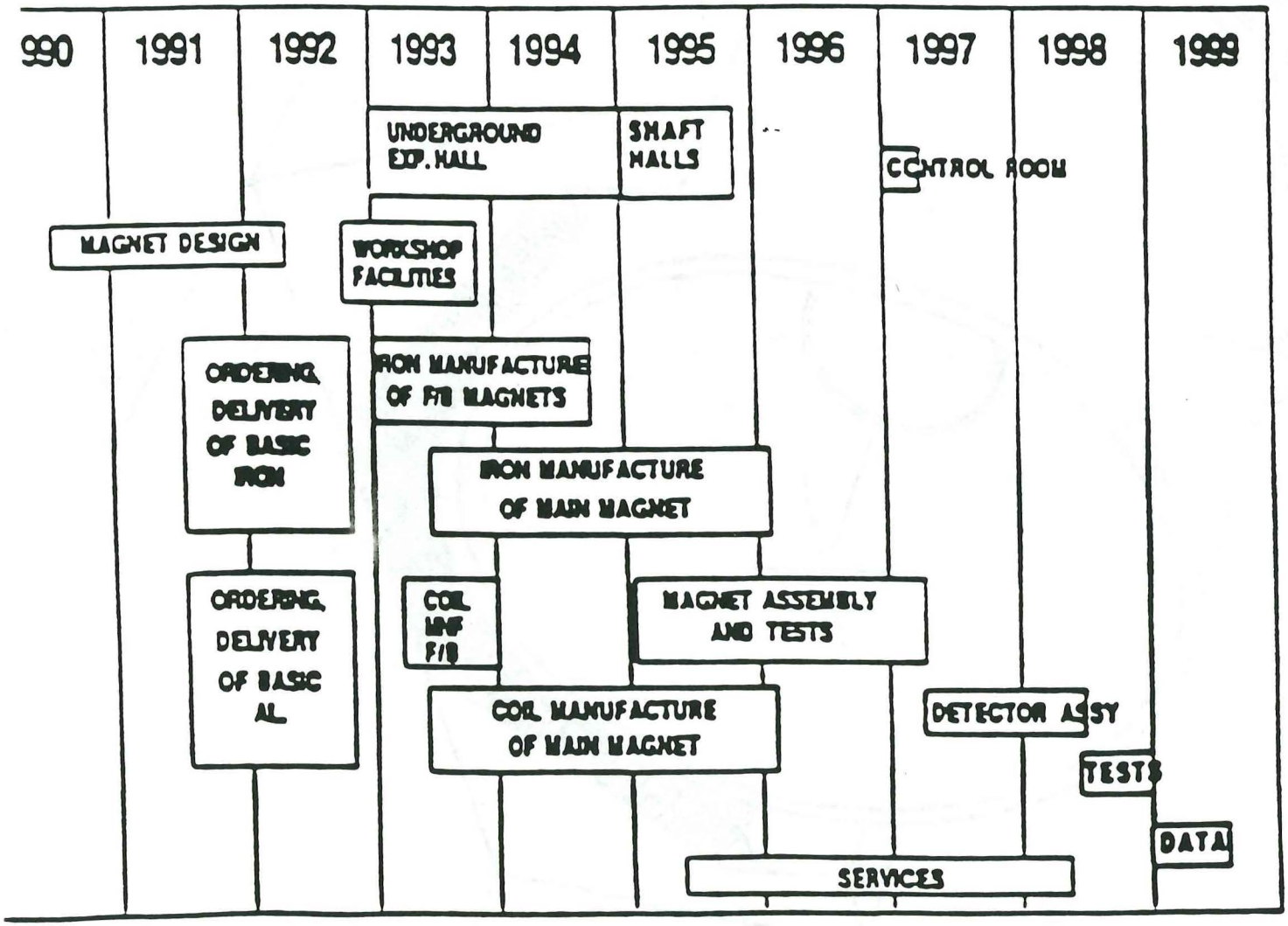

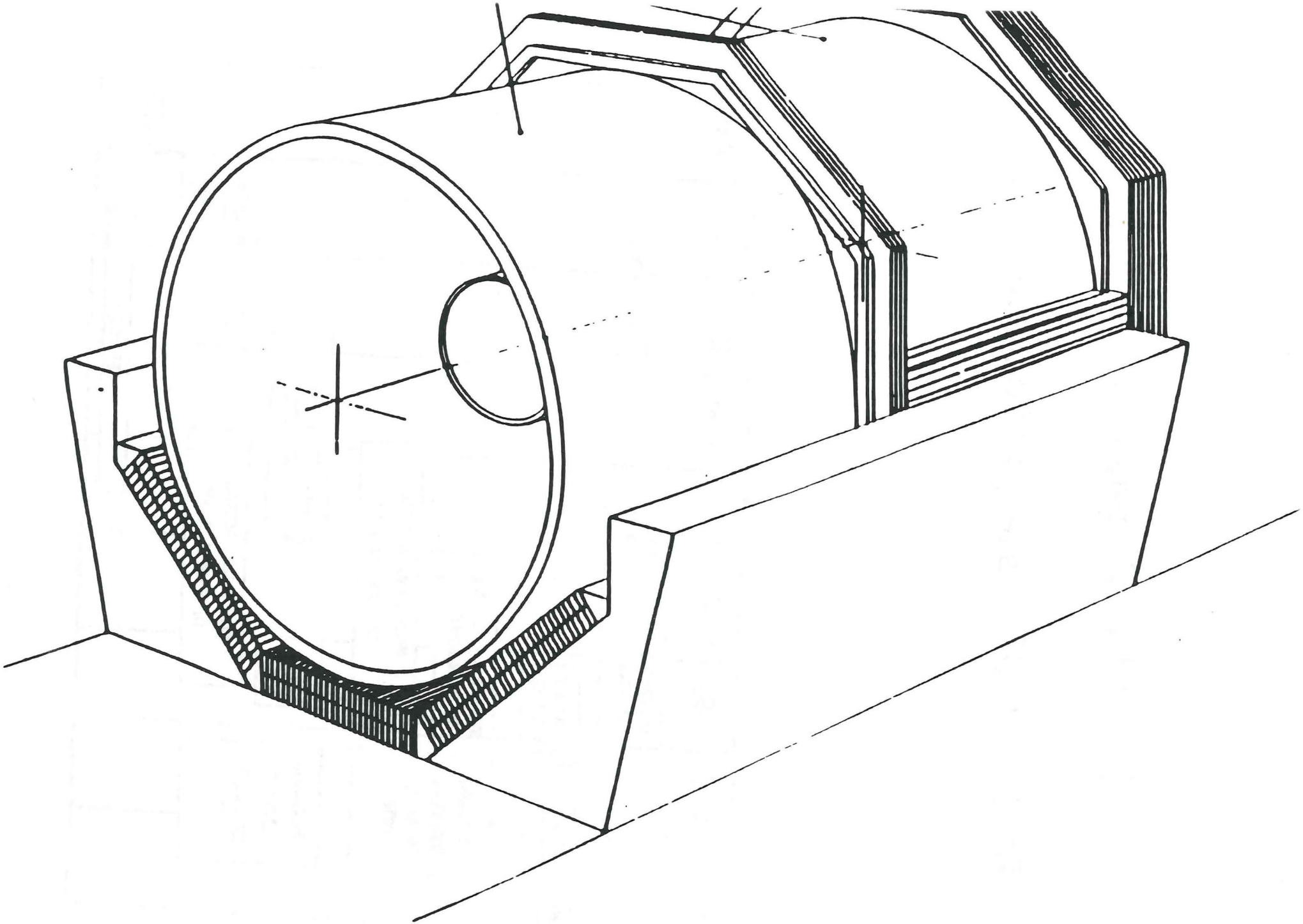

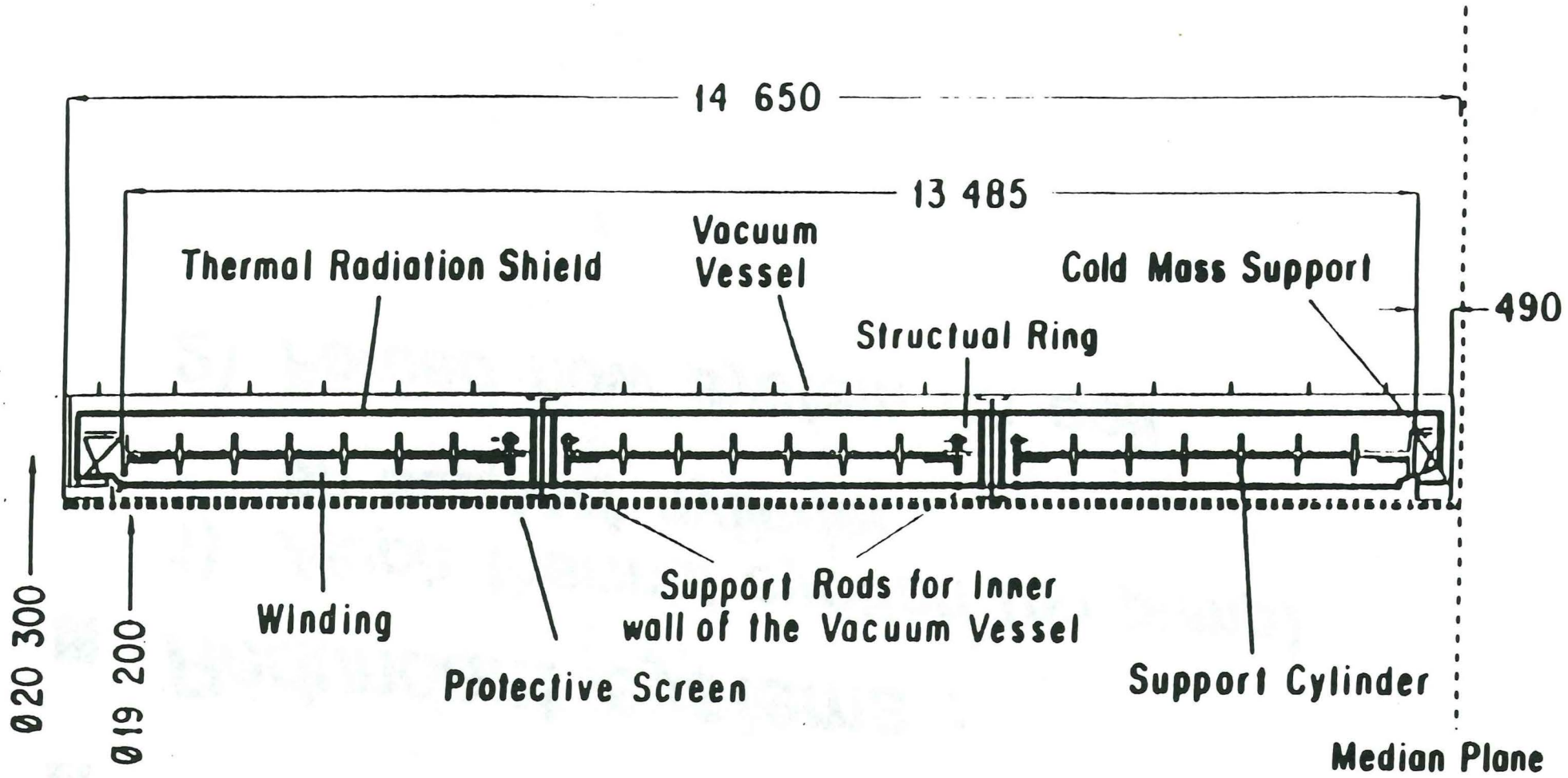
14 650
13 485
Thermal Radiation Shield
Vacuum Vessel
Structual Ring
Cold Mass Support
490
Winding
Protective Screen
Support Rods for Inner wall of the Vacuum Vessel
Support Cylinder
Median Plane
Ø20 300
Ø19 200

Superconducting Coil Cooling System

- *Livermore National Laboratory*
- *Redundant systems :*
  1) *Aleph thermal syphon (no pump) on support cylinder*
  2) *Forced flow system on coil*

Superconducting Coil

USSR R&D Program

Kurchatov Institute

Model Coil

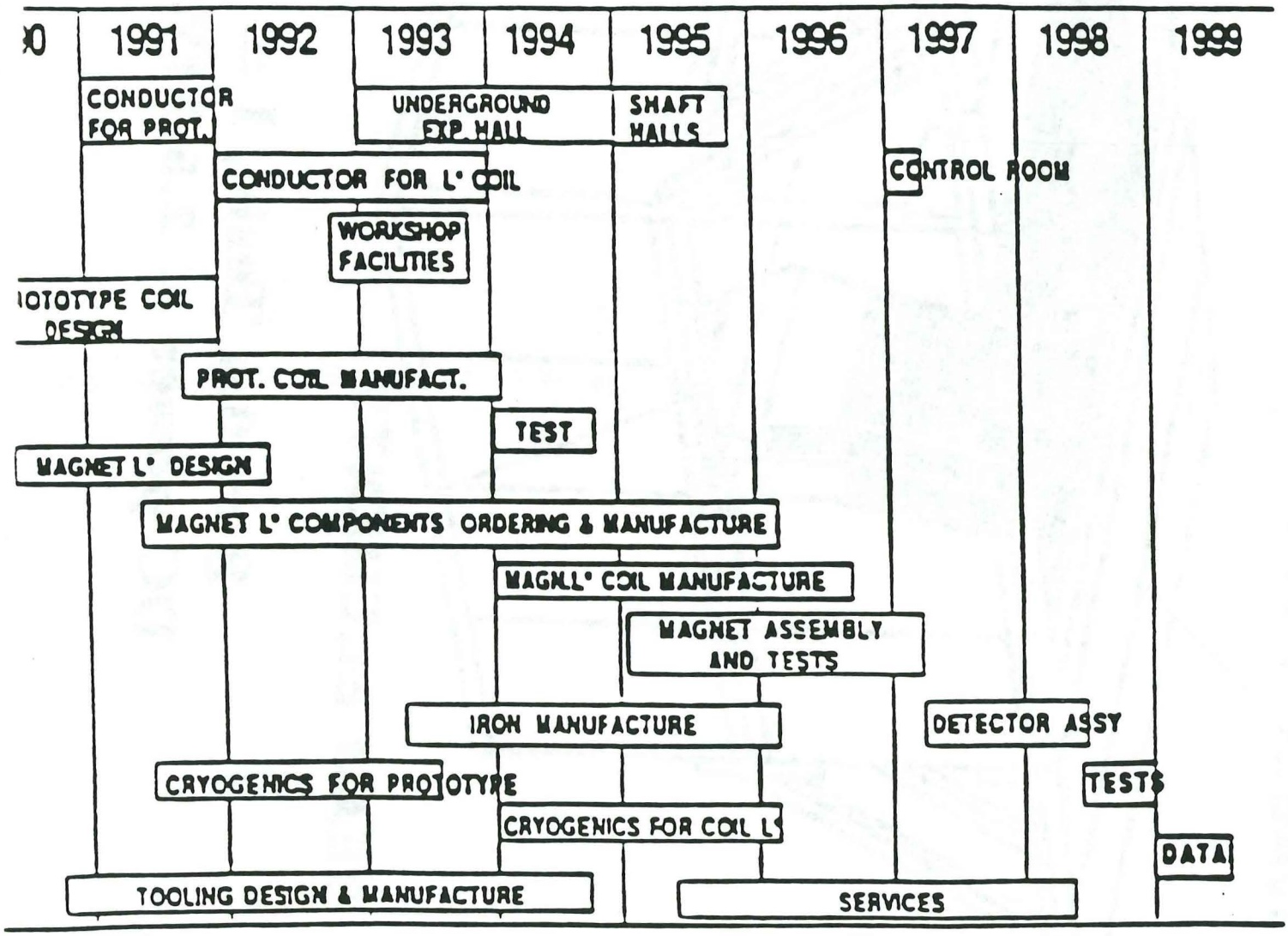

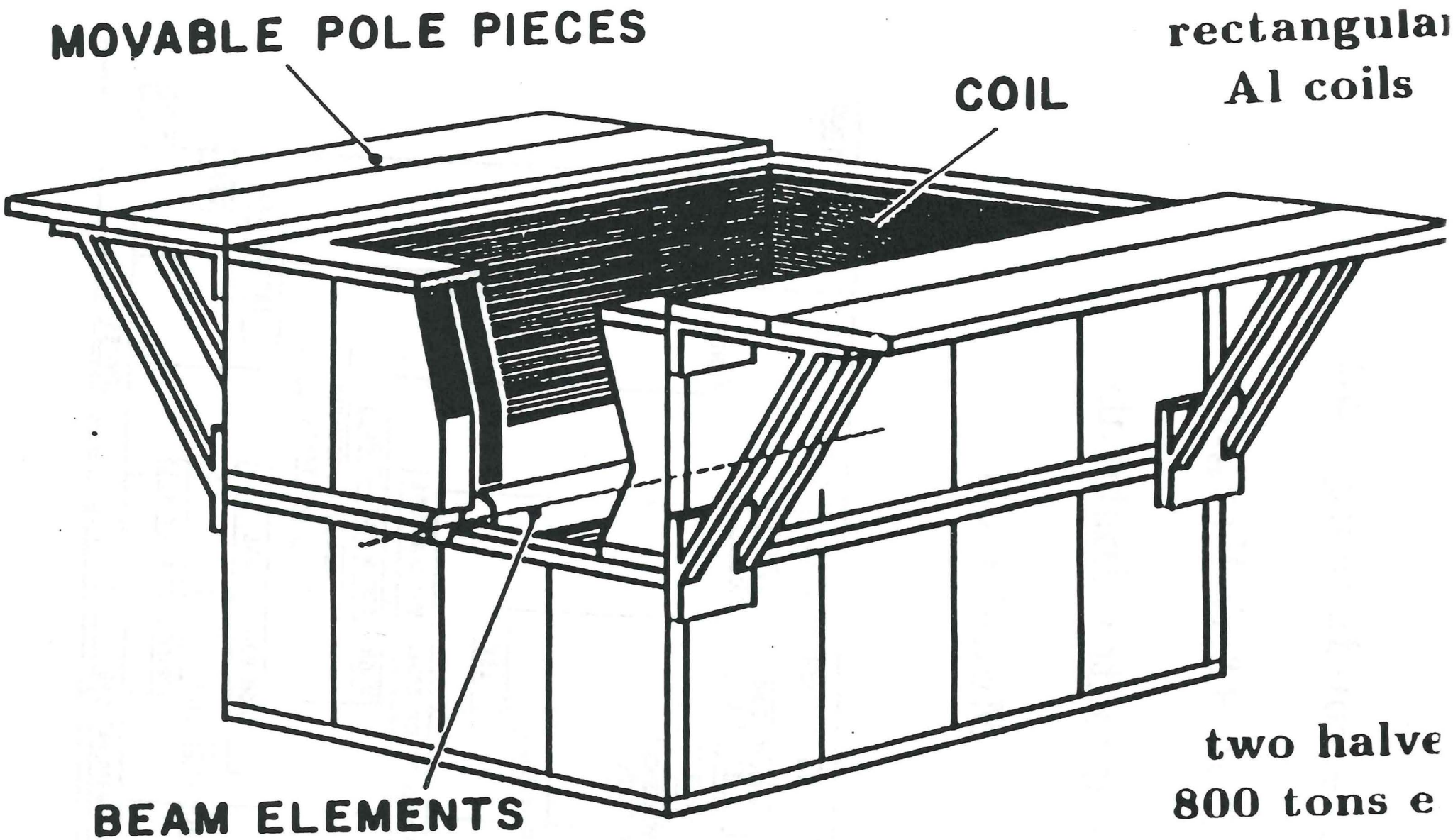

rectangular
Al coils

two halve
800 tons e

B = 0.3 Tesla, I = 16.3 kA

DC power = 2.5 MW/magnet

Magnet construction & Assembly
Participating Institutes :

USSR

Kurchatov Institute of Atomic Energy, Moscow
Institute of Theoretical & Experimental Physics, Moscow

Efremov Research Inst. of Electrophysical Apparata, Leningrad
All Union Research Institutes of Cable Industry, Moscow
Bochvar All Union Research Institute of Inorganic Materials, Moscow
Uhlba Metallurgical Plant, Ust-Kamenogorsk
Central Research Institute for Aerohydrodynamics, Moscow
Research Institute for Structural Materials "Prometei", Leningrad
Institute for Mounting and Assembly Technology, Moscow

USA

MIT Plasma Fusion Center, Cambridge
Lawrence Livermore National Laboratory, Livermore, CA
Oak Ridge National Laboratory, Oak Ridge, TN

R & D Funding Request
L* Magnet - FY 1991

	Request (k$)
10 Soviet Scientists at SSCL (at 30 k$/year/person)	300
Travel for 10 Scientists (at 2 k$/year/person)	20
Material and Supplies	180
TOTAL	500

A Precision Muon Detector

$$\frac{\Delta P}{P} \approx 2.4\% \quad \text{at} \quad P = 0.5 \text{ TeV}$$

$$2^0 < \ominus < 178^0$$

Momentum matching

$$P_{\text{central tracker}} = P_{\text{muon chamber}} + \Delta E_{H.C}$$

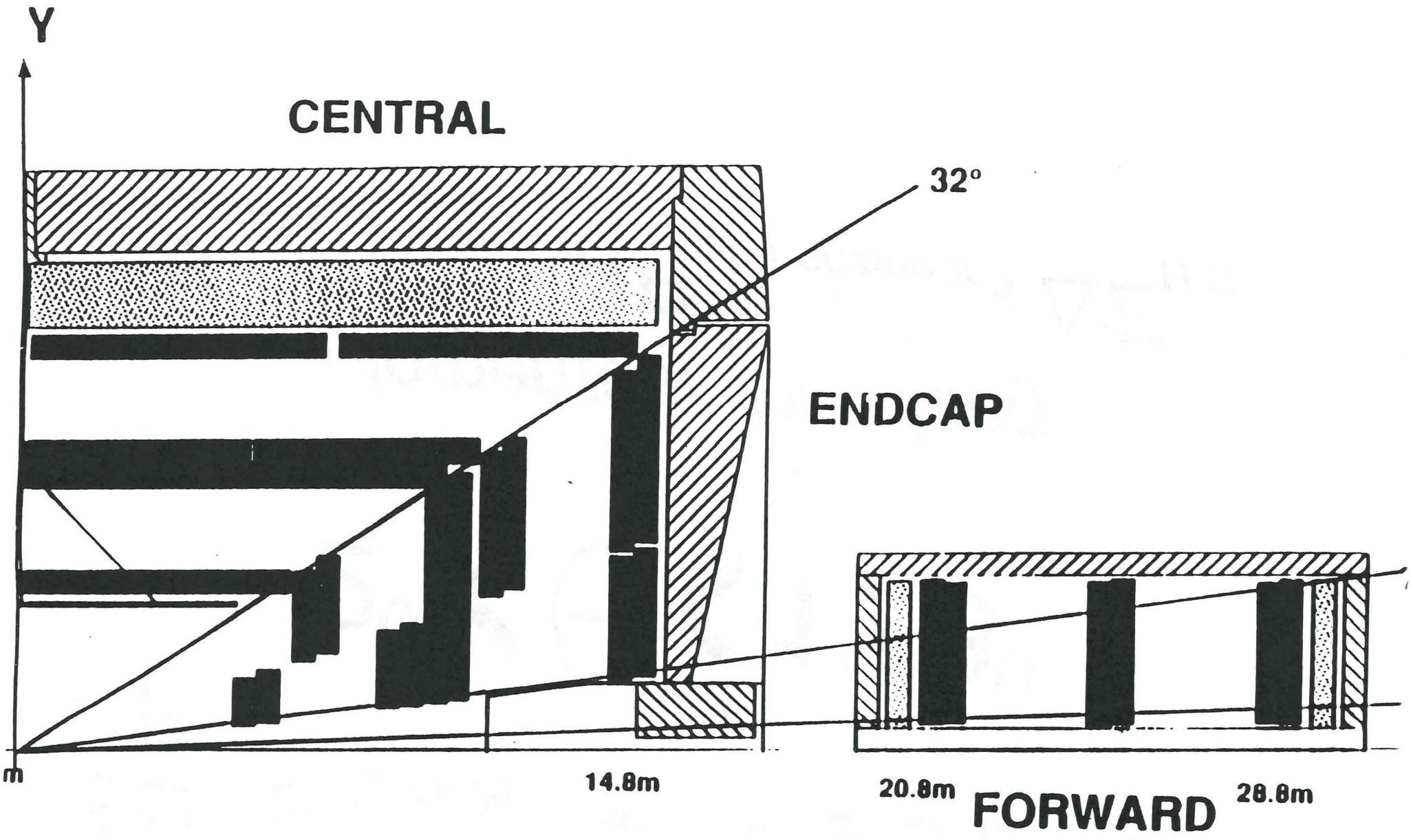

L* MUON SYSTEM

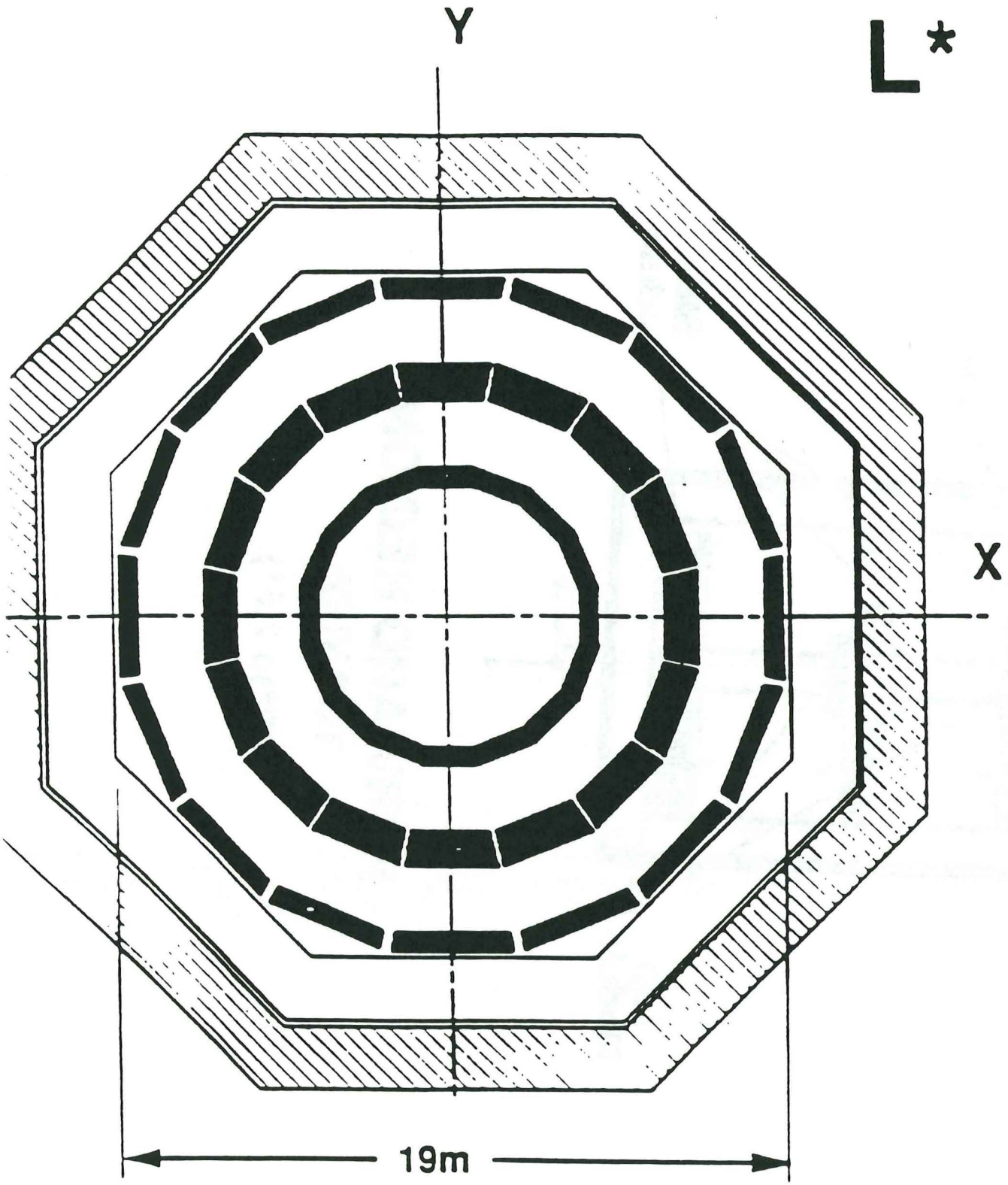

CENTRAL END VIEW

16 MODULES

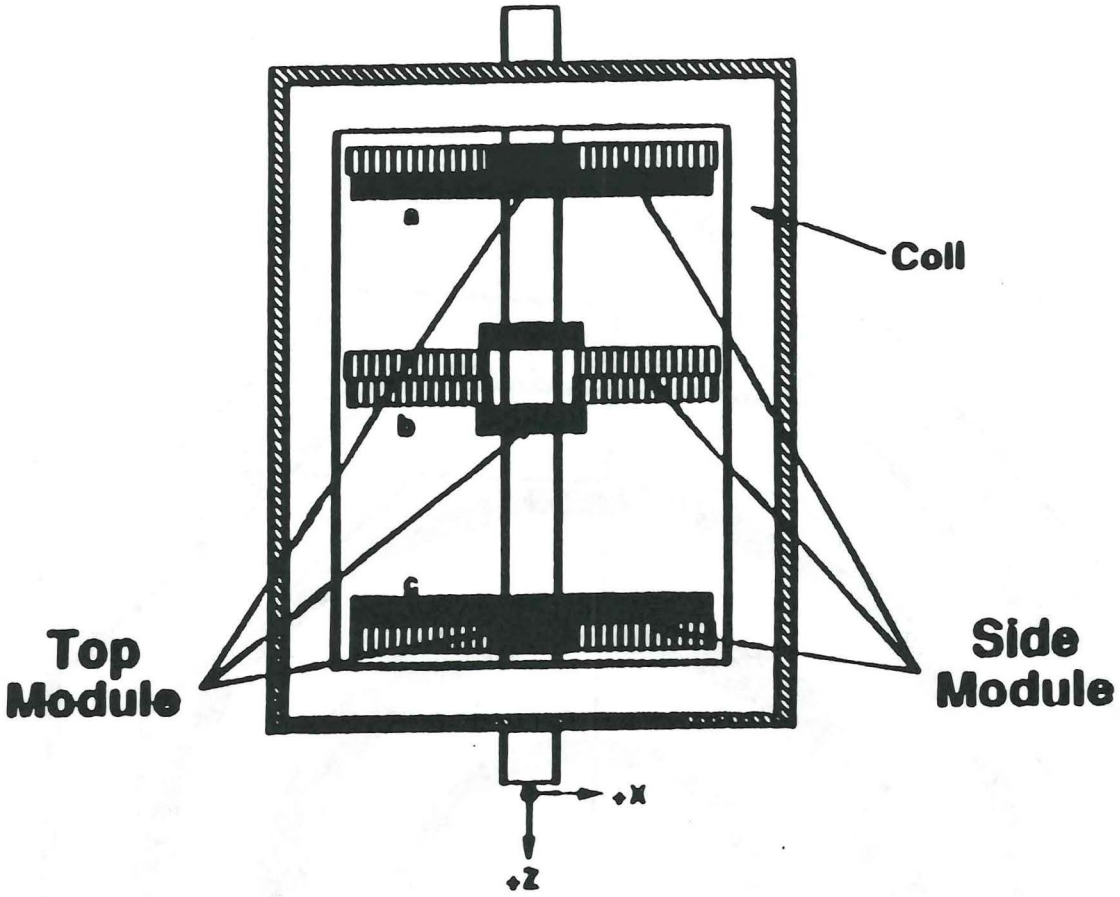

FORWARD REGION

TOP VIEW

(2°to 7.5°)

Forward 7.5 - 2°

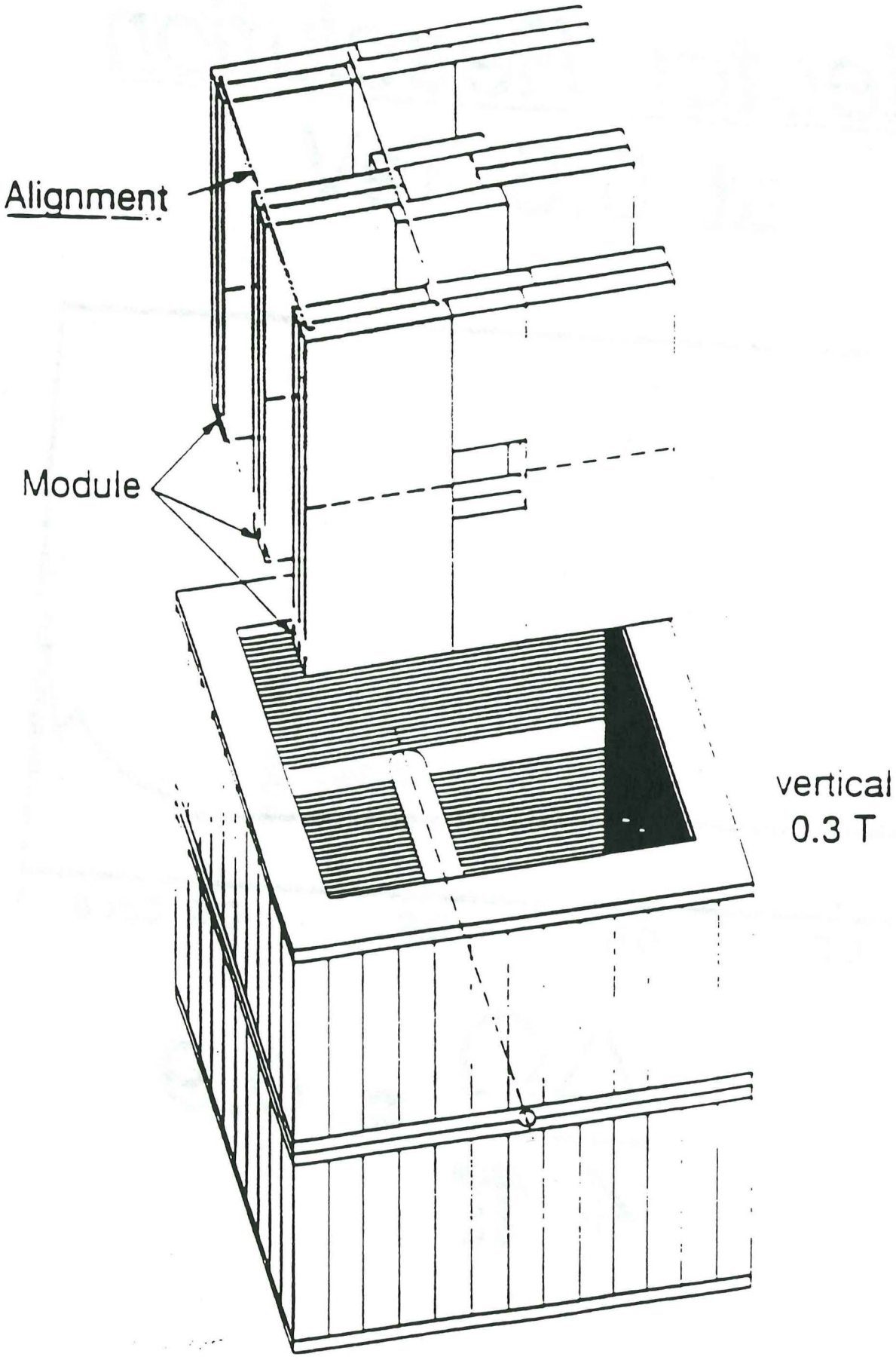

Detector Resolution
at 0.5 TeV

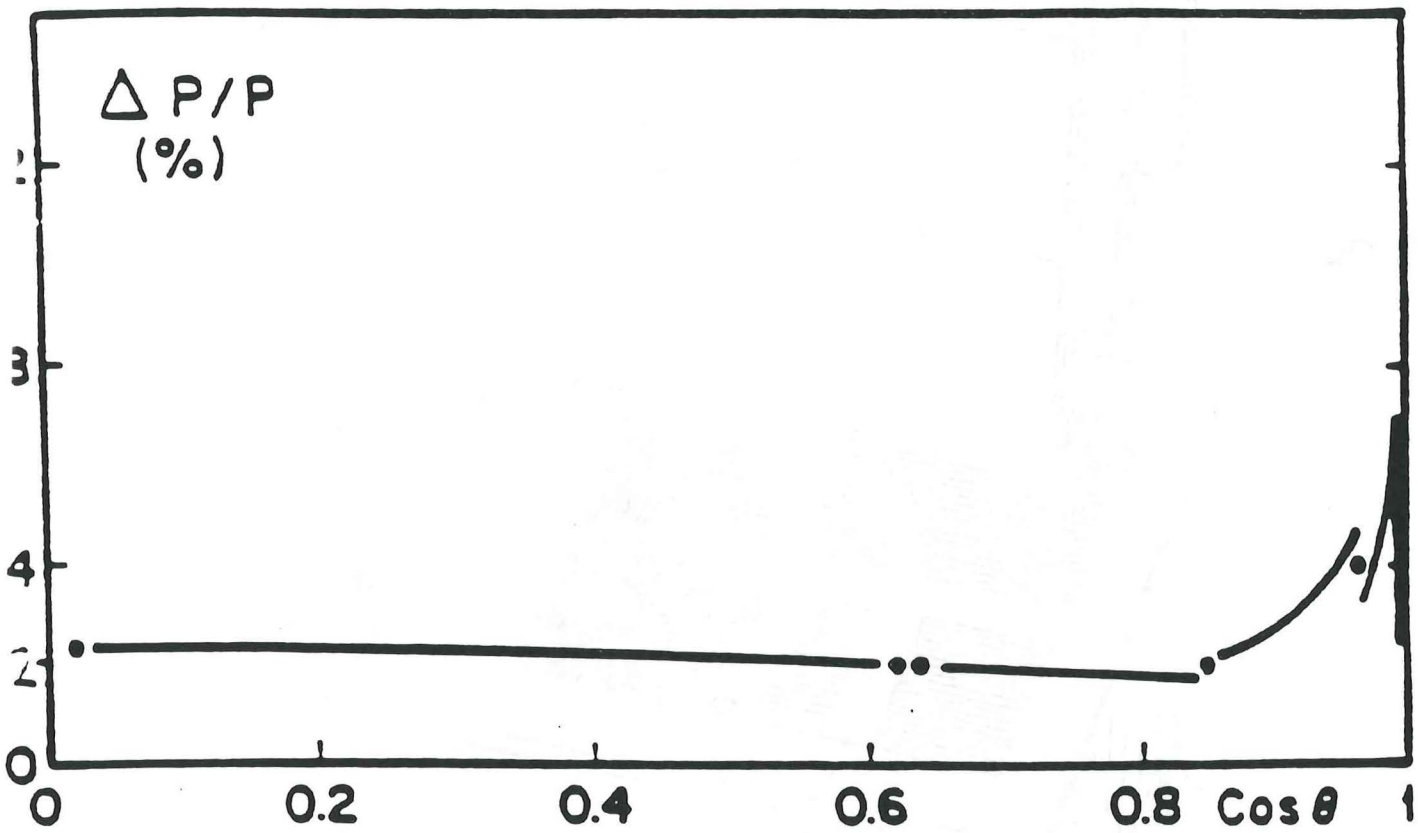

$$\frac{\Delta\Omega}{4\pi} = 0.9$$

Middle Chamber
32 + 32 wires offset

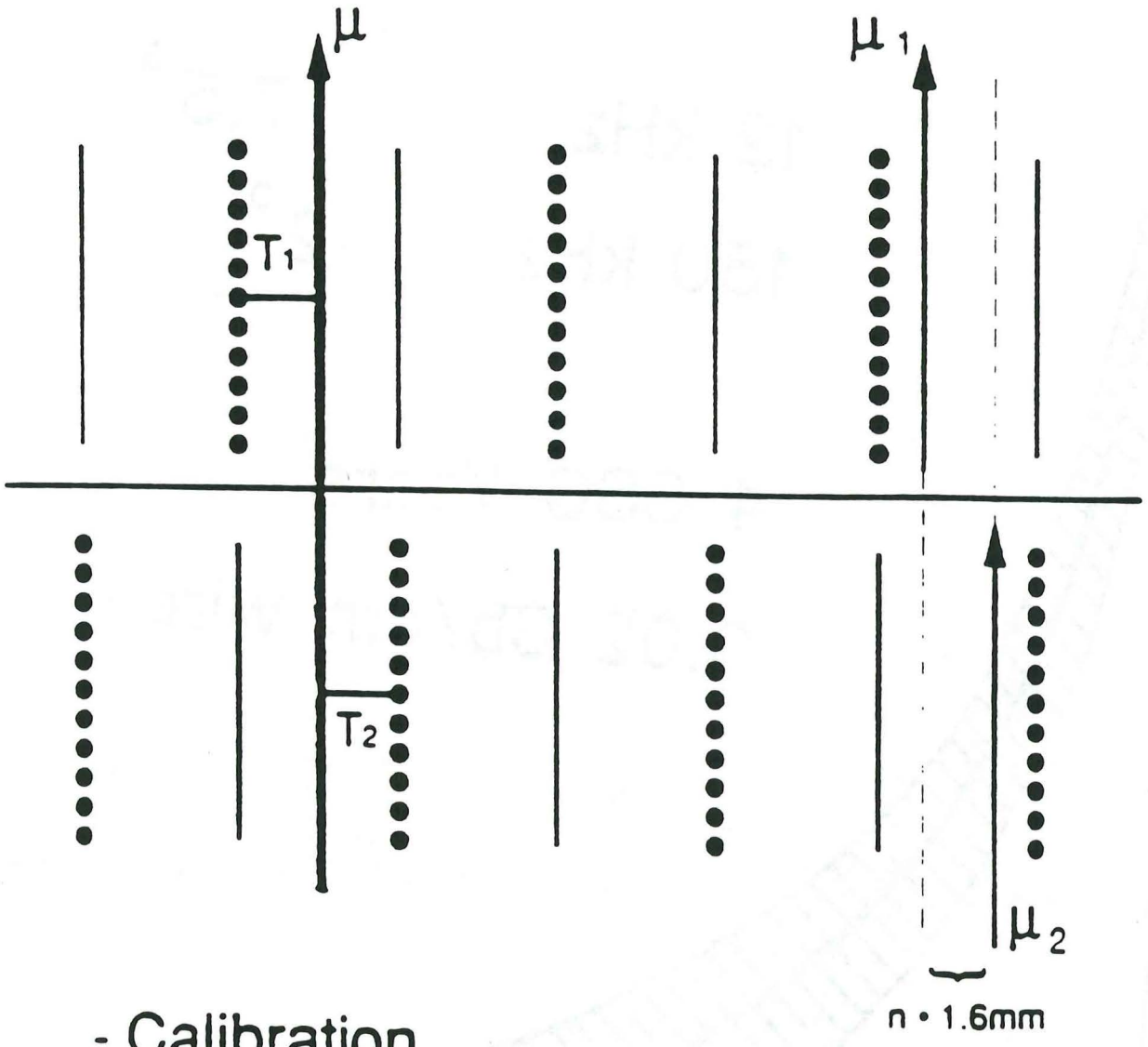

- Calibration
  $T_1 + T_2 = const.$

- Resolve
  L - R ambiguity

- Reject
  - n crossings off
  - cosmics, 4mm

RATES IN μ SYSTEM

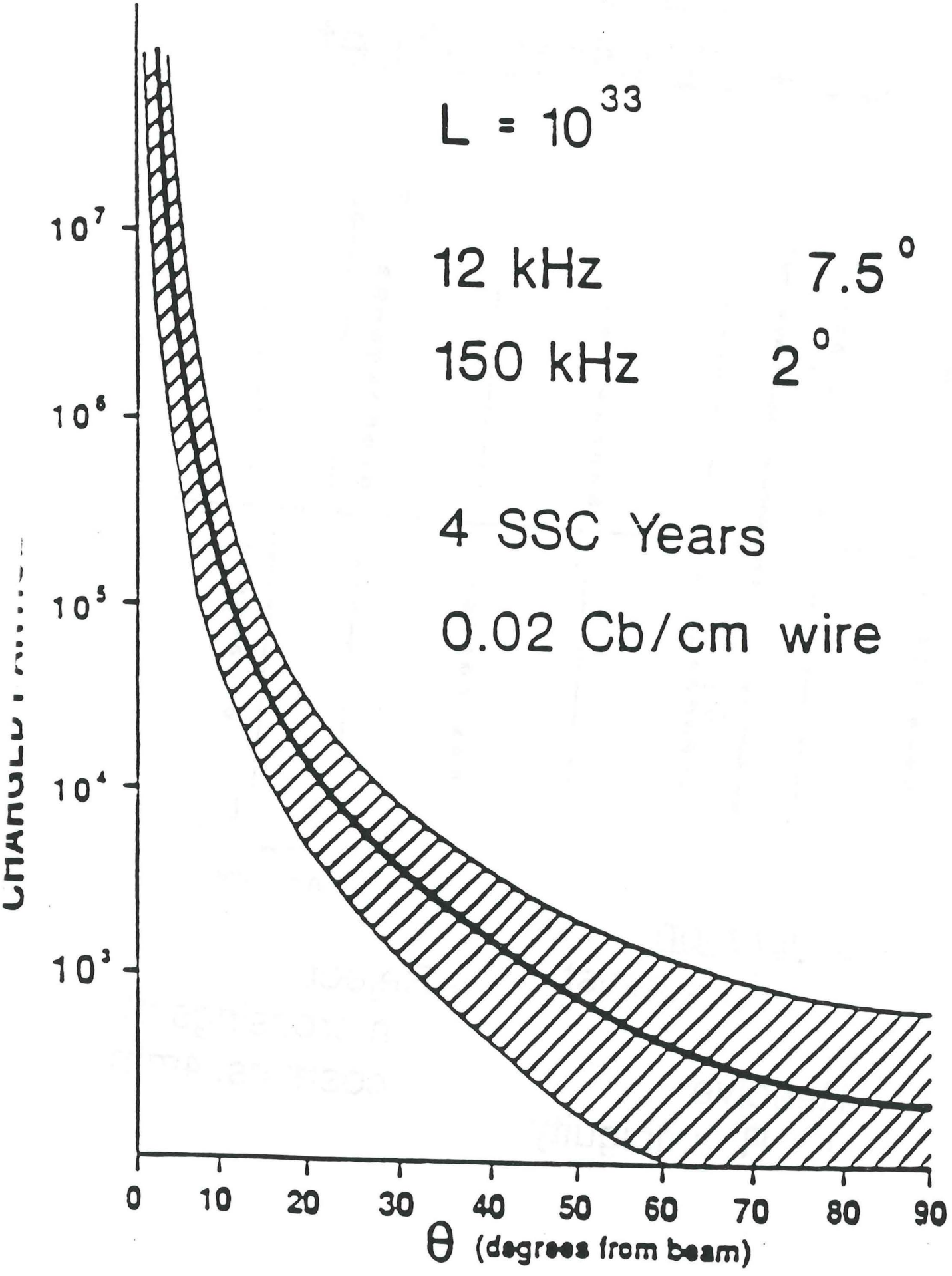

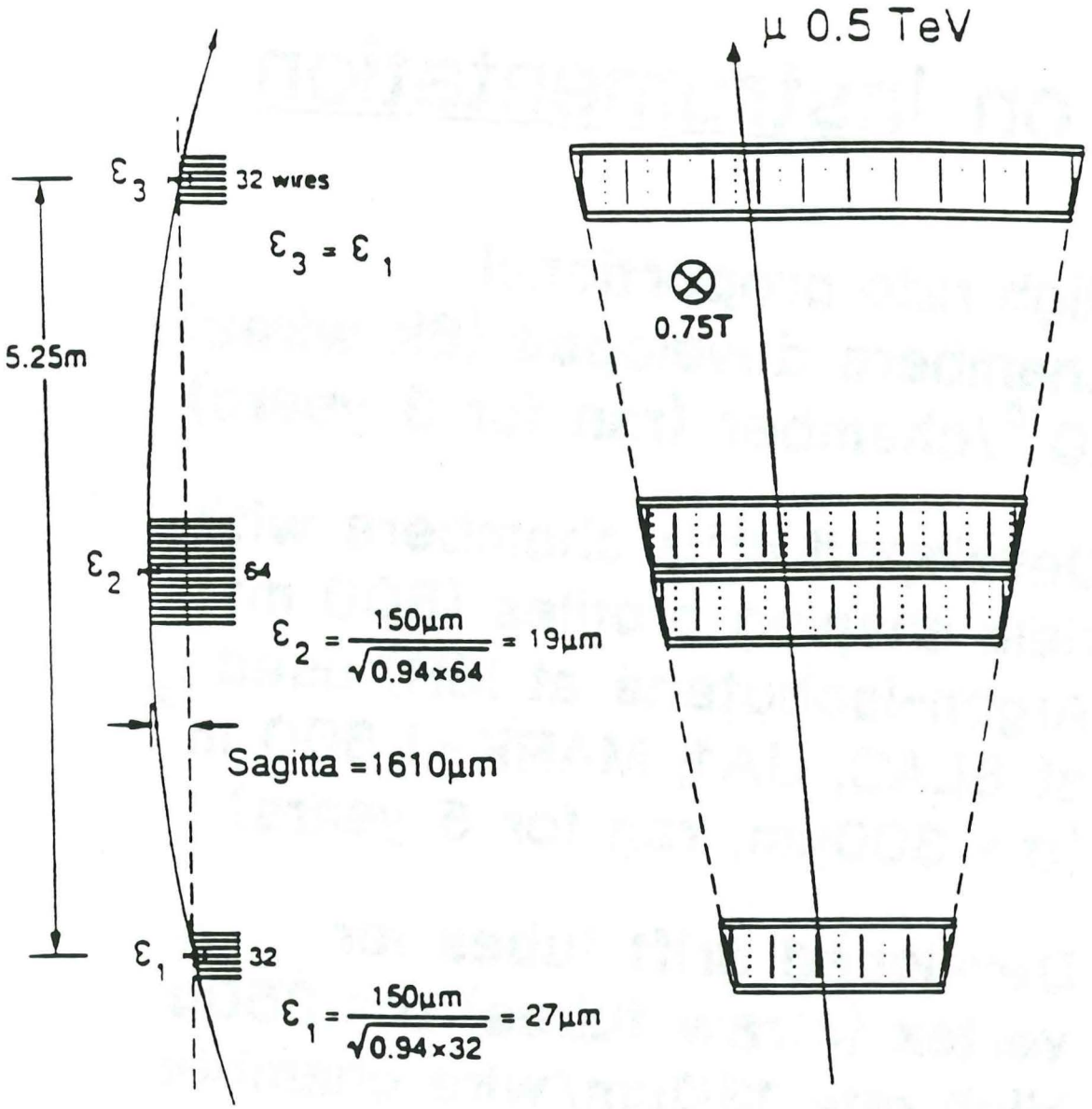

$$\Delta S = \sqrt{\frac{1}{2}\,\varepsilon_1^2 + \varepsilon_2^2 + \Delta S_{sys}^2 + \Delta S_{ms}^2}$$

$$= \sqrt{\frac{1}{2} 27\mu m^2 + 19\mu m^2 + 20\mu m^2 + 15\mu m^2}$$

$$= 37\mu m$$

$$\frac{\Delta S}{S} = 2.4\%$$

R&D on Instrumentation

1974 High rate proportional chambers developed (6k wires) 10^{10}/chamber (ran for 3 years)

1976 Developed drift chambers with field shaping profiles (800 m^2 Argon-Isobutane at ISR) used at SLAC, UA1; MARK-J 600 m^2 (σ = 300μm, ran for 5 years)

1979 Developed drift tubes for vertex (straw tubes) σ = 250μ High rate 130μm/wire chamber for ISABELLE

1982 Developed L3 multisampling drift chambers Δs = 50 μm alignment ≤ 30μm

1990 Continue R&D for L*

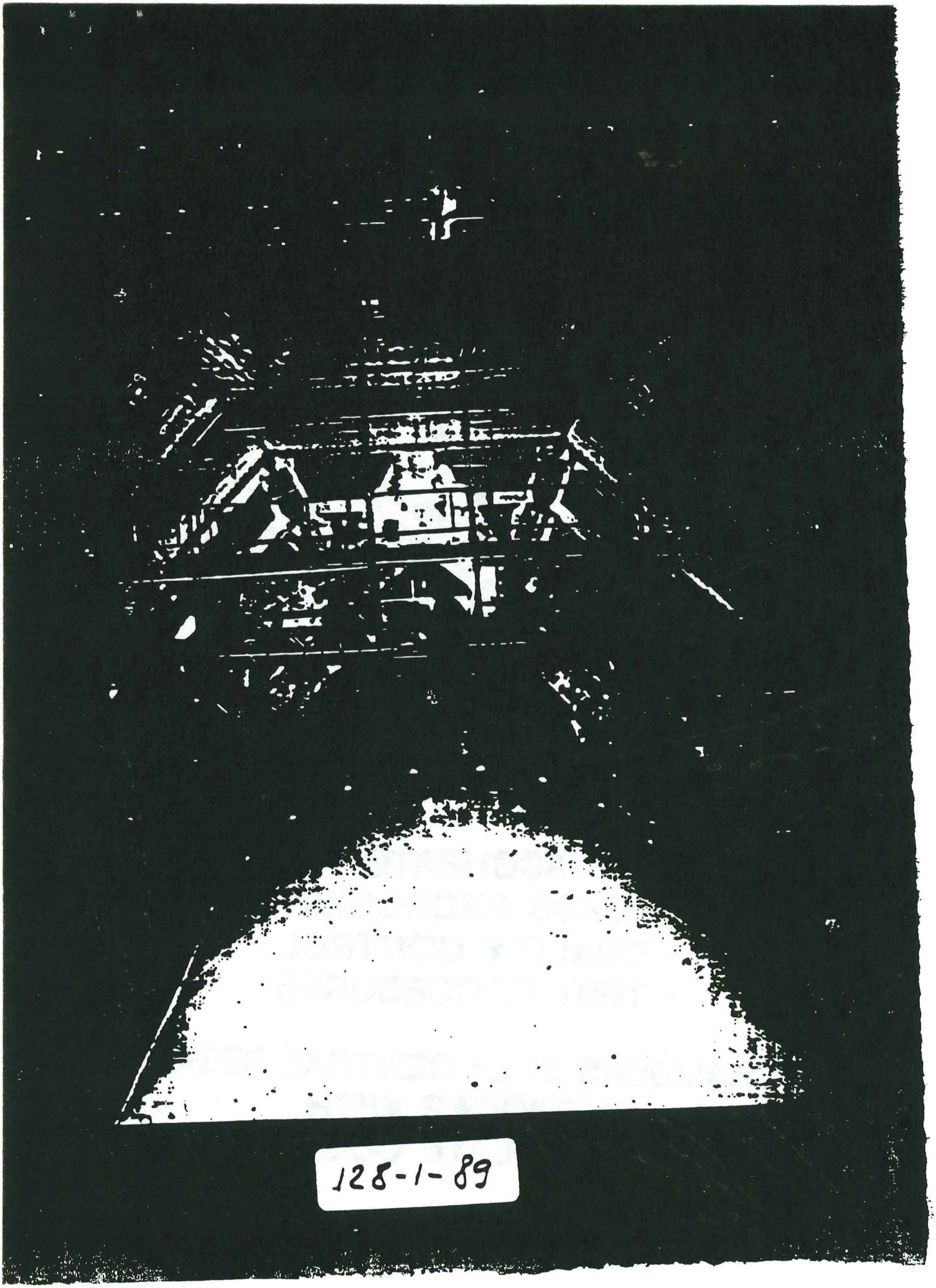

128-1-89

L3 AND L• PRECISION CHAMBERS

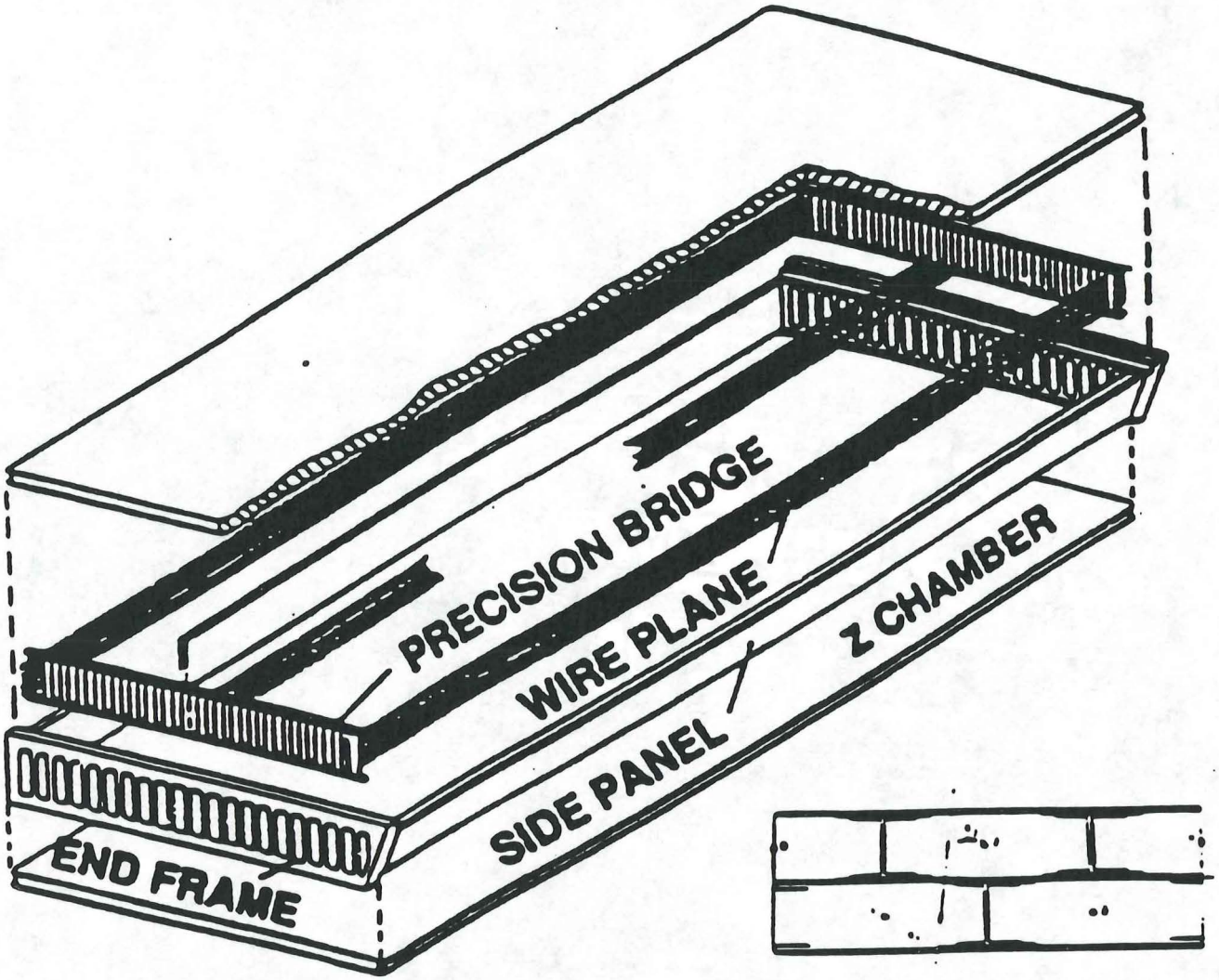

- ACCURATE
- MASS PRODUCED
- QUALITY CONTROL
- TEST PROCEDURES

Z CHAMBERS IN L• CENTRAL REGION
IN TRIGGER WITH
RESISTIVE PLATE COUNTERS

L3 AND L*
WIRE POSITIONING ACCURACY

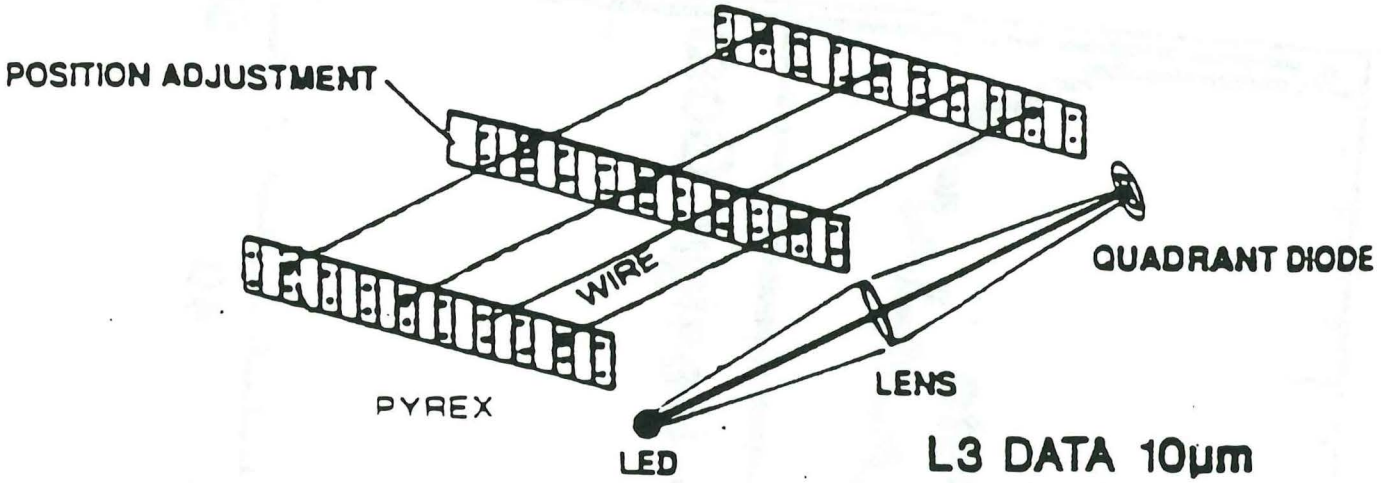

L3 DATA 10μm
L* 8μm

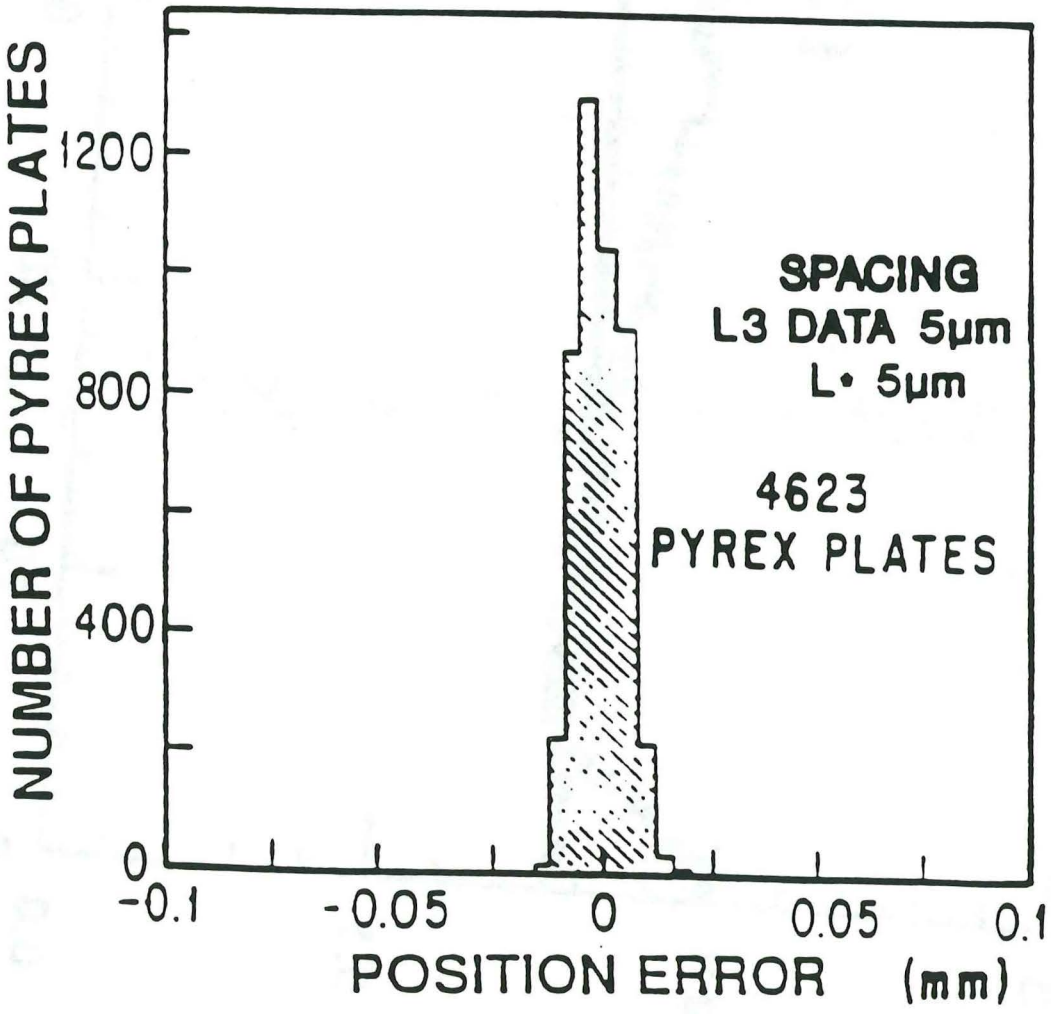

L* Single Wire Resolution

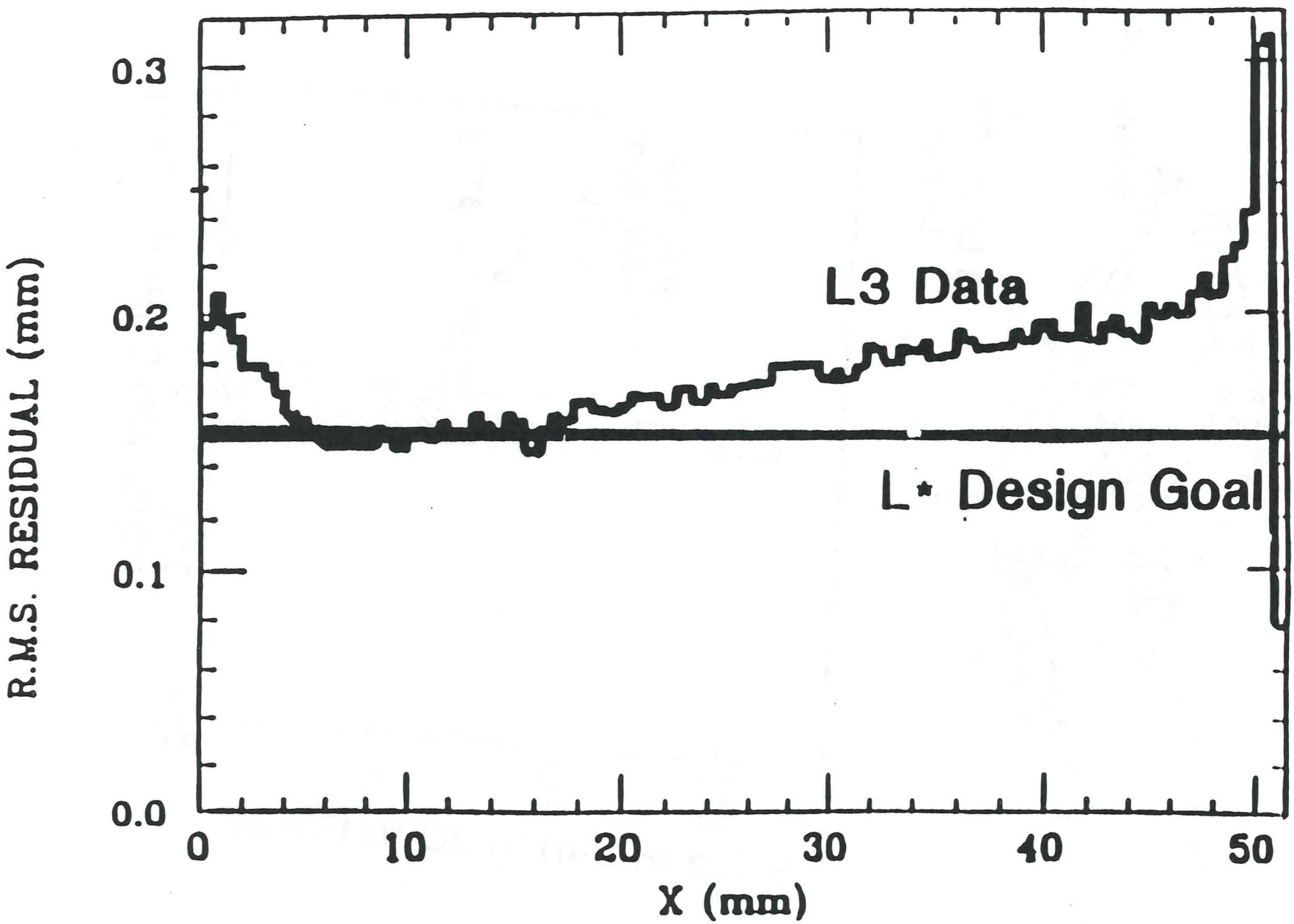

L* Alignment

	L*	L3 - Achieved
P-Measurement		
3 Layers - Absolute	8 μm	15 μm
Monitored - Relative	1 μm	0.2 μm
Global		
All Tracks Point To Intersection	0.7 mm	1.0 mm

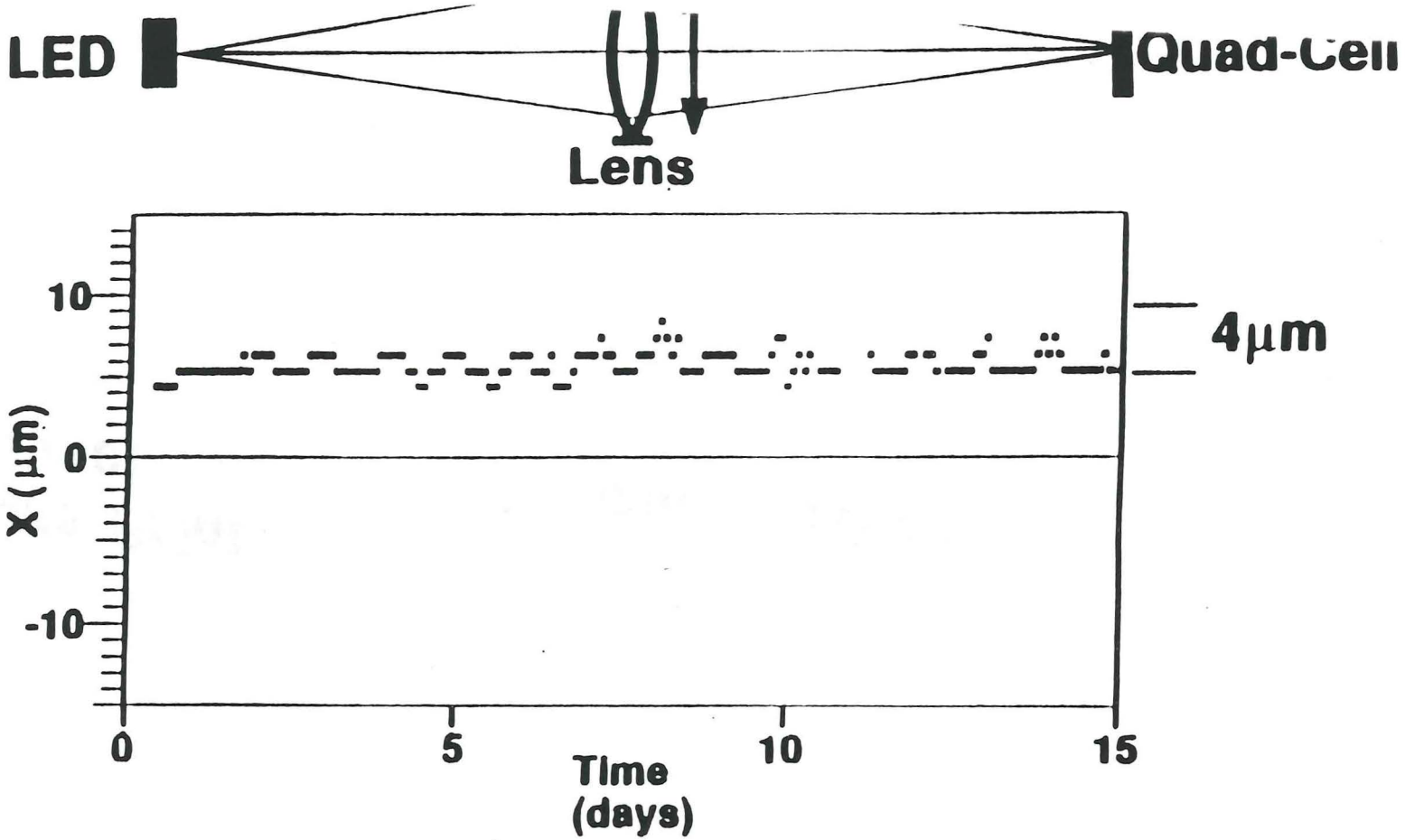

Fifteen -day stability of the L3 Muon Chambers within an octant

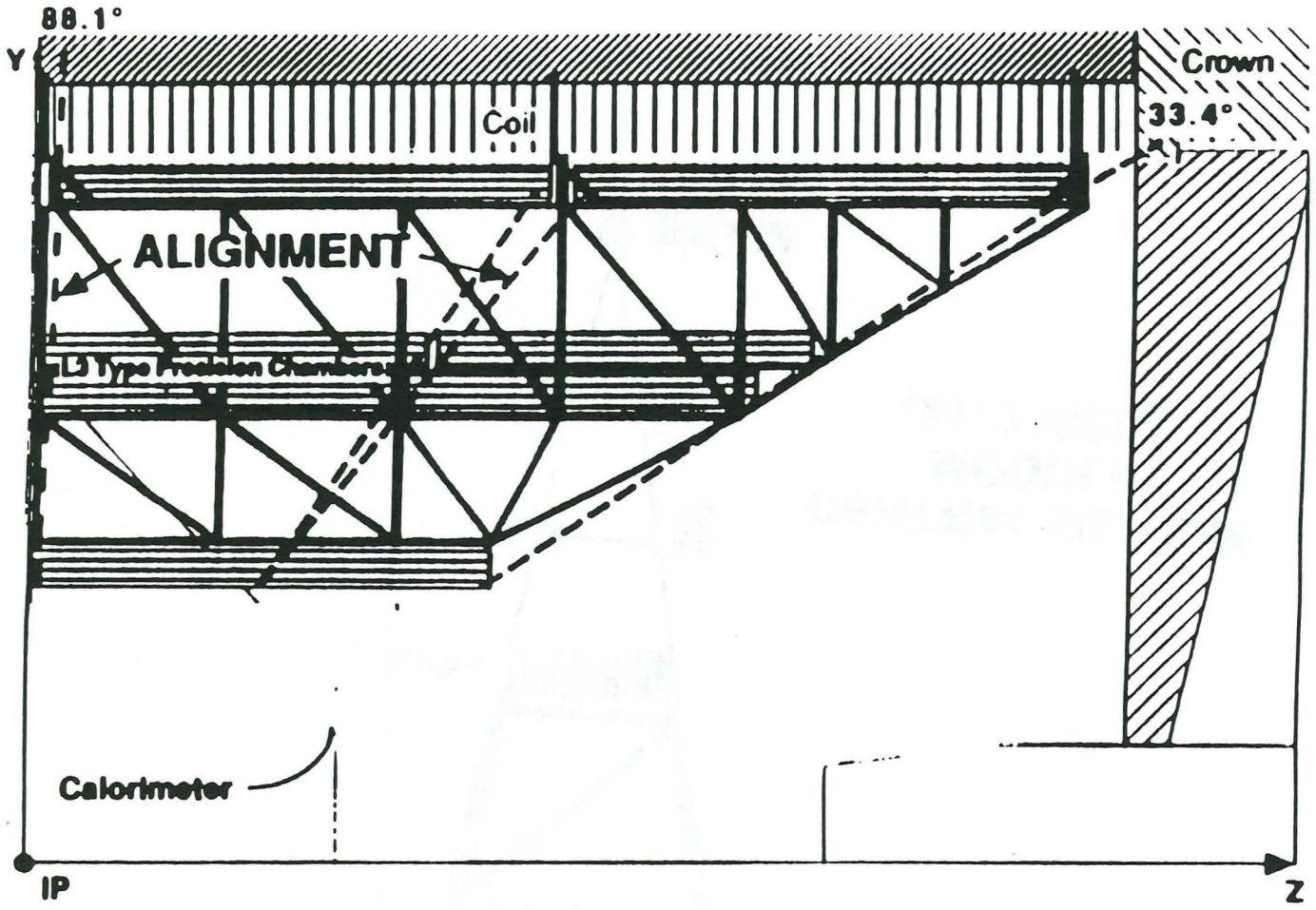

CENTRAL

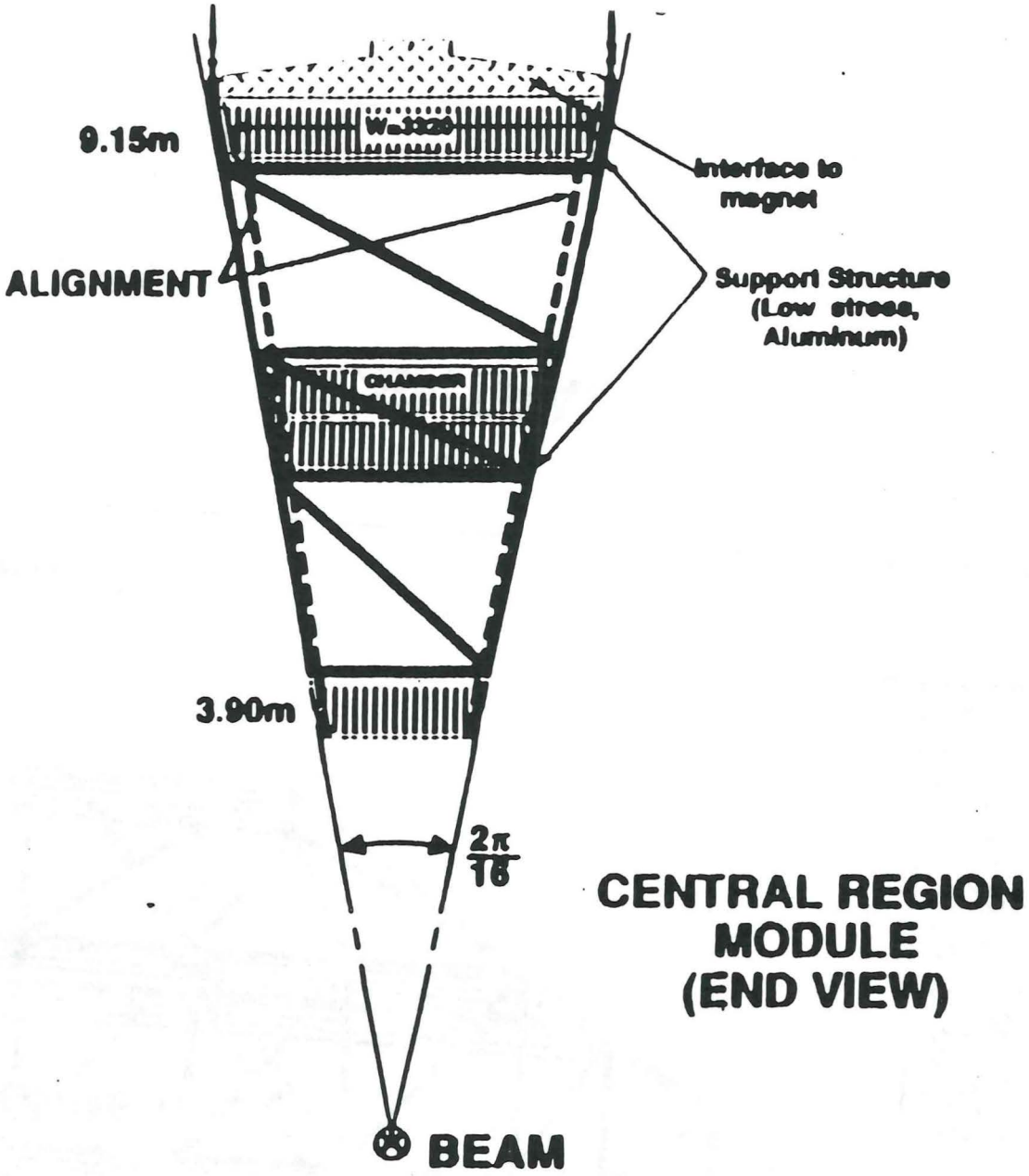

CENTRAL REGION MODULE (END VIEW)

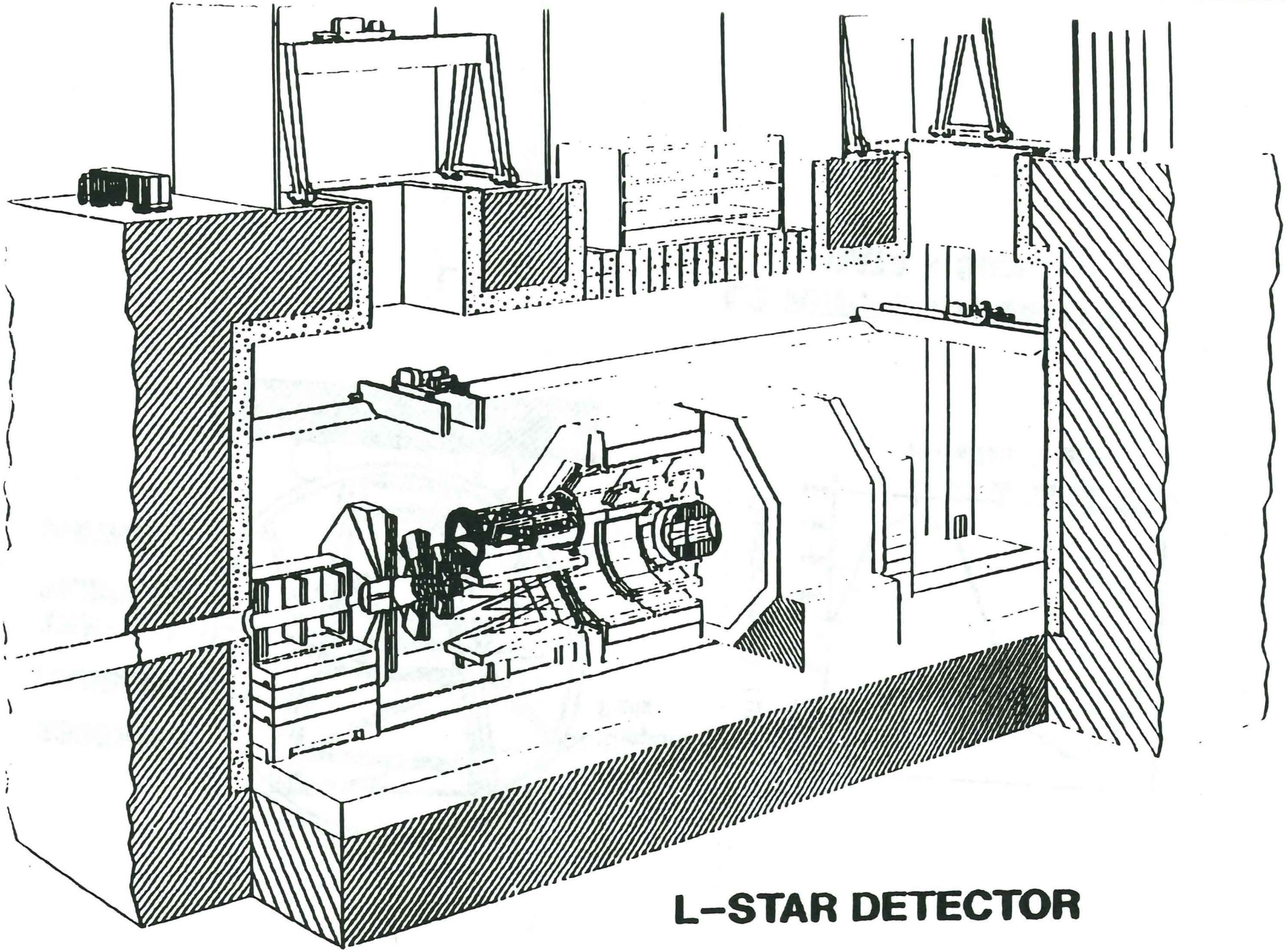

L–STAR DETECTOR

L* CHAMBER INSTALLATION

ASSEMBLY

HANDLING

TEST ALL MODULES

INSTALL

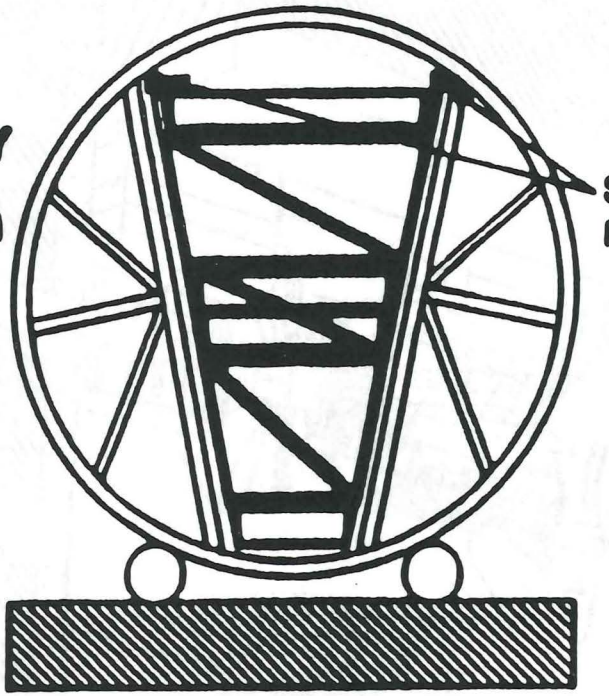

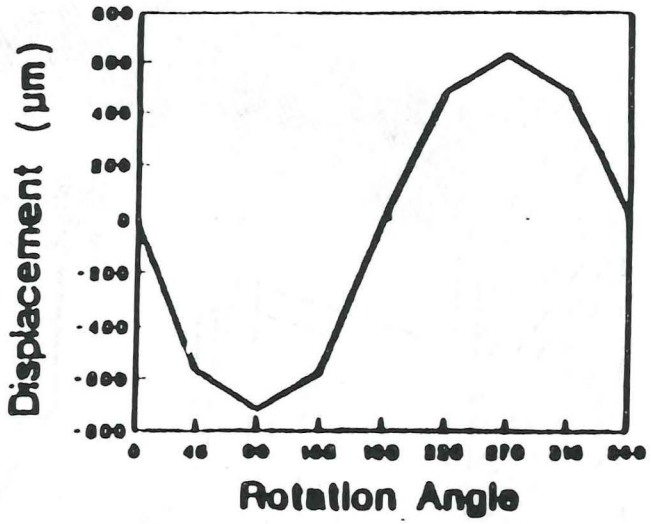

L*

L3 REPRODUCIBILITY
DATA < 6μm

L* R&D MILESTONES

	FY90	FY91	FY92
Request to DOE			
Muon Chambers	Freeze Conceptual Design	Produce & Evaluate Prototypes	Full Length Chamber Model
Gas	Complete Measurement Setup	Measure 10 Mixtures	Chamber with Final Cell
Structural Design & Analysis	Freeze Concepts	Detailed Design	Assemble, Evaluate Prototypes
	Complete All Structure Models	Prototypes	Computations for Alignment
		Finite Element Analysis	
Request to Swiss Authorities			
Alignment Systems	Design Test Stand	Evaluate Prototypes	Test System
Electronics & Data Transfer	Define Architecture	Develop Chips, Prototypes	Evaluate, Verify

DETECTOR CONSTRUCTION

CENTRAL	MIT, LLNL
ENDCAP	ETH
FORWARD	China

Fast Hadron Calorimeter

down to $\Theta > 2^0$

Also : very forward part down to $|\theta| = 0.3^0$

made of

lead-steel-silicon or liquid scintillator sandwich

Shaping time : 15 ns

Tower geometry :

$$\Delta\eta\,\Delta\varphi = 0.04 \times 0.04$$

9 longitudinal segmentation for muon identification, tracking & pattern recognition

us : 190/333 cm

caps : 204 Tons

ius : 20/138 cm

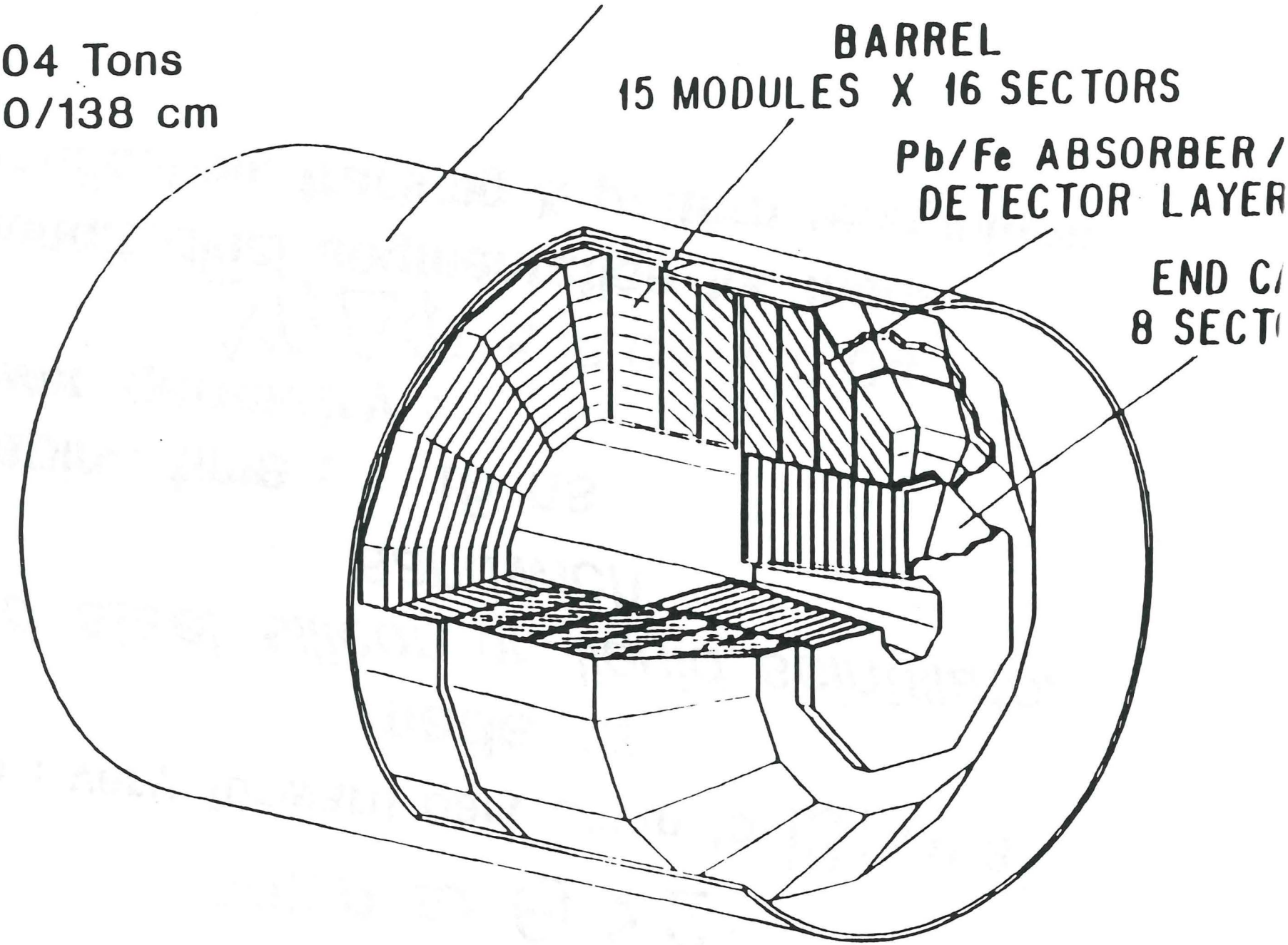

HADRON CALORIMETER

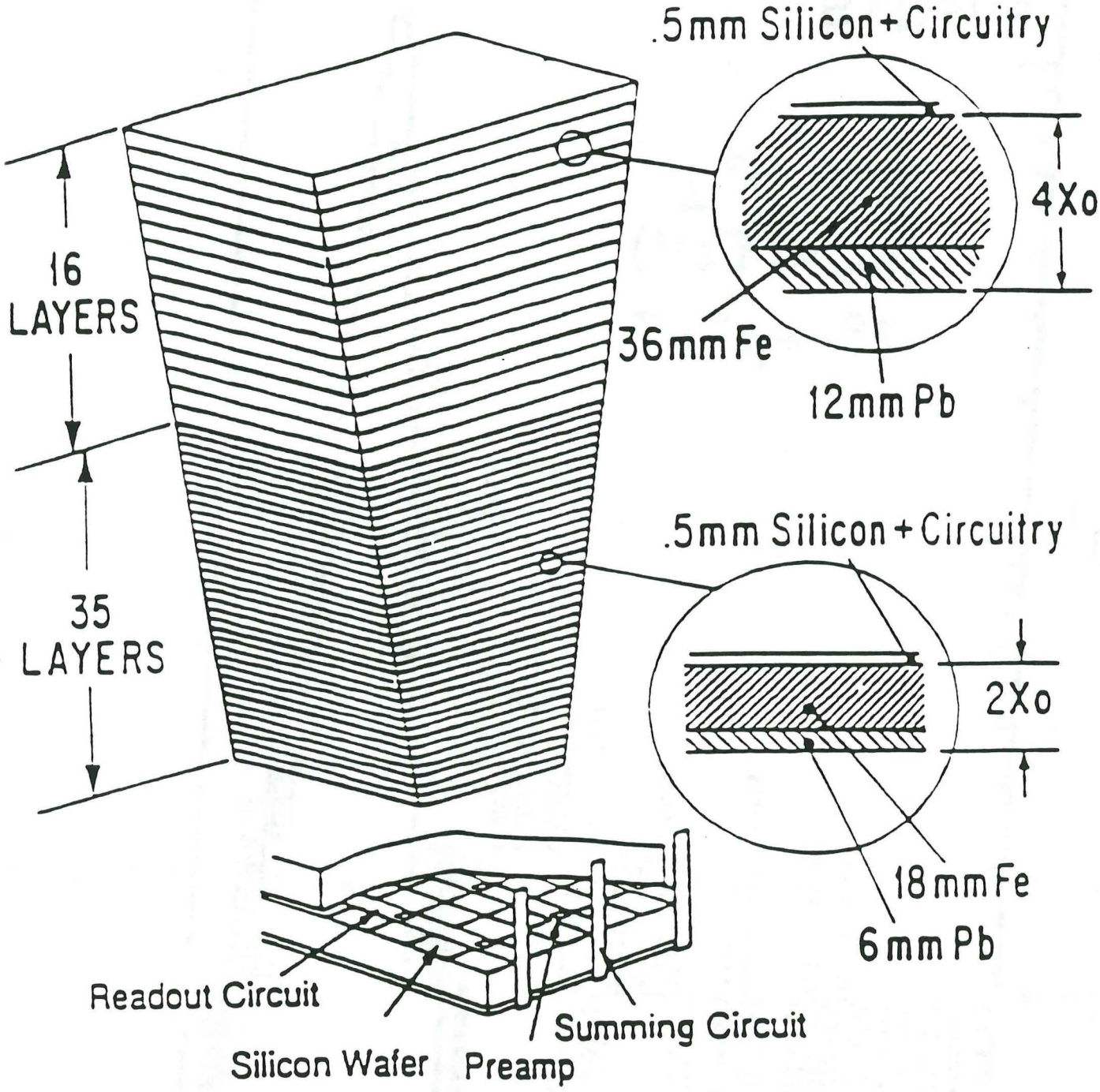

The calorimeter absorber/detector structure at 90°.

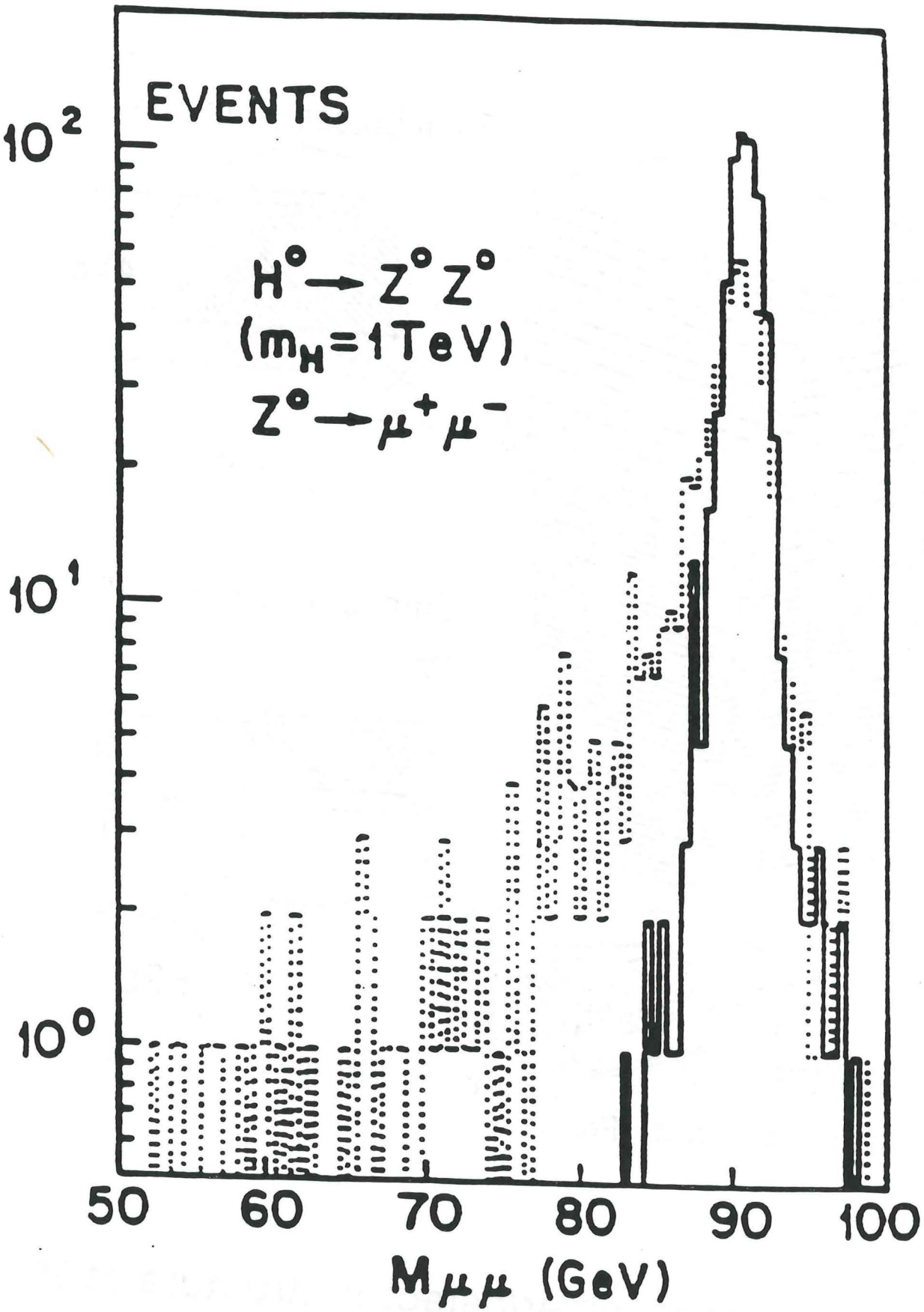

Deterioration of Z -› 2μ mass resolution due to fluctuations of muon energy loss in 12 λ calorimeter (dotted line). Correction for these fluctuations will be made by calorimeter sampling measurements (solid line).

25 Years of Electrons, Muons and Photons

64	DESY	72	BNL	74	ISR	78	PETRA	83	LEP	90
	$\gamma \to e^+ e^-$		$J \to e^+ e^-$		$p\ p \to \mu^+ \mu^-$		$e^+ e^- \to Q\bar{Q}g$		$Z^0 \to l^+ l^-, Q\bar{Q}$	
	QED $R < 10^{-14}$ cm $\rho, \omega, \phi \to e^+ e^-$ SU3		New Quarks		Scaling		Gluons - α_s $e^+ e^- \to \mu^+ \mu^-$ QED $R < 10^{-16}$ cm		3 Families g_A, g_V $B \to \mu + X$	
	$\frac{\Delta M}{M} = 1\%$		$\frac{\Delta M}{M} = 0.1\%$		$\Omega = 2\pi$		$\Omega = 4\pi$		$\Omega = 4\pi$	
	$\frac{ee}{hh} = 10^{-8}$		$\frac{ee}{hh} = 10^{-10}$		$\frac{\mu\mu}{hh} = 10^{-6}$		e, μ, jets		e, μ, γ $\frac{\Delta p}{p} = 1\%$	
	$10^{35} cm^{-2} s^{-1}$		$10^{36} cm^{-2} s^{-1}$		$10^{32} cm^{-2} s^{-1}$		$10^{30} cm^{-2} s^{-1}$		$10^{31} cm^{-2} s^{-1}$	
	$p_1 = p_2$		$p_1 = p_2$ high rate chambers		large area chambers				$p_1 = p_2$ (e, γ) $p_1 = p_2 + \Delta E$ (μ)	

Funding Request to SSCL
R&D for L* Detector

	FY90	FY91	FY92	TOTAL
MAGNET	0.0	0.5	0.5	1.0
MUON DETECTOR	1.0	4.6	2.8	8.4
HADRON CALORIMETER	0.0	2.6	2.1	4.7
E-M CALORIMETER	0.0	2.9	3.1	6.0
CENTRAL TRACKER	0.0	2.2	2.2	4.4
FORWARD CALORIMETER	0.0	0.4	0.4	0.8
DAQ + TRIGGER	0.0	2.9	4.2	7.1
COORDINATION	0.0	0.5	0.5	1.0
TOTAL	1.0	16.6	15.8	33.4

Europe Physicists in L★

Country	Institute	Number of Physicists	Spokesperson	
Switzerland	ETH Zürich	35	H.Hofer	Professor
	Univ. Geneva	1	M.Bourquin	Professor
Germany	RWTH Aachen	27	K.Lübelsmeyer	Director
Italy	Univ. Florence	12	P.Spillantini	Professor
	Univ. Milan	6	P.G.Rancoita	Professor
	Univ. Naples	12	C.Sciacca	Professor
	Univ. Rome	7	B.Borgia	Director
France	LAPP Annecy	4	M.Vivargent	Professor
Hungary	Budapest	5	E.Nagy	Professor
Bulgaria	CLANP Sofia	7	B.Betev	Professor

Asia Physicists in L★

Country	Institute	Physicists	Spokesperson
China	IHEP *Beijing*	53	S.X.Fang *Director*
	USTC *Hefei*	14	C.H.Gu *President*
	SIC *Shanghai*	28	J.K.Guo *Director*
Taiwan	High Energy Physics Group	11	H.M.Hsia *President*
Korea	Kyungpook Univ.	3	
	Gyeongsang Univ.	4	
	Chungnam Univ.	1	
	Cheonnam Univ.	1	
	Kangreung College	2	Y.Kim *Professor*
	Korea Univ. Seoul	1	D.Song *Professor*
	Seoul Univ.	1	
	Sangji College	1	
	Taegu Univ.	1	
Japan	Saitama College	1	T.Doke *Professor*
	Waseda Univ.	2	

USSR AT L*

MAGNET PROJECT RESPONSIBILITY:
KURCHATOV ATOMIC ENERGY INSTITUTE,MOSCOW
L* PARTICIPANTS 61: E.Velikhov Director General
S.Belyaev Research Director
N.Chernoplekov Division Leader

CALORIMETER PROJECT RESPONSIBILITY:
ITEP, MOSCOW
L* PARTICIPANTS 71: V.Shevchenko Vice Director
Yu.Galaktionov Division Leader

JINR, DUBNA
L* PARTICIPANTS 55: D.Kiss Director General
I.Savin Research Director
I.Golutvin Vice Director

IHEP, SERPUKHOV
L* PARTICIPANTS 10: A.Lebedev Division Leader

RESPONSIBILITY AREAS UNDER DISCUSSION:
YEREVAN PHISICS INSTITUTE,YEREVAN
L* PARTICIPANTS 21: A.Amatuni Director General

LENINGRAD NUCLEAR PHYSICS INSTITUTE:
L* PARTICIPANTS 29: A.Vorobyov Director General

INSTUTUTE OF NUCLEAR PHYSICS,NOVOSIBIRSK
L* PARTICIPANTS 3: A.Skrinsky Director General

INSTITUTE OF PHYSICS, TBILISI, GEORGIA
L* PARTICIPANTS 15

INSTITUTE OF PHYSICS, TARTU, ESTONIA
L* PARTICIPANTS 2

L* Support Outside US

Foreign countries will support the L Experiment through:*

Financial Support
Material
Complete Detector Subsystems
Workshop Infrastructure
Engineers and Technicians
Logistics Support

L★ Construction
Funding Proposal Under Discussion

Subdetector	USA (M$)	USSR	Europe + Asia
Magnet (Warm Coil)	68.3	★	-
Muon Detector	110.0	-	★
Hadron Calorimeter (Silicon)	50.8	★	-
E-M Calorimeter (BaF_2)	2.0	★	★
Central Tracker	40.0	★	★
Forward Calorimeter System	2.0	★	★
EDIA (10%)	27.3	★	★
TOTAL	300.4	★	★

L* Costs

To account the non-US support appropriately in a cost estimate mutual agreements are needed on:

1. labor costs
(normally not accounted for outside USA)

2. costs of social security charges
(normally not accounted for outside USA)

3. currency exchange rates
(Rb/$ - 1.6 or 0.6 ?)

4. existing workshops
(manpower & equipment usually not accounted for outside USA)

5. overhead charges
(normally not accounted for outside USA)

Infrastructure Support in Manyears
Construction of L3 Experiment

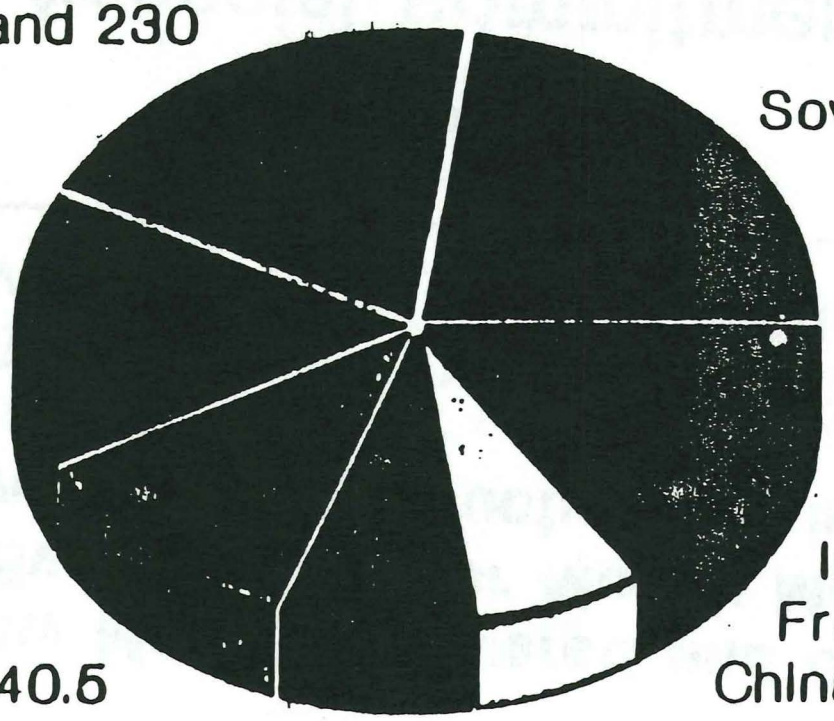

Total Support 1181.1 Manyears

L3 Money Matrix does not reflect the total contributions of the different funding agencies.

USA: Equipment and Salaries in Money Matrix

USSR: Raw Material delivered and converted into Swiss Francs for Money Matrix. Manpower and Infrastructure not included.

Others: Only Equipment included in Money Matrix. Manpower and Infrastructure not included.

L* Strategy:

No financial commitments.

Partners construct and deliver detector subsystems.

Cost and Funds - L3 Detector
Extracted from Money Matrix - Version 14 (kSF)

Subject	Cost	Funds				
		USA	USSR	CH	Others	Total
TEC	10286	-	-	6577	3709	10286
BGO Barrel	35531	20567	5605	2171	7174	35517
Had. Cal.	28465	5037	10350	4366	8712	28465
Muon Det.	41131	23908	-	1220	16014	41142
Magnet	40020	15388	7400	11000	6250	40038
Trigger	9801	4608	500	900	3793	9801
Computer	8817	8817	-	-	-	8817
Luml. Mon.	2022	1928	-	-	-	1928
Scint. Ctrs.	425	125	-	-	300	425
Para. & Assm.	1096	786	-	-	-	786
TOTAL	177594	81164	23855	26234	45952	177205

L*

Finances

Network Lines Serving L3

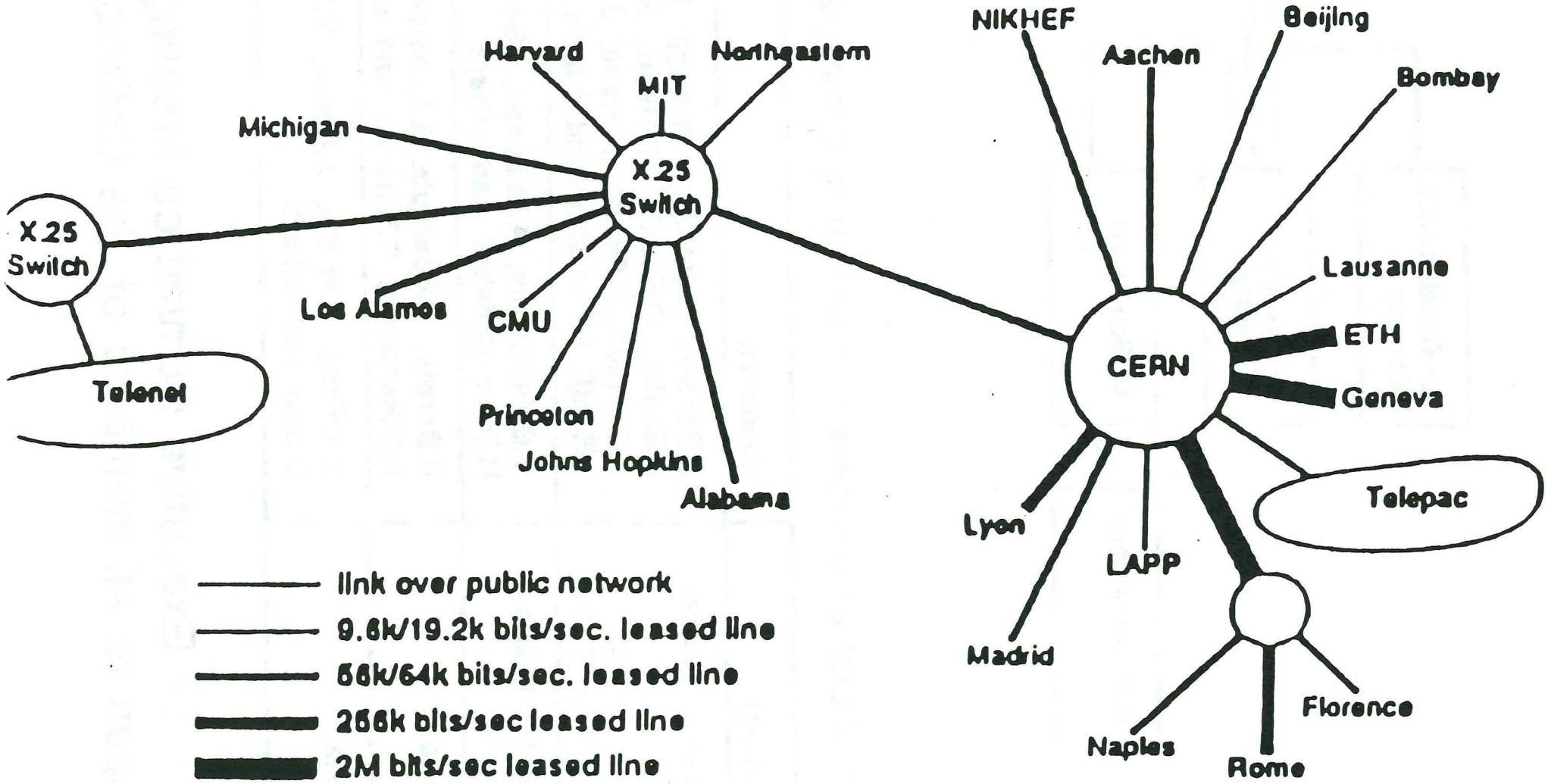

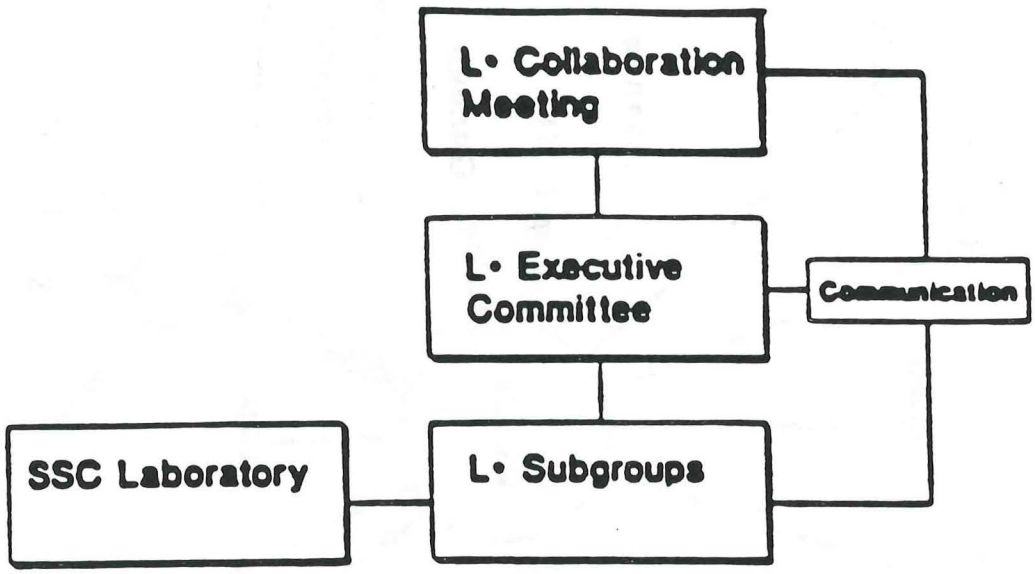

Partial List of Members - L• Executive Committee

Nations	Members
United States	U.Becker, J.Branson, W.Bugg, D.DiBitonto, A.Engler, O.Fackler, R.Heinz, H.Newman, A.Pevsner, P.Piroue, F.Plasil, J.Reidy, J.Rohlf, G.Sanders and others
Soviet Union	Y.Galaktionov, A.Lebedev, I.Savin, N.Tchernoplekov and others
Europe	B.Borgia, M.Bourquin, K.Lübelsmeyer, P.G.Rancoita, C.Sciacca and others
Asia	S.X.Fang, Z.W.Yin, A.Gurtu, Y.Y.Lee, D.Son and others

L• Executive Committee Meetings
open to all members of the Collaboration

True Potential of SSC:

To Explore the Unknown

Physics changes quickly

In 10 years, the examples presented here will most likely no longer be relevant.

These examples only serve as an illustration of the detector capability to search for new phenomena at the SSC

search for narrow dilepton resonances

very narrow Z' (E_6 inspired)

$\Gamma_{Z'} / M_{Z'} = 0.65\% - 3.8\%$

assume $M_{Z'} = 15$ TeV

with electromagnetic detector
L* can measure the *width*

with muon detector
L* can measure the *forward backward charge assymetry*

Note

the detector is 4 π

this will enable us to

reconstruct the $Z^0 \rightarrow q\bar{q}$ and $W^{\pm} \rightarrow q\bar{q}$

decays with mass resolution of $\approx$ *2 GeV*

We can also reconstruct the

$W^{\pm} \rightarrow \mu\nu$ *decay by measuring the missing energy to locate the neutrino* P_T

(2) Clean identification of :

$$Z \rightarrow l^+ l^-$$

requiring $\Delta M \approx \Gamma$

$$pp \rightarrow Z_o Z_o + x$$
$$\hookrightarrow \mu\mu \quad \hookrightarrow \text{jet+jet}$$

$$M(Z_o Z_o) \approx 2 \text{ TeV}$$

$$P_{(Z_o)} \approx 1 \text{ TeV} \qquad P_\mu \approx 0.5 \text{ TeV}$$

$$L^* : \Delta P/P \approx 2.4\% \quad \Delta M = \Gamma_z$$

(3) Clean identification of :

$$Z,W \rightarrow (Q,\bar{Q}) \rightarrow 2 \text{ jets}$$

use complete sampling calorimeter
(replace BaF_2)

we have: $\Delta E/E = (50/\sqrt{E} + 1.0)\%$

$$\Delta M = \Gamma_{w,z} \approx 2.5 \text{ GeV}$$

(1) *Speed of the Detector*

Yields of (1) - (3) are small
Runs at $10^{34} cm^{-2} sec^{-1}$

Central Tracker : ***use only scintillating fibers***
with $t = 5ns$ $\triangle Z = 1cm$

Calorimeter : 10-15ns

Measuring jets and leptons

Muon Chambers : $\ominus > 7.5^{0}$

If Mass of H^0 > 1 TeV or There is No Higgs

Then :

$$pp \longrightarrow Z^0 Z^0 \quad (1)$$

$$pp \longrightarrow W^{\pm} Z^0 \quad (2)$$

$$pp \longrightarrow W^{+} W^{-} \quad (3)$$

will increase with

$$M_{Z^0Z^0} \quad M_{W^{\pm}W^{\pm}} \quad M_{Z^0W^{\pm}}$$

and the longitudinal polarization will increase with M

At M > 1 TeV,

calculations of both signal and background may be even less reliable.

Nevertheless following properties of $L^{\star}$ are important for the success of this type of experiment

If the background (pile up, etc)
10 times worse
we cut

$$\sum P_T < (P_T^{\mu}/10 + 50) \text{ GeV}$$

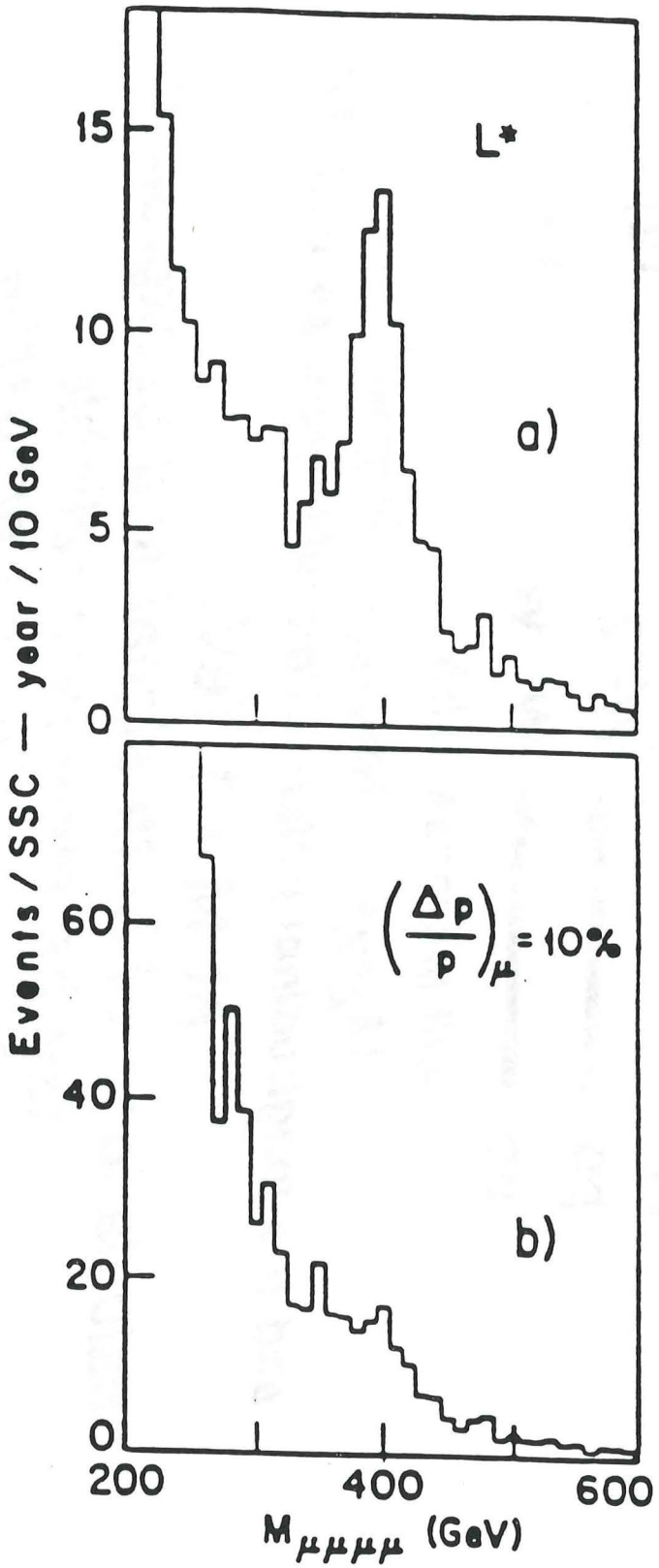

Remarks

We have selected the $H_o \rightarrow 4\,\mu$ *from the R cut requiring*

$$\sum P_T < \left(\frac{P^{\mu}{}_T}{10} + 5 \right) \text{ GeV}$$

We Assume :

the following backgrounds in the R cone must be small

(1) Hadron spray from beam gas

(2) Muon spray from upstream of the intersection region

(3) Pile-up of events

Example: $M_H = 400$ GeV

$$H^0 \rightarrow Z^0 Z^0 \rightarrow \mu^+\mu^- \ \mu^+\mu^-$$

Background:

$$pp \rightarrow q\bar{q} + X \rightarrow 4\mu + X$$

$$pp \rightarrow Z^0 Z^0 + X \rightarrow 4\mu + X$$

$$pp \rightarrow Z^0 + X \rightarrow 4\mu + X$$

Using the above cuts:

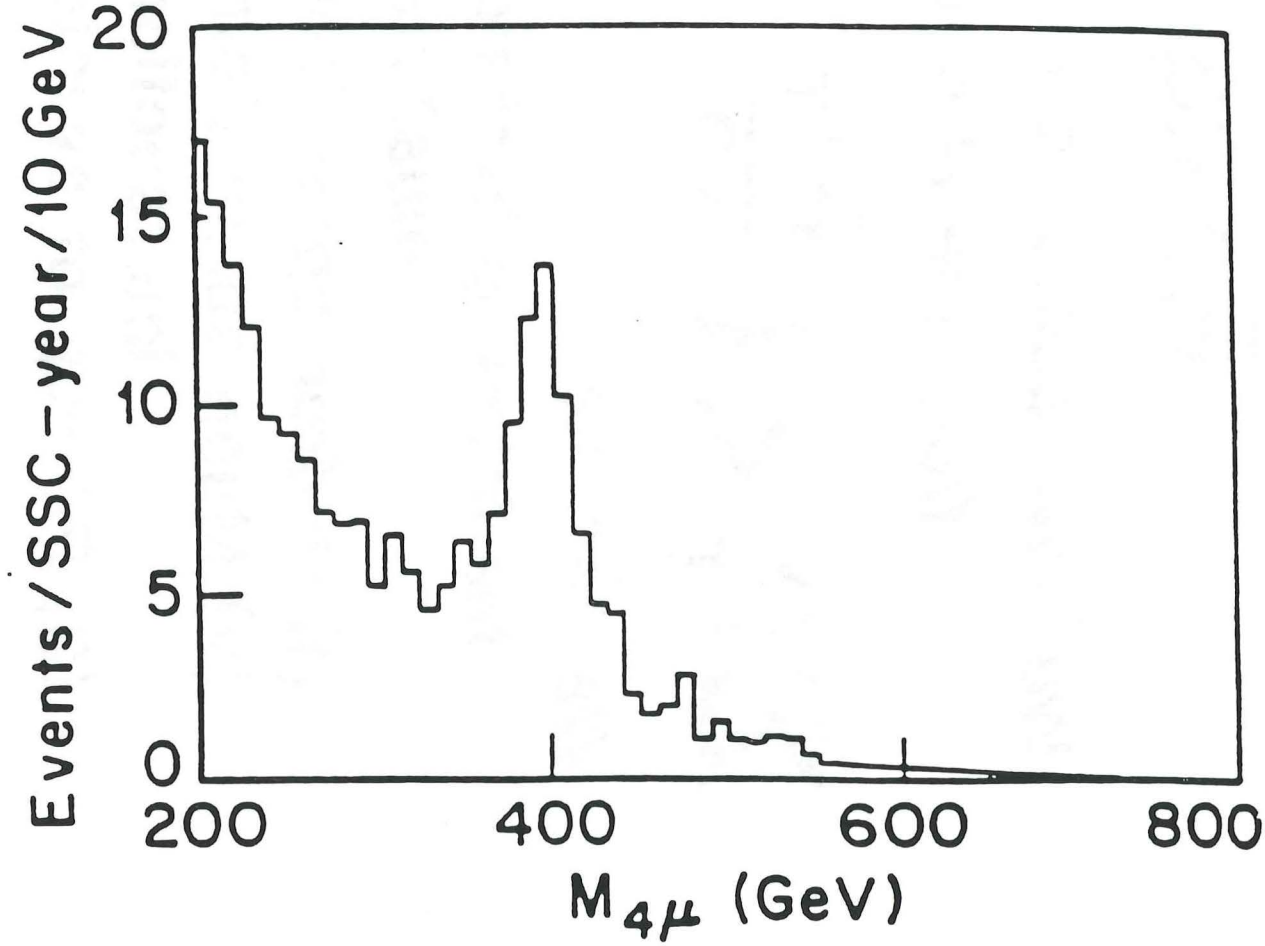

Electron Backgrounds

In addition to Muon Background

1. π^0
2. *Charge exchange*

A) *Momentum Energy Matching*
measuring momentum in
Central Tracker P and
energy in BaF_2 *: E*

P = E Rejection factor : 100

B) *Isolation cut :* Rejection factor : 20

Rejection of μ backgrounds.

1. $P_{\perp} > 5$ GeV

2. $P_{\mu} = P_{vertex}$ 2σ *Rejection : 20*

3. *Vertex matching :* *Rejection : 3*

4. *Isolation cut :* *Rejection : 20*

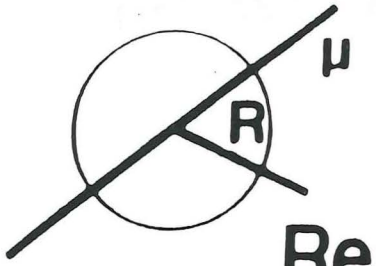

Require $\Sigma P_T < (5 + P_T(\mu)/10)$ GeV

$p + p \rightarrow H^0 + X$

$H^0 \rightarrow 4l$

$2M_Z < m < 800$ GeV

single μ backgrounds

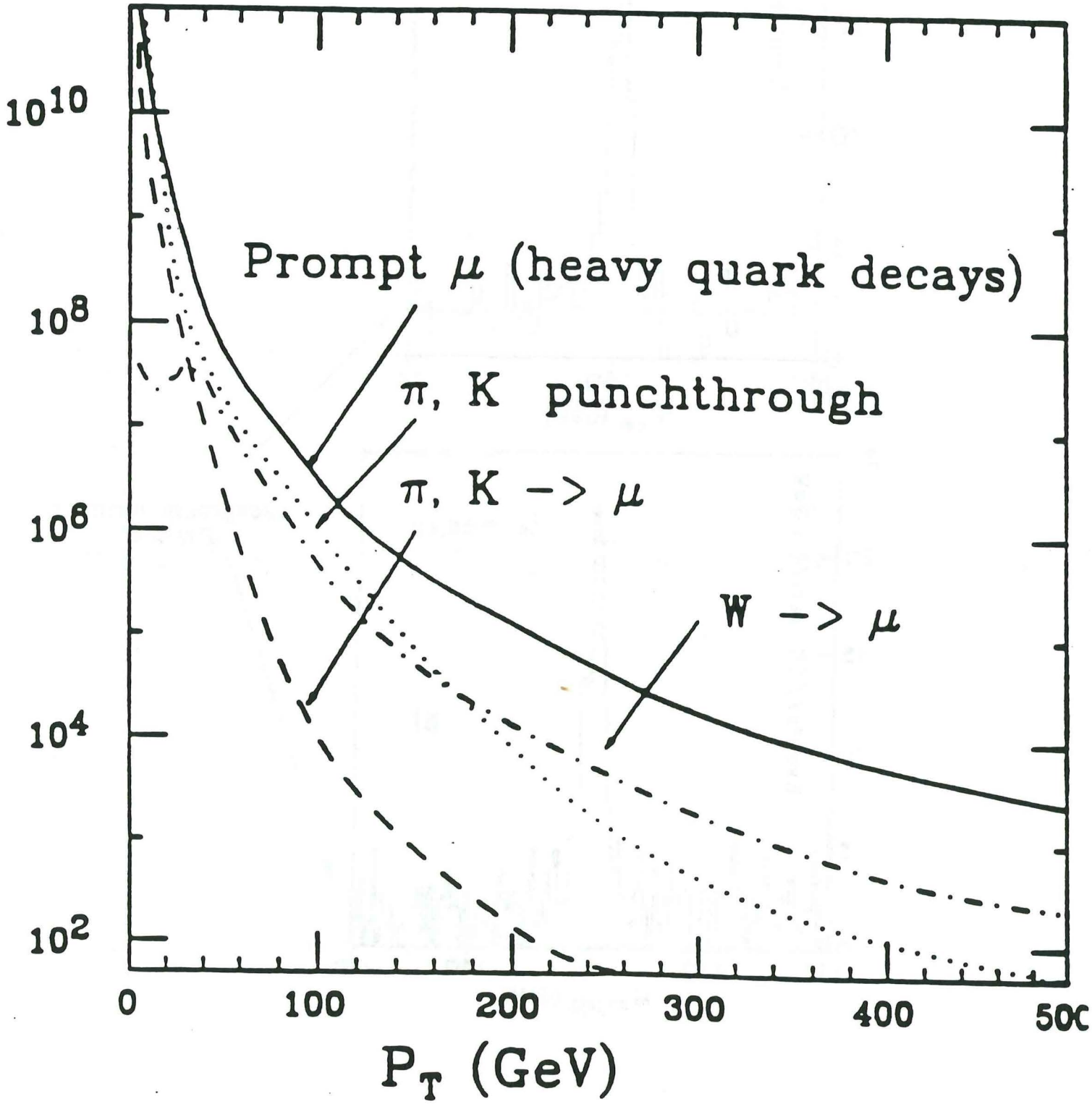

$140 < M_H < 180\ GeV$

$p + p \rightarrow H^0 + X \rightarrow Z_0 Z_0^* \rightarrow 4\text{leptons}$

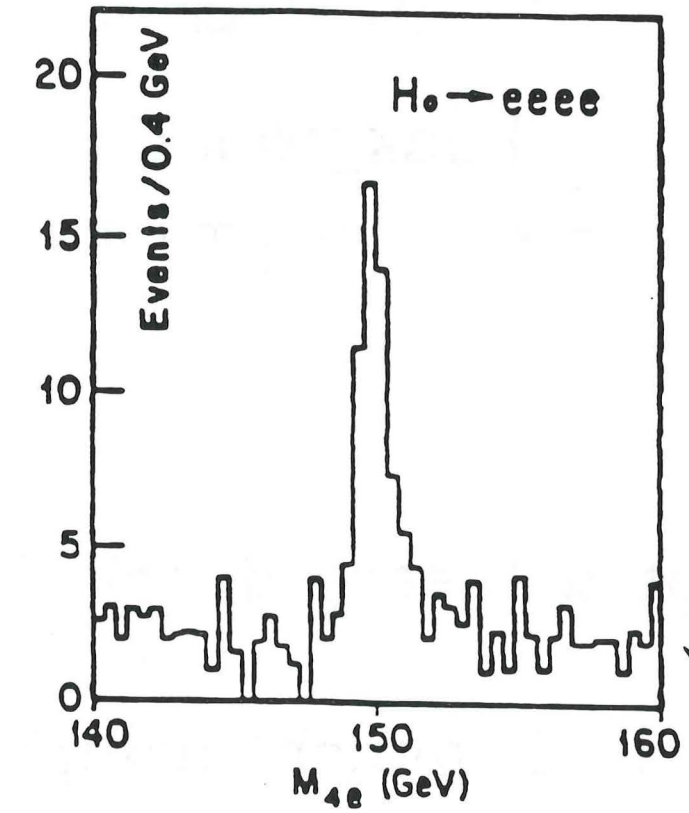

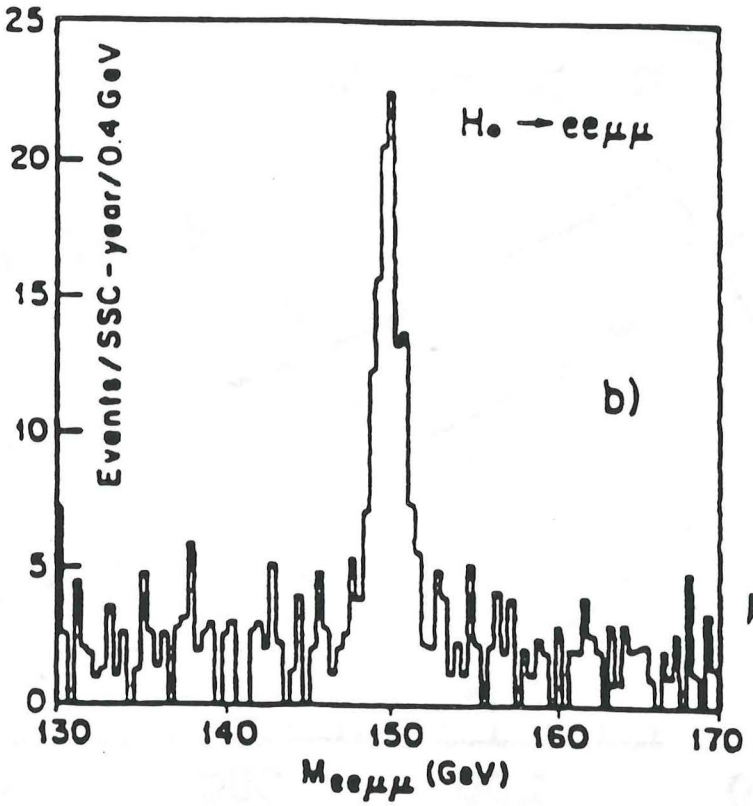

background includes
$Z\,t\bar{t} \rightarrow 4l$

$$\text{if } \sum_T < \left(\frac{E_T^{\gamma}}{10} + 15\right) \text{GeV}$$

Then the 100 GeV $H_0 \rightarrow \gamma\gamma$

signal/background ratio

will be 4.1σ

$$\sum E_T < \left(\frac{E_T^{\gamma}}{10} + 10\right) \text{GeV}$$

Then the 100 GeV $H_0 \rightarrow \gamma\gamma$

signal/background ratio

will change from 9σ *to* 6σ

Remarks

Assume there are
more backgrounds and pile-up

so the energy is much larger
in the $R < 0.6$ cone

and we must cut
at much higher energy

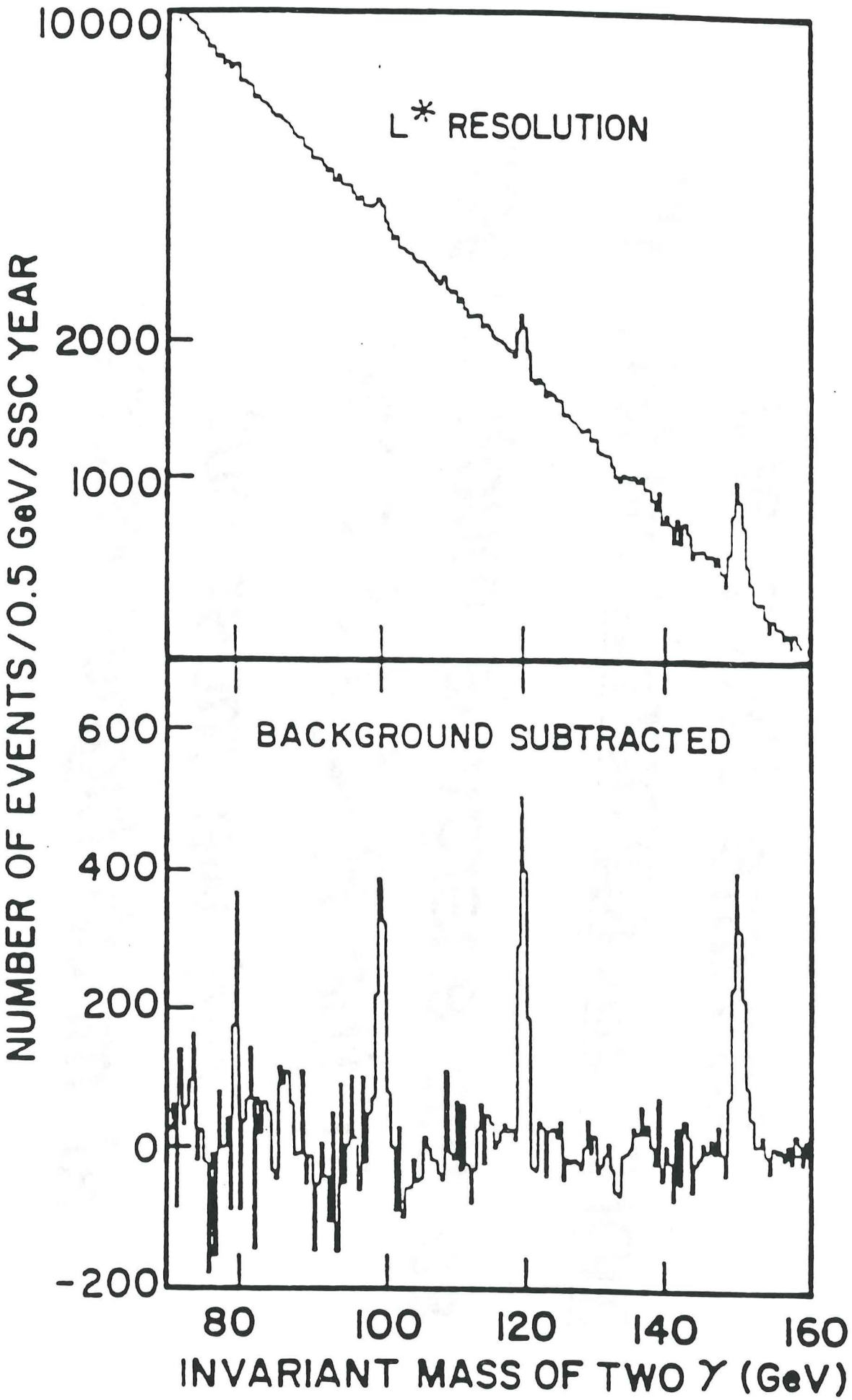
10000
2000
1000
L* RESOLUTION
600
400
200
0
-200
BACKGROUND SUBTRACTED
NUMBER OF EVENTS/0.5 GeV/SSC YEAR
80
100
120
140
160
INVARIANT MASS OF TWO γ (GeV)

Other Photon Backgrounds

- π^0 and γ production inside jets.

  $\sigma(pp \rightarrow jet\ jet) = 1.2mb$

  for $p_\perp(jet) > 20\ GeV$ and $|\eta| < 2.5$

- one isolated photon + jet

  - $\sigma(qg \rightarrow q\gamma) = 119$ nb

  - $\sigma(q\bar{q} \rightarrow g\gamma) = 6$ nb

Isolation Cut:

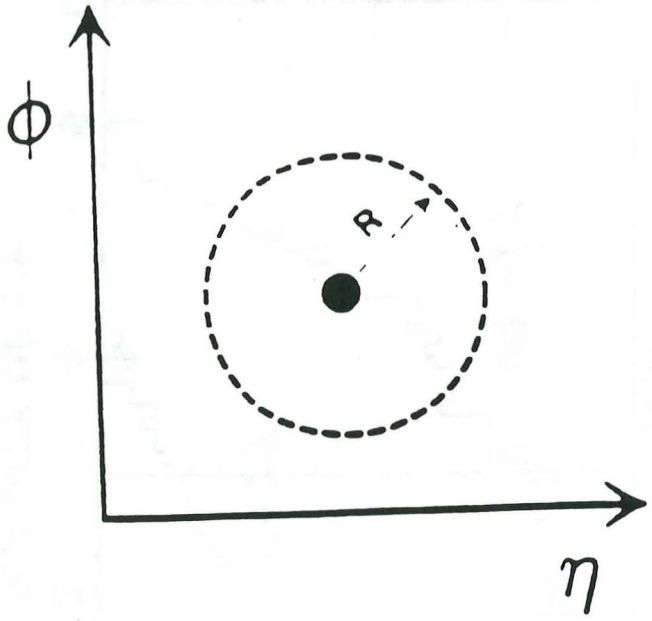

$$R = \sqrt{(\Delta\eta)^2 + (\Delta\phi)^2}$$

Requirement: $\Sigma E_T < E_T^\gamma/10+5\text{GeV}$

Background reduction: 10^{-1} (using R=0.6)

Isolated Photon Background:

$gg \rightarrow \gamma\gamma$ (493 pb)

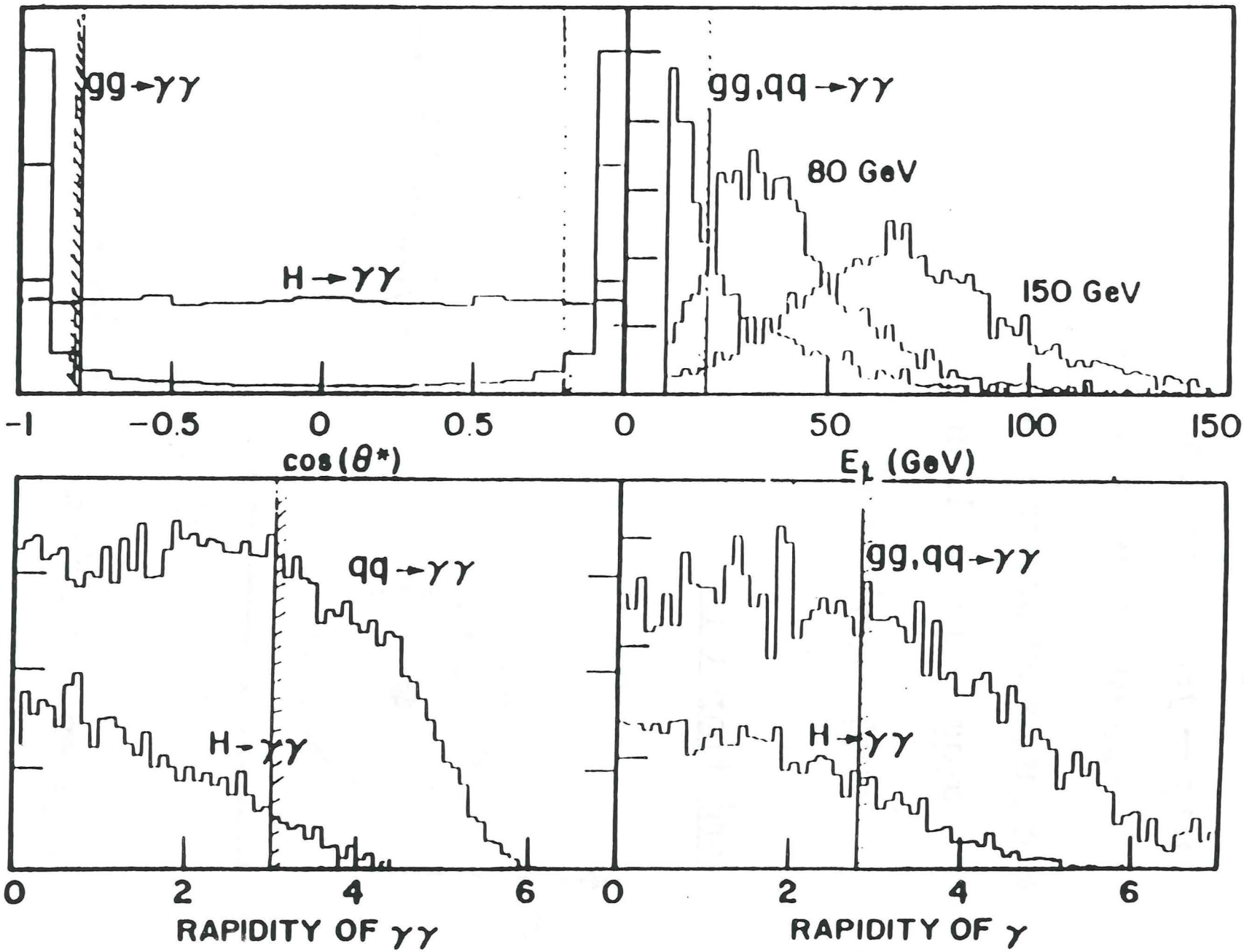

$80\ \text{GeV} < M_H < 160\ \text{GeV}$

$H^0 \to \gamma\gamma$

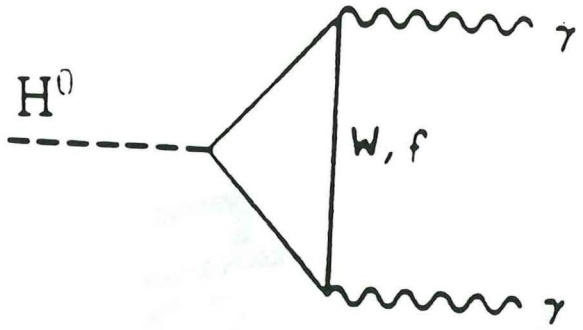

$\text{Br}(H^0 \to \gamma\gamma) = 10^{-4} - 10^{-3}$

$\sigma(pp \to H^0 \to \gamma\gamma) = 0.3\ \text{pb}$

Signature: Two isolated photons

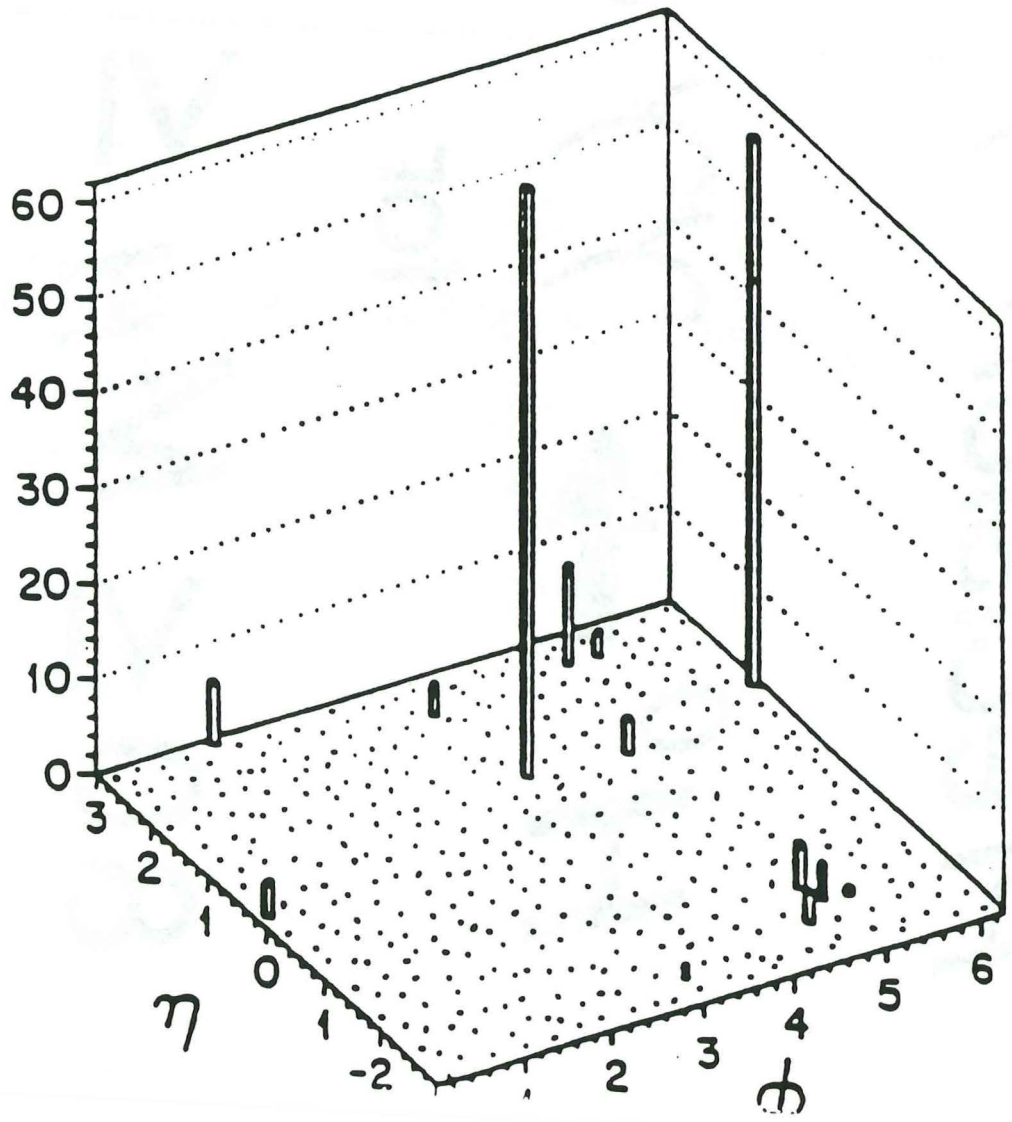

Physics of Precision γ and e

$H^0 \rightarrow \gamma\gamma$ Search

for

$$80 \leq M_H \leq 160 GeV$$

Higgs Mass

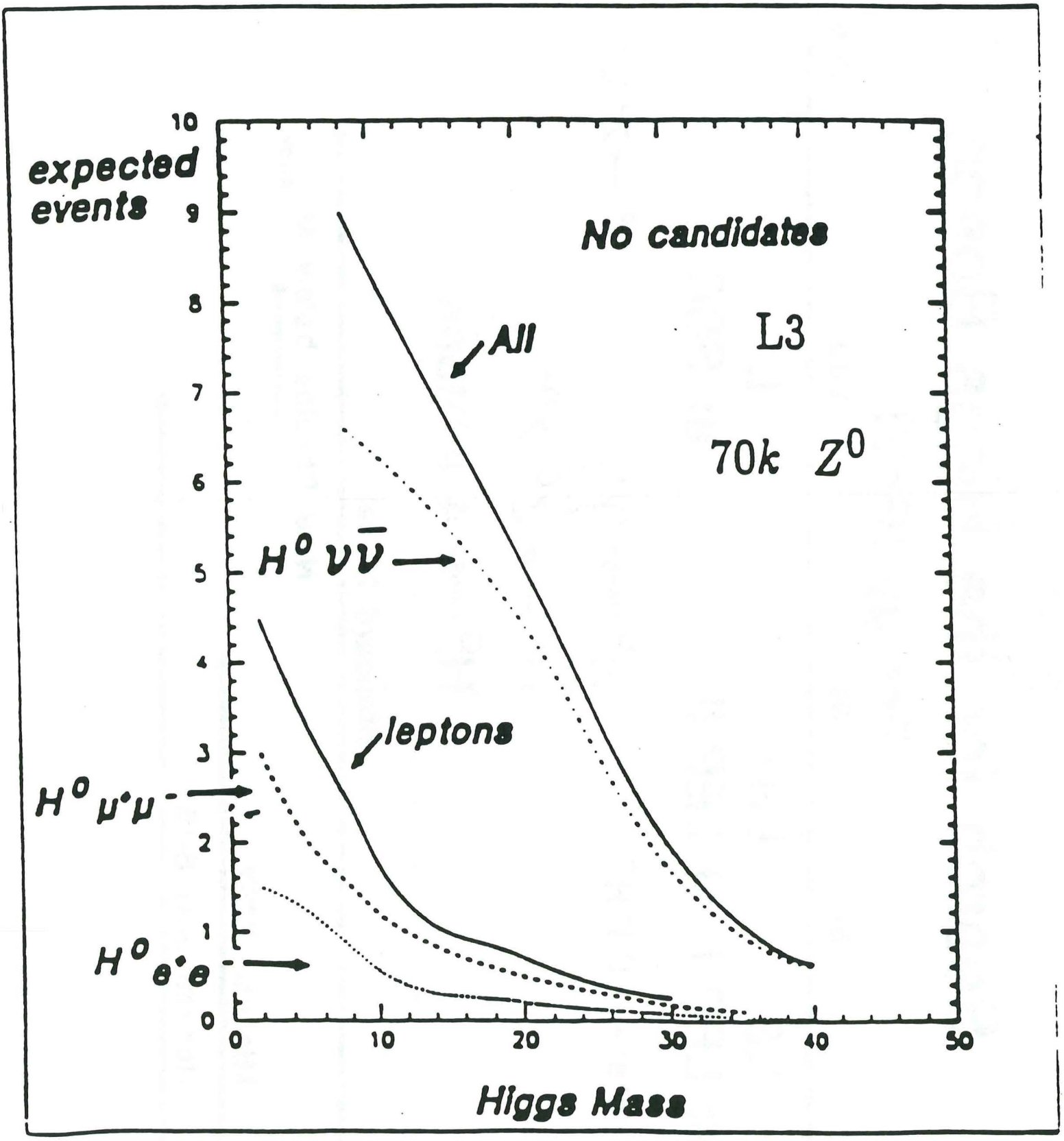
expected events
No candidates
All
L3
70k Z^0
$H^0 \nu\bar{\nu}$
leptons
$H^0 \mu^+\mu^-$
$H^0 e^+e^-$
Higgs Mass

Search for the Higgs Boson

Energy (GeV)

0 50 90 200 1000

L3 at LEP I

L3 at LEP II

L* at SSC

$e^+e^- \rightarrow l^+ l^- H^0$

$H^0 \rightarrow \gamma\gamma$

$H^0 \rightarrow Z^0 Z^{0*}$

$H^0 \rightarrow 4$ leptons

$H^0 \rightarrow Z^0 Z^0$

Standard Model

New Physics below M_{Planck}

Minimal SUSY

Non-minimal SUSY

L* Unique features

1. μ : $\frac{\Delta p}{p} = 2.4\%$ $p = .5$ TeV $2^\circ < \theta < 178^\circ$

$$P_\mu = P_{\text{central tracker}} + \Delta E$$

2. e. γ. : $\frac{\sigma}{E} = \left(\frac{1.3}{\sqrt{E}} + 0.5\right)\%$: $\Delta\theta = \Delta\varphi = 0.2^\circ$

Shaping time : 3 ns

$$P_{\text{central tracker}} = E_{BaF_2}$$

3. Jets : Shaping time : 15 ns

$$\frac{\sigma}{E} = \left(\frac{50}{\sqrt{E}} + 1.0\right)\% \text{ or } \frac{\sigma}{E} = \left(\frac{50}{\sqrt{E}} + 4.0\right)\%$$

4. Central tracker : $\frac{\Delta p}{p} = 0.5$ $p = 0.4$ TeV

Shaping time : 10 ns

L★ Assembly

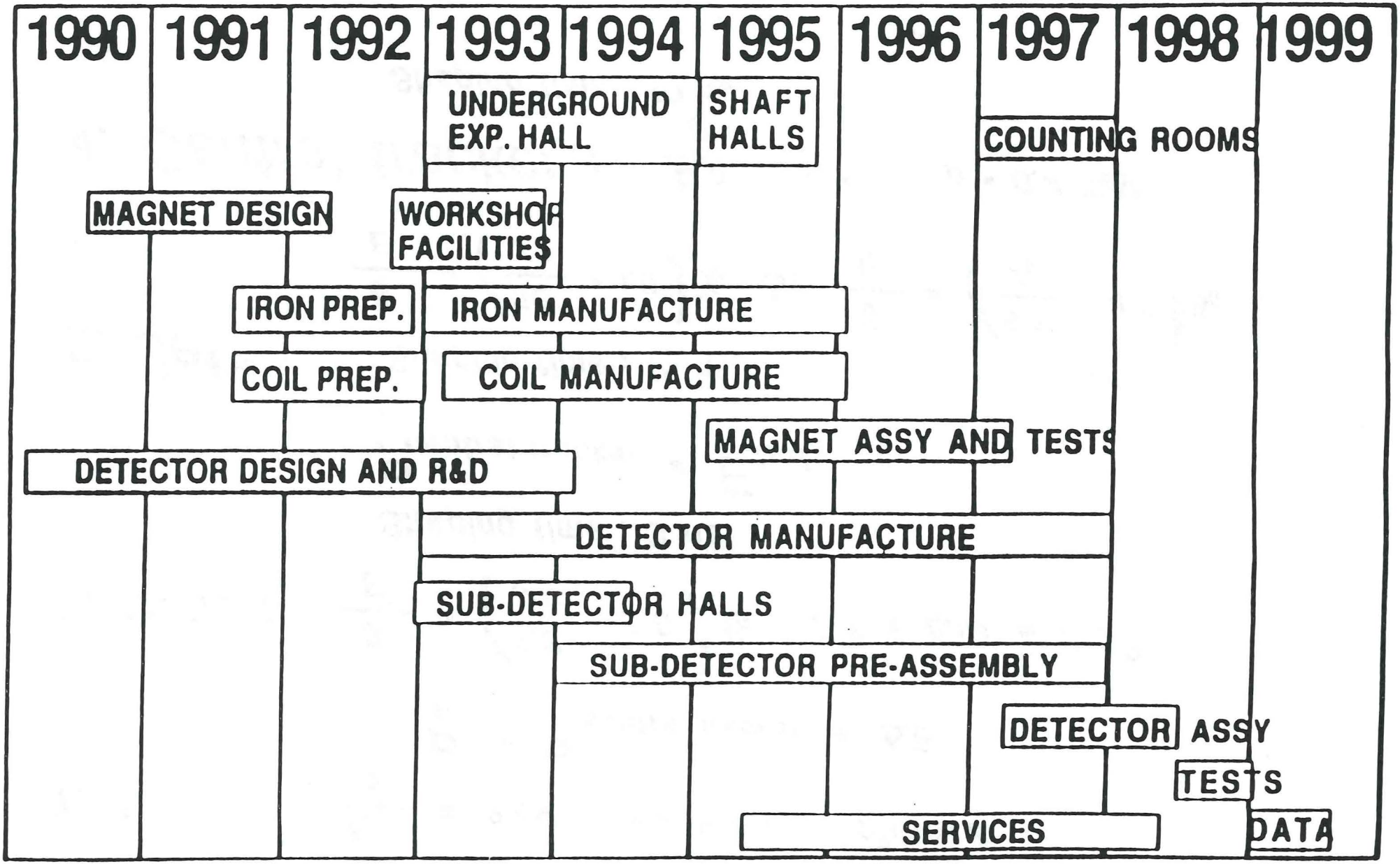
1990
1991
1992
1993
1994
1995
1996
1997
1998
1999
UNDERGROUND EXP. HALL
SHAFT HALLS
COUNTING ROOMS
MAGNET DESIGN
WORKSHOP FACILITIES
IRON PREP.
IRON MANUFACTURE
COIL PREP.
COIL MANUFACTURE
MAGNET ASSY AND TESTS
DETECTOR DESIGN AND R&D
DETECTOR MANUFACTURE
SUB-DETECTOR HALLS
SUB-DETECTOR PRE-ASSEMBLY
DETECTOR ASSY
TESTS
SERVICES
DATA

L* Installation Sequence

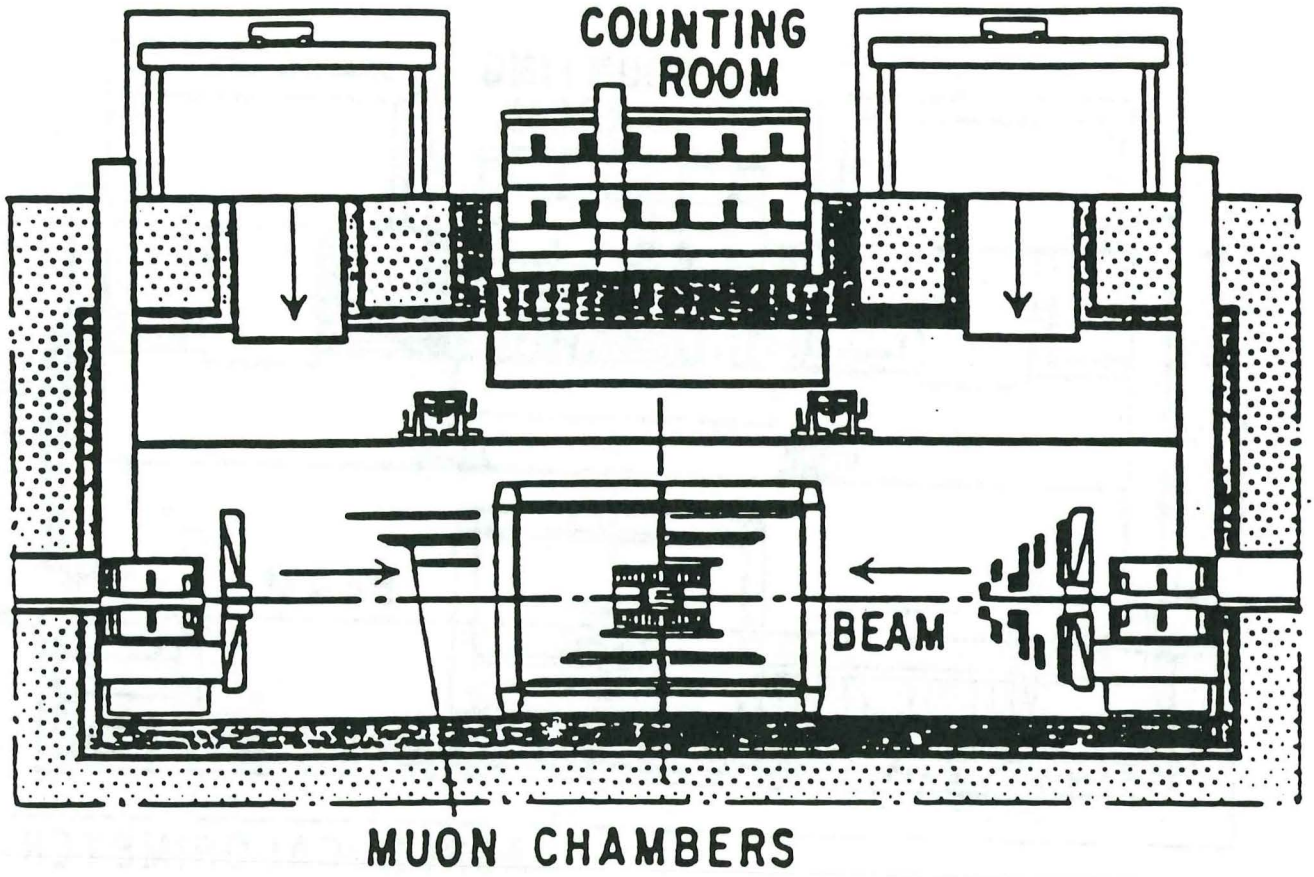

Step 5: Muon Detector installed.

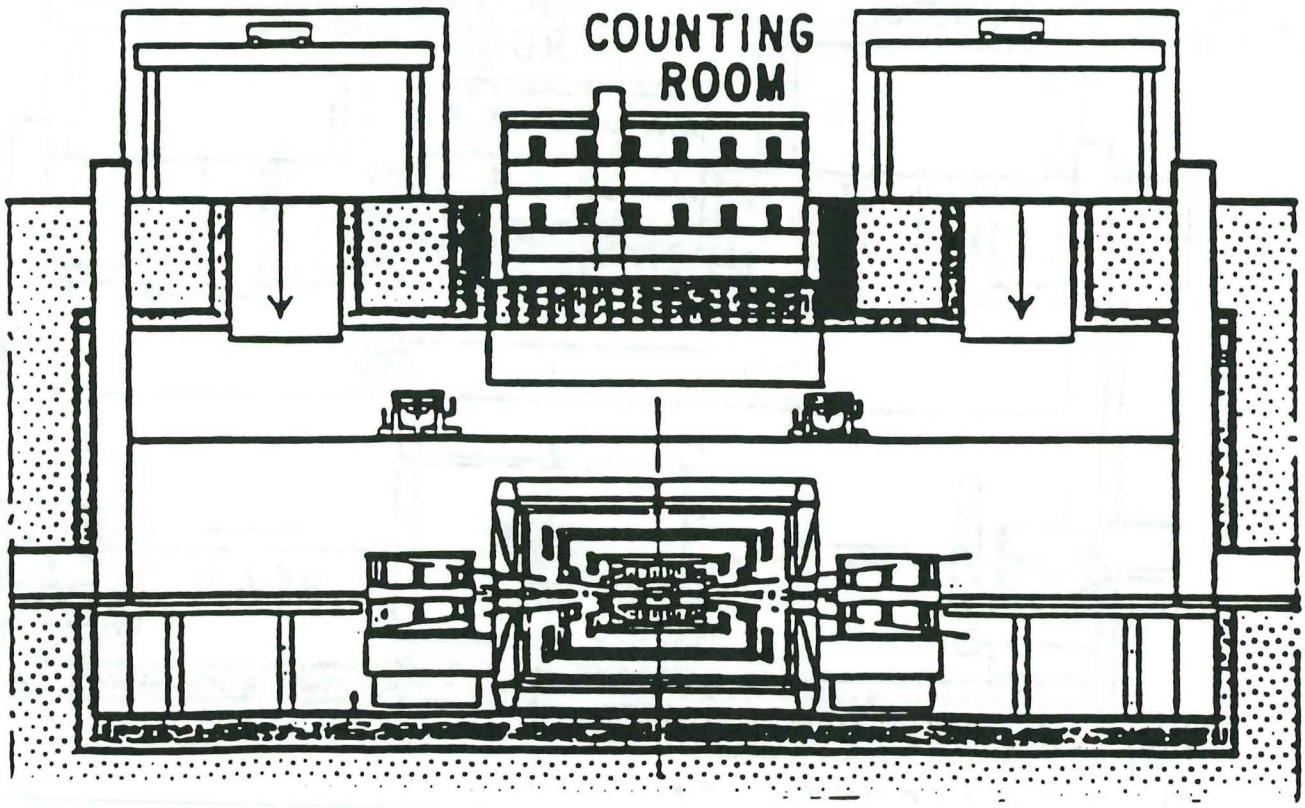

L* Installation Sequence

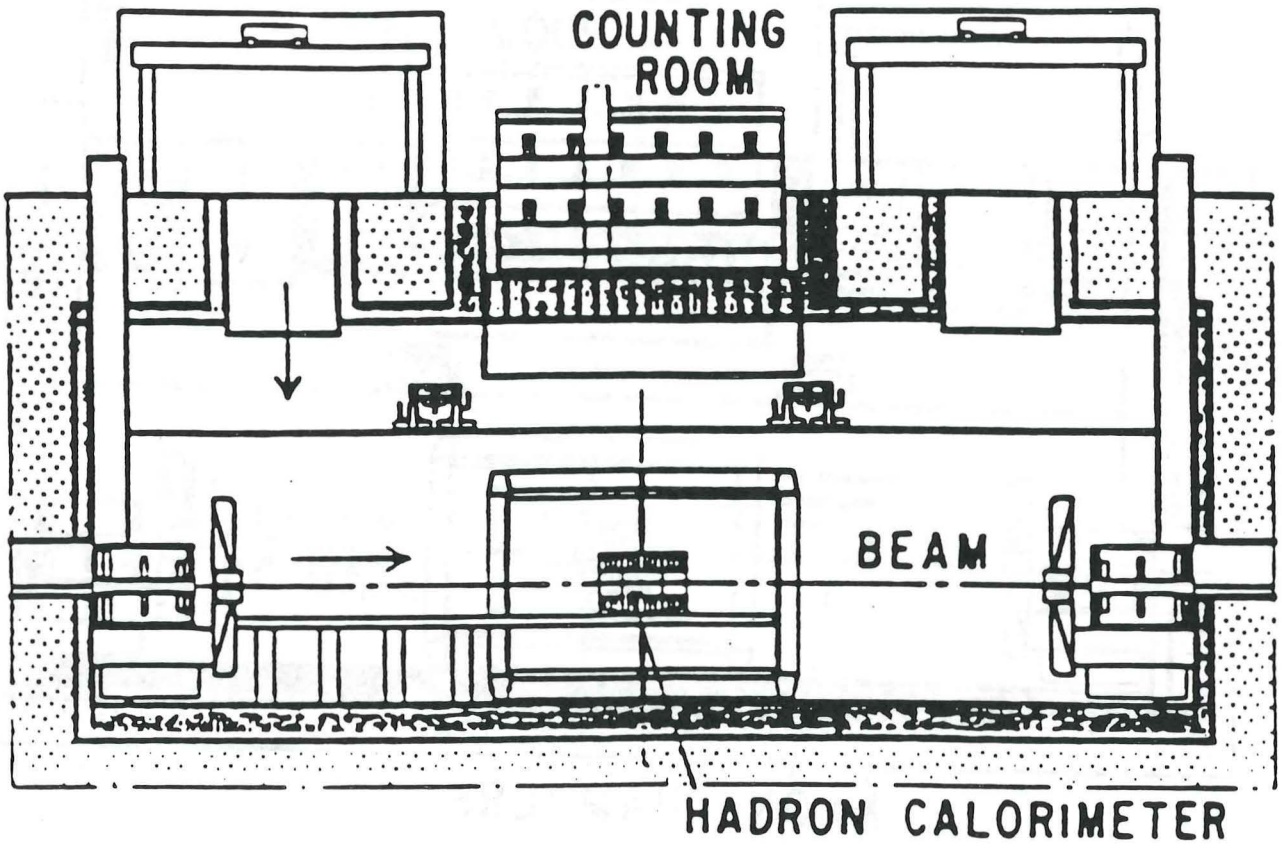

Step 3: Hadron Calorimeter installed.

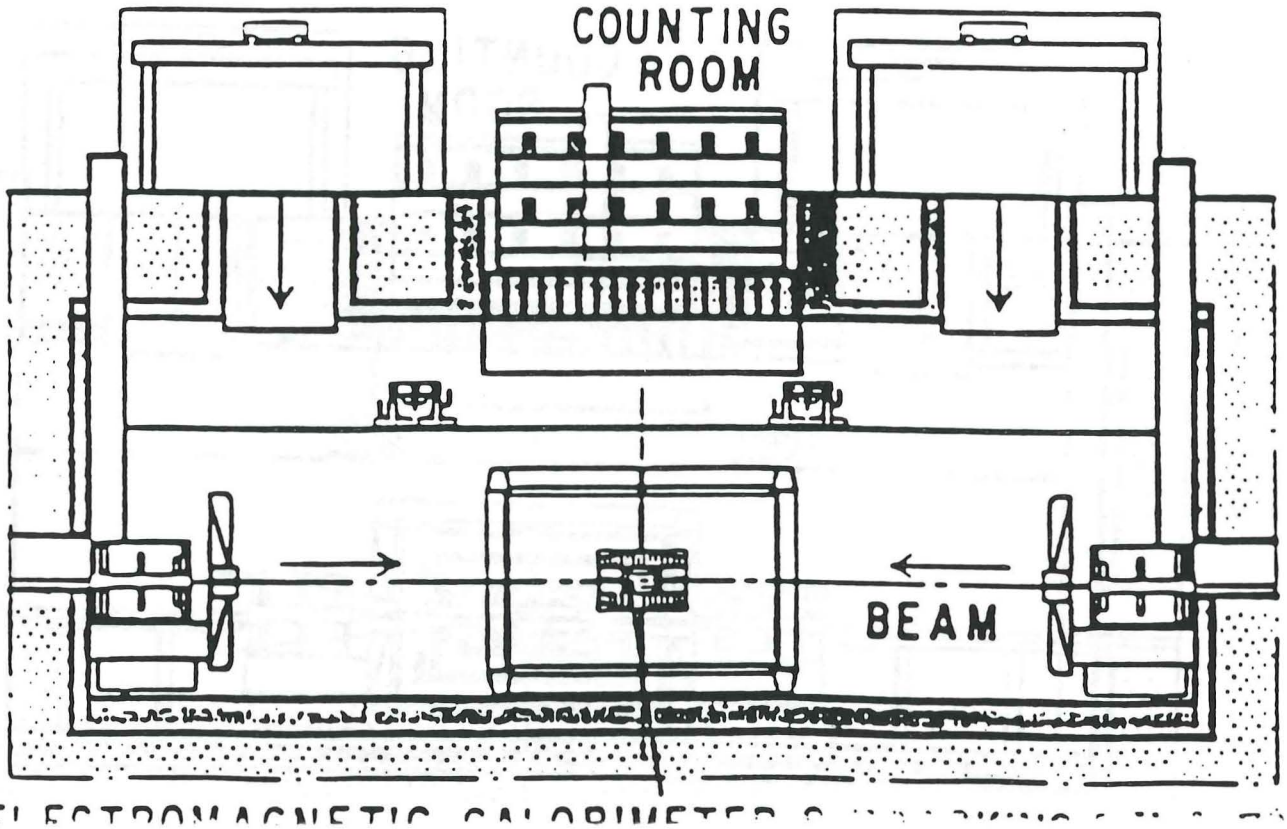

L* Installation Sequence

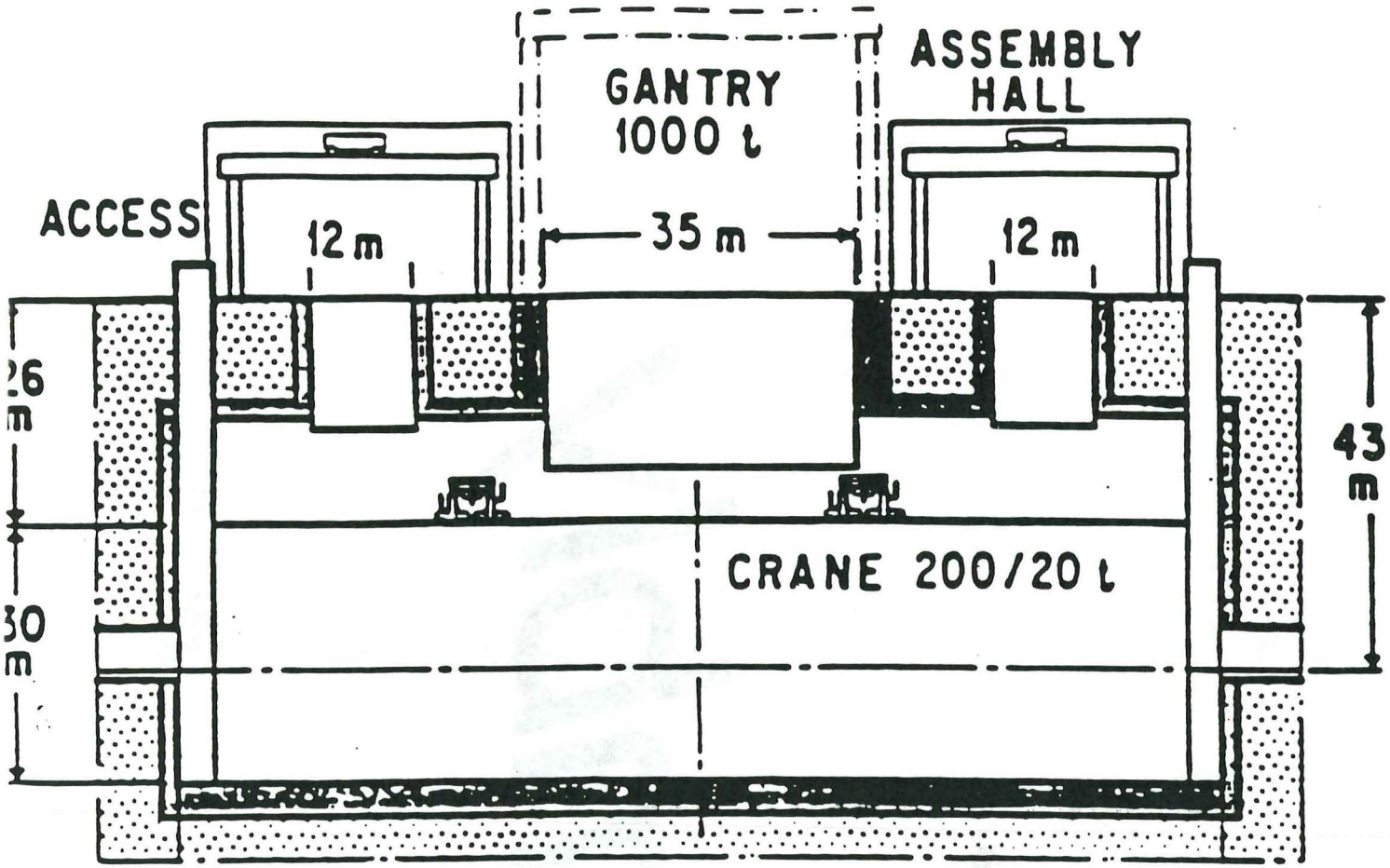

Step 1: Hall ready.

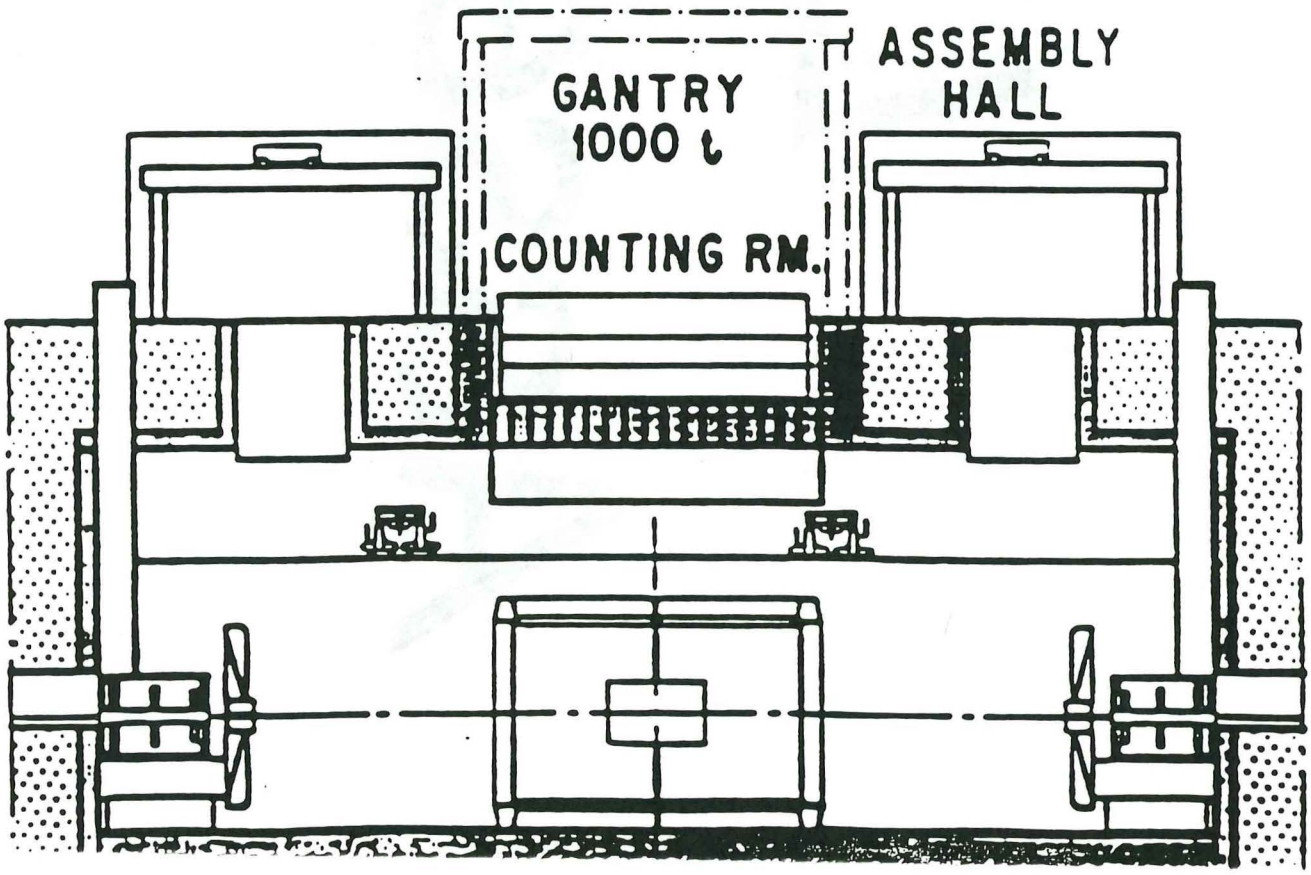

L*

Assembly

Technology and R/D for Data Digitizer

Muon Ch.
Straw Tube

1 ns Shift Register ⇒ Hit Enooder

Fiber Optics for Signal Transmission

BaF_2
Hadron Cal.

Analog or Digital Pipelined ADC

Analog Pipeline

- Switched Capacitor Array
- CCD

⇒ Slow ADC

Digital Pipeline

- Flash ADC
- Sigma Delta ADC

⇒ Fast Memory

22 bit Dynamic Range of BaF_2 requires R/D.

For L* We Need
Additional Techonologies

- *Very Fast front end Buffering*

  L3 : 500 μs *L* : 16 ns*

- *Fast Pipelined Level-1 Trigger*

  3 : 22 μs *L* : 16 ns*

- *Fast Event Builder*

  L3 : 16 Mb/s *L* : 1 Gb/s*

Requirement of Electronics

Subdetector	Signal	Resolution	Dynamic Range	Electronics	Channels
μ chambers	Timing	<1ns	1μs	Discrim. TDC	250,000
BaF_2 Calorimeter	Ampli.	0.1%	22bits	ADC	26,000
Hadron Cal. Si Pad	Ampli.	<1%	12bits	ADC	180,000
Straw tubes	Timing	<1ns	0.1μs	Discrim. TDC	75,000
Si microvertex	Hit	16ns		Special	76,000
Scintillating fiber	Hit	5ns		MCP tube Discrim.	50,000
Resistive Plate Counter	Hit	16ns		Discrim. TDC	20,000
				Total Readout Ch. ≈	700 k

L3 Trigger and Online System

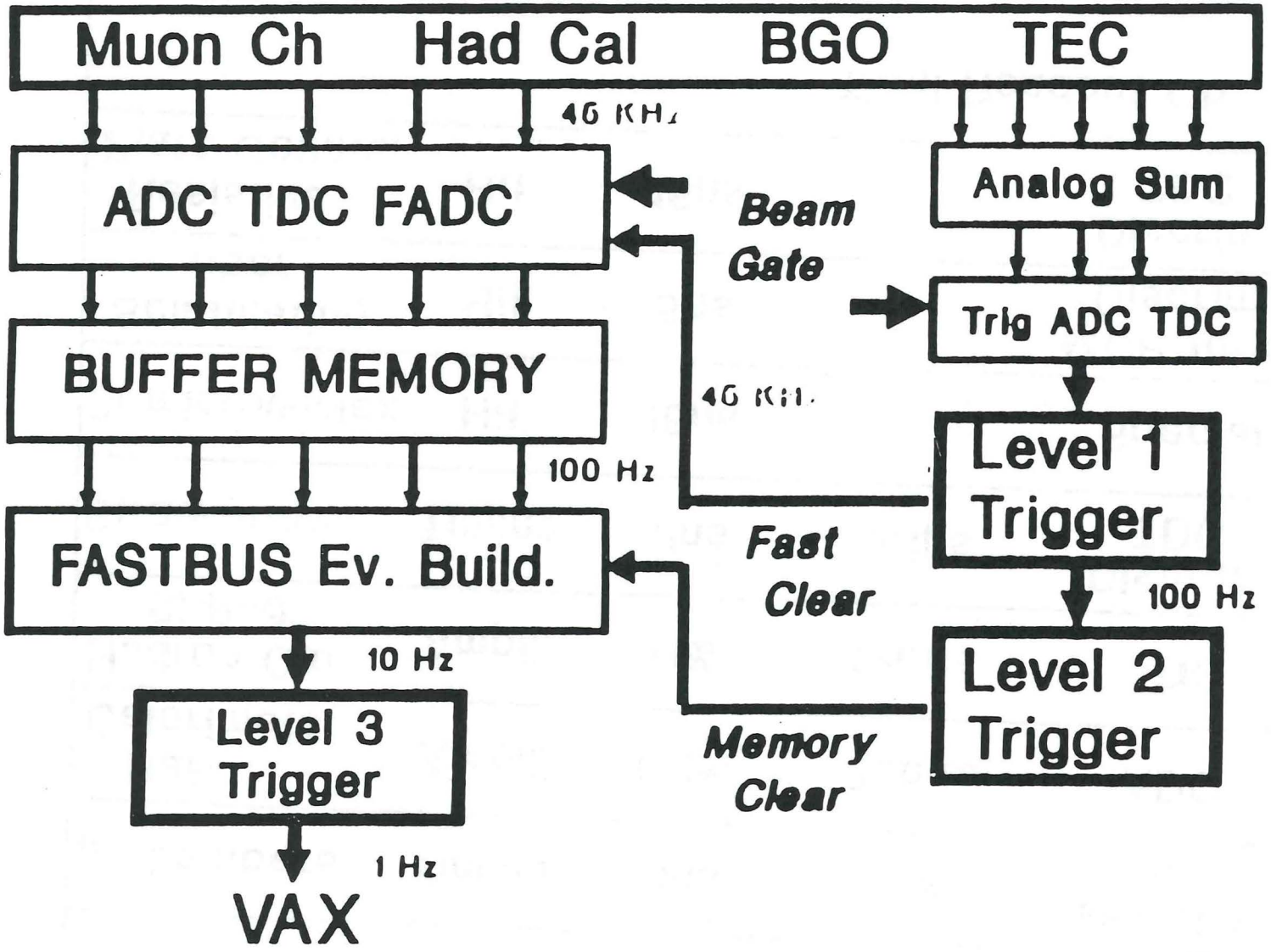

Trigger and Data Acquisition

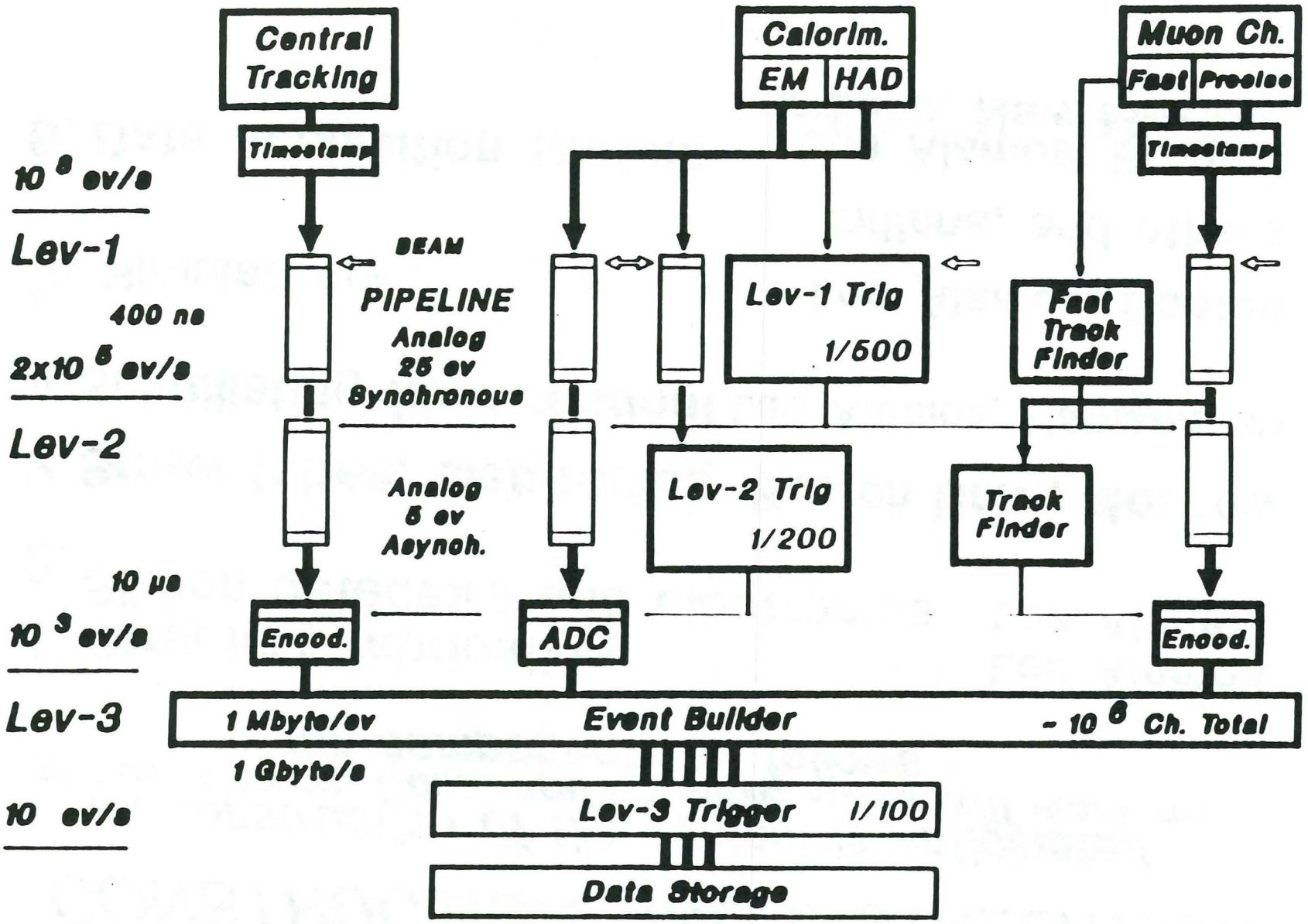

WORK FOR L★ CENTRAL TRACKER CONSTRUCTION AND INSTALLATION

All construction of the system is anticipated at Los Alamos. Collaborating universities will work on the components as follows :

1. Structure fabrication	Los Alamos
2. Silicon detectors and electronics	Los Alamos
3. Straw tubes, electronics	Boston Univ., Moscow
4. Scintillating fiber readout	Los Alamos, Hamamatsu
5. Simulations	Los Alamos, Boston Indiana, and others
6. Data acquisition system	Los Alamos, Boston, Indiana, New Mexico

Milestones for the L* Central Detector R&D Program

	FY 1991	FY 1992	FY 1993
Si Detectors	• Evaluate detectors	• Select strip length • Test at 10^{14} neutrons/cm^2	• Select final detector characteristics
Si Electronics	• Evaluate front end	• Test prototype front-end and optical link	• Finalize front-end and optical link
Si Structure	• Evaluate materials	• Stability and cooling test of full-scale prototype assemblies	• Finalize manufacturing plan
Straw Detectors	• Select gas • Measure drift velocity and Lorentz angle in 0.75-T field	• Complete tests at 10^{14} neutrons/cm^2 and 1 Coulomb/cm • Finalize design of 3-m-long straws	• Finalize manufacturing plan
Straw Electronics	• Evaluate front end	• Select front-end amplifiers	• Select optical link
Straw Structures	• Evaluate materials	• Complete stability and mechanical design	• Finalize manufacturing plan
Scint. Fiber Detectors	• Evaluate fibers	• Select fibers • Test at 10^{14} neutrons/cm^2	
Scint. Fiber Readout	• 3-D model of photo tube	• Prototype and test compact tube	• Test production tube
Scint. Fiber Structures		• Stability and mechanical tests	• Finalize manufacturing plan
Radiation Damage	• Prototype structure materials	• Complete tests on structural materials and detectors	
Simulations	• Complete code revision for neutron simulation	• Complete high-luminosity (10^{34}) design option	
System Integration	• Complete conceptual design of mounting, cabling, and	• Finalize mounting and alignment	• Finalize installation plan

ISAJET Monte Carlo study sample :

10 events overlap

(9 mini-bias events + 1 higgs event (m_H= 800 GeV))

$$\langle N_{ch} \rangle \sim 260,$$

$$\text{for } \theta_{particle} > 16^\circ$$

Efficiency of reconstruct vertex of 4 leptons ~100 %,

(Track find efficiency >90%)

Standard division of reconstruct event Z-coordinate,

$$\sigma_z = 0.85 \text{ cm}$$

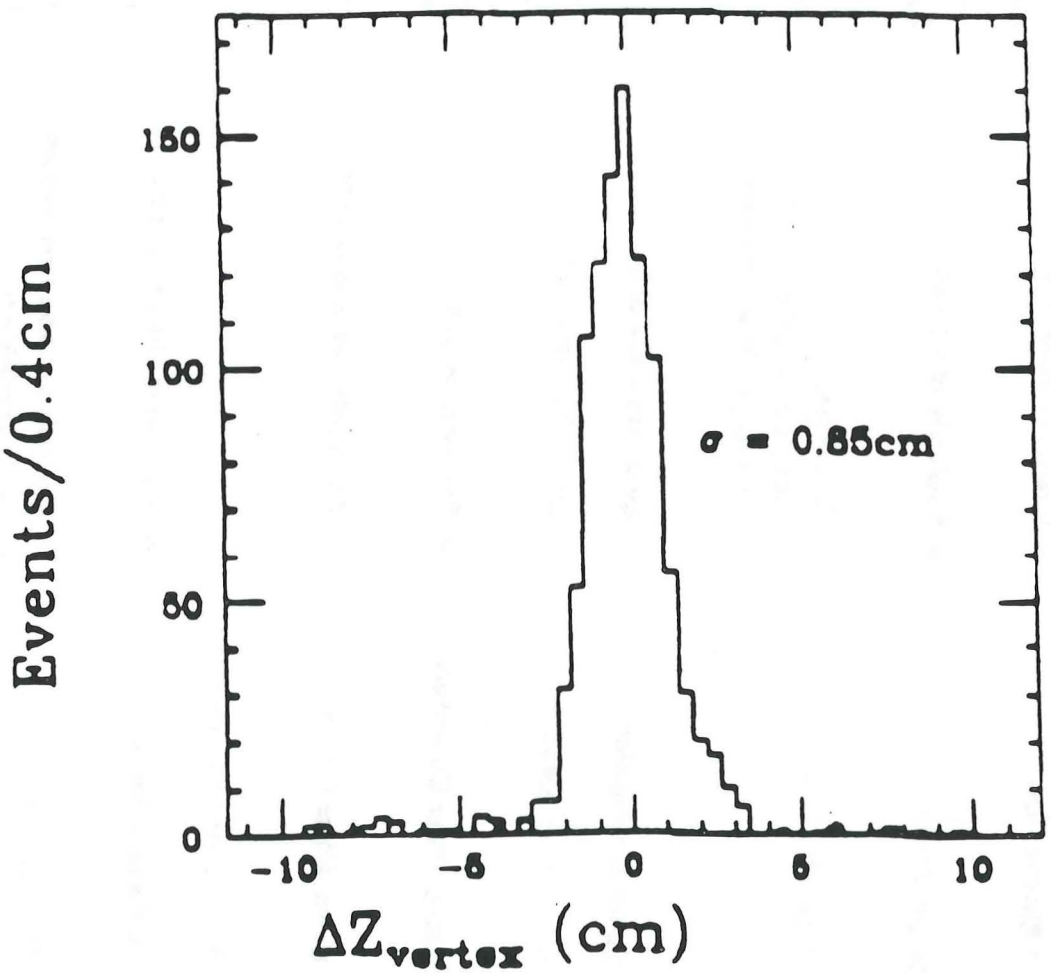

Straw Tubes

80 layers ***optically aligned within 25μ to silicon tracker***

Much work done at Boston University

➡ **3mm Diameter driftime ~ 15 ns**

$\sigma \approx 69\mu$

Tests : 4×10^{14} n/cm^2 ***(fission spectrum)***

➡ ***Performance stable***

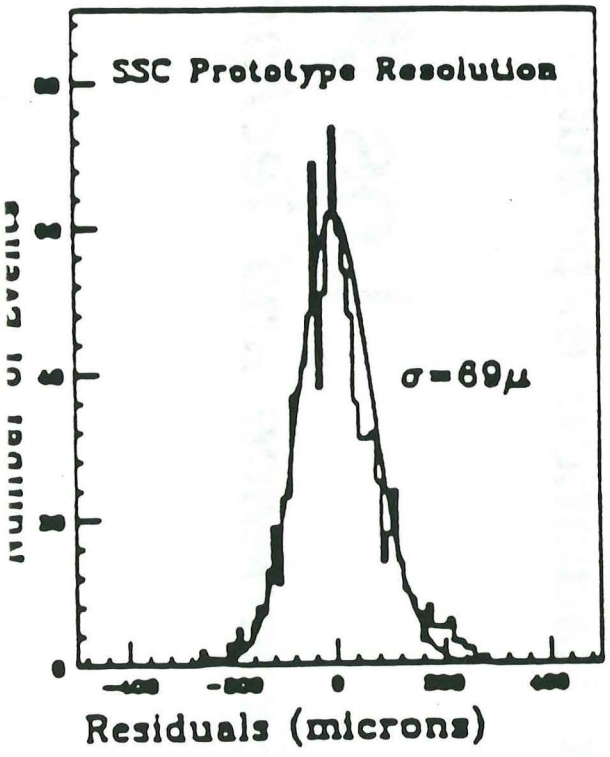

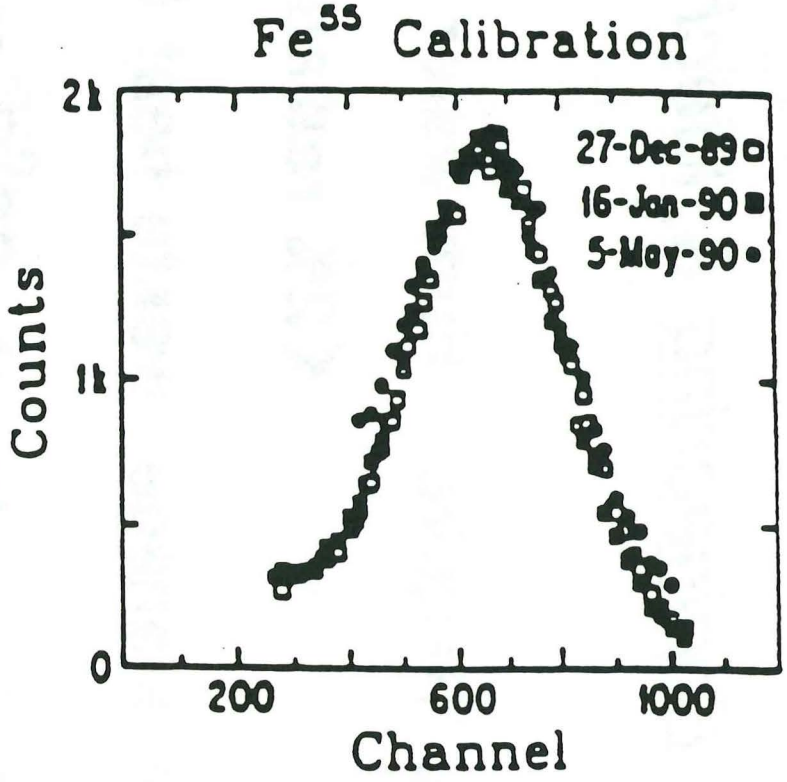

Engineering & Mechanical Design Issues

- Require 5μm wafer positional stability

  < 2% radiation length

- Manage waste heat (≈ 20 kW)

- Operate at -20^{0}C and + 10^{0}C

- Radiation exposure to be 10 Mrads over a 10-year service life

Los Alamos

Experience and Technology in Space & Reactor

Silicon detectors
are reverse-biased diodes

- Thickness = 300μm
- Collection time ~ 10 ns
- Voltage 25-200 V
- 32K electron-hole pairs for signals
- Noise < 1K electrons
- 25μm for inner layers, 50μm for outer layers
- with 5-mr stereo angle
- Radiation resistance to fluences :
  10^{14} neutrons/cm^2
- Front-end electronics mounted
  on the detectors

Radiation Calculations

by : Los Alamos

L geometry*

Neutron fluence
in
Central Tracker volume

with $0.13 X_o$
boron-polyethylene shield

$10^{12}/cm^2$ per year

1. *To distinguish* the sign e+ and e- *from a* 1 TeV particle

   $T \longrightarrow e^+ + e^-$

2. *To measure* the multiplicity of charged particles surrounding e and μ

3. *To measure* the momentum of e and μ to match with precision e and μ measurements in specialized e and μ detectors

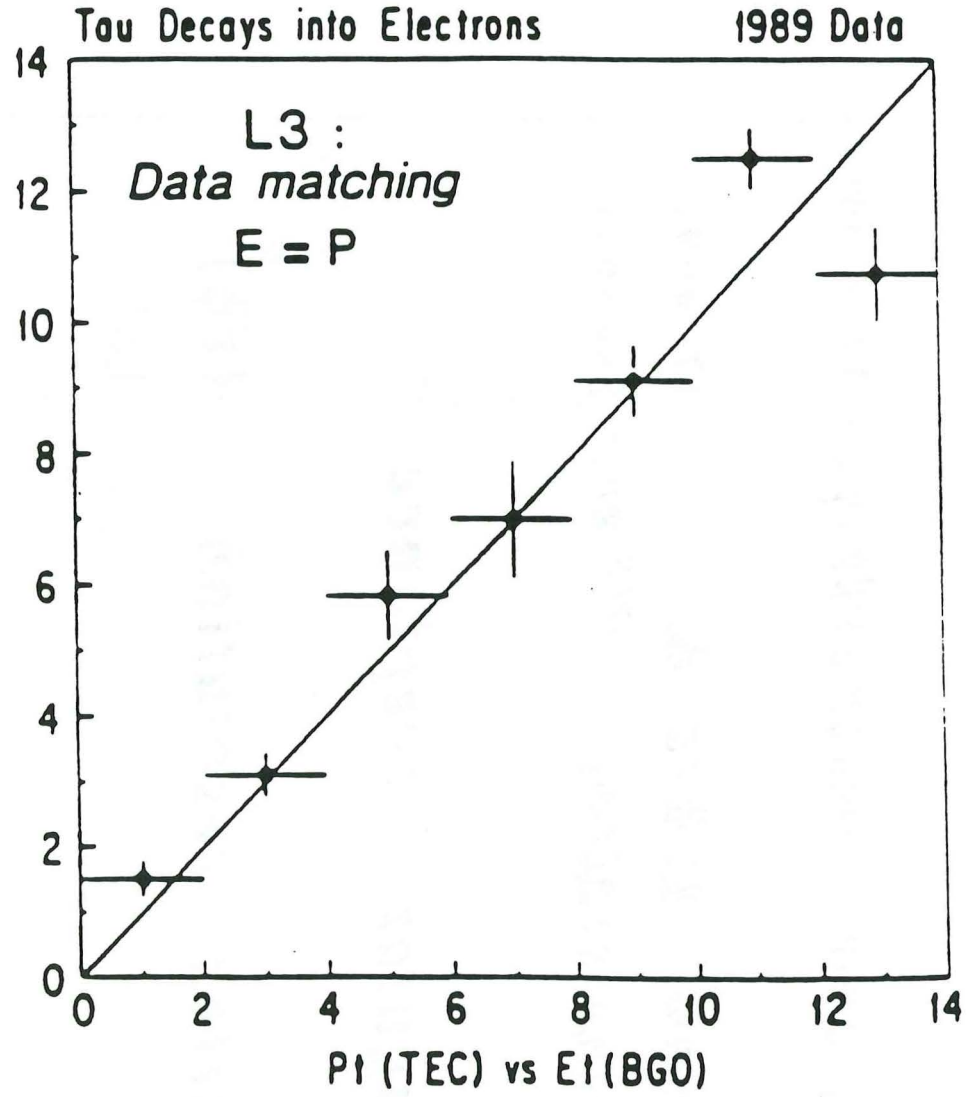

L* Central Tracker

silicon microstrips	(7.6 • 10⁶)	10 cm ≤ r ≤ 40 cm |z| ≤ 150 cm
straw tubes &	(75000)	40 cm < r ≤ 75 cm
scintillation fibers	(50000)	|z| ≤ 150 cm

angular acceptance $5° \leq \theta \leq 175°$

vertex resolution $(r\phi)$ 20 μm

(z) 1 mm

momentum resolution $\Delta p/p = 1.25 * 10^{-3} * p$ [GeV]

$\equiv$ 50 % @ 400 GeV

L* Central Tracker: Silicon Detector

radial layers	6	(r*ϕ , z) cylinders
forward layers	2*12	(r*ϕ , r) disks
strip pitch for inner (outer) layers	25 (50)	μm
stereo angle on alternate layers	5	mrad
single detector thickness	300	μm ($3.2 * 10^{-3} X_0$)
signal size for a mip	32000	q_e
signal to noise ratio	30/1	typical
signal collection time	10	ns
radiation resistance to fluences	10^{14}	neutrons/cm^2

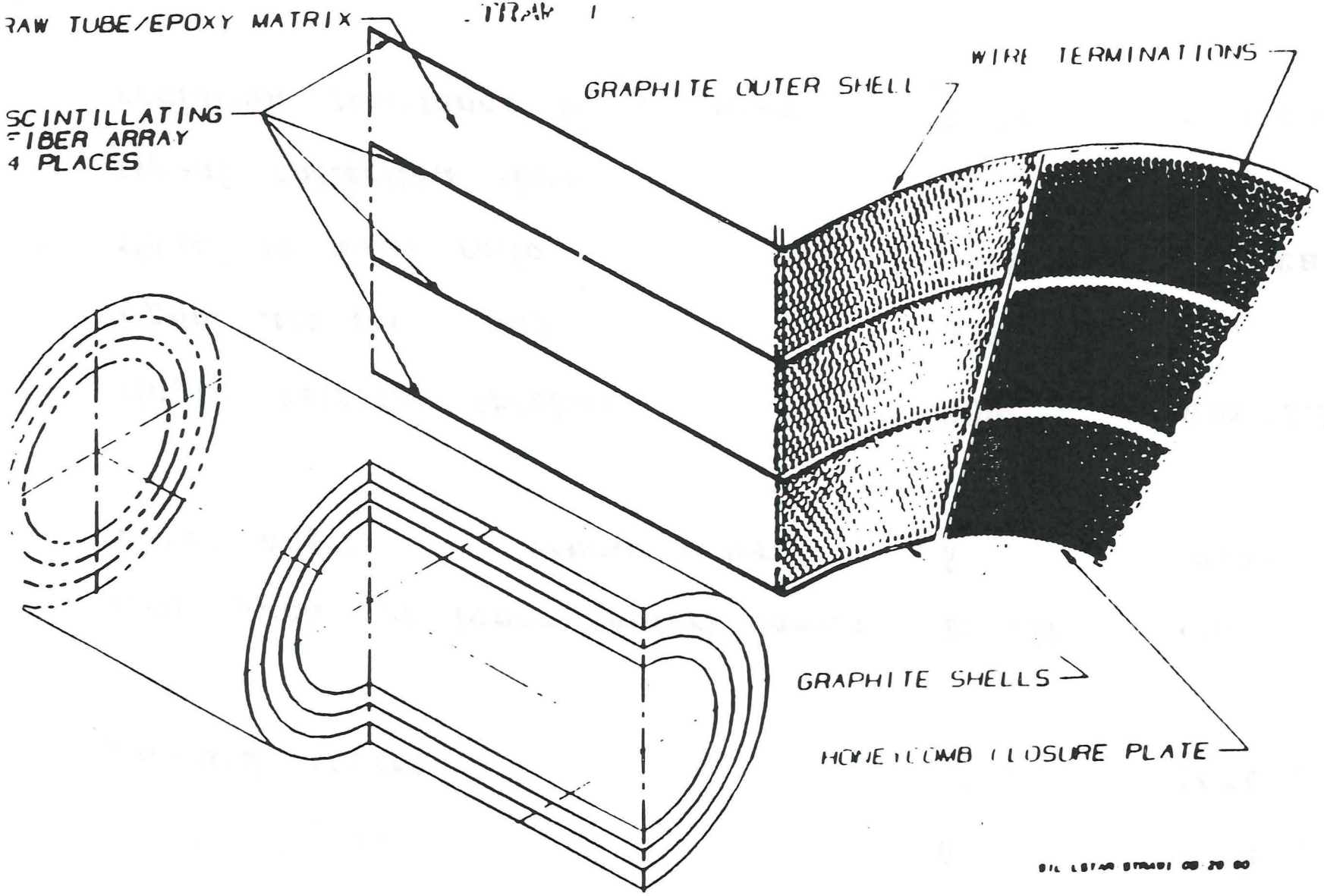
RAW TUBE/EPOXY MATRIX
SCINTILLATING
FIBER ARRAY
4 PLACES
GRAPHITE OUTER SHELL
WIRE TERMINATIONS
GRAPHITE SHELLS
HONEYCOMB CLOSURE PLATE

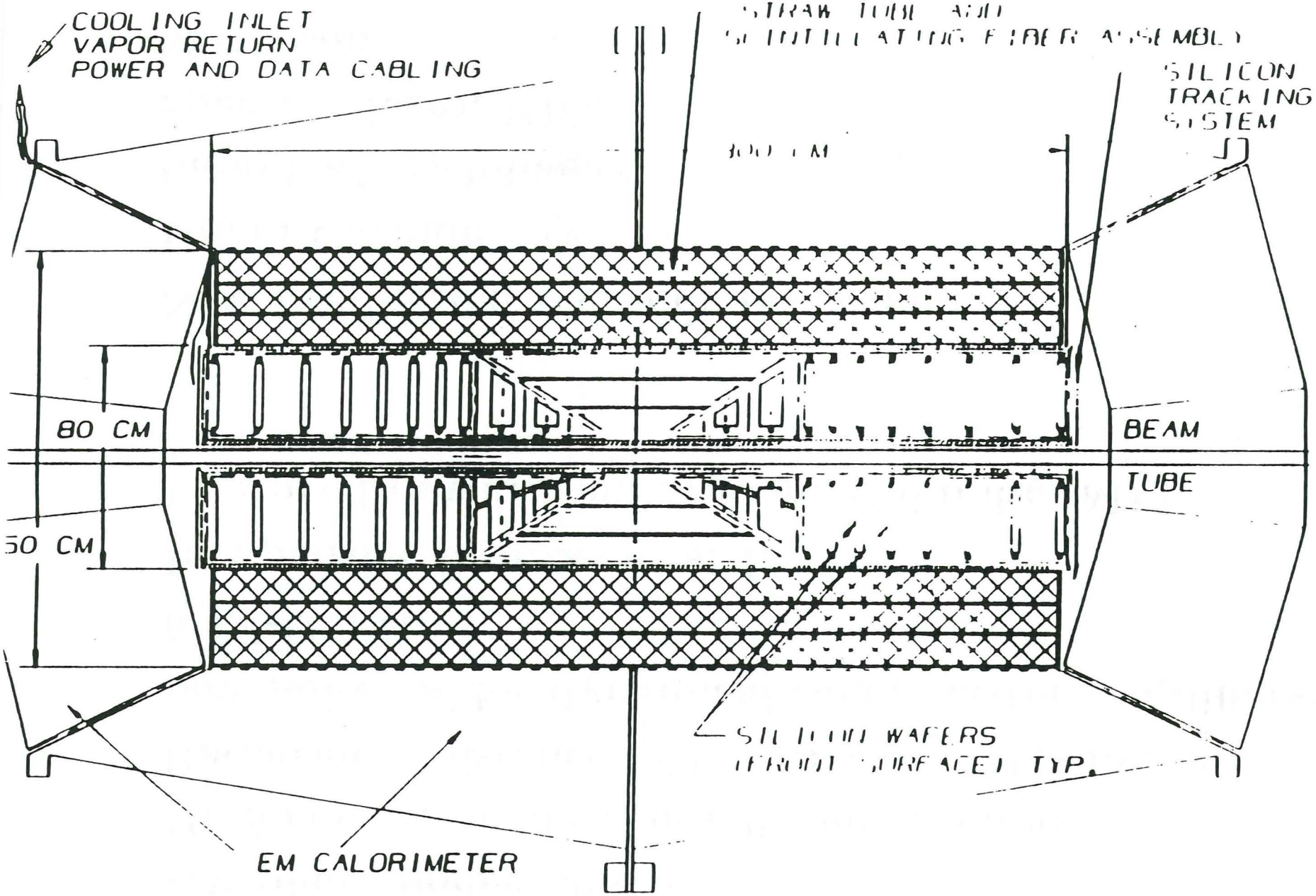
COOLING INLET
VAPOR RETURN
POWER AND DATA CABLING
SILICON
TRACKING
SYSTEM
80 CM
BEAM
TUBE
EM CALORIMETER

R & D needed on:

UV-photodiodes: Japan

Uniform light collection efficiency: Japan

Radiation resistance of UV-diodes: MIT-Japan

Low noise, wider dynamical range, faster amplifiers: MIT-ORNL

Inexpensive flash ADC's: LeCroy

Improved purification system: Columbia-MIT

New production methods for xenon:

Union Carbide

Liquid Air (Alphagaz)

Spectra Gases, INC.

Matheson

Stable α' signal provides reliable calibration.

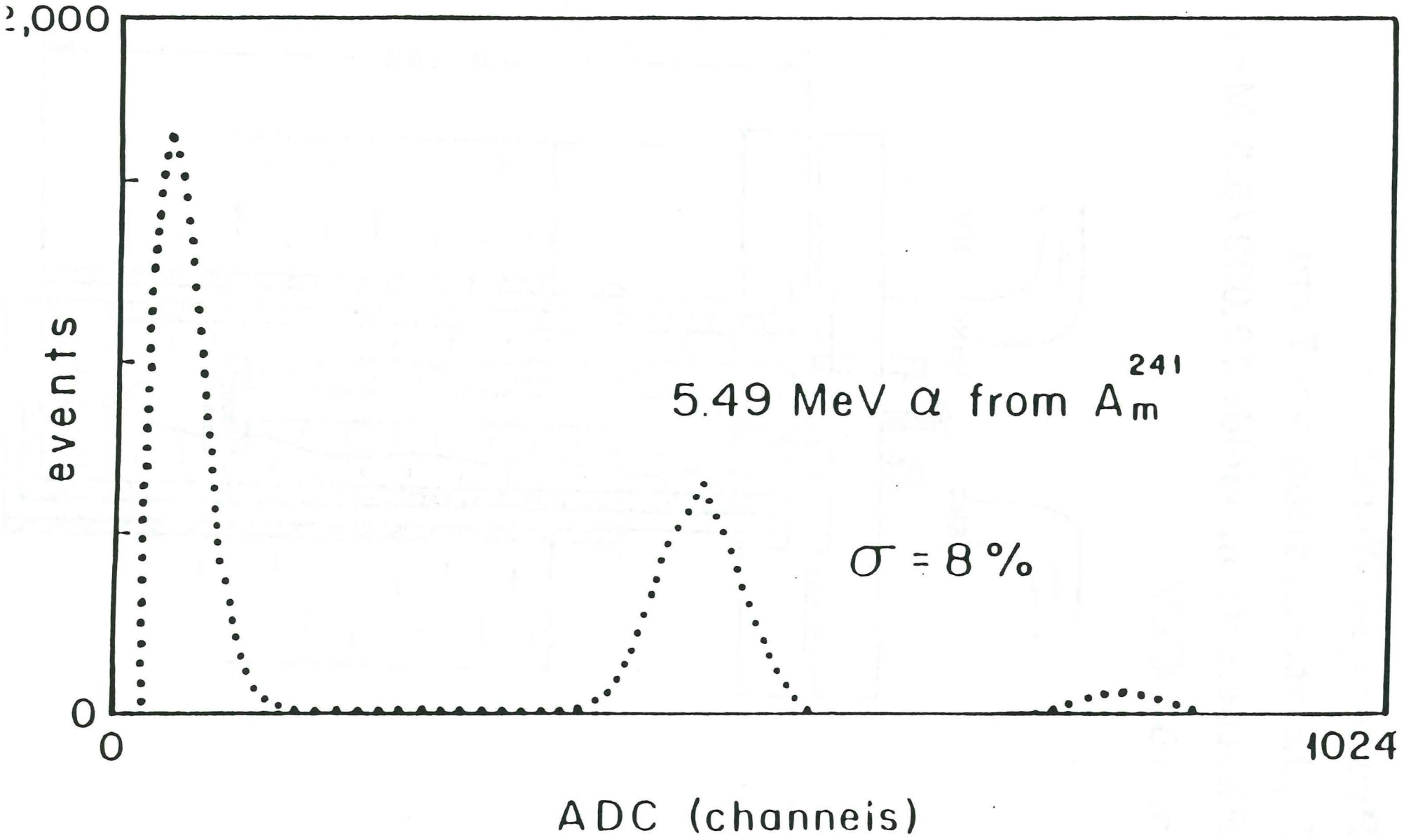

Proto-type Work:

Light attenuation >> 7 cm,

Photoelectron yield: 50,000/5.5 MeV α's or 10^7/GeV

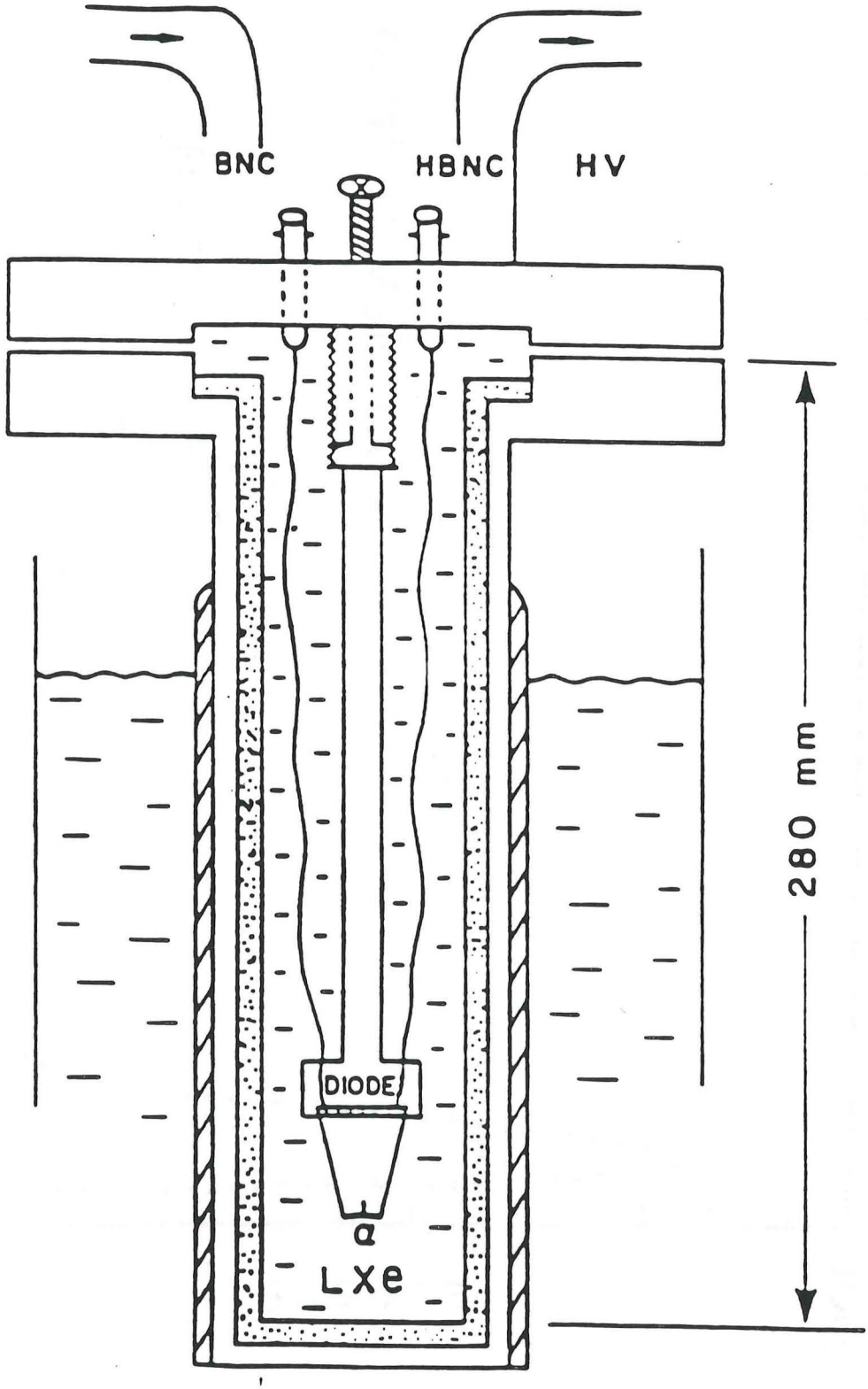

Components of LXe Cell

I. Photosensors

5 cm diameter (Waseda) or
1 cm * 1 cm (Hamamatsu).
Rise time: 10 ns
Quantum efficiency: 80% at 170 nm.
Operate in magnetic field.

II. UV Reflectors

100 μm kapton foil coated with Al and
MgF_2 with 85% reflectivity tested.

III. Amplifiers

10 ns rise time at 500 pf.

L* Electromagnetic Calorimeter
Liquid Xenon Option

Ellipsoidal Shape Covering $|\eta| < 3$
5.2 m Long; 2.8 m Diameter
15 m^3 Liquid Xenon
24,000 Cells
72,000 Readout Channels

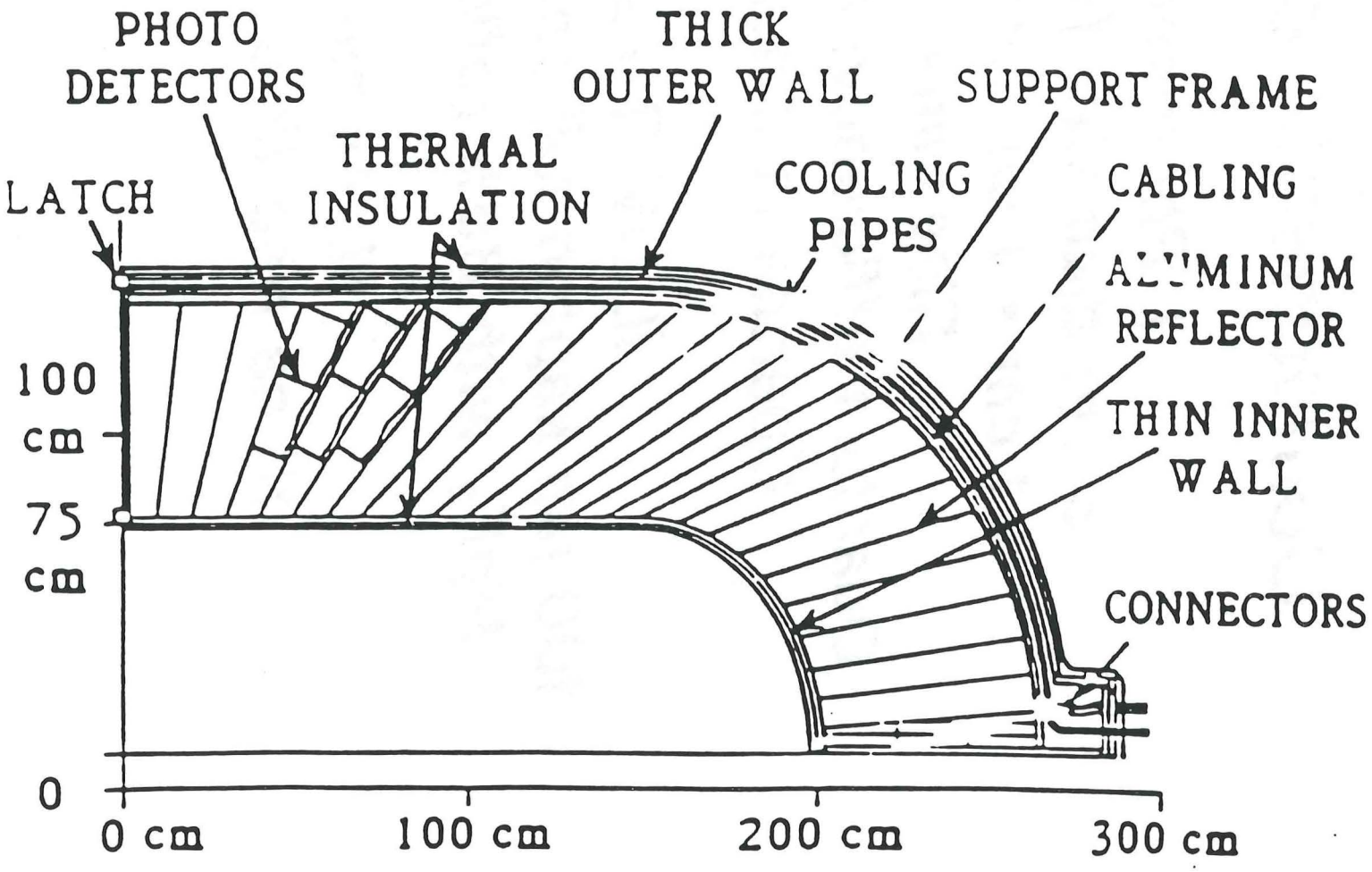

Construction: 1993 - 1997

Crystal Production: Shanghai, Beijing

Quality Control:
Caltech, Annecy, CMU, Aachen, Bombay

Radiation Hardness: Caltech, CMU

Mechanical Support: ORNL, Annecy, Aachen

Photodevice: Caltech, CMU, Aachen, Bombay

Electronics: Princeton, Caltech,
ORNL, Rome, Los Alamos, Geneva

RFQ Calibration: Caltech, CMU, Geneva

System Assembly: Caltech, Annecy, ORNL,
Princeton, Aachen, Geneva, Bombay

Crystal R&D Program
SIC (Shanghai) and BGRI (Beijing)

- **Mass Production Methods for Growing Fast, Transparent Rad Hard Crystals**
- **Use Pure and Doped BaF_2 Pilot Crystals**
- Systematic Study of Rare-Earth Especially La-Doped BaF_2 Crystals
- **Systematic Study of New Fluoride Crystal Scintillators: CeF_3, LaF_3, and other Rare-Earth Fluorides**

Manpower: 25-30 FTEs Per Year, For Three Years

CALIBRATION IN SITU

RFQ

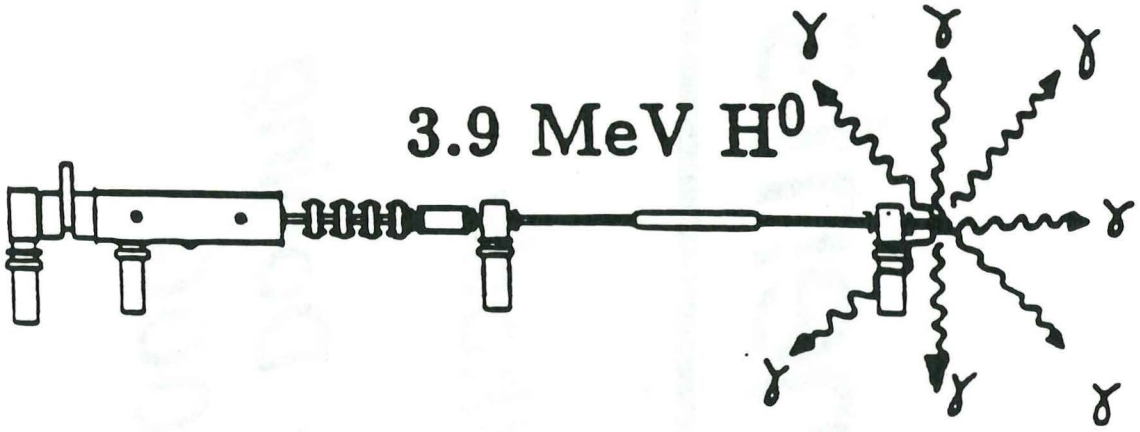

Up To 40 GeV Equivalent Per Crystal
Per 1 μsec RFQ Beam Pulse

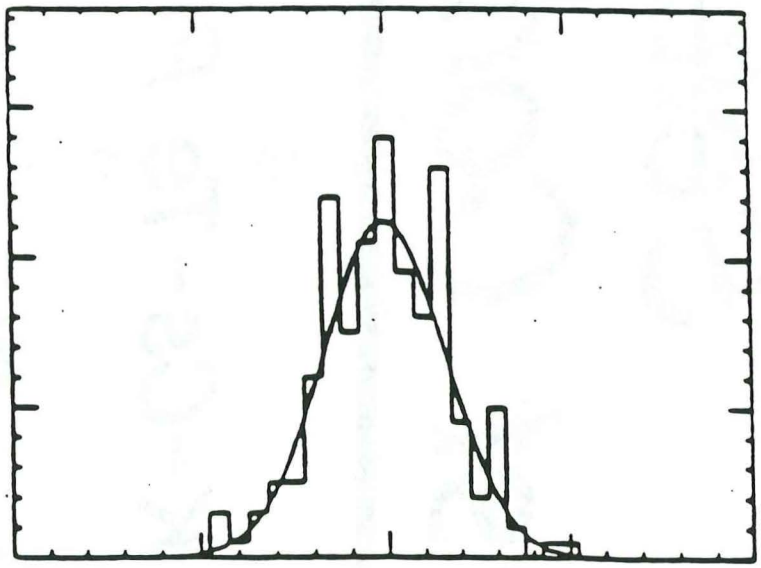

TEST RESULT:
RMS DEVIATION of PEAK= 0.3%

Scintillation of BaF_2

Select Fast Components

K-Cs-Te Photocathode

After Shaping, No La Doping
Effective F/S > 1000

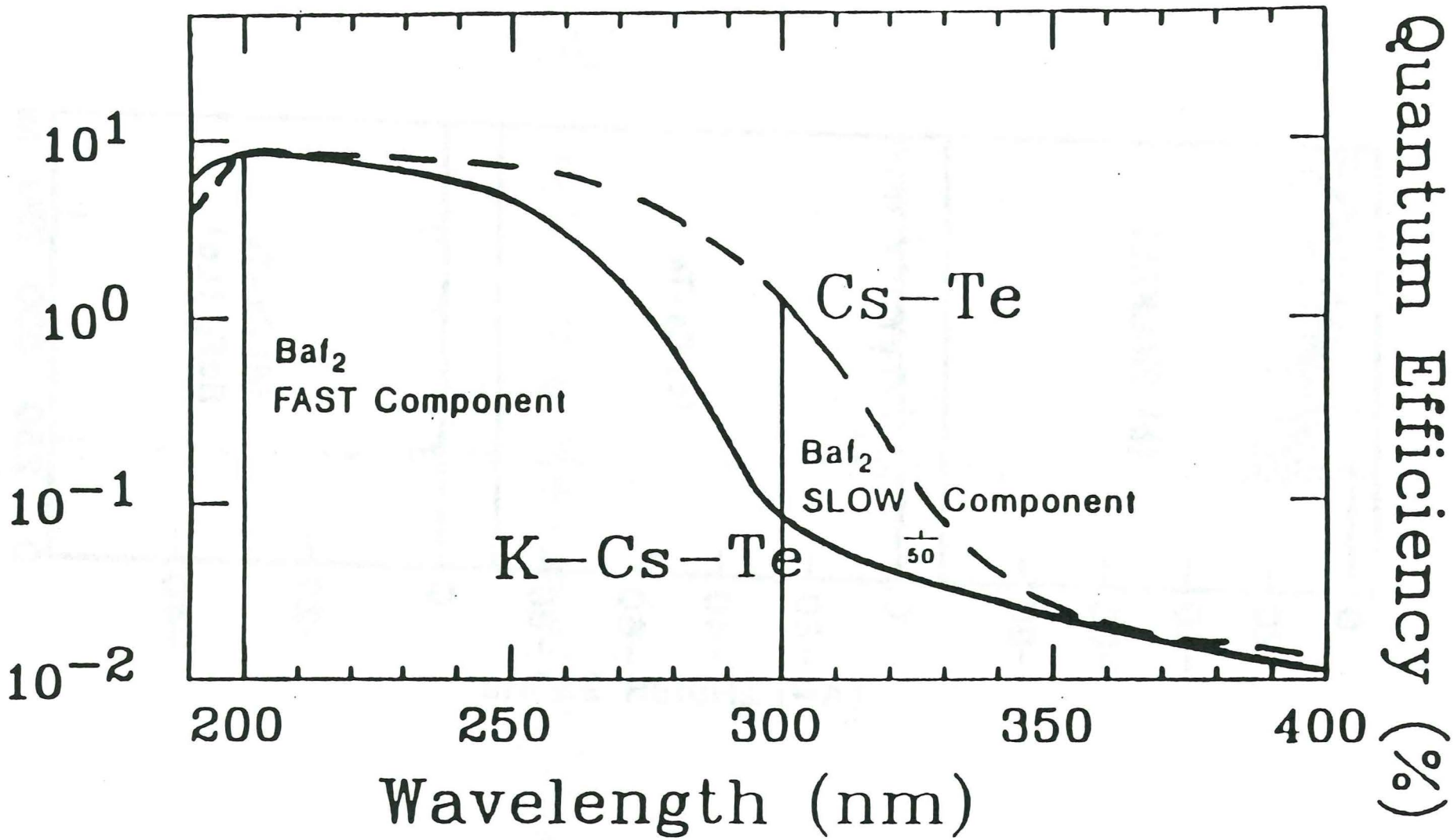
Quantum Efficiency (%)
10^1
10^0
10^{-1}
10^{-2}
Cs–Te
BaI_2
FAST Component
BaI_2
SLOW Component
$\frac{1}{50}$
K–Cs–Te
200
250
300
350
400
Wavelength (nm)

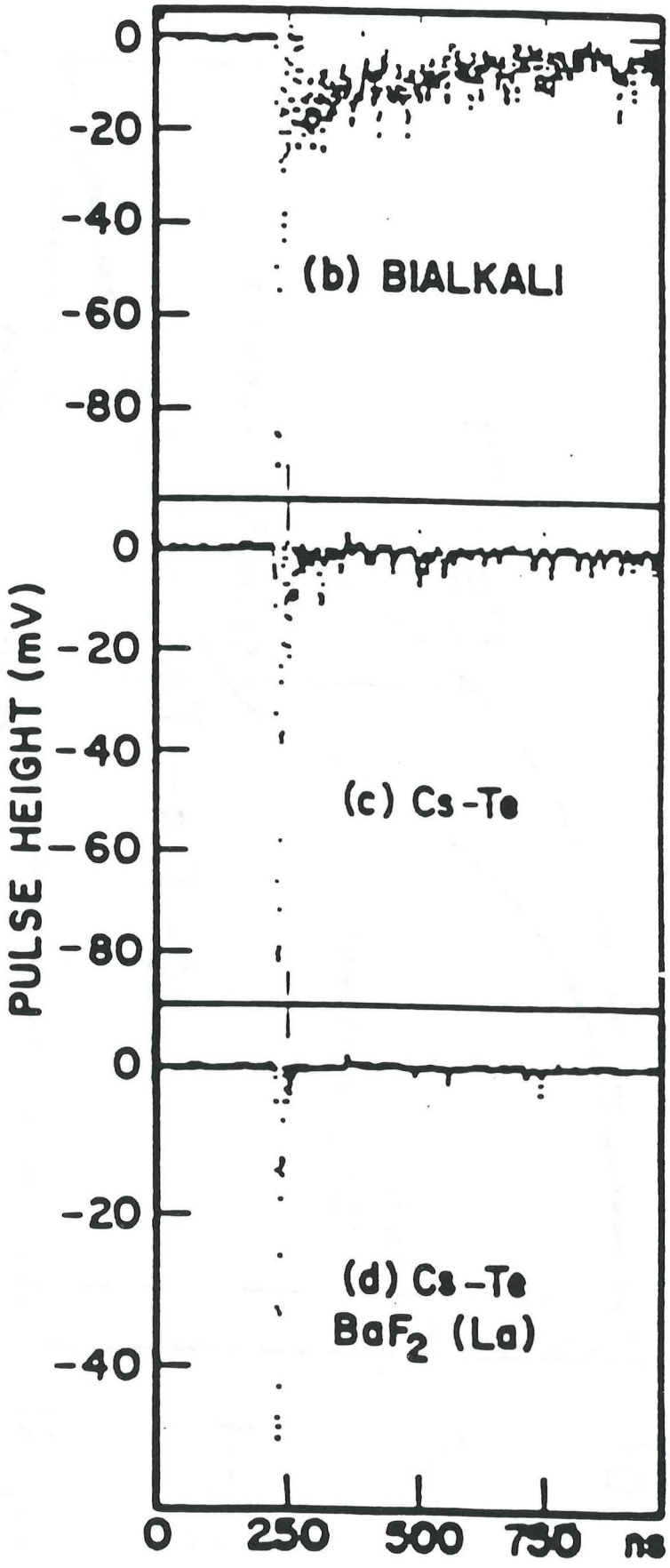
0
-20
-40
-60
-80
(b) BIALKALI
0
-20
-40
-60
-80
(c) Cs-Te
PULSE HEIGHT (mV)
0
-20
-40
(d) Cs-Te
BaF2 (La)
0
250
500
750
ns

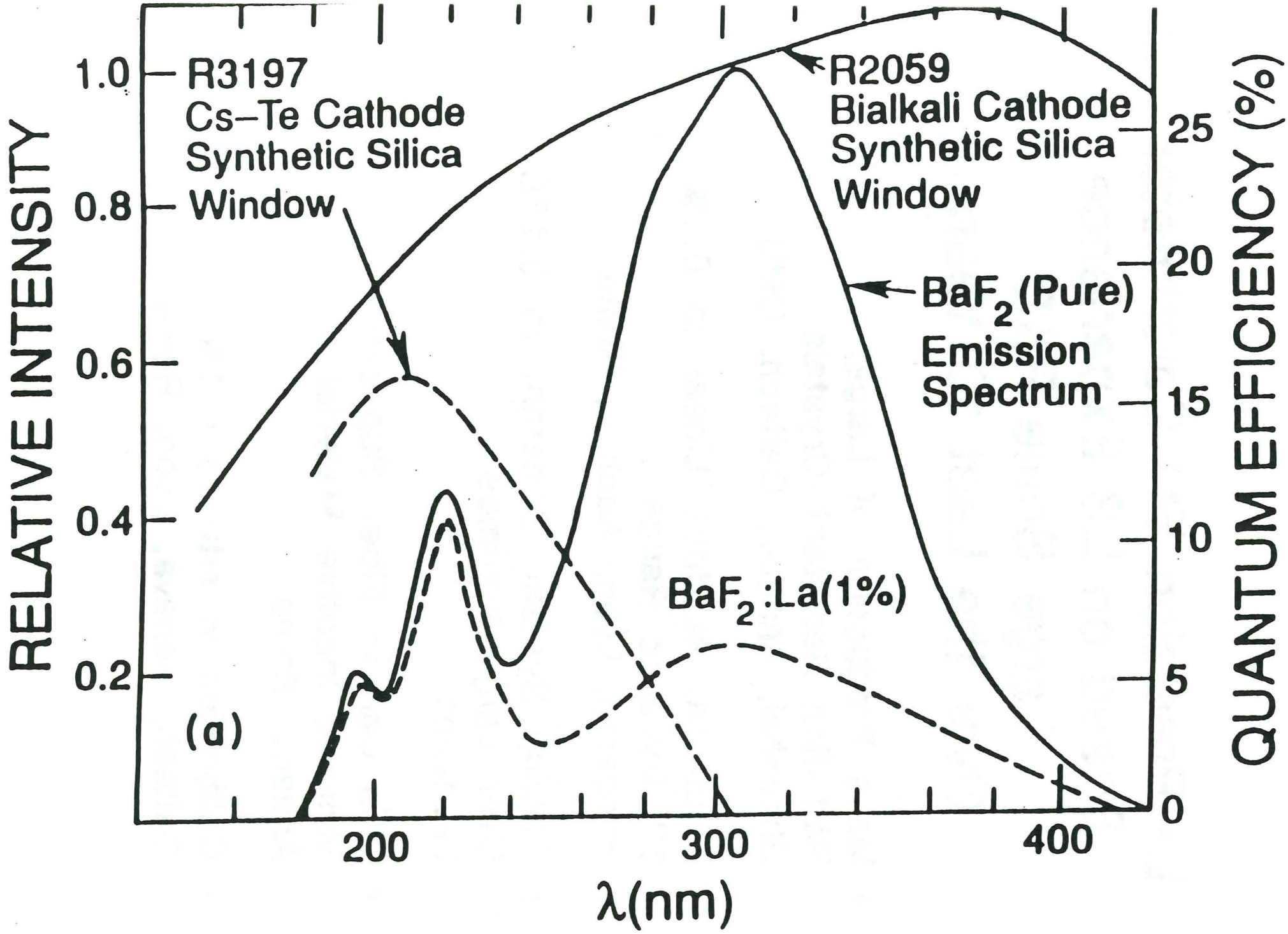
RELATIVE INTENSITY
1.0
0.8
0.6
0.4
0.2
R3197
Cs–Te Cathode
Synthetic Silica
Window
R2059
Bialkali Cathode
Synthetic Silica
Window
BaF2 (Pure)
Emission
Spectrum
BaF2 :La(1%)
(a)
200
300
400
λ(nm)
25
20
15
10
5
0
QUANTUM EFFICIENCY (%)

L* Precision EM Calorimeter Based on L3 Experience Large Scale R&D Over the Last 10 Years

- Mass Production of Large, Radiation Resistant Crystals
  Shanghai, Annecy, Caltech, CMU
- Electronic Readout: Linear to 0.1%
  10^6 Dynamic Range
  Princeton, Lyon, Aachen, Rome
- Cooling System: Constant to 0.1°C
  Over Large Volumes
  Lausanne
- Thin Carbon Fiber Support:
  Minimize Inactive Material
  Annecy, Rome
- Calibration in situ to < 1%
  Caltech, Geneva, Lyon, Rome

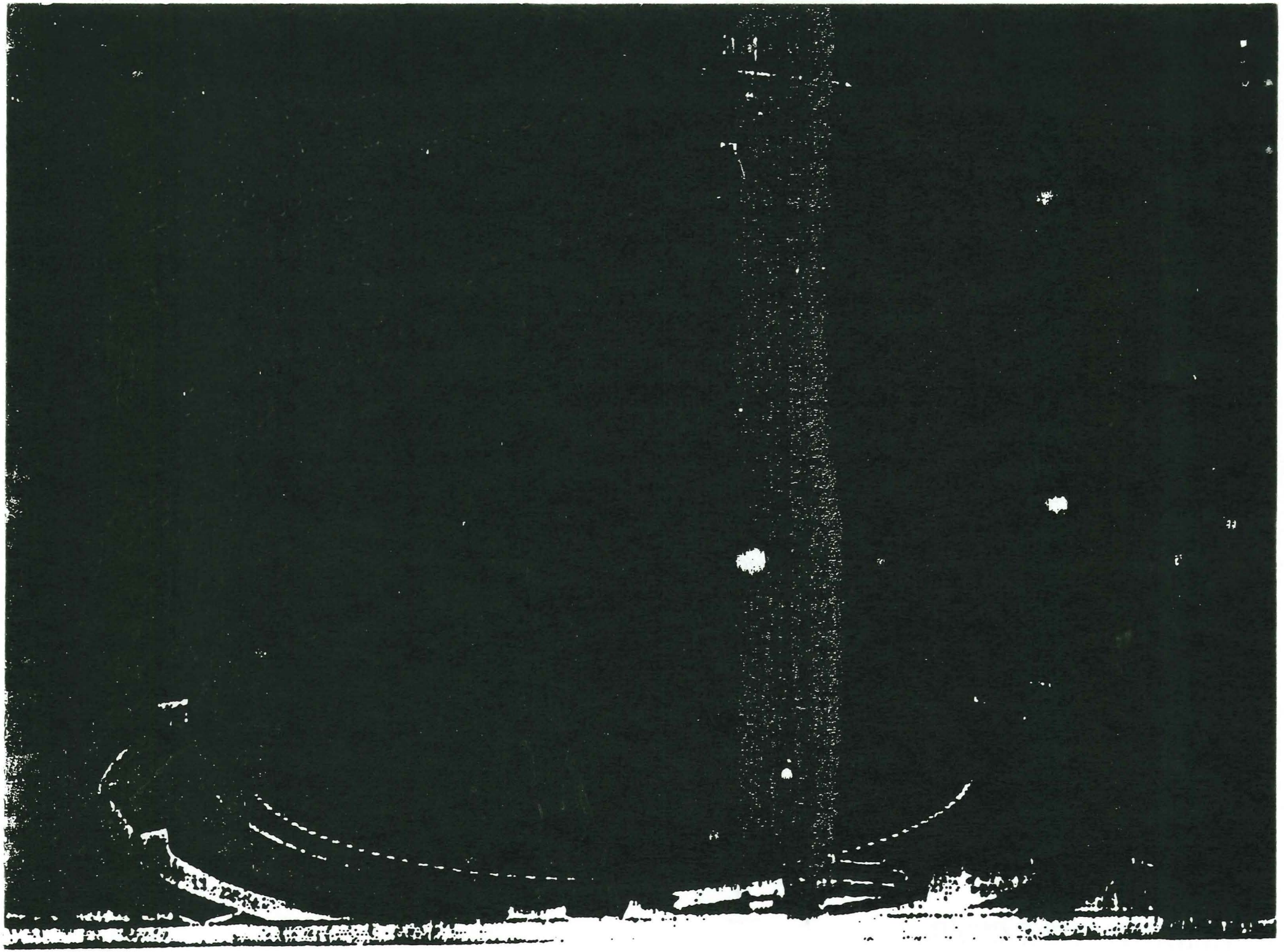

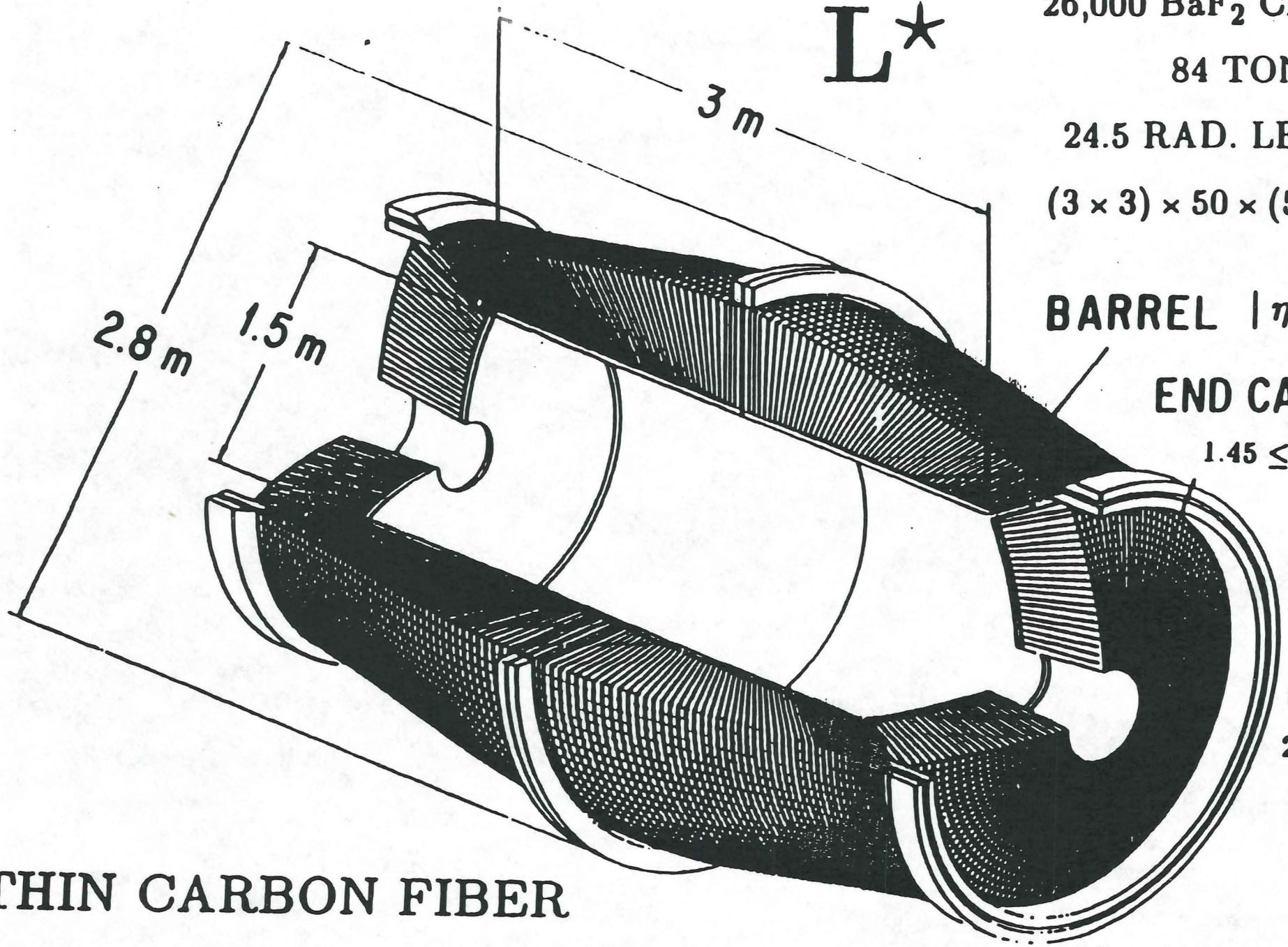

26,000 BaF_2 CRYSTALS

84 TONS

24.5 RAD. LENGTHS

$(3 \times 3) \times 50 \times (5 \times 5)$ cm^3

BARREL $|\eta| \leq 1.45$

END CAP

$1.45 \leq |\eta| \leq 2.8$

Forward Cone:

$z = \pm 10.5$

$2.8 \leq |\eta| \leq$

ΓHIN CARBON FIBER

)0-300μm TOLERANCES

L* Electromagnetic Calorimeter (BaF_2)

$$\frac{\sigma}{E} = \frac{1.3\%}{\sqrt{E}} + 0.5\%$$

- e/jet $\approx 10^{-4}$
- Shaping time 3 ns, gate in One Beam-Crossing
- Radiation Resistance
- $\Delta\theta = \Delta\varphi = 0.2^{\circ}$

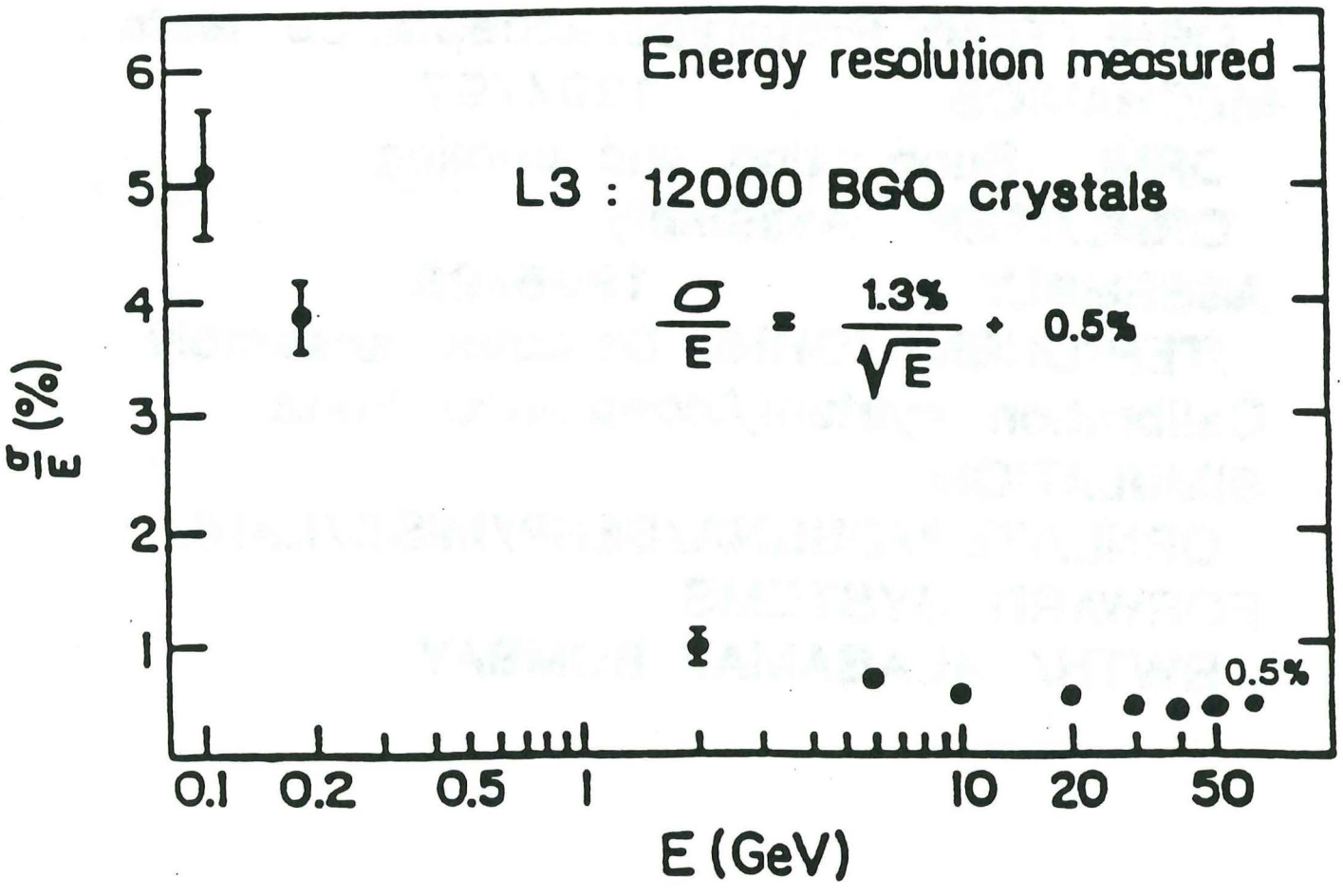

HC CONSTRUCTION
SILICON OPTION

CENTRAL AND ENDCAP REGIONS
DESIGN 1991/92
ORNL/ITEP/DUBNA/TENN
Si DETECTORS 1993/97
DUBNA/TENN R & D for production
DUBNA/ORNL Ingots and wafers, Qualit
ITEP/SERP Prototype construction
Tests at ITEP/ SERP, Quality control
ELECTRONICS 1993/97
ORNL/TENN Prototype/acceptance tests
MECHANICS 1994/97
ORNL Supporting and cooling
ORNL/ITEP Assembly
ASSEMBLY 1996/98
ITEP/DUBNA/ORNL Detector assembly
Calibration system, Acceptance tests
SIMULATION
ORNL/ITEP/DUBNA/SERP/MISS/LANL
FORWARD SYSTEMS
RWTH/ ALABAMA/ BOMBAY

HC CONSTRUCTION
LIQUID SCINT. OPTION

CENTRAL AND ENDCAP REGIONS

DESIGN 1991/92

ORNL/ITEP/LLNL/TENN

DETECTORS 1993/97

ITEP/ORNL R & D for production

ITEP/ORNL Detectors, Quality

ITEP/SERP Prototype construction

LLNL/ORNL Photodetectors

ELECTRONICS 1993/97

ORNL/TENN Prototype/acceptance tests

MECHANICS 1994/97

ORNL Supporting and cooling

ORNL/ITEP Assembly

ASSEMBLY 1996/98

ITEP/DUBNA/ORNL Detector assembly

Calibration system,Acceptance tests

SIMULATION

ORNL/ITEP/DUBNA/SERP/MISS/LANL

FORWARD SYSTEMS

RWTH/ ALABAMA/ BOMBAY

ward Calorimeter Systems

angular coverag

$0.3° \leq \theta \leq 6.7°$

$5.95 \geq \eta \geq 2.84$

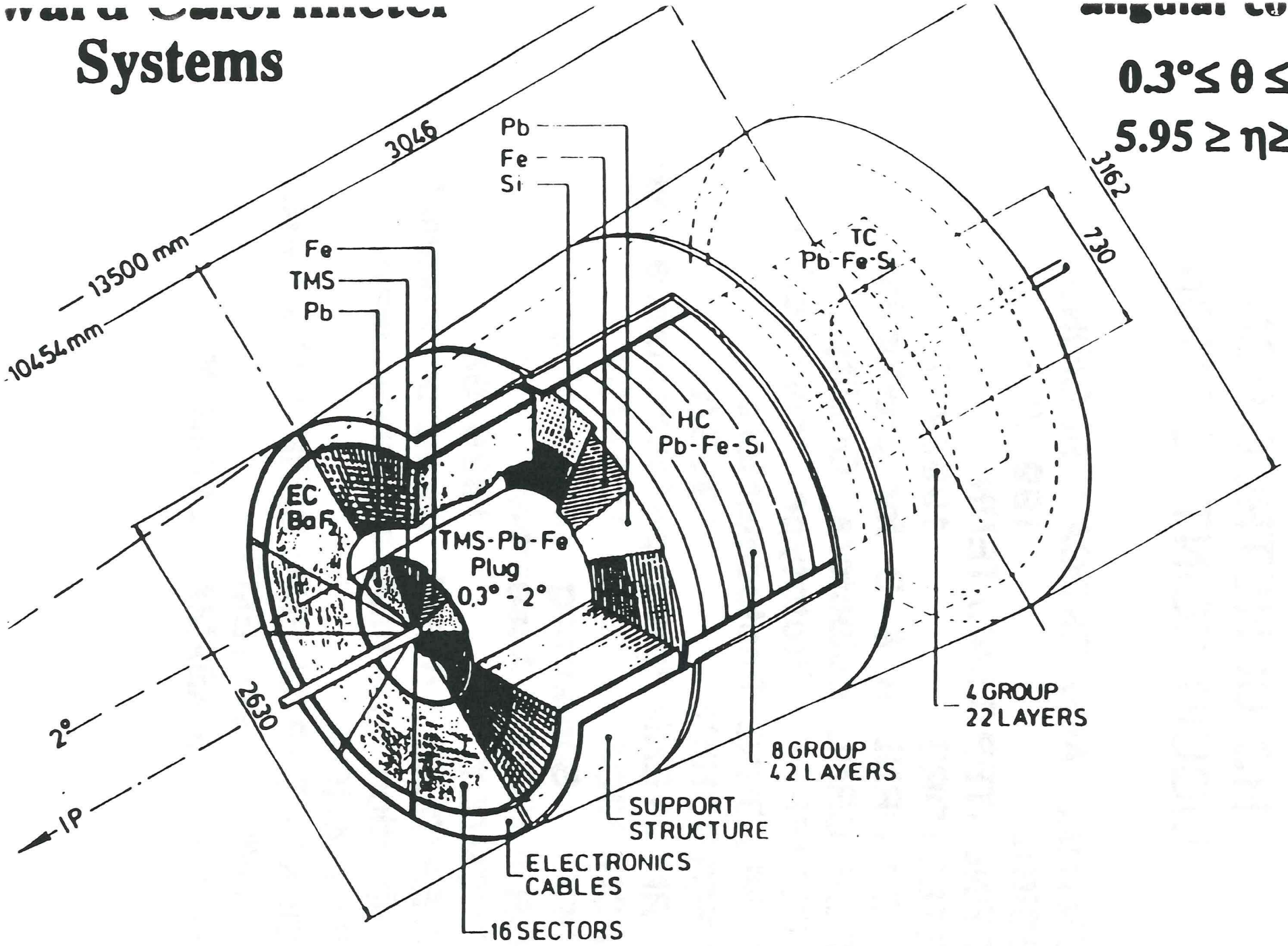

LIQUID SCINTILLATOR
R & D STATUS

ITEP a prototype detector plane

is under construction

Livermore will construct a cell and test it

with new photodetectors

ORNL together with ITEP will build

the hadron calorimeter prototype module

of 6 λ deep and test it

LIQUID SCINTILLATOR R&D ISSUES

* Light collection system optimization
* Scintillator should match the fiber both chemically and optically
* Fiber gluing and sealing techniques
* Photodetectors: fast, compact, stable, tolerant to magnetic field
* Radiation resistance of fibers

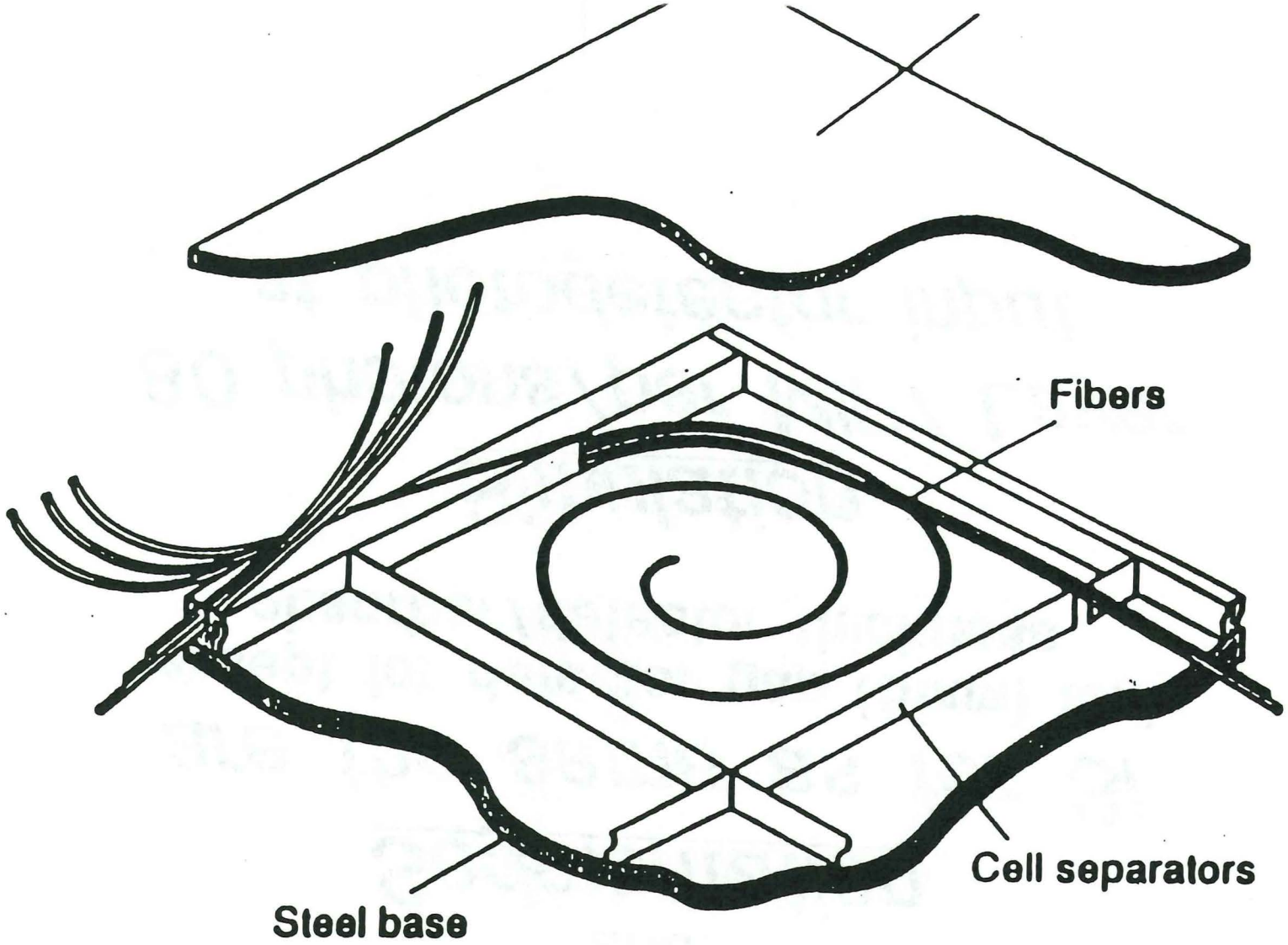

The light readout is made thru a fiber that spirals inside the liquid scintillator cell

Liquid Scintillator Option

Decay time : 2ns

Mechanical design

and

Segmentation

are the same as for Si

except for detector gap (5mm) and absorber/detector thickness

Simulation

80 photons/per MIP/ Layer

at photodetector input

SILICON DETECTOR
R & D PROGRAM

Started in 1988

40 ITEP and 30 Dubna physicists and engineers

ITEP, U Tenn, ORNL, Dubna construct
a silicon detector 0.5m x o.5m
to perform beam scan
of hadron and electron showers

ITEP, U Miss, RWTH (Aachen) coordinate
simulation studies

Silicon Procurement

Silicon detectors are from USSR
JINR *(Dubna) is coordinating the effort.*

➡ *Current crystal production :*
Ti-Mg Factory (TMF) Ukraine

- monocrystals 76mm, 10cm long
- annual production 5 - 6 tons

➡ *Current wafer production :*
Univ. of Bielorussia Research Center, Minsk

- performs slicing, lapping, polishing, thermal oxidation, photolitography, ion implantation
- annual production of 700'000 wafers

➡ *Silicon amount needed :*
5000m^2 or 24 tons (20% contingency included)
3'000'000 wafers

Silicon
Issues to be solved

(1) Cost

(2) e/h = 1 for Si/U

More tests of Si/Fe-Pb are under way (SICAPO)

(3) Radiation damage ***should be understood***

(4) Radiation hardness ***Silicon calorimeter should withstand total annual neutron fluence*** 10^{12} to 10^{13} neutrons/cm^2

Dose due to charged particles is less important

ADVANTAGES OF SILICON

- Speed : transit time 15-30 nsec
- Linear Response : no saturation
- Transverse and longitudinal segmentation:

  only limited by number of channels
- No cryogenics
- Insensitive to magnetic fields
- Monitoring : easy by source
- Mechanics : simple
- Stability in time : very good

RADIATION EFFECTS ON SILICON

- Radiation damage in silicon is bulk damage due to trap formation.
  Leakage current increase due to these traps is highly temperature dependent.
  We plan to operate the detector at $-20^{\bullet}C$
  This gives factor 30-80 in radiation hardness

- The traditional use of Si in nuclear spectroscopy required long shaping times and low noise, noise increase due to leakage increase was not tolerable.
  In case of 10ns shaping time the effect of noise due to leakage current is negligible.

These two factors provide 2 to 3 orders of magnitude improvement in Si radiation hardness.

Trigger Considerations

- *Fast energy trigger*

- *Fast isolated muon trigger is also possible due to fine longitudinal and transversal segmentation*

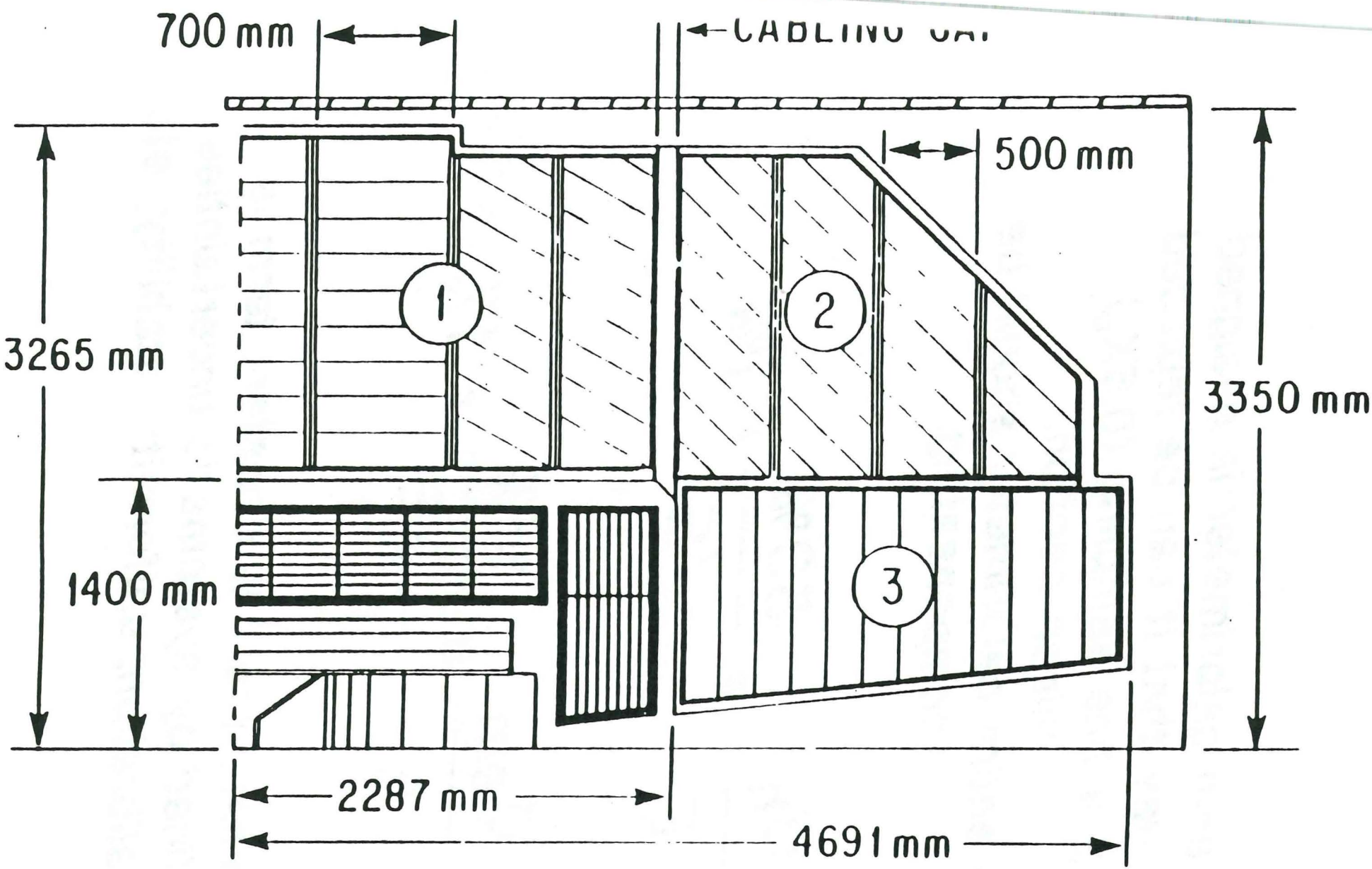

PROPOSED SILICON CALORIMETER
SIDE QUARTER SECTION

The e-m calorimeter is designed in a way that it can be replaced by a fine sampling ($0.5X_o$) silicon section.
The entire calorimeter should be compensating.

$$\frac{\sigma_h}{E} = \frac{50\%}{\sqrt{E}} + 1\%$$

$$\frac{\sigma_{em}}{E} = \frac{15\%}{\sqrt{E}} + 1\%$$

Where the 1 % constant term is defined by systematic uncertainties of calibration, uniformity, stability, etc.

EXPECTED ENERGY RESOLUTION

From our experience with the L3 calorimeter the jet energy resolution of the combined BaF_2 and Si/Fe-Pb calorimeter system will be:

$$\frac{\sigma_h}{E} = \frac{50\%}{\sqrt{E}} + 4\%$$

460-11-88